

AD708876

17

THE SPECTRUM OF ATMOSPHERIC TURBULENCE FOR HORIZONTAL  
VELOCITY COMPONENTS IN THE SURFACE BOUNDARY  
LAYER OF A SEA BREEZE CIRCULATION

Almazan

Report No. 22

May 1970

Reproduced by the  
CLEARINGHOUSE  
for Federal Scientific & Technical  
Information Springfield Va. 22151

ATMOSPHERIC  
SCIENCE GROUP



The University of Texas  
College of Engineering  
Austin, Texas 78712

This document has been approved  
for public release and sale; the  
copyright is retained.

203

ATMOSPHERIC SCIENCE GROUP  
College of Engineering  
The University of Texas  
Austin, Texas

Report No. 22

May 1970

THE SPECTRUM OF ATMOSPHERIC TURBULENCE FOR HORIZONTAL  
VELOCITY COMPONENTS IN THE SURFACE BOUNDARY  
LAYER OF A SEA BREEZE CIRCULATION

James A. Almazan

Sponsored by

National Science Foundation  
under Grants GA-367X1 and GA-16167  
and  
White Sands Missile Range  
under Contract DA-29-040-AMC-1802E

## FOREWORD

This report, which represents Dr. Almazan's doctoral dissertation, is the first in The University of Texas at Austin series to deal almost exclusively with the turbulent structure of the sea breeze circulation. Dr. Almazan designed the experiment, obtained the observations, reduced the data, and herein, presents his results. His statistical treatment of the data has been carried out in a carefully conceived fashion. Particularly interesting is his use of a "red noise" filter in the determination of significant spectral peaks over the wide frequency range which was observed.

Even though Dr. Almazan has done much with his data, it should be obvious that these data can be analyzed and interpreted in a number of ways. As time permits, Dr. Almazan intends to do more with these data, and it is hoped that others will find his spectra and associated statistics of value in advancing our knowledge of the turbulent structure of the atmospheric boundary layer.

The support for this study has come from many sources as indicated in the Acknowledgements. The major financial aid, however, has come from the National Science Foundation through Grants GA-367X1 and GA-16167. Because of an expressed interest in boundary layer turbulence and data reduction techniques, Dr. Almazan was supported for a few months from funds provided by the U. S. Army Electronics Research and Development Activity, Environmental Science Department of White Sands Missile Range under Contract DA-29-040-AMC-1802E. Field support was provided by the Field Observing Facility of The National Center for Atmospheric Research. The experiments were conducted on land owned by Mr. James White of Stowell, Texas. His cooperation is also gratefully acknowledged.

Norman K. Wagner  
Co-Principal Investigator

#### ACKNOWLEDGEMENTS

The author expresses his sincere gratitude to the following individuals for their contributions to the preparation of this dissertation:

Dr. Norman K. Wagner, who as supervising professor, provided guidance during the entire research project;

Professor K. H. Jehn, a member of the committee, who offered constructive suggestions in the preparation of the manuscript; and

Drs. J. O. Ledbetter and F. X. Bostick, members of the committee, who gave the manuscript a critical review.

Acknowledgement is also given for material contributions in the form of equipment and financial support to the following:

The National Weather Records Center, Environmental Sciences Service Administration, U. S. Dept. of Commerce;

The Atmospheric Science Group of the University of Texas at Austin;

White Sands Missile Range, U. S. Army;

The National Science Foundation;

The National Center for Atmospheric Research; and

The Computation Center of the University of Texas at Austin.

The author also extends his appreciation to Dr. Harold L. Crutcher, educational advisor of the National Weather Records Center, for the sustained moral support and helpful discussions during the past three years.

J.A.A.  
May 1970

# ABSTRACT

Spectral and cross-spectral analyses of horizontal wind components from data collected by the author on an experiment at the upper Texas coast are presented. The experiment was part of the Sea Breeze experiment of 1968 conducted by the Atmospheric Science Group of The University of Texas at Austin. The wind data are from instruments mounted at 1, 6.7, and 27 meter levels on two towers. One tower was 90 meters from the coastline and the other approximately 4.8 kilometers inland on a line perpendicular to the coastline.

The data were recorded simultaneously at both towers on analog tape and digitized electronically. Data samples analyzed are from a continuous 14-hour experiment which covered the land and sea breeze regimes of the sea breeze phenomenon, including the transition period. The sampling periods are approximately 17, 67, and 133 minutes.

An autocorrelation curve and spectrum are presented for each data sample. The spectrum is analyzed assuming hypotheses of "white noise" and "red noise." Confidence limits are placed on the spectral estimates. The physical interpretations of the results are postulated using G. I. Taylor's hypothesis. For the nighttime land breeze, it was found that the spectra of the longitudinal or downstream component data at the lower levels showed more energy at the higher frequencies than that of the lateral component. This was postulated as being caused by mechanical turbulence. The lateral component indicated long meandering waves. Furthermore, an elongation of the eddies with the wind was detected using the 67 minute sampling periods. The size of the eddies was found to increase upward. The cross-correlation of the same components between levels showed higher values laterally than downstream. For the daytime samples, the variance increased at the higher frequencies as

solar radiational heating increased. The downstream elongation was not detected as local horizontal isotropy was approached; furthermore, the horizontal size of the eddies did not increase appreciably with height. The cross-correlation of the same components between levels showed high correlation values laterally and longitudinally. From the data and the cross-correlations, it was indicated that the veering of the winds from a land to a sea breeze regime occurred at the top level first and at the bottom level last.

The spectra of the daytime onshore flow for the two locations are compared. The distribution of the energy among the frequency ranges is discussed for the three levels. The loss of energy by the longer waves and increase in energy by the shorter waves as convection increases are discussed for each level at both locations.

## TABLE OF CONTENTS

	Page
ACKNOWLEDGEMENTS	ii
ABSTRACT	iii
LIST OF FIGURES	vii
LIST OF TABLES	xiii
I. INTRODUCTION	1
A. Statement of the Problem	1
B. Atmospheric Turbulence	3
1. Statistical Description	3
2. Spectrum of Turbulence	9
3. Scales of Turbulence	15
II. EXPERIMENTAL PROCEDURES	19
A. Location and Description of Site	19
B. Description of Instruments	19
1. Wind Sensors	19
2. Temperature Sensors	21
3. Recorders	22
C. Instrumented Towers	22
D. Instrument Calibration	23
E. Analog-to-Digital Conversion	26
F. Data Reduction	29
III. DATA ANALYSIS AND DISCUSSION	32
A. Data Samples	32
B. Spectrum and Cross-Spectrum Analysis Formulae	36
C. Spectrum Representation and Significance Tests	44
D. Analysis of Data Samples	49

Table of Contents (cont'd)	Page
1. Evening Data Samples Taken at the Beach Tower	49
2. Evening Data Samples Taken at the Canal Tower	87
3. Daytime Data Samples Taken at the Beach Tower	96
4. Daytime Data Samples Taken at the Canal Tower	120
IV. SUMMARY AND CONCLUSIONS	149
APPENDIX A	157
APPENDIX B	159
APPENDIX C	171
APPENDIX D	178
APPENDIX E	185
APPENDIX F	188
BIBLIOGRAPHY	205



# LIST OF FIGURES

Figure No.		Page
1.1	Plots of the x- and y-components of Velocity at 1 Meter Level on the "Beach" Tower, 1047-1104 CDT	10
2.1	Area Map	20
2.2	Top View of Lowest Section of Telescoping "Beach" Tower Showing Orientation of Tower and Location of Aluminum Boom	24
2.3	Calibration Curve for a Microvane	25
2.4	Block Diagram of Analog-to-Digital Conversion	27
2.5	Example of Aliasing	27
3.1	Schematic Bivariate Distribution with One Vector Standard Deviation and Angle of Rotation of Major Axis	35
3.2	Spectrum of White Noise	45
3.3	Spectra of Red Noise for Lag 1 Autocorrelation Values of 0.0, 0.5, and 0.8	48
3.4	Autocorrelation Functions of Wind Components, Case I-BN	50
3.5	Spectra of Lateral Components at 1, 7, and 27 m Levels, Case I-BN	52
3.6	Spectrum Analysis of Lateral Component at 27 m. Data Prewhitened by Difference Filter $u(t)-0.6u(t-1)$ , Case I-BN	54

## List of Figures (cont'd)

Page

3.7	Spectrum Analysis of Lateral Component at 27 m. Data Prewhitened by Difference Filter $u(t)-u(t-1)$ , Case I-BN	56
3.8	Spectra of Longitudinal Components at 1, 7, and 27 m Levels, Case I-BN	57
3.9	Spectrum Analysis of Longitudinal Component at 27 m. Data Prewhitened by Difference Filter $u(t)-u(t-1)$ , Case I-BN	59
3.10	Cross-correlation Functions of Components, Case I-BN	60
3.11	Values of Coherence Between Components at 1 m, Case I-BN	62
3.12	Autocorrelation Functions of Wind Components, Case II-BN	65
3.13	Spectra of Lateral Components at 1, 7, and 27 m Levels, Case II-BN	66
3.14	Spectra of Longitudinal Components at 1, 7, and 27 m Levels, Case II-BN	68
3.15	Cross-correlation Functions of Components Between Levels, Case II-BN	70
3.16	Magnitude Spectra and Coherence Values for Lateral Components, Case II-BN	72
3.17	Magnitude Spectra and Coherence Values for Longitudinal Components, Case II-BN	73
3.18	Autocorrelation Functions of Wind Components, Case II-BN	75

List of Figures (cont'd)		Page
3.19	Spectra of Components at 1 m, Case III-BN	76
3.20	Spectra of Wind Components at 7 m, Case III-BN	77
3.21	Spectra of Wind Components at 27 m, Case III-BN	79
3.22	Spectra of Components at 27 m After Prewhitening of Data	80
3.23	Cross-correlation Functions of Longitudinal Components, Case III-BN	81
3.24	Autocorrelation Functions of Wind Components, Case IV-BN	83
3.25	Spectra of Wind Components at 1 m Level, Case IV-BN	84
3.26	Spectra of Wind Components at 7 m Level, Case IV-BN	85
3.27	Spectra of Components at 27 m Level After Pre- whitening of Data, Case IV-BN	86
3.28	Autocorrelation Functions of Wind Components, Case I-CN	89
3.29	Autocorrelation Functions of Wind Components, Case II-CN	91
3.30	Autocorrelation Functions of Wind Components, Case III-CN	92
3.31	Autocorrelation Functions of Wind Components, Case IV-CN	95
3.32	Autocorrelation Functions of Wind Components, Case I-BD	97
3.33	Spectra of Wind Components at 1 m Level, Case I-BD	98
3.34	Spectra of Wind Components at 7 m Level, Case I-BD	100

List of Figures (cont'd)	Page
3.35 Spectra of Wind Components at 27 m Level, Case I-BD	101
3.36 Cross-correlation Functions of Components, Case I-BD	103
3.37 Autocorrelation Functions of Wind Components, Case III-BD	104
3.38 Spectra of Wind Components at 1 m Level, Case III-BD	105
3.39 Spectra of Wind Components at 7 m Level, Case III-BD	106
3.40 Spectra of Wind Components at 27 m Level, Case III-BD	107
3.41 Autocorrelation Functions of Wind Components, Case II-BD	109
3.42 Spectra of Wind Components at 1 m Level, Case II-BD	110
3.43 Spectra of Wind Components at 7 m Level, Case II-BD	111
3.44 Spectra of Wind Components at 27 m Level, Case II-BD	112
3.45 Autocorrelation Functions, Case IV-BD	114
3.46 Spectra of Wind Components at 1 m Level, Case IV-BD	115
3.47 Autocorrelation Functions of Wind Components, Case V-BD	116
3.48 Spectra of Wind Components at 1 m Level, Case V-BD	117
3.49 Spectra of Wind Components at 7 m Level, Case V-BD	118
3.50 Spectra of Wind Components at 27 m Level, Case V-BD	119
3.51 Autocorrelation Functions of Wind Components, Case VII-BD	121
3.52 Spectra of Wind Components at 1 m Level, Case VII-BD	122
3.53 Spectra of Wind Components at 7 m Level, Case VII-BD	123
3.54 Cross-correlation Functions of Components Between Levels, Case VI-BD	124

List of Figures (cont'd)	Page
3.55 Autocorrelation Functions of Wind Components, Case I-CD	125
3.56 Spectra of Wind Components at 1 m Level, Case I-CD	127
3.57 Spectra of Wind Components at 7 m Level, Case I-CD	128
3.58 Spectra of Wind Components at 27 m Level, Case I-CD	129
3.59 Cross-correlation Functions of Components Between Levels, Case I-CD	130
3.60 Autocorrelation Functions of Wind Components, Case II-CD	132
3.61 Spectra of Wind Components at 1 m Level, Case II-CD	133
3.62 Spectra of Wind Components at 7 m Level, Case II-CD	134
3.63 Spectra of Wind Components at 27 m Level, Case II-CD	135
3.64 Cross-correlation Functions of Components Between Levels, Case II-CD	136
3.65 Autocorrelation Functions of Wind Components, Case III-CD	137
3.66 Spectra of Wind Components at 1 m Level, Case III-CD	138
3.67 Spectra of Wind Components at 7 m Level, Case III-CD	139
3.68 Spectra of Wind Components at 27 m Level, Case III-CD	140
3.69 Autocorrelation Functions of Wind Components, Case IV-CD	142
3.70 Autocorrelation Functions of Wind Components, Case VI-CD	143
3.71 Spectra of Wind Components at 1 m Level, Case IV-CD	144

List of Figures (cont'd)

Page

3.72	Spectra of Wind Components at 1 m Level, Case VI-CD	145
3.73	Cross-correlation Functions of Components Between Levels, Case IV-CD	146
3.74	Cross-correlation Functions of Components Between Levels, Case VI-CD	147
3.75	Autocorrelation Functions of Wind Components, Case VII-CD	148

# LIST OF TABLES

Table No.		Page
II.1	Regression Equations for Wind Sensors	26
III.1	Evening Cases Investigated, All Land Breeze Occurrences	33
III.2	Day Cases Investigated	33
III.3	Significant Values of Coherence, Case I-BN	61
III.4	Wavelengths Computed from Significant Frequencies, Case II-BN	67
III.5	Wavelengths Computed from Significant Frequencies, Case IV-BN	82
III.6	Comparison of Wavelengths at Beach and Canal Stations for Period 2213-2220 CDT	88
III.7	Wavelengths Computed from Significant Frequencies, Cases II-CN, III-CN, and IV-CN	93
III.8	Wavelengths Computed from Significant Frequencies, Case I-BD	99
III.9	Wavelengths Computed from Significant Frequencies, Case III-BD	108

## I. INTRODUCTION

### A. Statement of the Problem

The geophysical phenomenon known as turbulence has been the subject of numerous investigations which have led to theoretical and empirical treatises by geophysicists, mathematicians, statisticians and others in related disciplines. The problem of explaining the nature of turbulence, like many others in physics, can be approached in many ways. Some meteorologists tend to view atmospheric turbulence as a microscale phenomenon, since this is the most noticeable manifestation; however, departures from mean flow even on a global scale in the atmosphere are also manifestations of turbulence. In the final analysis, these and intermediate scales of turbulence are interrelated; therefore, this attempt to describe the aspects of a particular experiment of wind measurement should have a bearing on other scales of turbulence.

The main problem dealt with in this particular investigation is that of determining and analyzing the spectra of the horizontal wind velocity in the first thirty meters of the atmospheric boundary layer.

The particular hypothesis to be examined is that there are changes in the turbulent structure of the wind caused by earth surface characteristics, thermal stability, and radiational cooling and heating; and furthermore, that these changes can be detected by spectral analysis. The description of the physical phenomenon then follows from the interpretation of the spectra.

The wind data are from wind instruments mounted at three discrete elevations on two separate towers. The towers were situated approximately 4.8 kilometers (3 miles) apart on a line perpendicular to a coastline: one tower about 90 meters inland from the surf and the other 4.8 kilometers (km) inland.

The location was on the Texas coast approximately 65 km northeast of Galveston, Texas - an area characterized by a long straight coastline and



flat terrain consisting of marshland and grass. This was an ideal location for observing the wind from the Gulf as it is modified by the land mass. Different types of flow were also obtained because of the land-sea breeze phenomenon.

The experiment was part of a major meteorological undertaking by the Atmospheric Science Group of the University of Texas at Austin during the months of June and July, 1968. The experiment is described in Chapter II. Various phases such as the instrumentation, calibrations procedures, and data reduction are covered in detail.

The analyses and discussion of the data are given in Chapter III. Data samples include offshore flow or land breeze, and onshore flow or sea breeze, with other data samples covering the transition periods. Prior studies of the sea breeze phenomenon on a mesoscale have been made in the same area by Hsu (1967, 1969) and by McPherson (1968). The study presented here is a microscale analysis.

The spectral and cross-analyses and the interpretations are also given. The representations are discussed in detail. The results of the analysis are summarized in Chapter IV.

From the viewpoint of data gathering, this experiment utilized some of the latest techniques in the recording, digitizing, and data reduction phases. The method of observation is one of the foundations upon which the final analysis depends; in this experiment, the use of electronic tape recorders reduced the observer error and eliminated the inherent time-lag response error of a mechanical chart recorder.

One year after this particular experiment, another project of a much larger scale was undertaken by several federal governmental agencies, universities, private industry, and National Center for Atmospheric Research

in the Barbados Island region, with the cooperation of the Barbados government (Kuettner and Holland, 1969). The data-gathering techniques included some similar to the one described in this experiment. With the new Global Atmospheric Research Program (GARP) in the planning stages (Charney, 1969), undoubtedly other methods will be found to measure the physical phenomena of the atmosphere and to interpret the results.

## B. Atmospheric Turbulence

### 1. Statistical Description

The geophysical problem of turbulence in the atmospheric boundary layer may be most conveniently approached by considering the earth's surface as a rigid boundary which is heated during the daytime by solar radiation and is cooled at night by infrared radiational heat loss. This diurnal cyclic process in turn heats and cools the adjacent air which flows over the earth's surface. The immediate effect is the density gradient and associated positive or negative buoyancy created by the temperature differences resulting in the rising or lowering of the air. At this point other factors such as wind velocity, roughness of terrain, and gravity become important.

In the laboratory, Osborne Reynold's familiar classical experiment of the stream of dye flowing through a pipe showed that laminar flow existed until a certain value of the Reynolds number was achieved. Reynolds number is defined by  $Re = Ud/\nu$ , where  $U$  is the mean velocity of the fluid,  $d$  is the diameter of the pipe, and  $\nu$  is the kinematic viscosity, i.e., the ratio of the dynamic viscosity to the density. Above this critical value, the character of the flow becomes "disorderly" or "turbulent", causing the velocity profile, which was a parabolic conic section during the laminar state, to change its shape. The single streak of the dye is completely distorted downstream. This phenomenon, which may be called mixing, causes an ever-increasing transfer of

heat and momentum downstream from one layer to adjoining layers. According to Reynolds, the composite nature of the flow is one of a mean motion. This complicated motion is of a random character; a specific "eddy" or fluctuation cannot be predicted in space or time by an explicit mathematical formulation.

The concept of a mean motion with an eddying motion superimposed on it may perhaps be restated as a stochastic geophysical process. This may be interpreted as a geophysical phenomenon made up of a deterministic component and a non-deterministic component, the mean motion being the deterministic part. A deterministic process is defined as one which may be expressed by an explicit mathematical function, e.g., a sine wave. A completely non-deterministic process represents complete chaos, e.g., a random process. In general, all geophysical processes are stochastic in nature, in the sense that even orderly processes usually contain a non-deterministic component.

Applying this concept to the atmosphere, a somewhat laminar type of flow may be envisioned during the nighttime hours under clear skies and stable thermal stratification in layers near the ground; however, because of the surface roughness and variations in the density of the medium, the layers immediately adjacent to the ground (lower boundary) are not laminar. This differential density process is not present in the (Reynolds) laboratory experiment of the dye streak and increasing fluid velocities. The problem then, albeit analogous, is more complicated in the atmosphere even under the most favorable atmospheric conditions.

Notwithstanding, the problem may be attacked from a physical point of view and the equations of motion of an incompressible viscous fluid and the equation of continuity may be used as a foundation.

If a geophysical realization such as an anemometer recording of the wind velocity component,  $u$ , in the  $x$  direction of a Cartesian coordinate system

is given, the realization may be said to represent a stochastic process. Thus  $u$  may be represented by a mean motion plus a random or fluctuating motion, or  $u = \bar{u} + u'$ . The overbar represents a mean value defined by

$$\bar{u} = \lim_{T \rightarrow \infty} \frac{1}{T} \int_{-T/2}^{T/2} u(t) dt$$

where  $T$  is the time interval of the realization and  $t$  is the time. The fluctuation is represented by  $u'$ . (In order for the  $u'$  to be random, the mean value of  $u'$  must be equal to zero.) Similarly, the component in the  $y$  and  $z$  directions,  $v$  and  $w$ , respectively, are given by  $v = \bar{v} + v'$  and  $w = \bar{w} + w'$ .

The turbulent form of the Navier-Stokes equations of motion may be written in an Eulerian frame as

$$\begin{aligned} \rho \frac{\partial \bar{u}}{\partial t} &= \rho \bar{F}_x + \frac{\partial}{\partial x} (\bar{\tau}_{xx} - \rho \bar{u}^2 - \rho \overline{u'^2}) + \frac{\partial}{\partial y} (\bar{\tau}_{xy} - \rho \bar{u} \bar{v} - \rho \overline{u'v'}) \\ &\quad + \frac{\partial}{\partial z} (\bar{\tau}_{zx} - \rho \bar{u} \bar{w} - \rho \overline{u'w'}) \\ \rho \frac{\partial \bar{v}}{\partial t} &= \rho \bar{F}_y + \frac{\partial}{\partial x} (\bar{\tau}_{xy} - \rho \bar{u} \bar{v} - \rho \overline{u'v'}) + \frac{\partial}{\partial y} (\bar{\tau}_{yy} - \rho \bar{v}^2 - \rho \overline{v'^2}) \\ &\quad + \frac{\partial}{\partial z} (\bar{\tau}_{yz} - \rho \bar{v} \bar{w} - \rho \overline{v'w'}) \\ \rho \frac{\partial \bar{w}}{\partial t} &= \rho \bar{F}_z + \frac{\partial}{\partial x} (\bar{\tau}_{xz} - \rho \bar{u} \bar{w} - \rho \overline{u'w'}) + \frac{\partial}{\partial y} (\bar{\tau}_{yz} - \rho \bar{v} \bar{w} - \rho \overline{v'w'}) \\ &\quad + \frac{\partial}{\partial z} (\bar{\tau}_{zz} - \rho \bar{w}^2 - \rho \overline{w'^2}) \end{aligned} \tag{1.1}$$

where  $\bar{F}_x, \bar{F}_y, \bar{F}_z$  are the external forces such as friction, gravity, Coriolis, per unit mass,  $\rho$  is density of the medium, and  $\bar{\tau}_{xy}, \bar{\tau}_{xz}, \bar{\tau}_{yz}$  and  $\bar{\tau}_{xx}, \bar{\tau}_{yy}, \bar{\tau}_{zz}$  are the mean tangential and normal viscous stresses. The Reynolds stresses (also called apparent or virtual stresses) are  $\rho \overline{u'^2}$ ,  $\rho \overline{u'v'}$ ,  $\rho \overline{u'w'}$ ,  $\rho \overline{v'^2}$ ,  $\rho \overline{w'^2}$ , and  $\rho \overline{v'w'}$ . These express the effect of the velocity fluctuations in transporting momentum across a specified surface in the fluid.

It is important to note that these stresses are in the form of correlation coefficients, for

$$R_{xy} = \frac{\overline{xy}}{\sqrt{\overline{x^2}}\sqrt{\overline{y^2}}} = \frac{\sum (x - \bar{x})(y - \bar{y})}{Ns_x s_y}$$

are the equations for the correlation between variables  $x$  and  $y$ , where  $s_x$  and  $s_y$  are the sample standard deviations. This shows that the virtual stresses are proportional to the correlation coefficient between the components of turbulent velocity observed at a fixed point in an Eulerian frame of reference.

G. I. Taylor's theorem (1921) showed that the dispersion of a group of particles in a statistically uniform field of flow; i.e., one in which the mean eddy energy  $\rho \overline{u'^2}$  is constant with respect to time and space, is determined by the magnitude of the velocity variance of the fluctuations  $\overline{u'^2}$  and the nature of the correlation between fluctuations which act on the particle at different times.

Specifically, the Lagrangian correlation is given by

$$R(\xi) = \frac{\overline{u'(t) u'(t + \xi)}}{\overline{u'^2}} \quad (1.2)$$

and denotes the correlation of  $u'$  at times  $t$  and  $t + \xi$ .

Integrating Eq. (1.2) with respect to  $\xi$ ,

$$\left. \begin{aligned} \overline{u'^2} \int_0^t R(\xi) d\xi &= \int_0^t \overline{u'(t) u'(t + \xi)} d\xi \\ &= \overline{u'(t) \int_0^t u'(t + \xi) d\xi} \\ &= \overline{u'(t) X} \end{aligned} \right\} \quad (1.3)$$

where  $X$  is the distance traveled by the particle in a time  $t$  because of the eddy motion. Since

$$\overline{u'(t)X} = \frac{1}{2} \frac{d}{dt} \overline{X^2} \quad (1.4)$$

the following equation may be written:

$$\overline{X^2} = 2 \overline{u'^2} \int_0^T \int_0^t R(\xi) d\xi dt \quad (1.5)$$

This shows that the distance travelled in time  $T$  by the particle is expressed by  $T$ ,  $\overline{u'^2}$  and  $R(\xi)$ . Hence the diffusion of the particle is reduced to a single quantity - the correlation coefficient between the particle velocity at time  $t$  and time  $t + \xi$ .

If the time of diffusion  $t$  is small so that the correlation is essentially still close to the initial value of unity, then by Eqs. (1.4) and (1.5)

$$\frac{1}{2} \frac{d}{dt} \overline{X^2} = \overline{u'^2} t$$

and

$$\overline{x^2} = \sqrt{\overline{u'^2}} t \quad (1.6)$$

If the diffusion is in a stream of air moving with velocity  $U$  and the dispersion is observed at a distance  $x$  downstream from the source, then, by substituting  $t = x/U$  in Eq. (1.6)

$$\frac{\sqrt{\overline{x^2}}}{x} = \frac{\sqrt{\overline{u'^2}}}{U}$$

The analysis also yields a length  $L_L$ , given by

$$\overline{x u'^2} = L_L \sqrt{\overline{u'^2}} = \overline{u'^2} \int_0^{t_0} R(\xi) d\xi$$

or

$$L_L = \sqrt{\overline{u'^2}} \int_0^t R(\xi) d\xi \quad (1.7)$$

when the irregular motion is such that a time  $t_0$  is found in which  $R(\xi) = 0$  for all  $\xi$  greater than  $t_0$ . This length,  $L_L$ , is called the Lagrangian integral scale (length). According to Taylor (1935, p. 425), this "...bears the same relationship to diffusion by turbulent motion that the mean free path does to molecular diffusion." Taylor (op. cit.) showed that the theory of the "scales" of turbulence could be applied to either the Lagrangian or the Eulerian concepts of fluid flow. His method was first used by Mr. L. F. G. Simmons (Taylor, 1935, p. 444; 1937, p. 499) who used a wind tunnel to find experimentally the correlation between the turbulent components of velocity  $u$  and

$u_y$  at two points a distance  $y$  apart across the direction of flow behind a honeycomb with square wire mesh grid. Statistically, if the correlation  $R(y)$  is plotted against  $y$ , the curve should represent the distribution of  $u$  along the  $y$  axis. If the points are many "eddy" diameters apart, the correlation should drop to zero. At this point of zero correlation, an integral "scale" is defined by  $L_E = \int_0^y R(y) dy$ , referred to by Taylor (1935, p. 426) as the "average size of the eddies" in an Eulerian system.

Thus, the two scales defined are

$$L_E = \int_0^y R(y) dy \quad (\text{length})$$

$$L_L = \sqrt{u'^2} \int_0^t R(\xi) d\xi \quad (\text{time})$$

where  $L_L$  is the Lagrangian integral scale of Eq. (1.7).

Later, Simmons and Slater (Taylor, 1938) showed how the energy of the fluctuations could be distributed among the motions of different scale lengths or eddy diameters, i.e., the existence of a spectrum of turbulence. In his article Taylor (op. cit.) discussed the "connexion between the spectrum of turbulence measured at a fixed point, and the correlation between simultaneous values of velocity measured at two points." This is explained in the following section.

## 2. Spectrum of Turbulence

The plots of  $x$  and  $y$  wind components shown in Fig. 1.1 are examples of actual values of the raw data obtained in the field experiment to be described in Chapter II. Note that the fluctuations appear to be random; i.e., there are no discernable periodic components in the data.



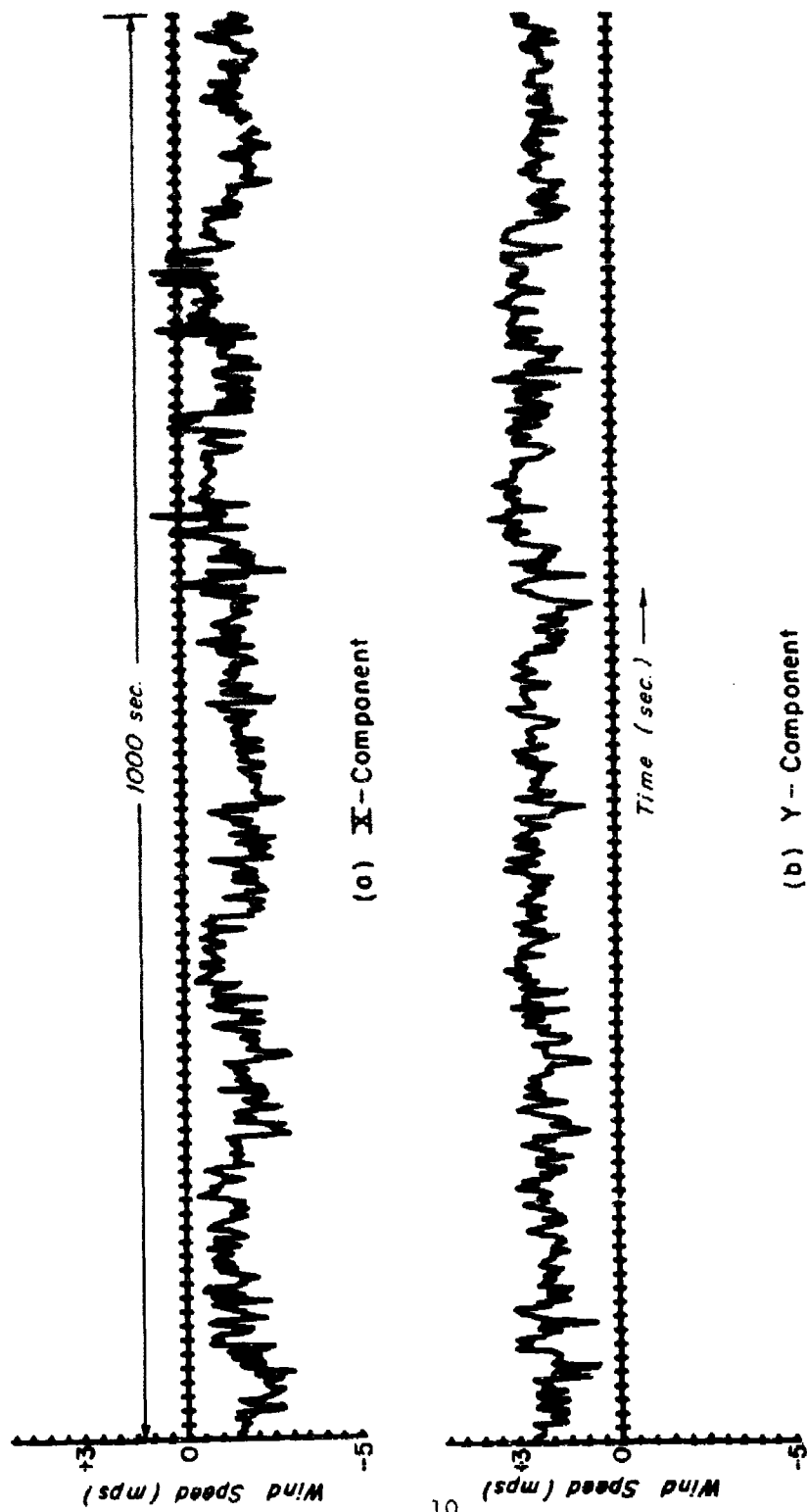


Fig. 1.1 Plots of the x- and y-components of Velocity at 1 Meter Level on the "Beach" Tower, 1047-1104 CDT

If the x-component of eddy velocities is resolved at a fixed point into harmonic components, the variance  $\overline{u'^2}$  is the sum of the contributions from all frequencies. This value  $\overline{u'^2}$  is a measure of the average level of turbulent energy over all frequencies involved in the turbulent motion.

Between the frequencies  $f$  and  $f + df$ , there is some energy fraction. Therefore, if the total energy is given by  $\overline{u'^2}$ , then  $\overline{u'^2} F(f)df$  is the energy contribution to  $\overline{u'^2}$  from frequencies between  $f$  and  $f + df$ . Thus

$$\int_0^{\infty} F(f)df = 1.$$

Also,

$$\overline{u'^2} = \int_0^{\infty} \overline{u'^2} F(f)df \quad (1.8)$$

A form of the spectrum curve is obtained if the spectrum function  $F(f)$  is plotted against frequency  $f$ .

By definition, Fourier integrals are definite integrals which represent an arbitrary function in an unlimited interval (Carslaw, 1950, p. 311). To show that  $\overline{u'^2}$  is the sum of all contributions, the Fourier integral and a form of Parseval's theorem are used.

Let  $u' = \phi(t)$ . The Fourier coefficients are given by

$$\left. \begin{aligned} I_1(f) &= \frac{1}{\pi} \int_{-\infty}^{\infty} \phi(t) \cos 2\pi f t dt \\ I_2(f) &= \frac{1}{\pi} \int_{-\infty}^{\infty} \phi(t) \sin 2\pi f t dt \end{aligned} \right\} \quad (1.9)$$

and therefore,

$$u' = \phi(t) = 2\pi \int_{-\infty}^{\infty} [I_1(f) \cos 2\pi ft + I_2(f) \sin 2\pi ft] df \quad (1.10)$$

Parseval's Theorem states:

$$\frac{1}{\pi} \int_{-\infty}^{\infty} \phi^2(t) dt = \frac{a_0^2}{2} + \sum_{m=1}^{\infty} (a_m^2 + b_m^2) \quad (1.11)$$

Applying the theorem to Eq. (1.10),

$$\int_{-\infty}^{\infty} [\phi(t)]^2 dt = 2\pi^2 \int_{-\infty}^{\infty} [I_1^2 + I_2^2] df \quad (1.12)$$

If the integrals in Eq. set (1.9) and the left side of Eq. (1.12) are taken over a long period of time  $T$  instead of infinity, then, for a constant variance of velocity fluctuations,

$$\overline{\phi(t)^2} = \overline{u'^2} = 2\pi^2 \int_0^{\infty} \lim_{T \rightarrow \infty} \frac{I_1^2 + I_2^2}{T} df \quad (1.13)$$

Comparing this result with the turbulent spectrum of Eq. (1.8), we can write

$$u'^2 F(f) = 2\pi^2 \lim_{T \rightarrow \infty} \frac{I_1^2 + I_2^2}{T} \quad (1.14)$$

where the quantity  $2\pi^2 \lim_{T \rightarrow \infty} \frac{I_1^2 + I_2^2}{T}$  is the contributions to  $\overline{u'^2}$  from the components of frequency between  $f$  and  $f + df$ .

At this point, a general interpretation of the spectrum curve and the correlation curve obtained from a geophysical realization such as the aforementioned (Fig. 1.3) plots of the x- and y-components of wind velocity will be given. Two general cases are considered; namely, (1) variations from small eddies carried by the wind stream (of mean velocity  $\bar{U}$ ) past a fixed point, and (2) variations from large eddies carried by the wind stream.

For the first case of small eddies, the energy should be confined more to the high frequencies; therefore, the spectrum curve should show higher energy contributions in the higher frequencies than in the case of the larger eddies. However, the correlation function should be just the opposite in that the case of the longer eddies show higher correlations at longer lag (time) periods than in the case of the small eddies. This is easy to conceive, since the fluctuations in the this case are more rapid. Also, this should result in high correlation a short distance  $x$  from the fixed point and decreasing correlation as  $x$  increases away from the point of measurement.

Taylor (1938, p. 478) assumed that if the wind velocity which carried the eddies was very much greater than the turbulent velocity, the changes in  $u'$  at the fixed point were due to an unchanging pattern of turbulent motion over the point, or

$$u' = u'(t') = u'(x/\bar{U})$$

where  $\bar{U}$  is the mean wind velocity. Note that the ratio  $u'/\bar{U} \rightarrow 0$  as  $\bar{U}$  increases. Assuming this is true for small values of the ratio, then

$$R(t) = \frac{\overline{u'(t) u'(t + t')}}{\overline{u'^2}}$$

and

$$R(t) = \frac{\overline{u'(t) u'(t + x/\bar{U})}}{\overline{u'^2}}$$

Generalizing Parseval's Theorem and applying it as in Eq. (1.13)\*,

$$\overline{u'(t) u'(t + x/\bar{U})} = 2\pi^2 \int_0^\infty \lim_{T \rightarrow \infty} \frac{I_1^2 + I_2^2}{T} \cos(2\pi F \frac{x}{\bar{U}}) df \quad (1.15)$$

and from Eq. (1.14),

$$\overline{u'(t) u'(t + x/\bar{U})} = \overline{u'^2} \int_0^\infty F(f) \cos(2\pi F \frac{x}{\bar{U}}) df \quad (1.16)$$

Thus

$$\frac{\overline{u'(t) u'(t + x/\bar{U})}}{\overline{u'^2}} = \int_0^\infty F(f) \cos(2\pi F \frac{x}{\bar{U}}) df \quad (1.17)$$

or

$$R(x) = \int_0^\infty F(f) \cos(2\pi F \frac{x}{\bar{U}}) df \quad (1.18)$$

By Fourier transforms the Fourier integral, for  $f(x)$  an even function, may be written

$$\left. \begin{aligned} f(x) &= \frac{2}{\sqrt{2\pi}} \int_0^\infty g(\rho) \cos \rho x d\rho \\ g(\rho) &= \frac{2}{\sqrt{2\pi}} \int_0^\infty f(x) \cos \rho x dx \end{aligned} \right\} \quad (1.19)$$

---

\*This discussion follows essentially Haurwitz (1968).

Substituting the following values in the above equations:

$$\rho = \frac{2 \pi F}{U}, \quad F(x) = R(x), \quad \text{and} \quad g(\rho) = \frac{\overline{U} F(f)}{2 \sqrt{2\pi}}$$

Eq. set (1.19) becomes

$$\left. \begin{aligned} R(x) &= \int_0^{\infty} F(f) \cos \left( 2 \pi F \frac{x}{U} \right) df \\ F(f) &= \frac{1}{U} \int_0^{\infty} R(x) \cos \left( 2 \pi F \frac{x}{U} \right) dx \end{aligned} \right\} \quad (1.20)$$

Therefore,  $R(x)$  and the spectrum function  $\frac{\overline{U} F(f)}{2 \sqrt{2 \pi}}$  are Fourier transforms of one another; that is, if the correlation function of the values at time  $t$  and at time  $t + t'$  is known, the spectrum function may be found, and vice-versa.

### 3. Scales of Turbulence

The two scales derived by Taylor were the Lagrangian integral scale given by  $L_L = \overline{u'^2} \int_0^{\infty} R(\xi) d\xi$  and the Eulerian scale given by  $L_E = \int_0^{\infty} R(y) dy$ . The Lagrangian scale was derived as an analogy to the mean free path of molecular motion; the Eulerian length scale was interpreted as a possible "average size of the eddies." Another scale which may be obtained is the Lagrangian time integral scale given by  $t_L = \int_0^{\infty} R(\xi) d\xi$ .

The correlation functions computed from the data obtained throughout the experiment to be described in Chapter III were such that the Eulerian time integral scale is given by

$$t_E = \int_0^{\infty} R(t) dt \quad (1.21)$$

The existence of such an integral scale is sufficient to imply an ergodic process. This is based on the equality of the ensemble average and the temporal average of any member of the ensemble which may be found as follows:

Given a stationary ensemble of stationary functions  $u(t)$ , the ensemble average of  $u(t)$  is the expected value  $E | u(t) |$ . The time or temporal average is

$$\lim_{T \rightarrow \infty} \frac{1}{T} \int_{-T/2}^{T/2} u(t) dt$$

The condition that these averages be the same may be met by requiring that the ensemble average of the square of the difference between the two averages converge to zero; that is,

$$E \left| \left[ \frac{1}{T} \int_{-T/2}^{T/2} u(t) dt - E | u(t) | \right]^2 \right| \rightarrow 0 \text{ as } T \rightarrow \infty \quad (1.22)$$

Lumley (1962) has shown that a sufficient condition for the expected value to converge to zero is that the integral obtained by expanding, interchanging integration and ensemble averages, and noting that the correlations  $R(t) = R(-t)$  from Eq. (1.22)

$$\int_0^T \left(1 - \frac{t}{T}\right) R(t) dt \rightarrow 0 \text{ as } T \rightarrow \infty \quad (1.23)$$

where  $R(t)$  is the correlation coefficient, converge to a finite value. If  $\int_0^\infty R(t) dt = t_E$  exists, which is some finite time interval, then the integral in Eq. (1.23) has a finite value.

The Fourier transform pair of the Eulerian space correlation  $R(x)$  and the spectrum function  $F(f)$  given in Eq. set (1.20) were

$$R(x) = \int_0^{\infty} F(f) \cos \frac{2 \pi f x}{\bar{U}} df$$

$$F(f) = \frac{4}{\bar{U}} \int_0^{\infty} R(x) \cos \frac{2 \pi f x}{\bar{U}} dx$$

From Taylor's hypothesis,  $t = x/\bar{U}$ , where  $t$  is the time,  $x$  is the distance between two points and  $\bar{U}$  is the mean wind speed

$$\left. \begin{aligned} R(t) &= \int_0^{\infty} F(f) \cos 2 \pi f t dt \\ F(f) &= 4 \int_0^{\infty} R(t) \cos 2 \pi f t dt \end{aligned} \right\} \quad (1.24)$$

At frequency zero,  $F(0) = 4 \int_0^{\infty} R(t) dt$ , and from Eq. (1.21),  $F(0) = 4t_E$ . This states that the Eulerian time integral scale is equal to one-fourth the zero intercept of the spectral estimate. This zero frequency corresponds to a wave of infinite length (a straight line), which implies again that the integral scale must exist and be finite; otherwise the eddy energy in the atmosphere would be infinite (Munn, 1966 p. 76).

Panofsky et al (1958) have shown that  $R(t)$  and  $R(x)$  are nearly equal for low levels of turbulence intensity, which is given by the ratio of the standard deviation of the wind speed and the mean downstream wind velocity. The relationships between the Lagrangian and Eulerian spacial and temporal correlations are more complex, and only a few studies of these have been made. Corrsin (1963) found that the Lagrangian time integral scale is roughly equal to the Eulerian length integral scale divided by the root-mean-square velocity at high Reynolds numbers. Similarly, Eulerian time scales give values approximately equal to the Lagrangian scales.



A basic method of viewing the relationships is to follow Taylor's hypothesis. The Lagrangian time scale  $t_L$  is given by  $t_L = L_L / u'$  where  $L_L$  is the Lagrangian length scale and  $u'$  is the eddy velocity; the Eulerian time scale is given by  $t_E = L_E / \bar{U}$  where  $L_E$  is the Eulerian length scale and  $\bar{U}$  is the mean velocity. The ratio of  $t_L$  to  $t_E$  should be inversely proportional to the intensity of the turbulence,  $I$ . This may be written as

$$\frac{t_L}{t_E} = \beta = \frac{\bar{U} I t_L}{L_E}$$

Pasquill (1963) also showed that the Eulerian autocorrelation  $R(t_E)$  is equal to the Lagrangian autocorrelation  $R(t_L)$  when  $\beta t_L = t_E$ .

The basic theory upon which the spectrum analysis of the wind components is based has been presented in the above discussions. Interest now can be centered on two main areas; namely, (1) obtaining the data to be analyzed, and (2) applying the necessary statistical operations and recent developments in spectrum analysis to get meaningful information.

## II. EXPERIMENTAL PROCEDURES

### A. Location and Description of Site

The experiments were conducted by the Atmospheric Science Group of the University of Texas (Austin) on the Texas Gulf coast approximately forty miles northeast of Galveston, Texas during the month of June, 1968. Fig. 2.1 is a map of the area. The coastline is nearly straight for more than forty miles; inland, the terrain is flat, rising only approximately ten feet in fifteen miles perpendicular to the coast.

Two telescoping towers were erected, each 30 meters in height when fully extended (manufactured by the Rohn Co.); one was located approximately 90 meters from the beach and the other 4.8 km inland on a line perpendicular to the coast near the intracoastal canal shown in Fig. 2.1. (Henceforth, the towers will be referred to as the "Beach" tower and the "Canal" tower.) The only vegetation between the two towers consisted of different types of grasses about one-third to nearly one meter in height. The Canal tower was erected on a clearing about 10 meters in diameter. Otherwise, there were no structures or obstacles to interfere with the wind flow between and around the two towers.

### B. Description of Instruments

1. Wind sensors: The wind direction and wind speed sensing instruments utilized throughout the experiment were, respectively, Gill microvanes and Gill 3-cup anemometers manufactured by the R. M. Young Co. Some of the specifications (nominal values) furnished by the manufacturer are as follows:

Microvane: Model 12301 - delay distance (50% recovery), 0.95 m  
damping ratio, 0.44  
maximum overshoot for sinusoidal fluctuations, 25%  
construction - aluminum alloy with four polystyrene fins  
dimension - 72.5 cm

3-cup anemometer: Model 12101 - distance constant (63% recovery) = 2.8 m  
threshold sensitivity with tachometer generator 0.45 -  
0.54 mps

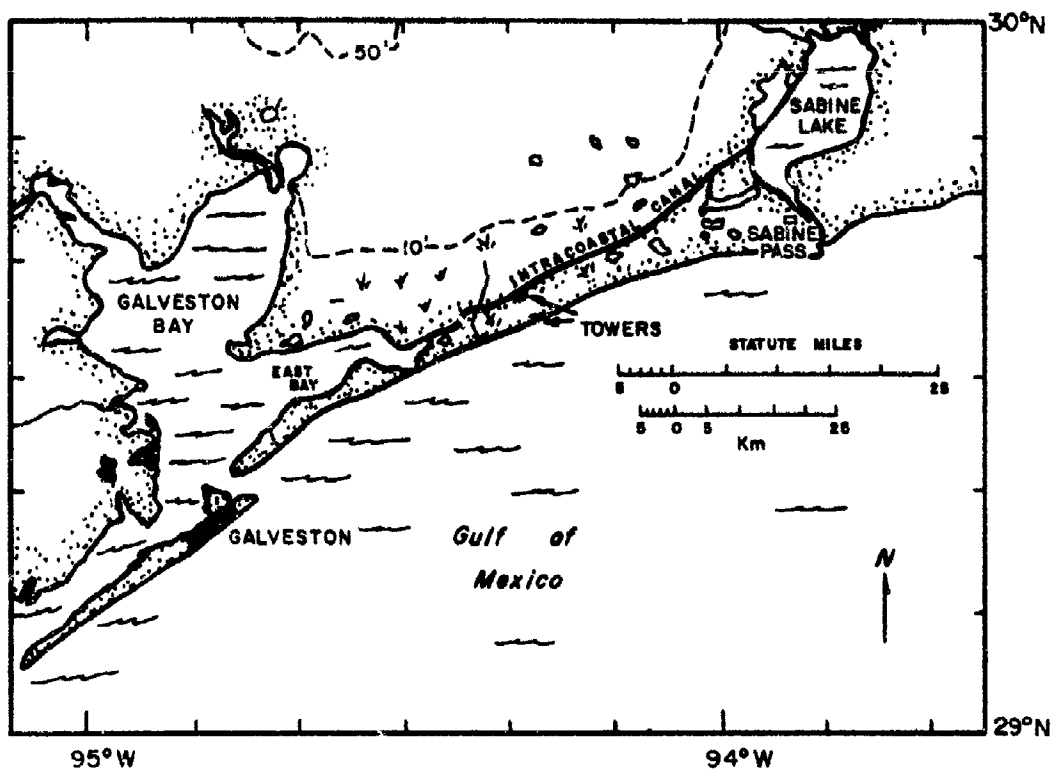


Fig. 2.1 Area Map

The power supply translators were built by Mr. Tom Phillips of the Atmospheric Science Group of the University of Texas.

The time constant of a geophysical transducer may be defined as the period required for the transducer to respond to 63.2 percent,  $\left[ (1 - 1/e) \right]$ , where  $e \approx 2.718$  of a step change in the signal. In this case, the geophysical phenomenon is wind; therefore, a more appropriate term "distance constant" is used to describe the nominal performance of the instrument. The distance constant of a wind sensor is defined as the length of air column required to cause the sensor to respond to 63.2 percent of the square-wave change in speed. This term more aptly describes the performance because it is independent of wind velocity; e.g., if the time constant were 3.0 seconds for an instrument taken from still air to an environment of 3.0 mps, then the same instrument would have a time constant of only 1.5 seconds if it were taken from still air to a 6 mps wind speed. In each case the same length of air must pass for the stepwise change of 63.2 percent. From the specification given above for the anemometer, a wind speed of 2.71 mps would give 63.2 percent change in one second.

## 2. Temperature Sensors

The wet bulb and dry bulb temperatures were measured by bead thermistors housed in a device developed by the Atmospheric Science Group at the University of Texas. The wet bulb temperature sensor was covered with an elongated muslin wick which had one end immersed in distilled water.

The thermistors were accurate to  $\pm 0.1^{\circ}$  Celsius and had a time constant of approximately one second. A squirrel-cage fan was used to continuously aspirate the system internally where the sensors were mounted.

A complete sounding was taken every eight minutes. This slow ascent or descent of the device gave ample time for the sensors to adjust to the

environment and record representative readings since the ascent-descent velocity was about 5 cm per second.

### 3. Recorders

The D. C. signals of the wind direction and wind speed sensors were recorded on eight channel Precision Instrument analog tape recorders, Model 6100. One recorder was used at each of the sites. The number of available analog recording channels was the limiting factor on the number of wind measurement levels recorded. Simultaneous recordings of wind speed and direction were obtained for the 1 m, 6.7 m, and 27 m levels at both towers. One of the channels was used to record reference pulses, the other for voice recordings of time and tape footage for reference. All recordings were made at 0.375 inches per second, allowing nearly 14 hours of continuous analog recording on a standard 1800-foot reel of magnetic tape.

The wet bulb and dry bulb temperatures were recorded on Esterline-Angus Graphic Ammeter strip chart recorders. Reference marks for time and tape footage coincided with the voice recordings on magnetic tape. These strip chart recorders also show the position of the instrument package by a separate side marking pen for the top and bottom points of the temperature package cycle.

The tape recorders and strip chart recorders were installed in air-conditioned van-type vehicles. The air conditioning and fans were installed to cool and circulate the air inside the vehicle as a precaution against malfunctions of the tape recorders. This was a necessary measure since the site was located in humid marshland and the experiments were conducted in June.

### C. Instrumented Towers

The wind directional vanes and 3-cup anemometers described in Section

B were mounted on the Beach tower on 2 meter long aluminum booms at 1.0, 1.9, 3.0, 4.5, 6.7, 11.7, and 27.0 meters above the ground. At the Canal tower the instruments were mounted at 1.0, 3.0, 6.7, 11.7, and 27.0 meters on 5 separate booms. The booms were placed on the towers so that any interference induced by the tower structural members would coincide with the approximate 5-degree electrically open zone of the potentiometers in the wind vane as shown in Fig. 2.2. Any expected interference would probably occur when the wind was from a north-northeasterly direction.

Only three levels were used for the turbulence measurements described in this report; these were the 1.0, 6.7, and 27.0 meter levels.

The dry and wet bulb temperature sensors described in Section B were mounted on a rope-pulley mechanism which raised and lowered the sensors, completing one cycle every 16 minutes from 1.5 meters to 25.3 meters.

#### D. Instrument Calibration

The Gill Microvanes were calibrated in the laboratory at the University of Texas at Austin prior to the experiments. Calibration curves for microvane #1 is shown in Fig. 2.3. The calibrations were repeated just prior to mounting the instruments to insure that no damage had occurred in the packing, transporting, and unpacking. The wind speed calibrations of the 3-cup anemometers made in the laboratory and prior to conducting the experiments were limited to a single maximum output calibration at 1800 RPM (equal to 22.35 mps) listed in the specification. The maximum output voltages for tape recordings were set at 1.000 volt ( $\pm 0.005$ ), which equaled  $\approx 9$  mps, since no speeds higher than this value were anticipated. After performing the experiments, the anemometers were checked again for the calibration value at 1800 RPM. Wind tunnel calibration measurements at the low wind speed values were made using a hot-wire anemometer as a cross-reference. The regression

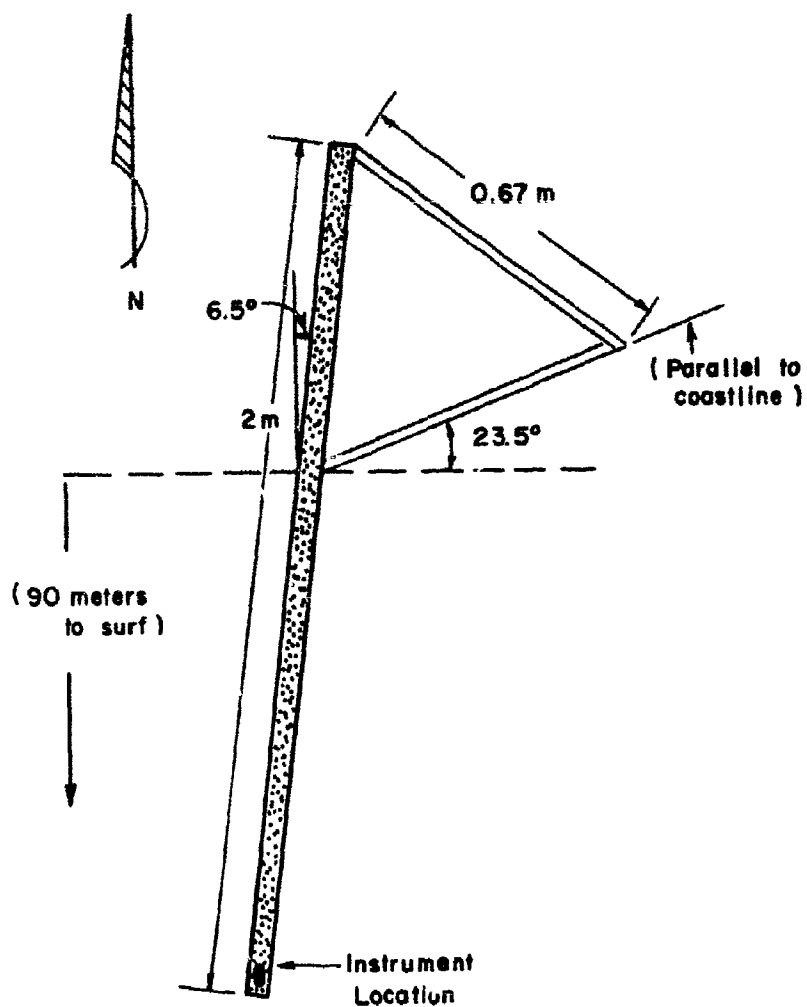


Fig. 2.2 Top View of Lowest Section of Telescoping "Beach" Tower Showing Orientation of Tower and Location of Aluminum Boom

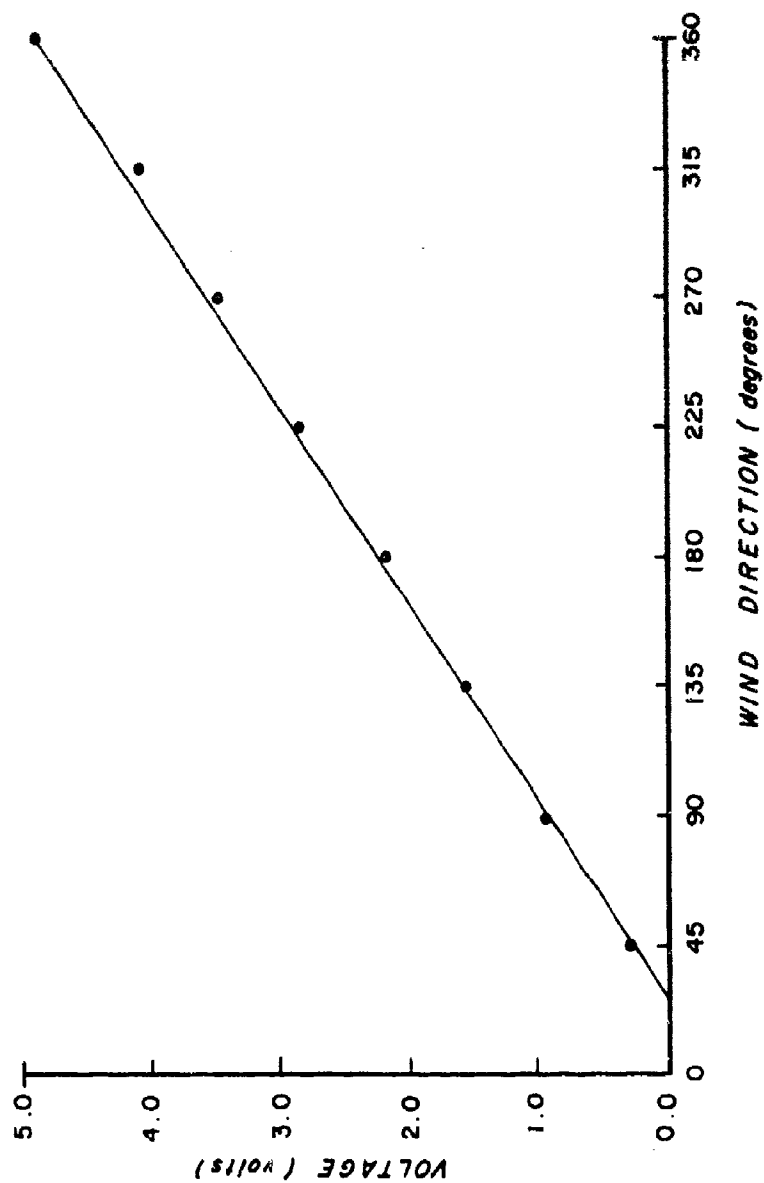


Fig. 2.3 Calibration Curve for a Microvane



curves were computed for each of the microvanes and each of the anemometers using a least-squares technique. Table II.1 shows the regression equations for the six sensors used in the tower experiment. The equations are of the form  $y = mx + b$ , where  $b$  is the  $y$  intercept,  $m$  is the slope, and  $x$  the abscissa.

All data pertaining to a particular sensor were reduced using its respective calibration curve.

Table II.1--Regression  
Equations for Wind Sensors

<u>Microvane No.</u> ( $x$ in degrees of arc, $y$ in volts)	<u>3-cup Anemometer</u> ( $x$ in meters per second, $y$ in volts)
1. $y = 0.004008x - 0.1050$	$y = 0.1555x - 0.01115$
2. $y = 0.004074x - 0.1005$	$y = 0.1587x - 0.02388$
3. $y = 0.004028x - 0.1171$	$y = 0.1577x - 0.01625$
4. $y = 0.003911x - 0.0843$	$y = 0.1632x - 0.03967$
5. $y = 0.003976x - 0.0975$	$y = 0.1516x - 0.01067$
6. $y = 0.004026x - 0.0995$	$y = 0.1607x - 0.02661$

#### E. Analog-to-Digital Conversion

The time series of signals recorded in the field experiments were digitized in the laboratory using the equipment shown in the block diagram, Fig. 2.4.

The two other speeds were available for playback, namely  $3 \frac{3}{4}$  and  $7 \frac{1}{2}$  ips. The analogue to digital voltmeter (Dana model 5403) coupled with the digital tape recorder (Precision Instruments Model 1167) had a sampling rate which could be varied up to 40 samples per second. A low frequency oscillator and trigger generator (square wave) were used to control the sample rate; these are shown as the sample rate generator in the block diagram.

In order to reduce the time of digitizing, a playback speed of  $3 \frac{3}{4}$  ips was used with a sampling rate of 5 samples per second. Since this speed is 10 times faster than the recording speed, the real time was 100 seconds of

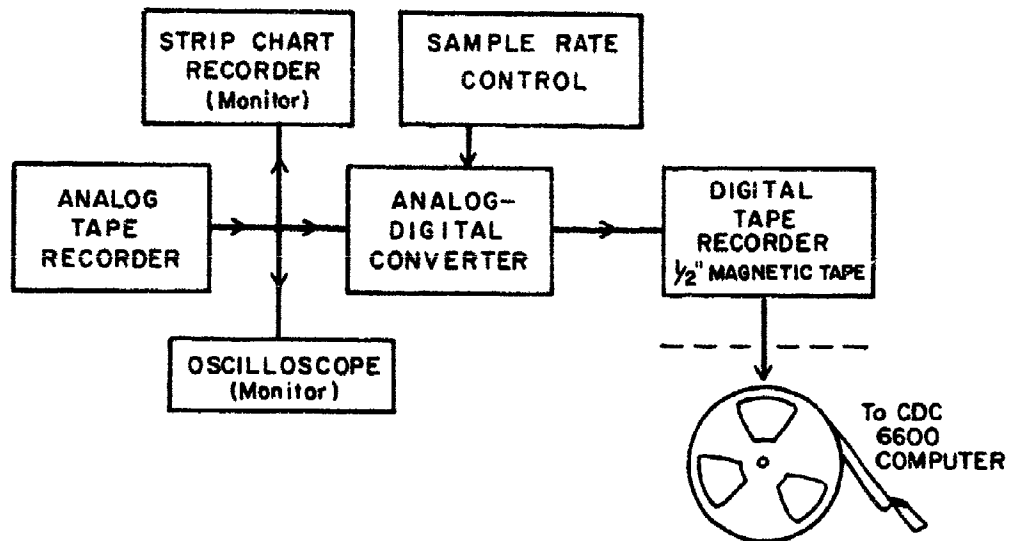


Fig. 2.4 Block Diagram of Analog-to-Digital Conversion

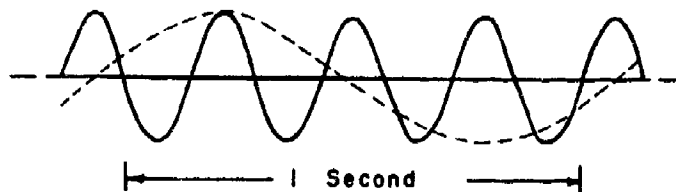


Fig. 2.5 Example of Aliasing

digitized data for 10 seconds of digitizing time. At a rate of 5 samples per second, the real time sampling rate equaled 0.5 samples per second, or 2 seconds per sample. This is the sampling used throughout the entire set of digitized data samples, although other sampling rates were tried to test for aliasing. The speed of 2 seconds per sample was found to be the optimum. The Speedomax W recorder (Leeds and Northrup Co.) shown in the diagram as the Chart Recorder, served both as a secondary signal monitor and as a quick data record. With it, the performance of the tape recorder could be monitored, and the geophysical signal plot served as a reference for actual visual interpretations of the signals and permanent records. Interpretations of stationarity, best intervals, and instrument behavior were valuable as first approximations by use of these charts.

The problem of aliasing is always present when analog records are digitized. The digitized data or data sample are said to be aliased if under-sampling occurred in the digitizing of the data. Fig. 2.5 shows an example of aliasing. A signal with frequency of 4 Hz is shown by the solid line. The circles depict the sampling points, giving an apparent frequency of 1 Hz as shown by the dotted line.

Mathematically, if  $h$  is the sampling interval, the Nyquist frequency is given by  $f_N = 1/2 h$ . This frequency is the highest frequency that may be detected with data sampled at intervals  $h$ . All other frequencies higher than  $f_N$  will be "folded" into a lower frequency between zero and  $1/2 h$ .

There are essentially two ways of avoiding this aliasing problem. One is to determine the sampling interval  $h$  prior to digitizing; the other is to pre-filter the raw data to remove the frequencies higher than  $f_N$ . The first method has been used throughout all the samples used in the experiments.

Another point to be considered is that the time series obtained

were from physical instruments which had inherent inertia. These time series are said to be "Band-limited" for no frequencies higher than a certain maximum frequency  $f_0$  are contained. This frequency  $f_0$  is determined by the frequency response of the instrument. This feature then facilitates the task of finding the Nyquist frequency because, for a given set of atmospheric conditions to be measured,  $f_0 = f_N$ . This frequency may be found (approximately) by using the specifications and calibration data of the instrument.

Another problem to be considered initially is one of whether to make analog recordings or to digitize directly from the sensor, for the latter is less time consuming and more direct. The problem involves the proper sampling rate; undersampling causes aliasing problems and oversampling is inefficient. The matter of convenience of the direct digitizing method sacrifices the optional sampling rate which is the main advantage of the analog method. For example, 10 to 14 hours of recordings might be made of a geophysical process such as the wind. Afterward, the digitizing interval might be varied to test for aliasing and to find the optimum rate. If considerable changes occur, such as wind speed of 2 mps gradually increasing to 10 mps, the optimum sampling rate will differ in each case, and can be readily changed. On the other hand, for a direct digitized record, the sampling rate or rates have been fixed, and cannot be varied. Constant monitoring by the investigator is needed when the data are being recorded in order to change the sampling rate if required.

#### F. Data Reduction

The analog records on magnetic tape were first played back and recorded on strip charts using the Speedomax recorder. Time "hacks" and footage were noted on the strip charts for reference marks. One set of data from a tower thus required six different strip chart recordings. Appendix A,

Fig. A.1, shows a sample from the beach location for June 11-13, 1968. The records were then examined for any instrument malfunctions and power failures which may have occurred. More important, however, was the actual first approximation of any obvious trends. Also, since wind statistics were to be computed, different sample domains could be obtained by visual observation of the record. For example, the gross statistics such as second moments about the mean (variance) would be different for stable atmospheric conditions as compared with unstable conditions, for two different populations are involved. Although the statistics could be computed, bimodal distribution and other configurations could result. By a visual inspection of the data, "best" sampling periods may be obtained.

Once the sampling periods of records were determined, the analog records were digitized by playing one channel at a time through the DANA digital voltmeter. The sampling interval was determined by means of an electronic clock mechanism as shown in Fig. 2.4. The reference pulses on one of the channels served as starting "marks" for the digitizing of all the channels, since the starting points had to be exact. Strip chart recordings were also made during the digitizing process. An oscilloscope was also used as a visual monitor of the output signal, since the Sreedmax recorder had an inherent time delay and high frequency interference could not be detected as readily as on the oscilloscope.

The number of data points in each sampling record was between 4200 and 6400; thus a continuous record without inter-record gaps or end-of-files was obtained for 8400 seconds (140 minutes) up to 12,800 seconds (213 minutes).

The half-inch magnetic tapes with the discrete data samples were then processed in the Control Data Corporation 6600 computer at the University of Texas Computation Center. Additional checks were made on the quality of

the data. These were:

- (1) The digital voltmeter occasionally quantized a value of 9.999 volts. In a record of 500 samples, about 4 of these 9.999 values would be found. Rather than compute a statistical analysis of the adjoining points to substitute for these high values, the two adjoining values were simply added and divided by two. The result was substituted for the high value in question.
- (2) The number of data points selected for each data sample was 4000. The data sample of 4000 was taken from the 4200 to 6400 data points at a "best" interval to insure some degree of stationarity for the data samples.
- (3) Certain segments of the data were plotted and compared with the strip chart records to check for aliasing. The raw data were then converted into wind direction in degrees and wind speeds in meters per second. The individual calibration curves obtained by the linear regression best fit were used for each of the data points from a particular sample. The values obtained for wind speed and direction were printed out for further visual inspection.

### III. DATA ANALYSIS AND DISCUSSION

#### A. Data Samples

The data samples for the study are taken from a continuous experiment which began at 2200 CDT on the 12th of June and ended on the 13th at 1300 CDT. This continuous run helped insure that the instruments and equipment all were calibrated the same since daytime and nighttime comparisons were to be made. The data samples and the code to be used throughout this chapter are as shown in Table III.1 for evening samples and Table III.2 for the daytime samples.

The evening samples all occurred during a land breeze. The differences between them are the sampling periods and the time of observation. The daytime samples are more diversified in that the sea breeze phenomenon exists during the period encompassing the samples, first at the beach and later inland.

The land-sea breeze circulation ideally occurs under certain conditions, one of which is that during this period the area surface winds should not be controlled by a synoptic flow pattern. During the evening when the land surface cools by radiation, the sea surface, because of its physical characteristics, maintains a more constant temperature. Therefore, the air will flow from land to sea. This land breeze is characterized by very light winds, usually less than 5 mps.

During the morning daylight hours, as the land surface becomes warmer than the sea surface, the flow is reversed. This reversal of the wind flow is usually characterized by veering (clockwise turning) of the wind with time. The daytime samples were taken during the veering of this wind and 30 minutes after the wind veered from ENE to ESE. Hsu (1969) has made a mesoscale study of the sea breeze using data obtained previously with surface observations, radiosondes, pilot balloons, and aircraft observations. A study of the land

Table III.1. Evening Cases Investigated  
All Land Breeze Occurrences

Code		Date and Time (CDT)	Period Sampled (sec)
Beach Night	Canal Night		
I-BN	I-CN	12/2213-2230	1000
II-BN	II-CN	12/2213-2320	4000
III-BN	III-CN	12/2320-13/0027	4000
IV-BN	IV-CN	12/2213-13/0027	8000

Table III.2. Day Cases Investigated

Code	Date and Time (CDT)	Period Sampled (sec)	Remarks
(Beach Day)			
I-BD	13/1000-1017	1000	Easterly Flow
II-BD	13/1017-1034	1000	Beginning of Sea Breeze
III-BD	13/1005-1022	1000	Beginning of Sea Breeze
IV-BD	13/1047-1104	1000	30 min after Sea Breeze Started
V-BD	13/1103-1120	1000	Same time as Canal IV-CD
VI-BD	13/1000-1107	4000	Beginning of Sea Breeze
VII-BD	13/1103-1214	4000	Sea Breeze Regime
(Canal Day)			
I-CD	13/1103-1120	1000	Land Breeze Regime
II-CD	13/1155-1212	1000	Beginning of Sea Breeze
III-CD	13/1236-1253	1000	30 min after Sea Breeze Started
IV-CD	13/1103-1210	4000	Land Breeze Generally (Same time as Beach)
V-CD	13/1155-1302	4000	Beginning of Sea Breeze
VI-CD	13/1210-1317	4000	Sea Breeze Regime
VII-CD	13/1103-1317	8000	Land and Sea Breeze Regimes



breeze in this same area has been made by Feit (1969). McPherson (1968) describes the sea breeze with a 3-dimensional numerical model.

In order to perform the analysis of the horizontal wind components the digitized data in the form of wind speed,  $V$ , and wind direction,  $\theta$ , were transposed to horizontal components  $X$  and  $Y$  by the orthogonal transformation

$$X = |V| \sin (\theta + \pi)$$

$$Y = |V| \cos (\theta + \pi)$$

The  $X$  is positive for a wind from the west, and negative for an east wind;  $Y$  is positive for a wind from the south and negative for a north wind. Thus, conventional vector notation agrees with meteorological convention since a resultant vector is 180 degrees from a resultant wind vector. The statistics for a bivariate normal distribution (Crutcher, 1957) were computed for these components; a graphical representation of these statistics is shown in Fig. 3.1 for a hypothetical case. The conic section with a vector radius equal to the standard deviation theoretically contains approximately 63 percent of the  $(X, Y)$  coordinates or, adding 180 degrees to the vector angles, this ellipse contains 63 percent of the wind origins. The ellipse is obtained from the various statistical parameters computed as shown in Appendix D for the  $x$ - and  $y$ -components.

The sample records then were grouped into 500 data points each by taking 500 samples for the 1000-sec periods (1 sample per 2 seconds), arithmetically averaging 4 consecutive samples to get 500 samples for the 4000 sec periods, and averaging every 8 for the 8000 sec periods. A few examples of these 500-point records for the  $x$ - and  $y$ -components are shown in Appendix B for daytime and evening cases. Statistical frequency distributions were made

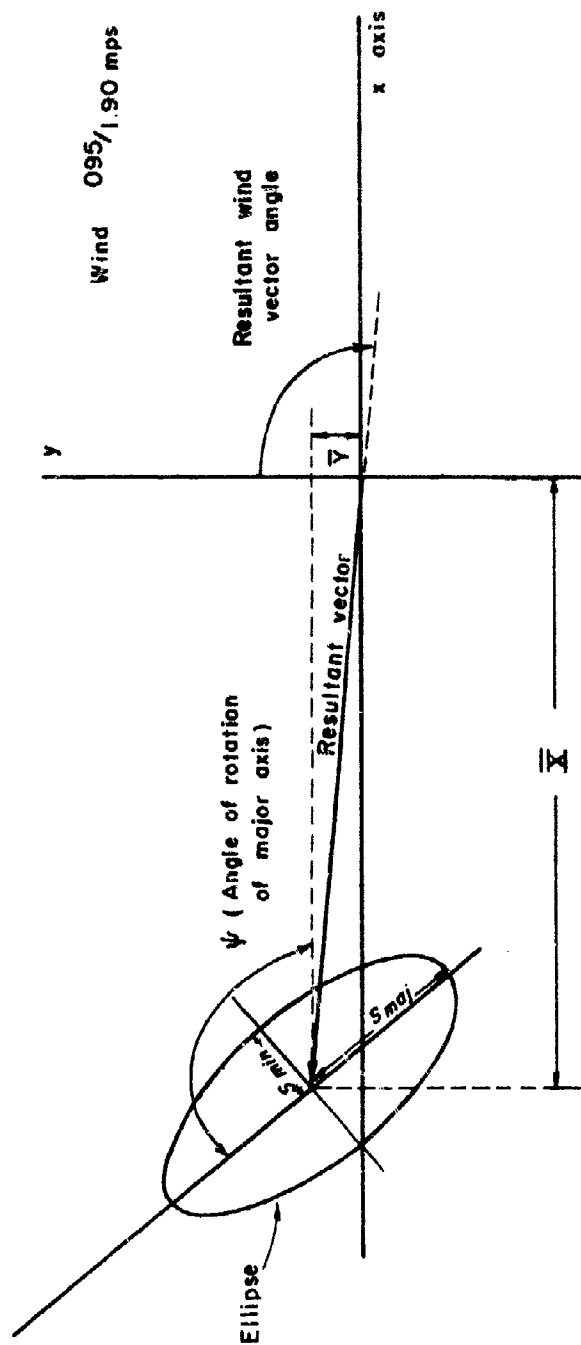


Fig. 3.1 Schematic Bivariate Distribution with One Vector  
Standard Deviation and Angle of Rotation of  
Major Axis

of the sample records and a chi-square goodness-of-fit test for normality also was made (Appendix C). The bivariate statistics computed are shown in Appendix D.

Before computing the spectra, the coordinate axes were rotated to coincide with the resultant or mean wind vector by the transformations

$$u = X \cos \theta - Y \sin \theta$$

$$v = X \sin \theta + Y \cos \theta$$

where  $\theta$  is the angle of rotation. This was done in order to obtain a downstream wind; that is, a mean wind parallel to the x-axis. Taylor's hypothesis could then be applied. Therefore, the downstream, or longitudinal, wind is the u-component and its mean value is the mean wind speed. The cross wind, or lateral wind, is the v-component and has a zero mean value.

#### B. Spectrum and Cross-Spectrum Analysis Formulae

In Chapter I, the development of the statistical theory of turbulence showed the relationship between the autocorrelation function and the modified spectrum function. The spectrum analysis technique, as performed on the data, is a fairly new development. According to Tukey (1968), the beginnings of modern spectrum analysis were developed independently by him and by Bartlett in the late 1940's. More recent developments include the utilization of the "fast Fourier transform" (Gentlemen and Sande, 1966).

The following formulae are essentially those of Blackman and Tukey (1958) and Bendat and Piersol (1968). Some of the problems involved in obtaining the spectral lines, such as aliasing, stability, truncation, etc., have been investigated by Eddy, Duchon, and Almazan (1968).

**Autocovariance Function:** This function gives the dependence of one

value on the neighboring values. For a purely random series the values are independent and no correlation is found; however, when the measurements are of a geophysical signal, there will normally exist some correlation between the values of  $x(t)$  at time  $t$  and time  $t + \tau$ , where  $\tau$  is the lag. The autocovariance function may be expressed by

$$C(\tau) = \int_{-\infty}^{\infty} \int_{-\infty}^{\infty} x(t) x(t + \tau) dx(t) dx(t + \tau) \quad (3.1)$$

for a stationary time series. From the ergodic hypothesis, ensemble averages are equal to time averages, hence Eq. (3.1) may be written

$$C(\tau) = \lim_{T \rightarrow \infty} \frac{1}{T} \int_{-T/2}^{T/2} x(t) x(t + \tau) dt \quad (3.2)$$

The autocovariance  $C(\tau)$  and autocorrelation function  $R(\tau)$  are related by the ratio  $R(\tau) = C(\tau)/C(0)$  where  $C(0)$  is the covariance at lag zero. This form shows that division by  $C(0)$  is equivalent to normalizing the covariance because the covariance at lag zero is equal to the variance. All the raw data were initially normalized by the procedure  $z = (x - \bar{x})/s_x$  where  $s_x$  is the sample standard deviation.

The form of the summation equation used in the computations is

$$R(\tau) = \frac{1}{N - k} \sum_{N=1}^{N-k} x_N x_{N+k} \quad k = 0, 1, 2, \dots, M \quad (3.3)$$

where  $M$  is the maximum lag. The value for the maximum lag was taken as 10 percent of the total number of data points.

**Spectral Function and Estimate:** The raw spectral estimate for normalized discrete data with a mean of zero may be given by

$$G_x(f) = 2h \left[ R(0) + 2 \sum_{r=1}^{M-1} R_r \cos \left( \frac{\pi r f}{f_N} \right) + R_M \cos \left( \frac{\pi M f}{f_N} \right) \right] \quad (3.4)$$

where  $h$  is the sampling interval,  $f_N$  the Nyquist frequency,  $M$  the maximum lag, and  $r = 0, 1, 2, \dots, M$ . The raw spectral estimates were computed for the normalized data by using the following form

$$G_x(f) = 2h \left[ R(0) + 2 \sum_{r=1}^{M-1} R_r \cos \frac{\pi r k}{M} + (-1)^k R_M \right] \quad (3.5)$$

where  $k = 0, 1, 2, \dots, M$ , the harmonic corresponding to the frequency  $f = kf_N/M$ . This gives the spectral estimate at discrete frequencies for the positive and negative sides of the two-sided spectrum.

**Smoothing of Spectral Estimates:** There are several "windows" which are used in smoothing spectral estimates. One of the simplest is "Hanning", named after the Austrian meteorologist von Hann who smoothed meteorological data (but not for spectrum analysis) by using the coefficients. (Other windows sometimes used by spectrum analyzers are Hamming, Parzen, and Bartlett, plus others.) The Hanning lag window weighting function may be defined in terms of a multiplier given by

$$\begin{aligned} D(k) &= \left( 1 + \cos \frac{\pi k}{M} \right) & k &= 0, 1, 2, \dots, M \\ &= 0 & k &> M \end{aligned} \quad (3.6)$$

Using the spectral estimates of the data obtained by Eq. (3.5), the equivalent smoothing of the estimates were computed by

$$\begin{aligned}
G_0^i &= 0.5 G_0 + 0.25 G_1 \\
G_1^i &= 0.5 G_0 + 0.5 G_1 + 0.25 G_2 \\
G_2^i &= 0.25 G_{k-1} + 0.5 G_k + 0.25 G_{k+1} \quad k = 2, 3, \dots, M \\
G_M^i &= 0.5 G_{M-1} + 0.5 G_M
\end{aligned} \tag{3.7}$$

**Cross-covariance Function and Estimate:** The cross-covariance function for two sets of data  $x$  and  $y$  is a measure of the dependence of the values of  $x$  on those of  $y$ . The cross-covariance estimates for a data sample may be taken exactly as for the autocovariance function given by Eq. (3.1); that is,

$$C_{xy}(\tau) \lim_{T \rightarrow \infty} \frac{1}{T} \int_{-T/2}^{T/2} x(t) y(t + \tau) dt \tag{3.8}$$

Similarly, the cross-correlation function for the sampled data was computed using

$$R_{xy}(\tau) = \frac{1}{N-k} \sum_{N=1}^{N-k} x_N y_{N+k}$$

and

$$R_{yx}(\tau) = \frac{1}{N-k} \sum_{N=1}^{N-k} y_N x_{N+k}$$
(3.9)

**Cross-Spectral Function and Estimate:** The cross-spectral function for two time series is the Fourier transform of the cross-correlation function, exactly as for the single record Fourier transform pair. This cross-spectral function, however, is mathematically a two-sided complex valued function given by

$$G_{xy}(\bar{f}) = C_{xy}(\bar{f}) - i Q_{xy}(\bar{f}) \tag{3.10}$$

where  $Co_{xy}$  is the "co-spectral" function (even) and  $iQ_{xy}$ , the complex term, is the "quadrature" function. The co-spectrum is a measure of the covariance between the in-phase components of the two series; whereas the quadrature spectrum is a measure of the out-of-phase frequency components, the out-of-phase being one-quarter period.

Eq. (3.10) may also be written

$$G_{xy}(f) = |G_{xy}(f)| e^{-i\hat{\phi}_{xy}(f)} \quad (3.11)$$

where the modulus, or magnitude, is defined as

$$|G_{xy}(f)| = \{[Co_{xy}(f)]^2 + [Q_{xy}(f)]^2\}^{1/2} \quad (3.12)$$

and the phase angle  $\hat{\phi}$  by

$$\hat{\phi}_{xy}(f) = \tan^{-1} [Q_{xy}(f) / Co_{xy}(f)] \quad (3.13)$$

The magnitude spectrum shows whether the "amplitude" of the component at a frequency  $f$  in series  $x$  is associated with a large or small amplitude at the same frequency in series  $y$ . The phase angle determines whether the frequency components in series  $x$  lead or lag the components of series  $y$  for a given frequency.

In the data analysis, the raw cross-spectral estimates were computed for  $M + 1$  discrete frequencies at  $k$  harmonics corresponding to  $f = f_N k / M$  for  $k = 0, 1, 2, \dots, M$  by

$$Co_k = 2h \left[ A_0 + 2 \sum_{r=1}^{M-1} A_r \cos \left( \frac{\pi r k}{M} \right) + (-1)^k A_M \right] \quad (3.14)$$

where

$$A_r = 0.5 [R_{xy}(\tau) + R_{yx}(\tau)] \quad r = 0, 1, \dots, M$$

and

(3.15)

$$Q_{xy} = 4h \sum_{r=1}^{M-1} B_r \sin\left(\frac{\pi r k}{M}\right)$$

where

$$B_r = 0.5 [R_{xy}(\tau) - R_{yx}(\tau)] \quad r = 0, 1, 2, \dots, M.$$

Finally, the raw estimates were Hanned by the following:

$$C_d^h(0) = 0.5 C_0(1) + 0.25 C_0(2)$$

$$C_d^h(1) = 0.5 C_0(1) + 0.5 C_0(2) + 0.25 C_0(3)$$

$$C_d^h(k) = 0.25 C_0(k-1) + 0.5 C_0(k) + 0.25 C_0(k+1)$$

$$C_d^h(M) = 0.5 C_0(M) + 0.5 C_0(M-1)$$

$$Q^h(0) = 0.0$$

$$Q^h(1) = 0.5 Q(1) + 0.5 Q(2) + 0.25 Q(3)$$

$$Q^h(k) = 0.25 Q(k-1) + 0.5 Q(k) + 0.25 Q(k+1)$$

$$Q^h(M) = 0.25 Q(M-1)$$

Coherence Function: The coherence function may be given by

$$\text{Coh}(f) = \frac{|G_{xy}(f)|^2}{G_x(f) G_y(f)} \quad (3.18)$$



where  $G_x$  and  $G_y$  are the variance spectral estimates. This form of the coherence function is real-valued and has a magnitude range from zero to one. It is a measure of the correlation between time series  $x$  and time series  $y$  at particular frequencies. If the value is zero, the series are said to be incoherent at that frequency; if completely coherent, the value of coherency is unity.

The coherence function was computed using the Hanned variance spectral estimates for digitized data given by Eq. (3.7) and Hanned co-spectral and quadrature estimates given by Eqs. (3.16) and (3.17). Thus,

$$\text{Coh } (f) = \frac{[\text{Co}'(f)]^2 + [\text{Q}'(f)]^2}{G'_x(f) G'_y(f)} \quad (3.19)$$

is the equation used.

**Rejection Filtration:** A filter usually refers to an algebraic expression used on a set of data to isolate periodic components of a particular size either to examine, modify, or remove these components from the set (Eddy et al, Chap. 9). The process of filtering, when used in conjunction with variance spectrum analysis, is sometimes referred to as "prewhitening". This implies that the spectral estimates are filtered in an attempt to flatten or make more even the spectral estimates so as to resemble those of the "white noise" spectrum to be discussed in Sec. C below.

As in nearly all aspects of spectrum analyses, indiscriminate (not in a statistical sense) use of filters may result in erroneous significant peaks in the spectral lines.

The need for two spectral analyses, one using raw data and another using filtered data, is evident in working with geophysical data involving turbulence measurements. In Chapter II, the statistical theory of turbulence

involved the mean wind and fluctuations superimposed on it. This mean wind constitutes the longer waves. Intuitively, if the raw data are used to compute the variance spectrum for a stable atmosphere at a height above 5 m, nearly all of the variance will be concentrated toward low frequencies. The small amount of variance which is distributed among the higher frequencies will be difficult to discern. Once the data have been analyzed to assess the importance of the large low frequency spectral peaks, the data may be filtered to reject the low frequencies. This allows the higher frequencies to be examined for fluctuations by performing a second spectrum analysis on the filtered data.

In the actual analysis, spectral estimates were obtained using the raw data (normalized) and the results examined. Since the object was to remove the low frequencies for the second spectral analysis, a difference filter given by  $y(t) = x(t) - x(t - 1)$  was used on the original wind components. The gain function of this filter is given by

$$\text{Gain}(f) = 2 |\sin \pi f|$$

The computation and graphical plot of this gain function is shown in Appendix D. This spectral window multiplies the Hanned spectral estimates by  $(2 - 2\cos 2\pi f)$  as shown in the appendix; therefore, if the "true" estimates are required, division by this value is necessary.

Another high-pass filter used in the analysis was the difference filter  $y(t) = x(t) - 0.6x(t - 1)$  which does not attenuate the low frequencies as much as the previous one. The spectral estimates are multiplied by  $(1.2 - 3.6\cos 2\pi f)$  as a result of using this filter.

### C. Spectrum Representation and Significance Tests

The variance spectra of the horizontal components have been computed using normalized data and the Hanned estimates. These are represented in the simplest form:  $F(f)$  vs.  $f$ . The trend in geophysics has been to use logarithmic representation with the spectral estimate  $F(f)$  as the ordinate and  $\log f$  as the abscissa; also,  $f \cdot F(f)$  vs.  $\log f$  is sometimes used so as to represent the variance by the area between the frequencies.

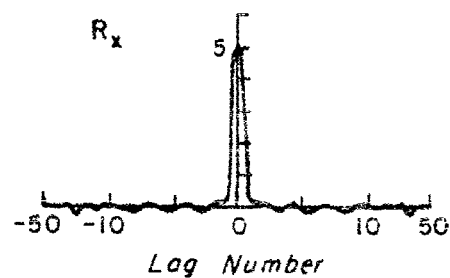
In the spectrum representation, the abscissa is the frequency, labeled from 0.00 to 0.50 cycles per data interval. The data intervals in the real data are 2 seconds, 8 seconds, and 16 seconds.

If a data set consisting of  $N$  random numbers is used ( $N$  large), the spectrum obtained is said to be one of white noise, for the total variance is distributed non-preferentially (theoretically, equally) among all the lines. Therefore, dividing the line variances by the total variance as follows

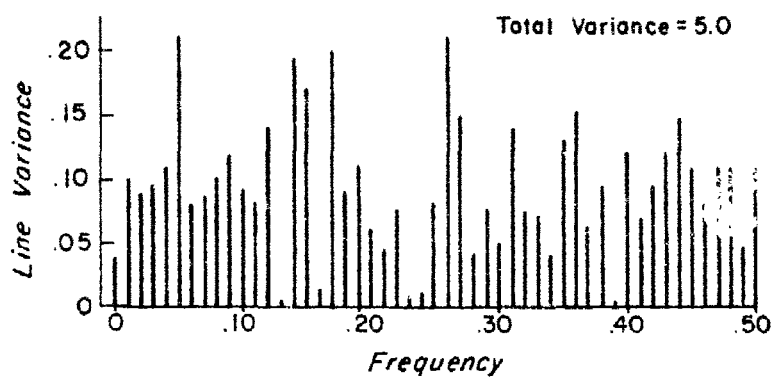
$$\begin{aligned} L_k &= \frac{\text{line variance}}{\text{total variance}/M} & \text{for } k = 1, 2, \dots, M-1 \\ L_k &= \frac{\text{line variance}}{\text{total variance}/2M} & \text{for } k = 0 \text{ and } M \end{aligned} \quad (3.20)$$

the "line ratios" are obtained. The value of unity, then, should be the theoretical value for white noise. Thus in the spectrum representation, the ordinate values represent the ratio of the spectral estimate (line variance) and the line variance from a set of random data.

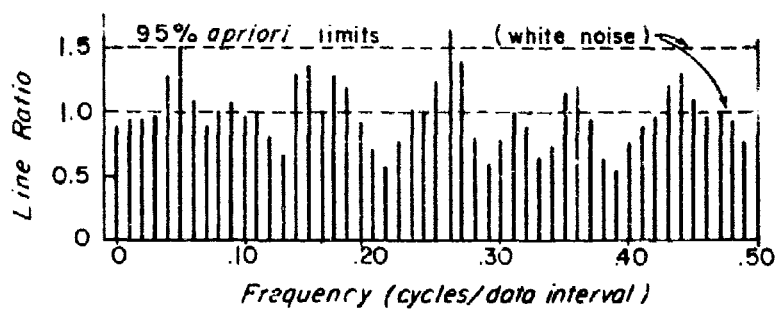
Fig. 3.2 shows a spectrum of a set of 500 random numbers with a mean value of zero and a sample variance of 5. The spectrum in (c) shows some values below the theoretical value of 1.0 and some values above. Clearly, in order for the null hypothesis of white noise to be meaningful, confidence limits



(a) Auto-covariance Function



(b) Raw Spectrum



(c) Hanned Spectrum Using Line Ratios

Fig. 3.2 Spectrum of White Noise

are needed.

The white noise hypothesis made in this analyses is that the spectral estimates obtained from the wind data and those obtained from a set of random numbers are the same. Two confidence limits are computed; namely, the a priori and the a posteriori. As the names imply, the former makes the hypothesis that the estimates or line ratios to be computed will have significantly higher peaks at some expected frequencies, whereas the latter name implies that the spectrum has been computed and the peaks will be found. The a posteriori concept is explained by Eddy, et al (1968, pp. 261-65).

The confidence limits for white spectra were found to be as follows:

95%	1.99 <u>a posteriori</u>
	1.50 <u>a priori</u>
mean	1.00
5%	0.60 <u>a priori</u>
	0.37 <u>a posteriori</u>

These were obtained with a stochastic model which consisted of 500 spectrum analyses of 500 sets of random numbers. The procedure employed is similar to that of a Monte Carlo simulation model. The details are given both by Duchon (1968, Chap. V) and Almazan (1968, Chap. VII).

In spectral analysis of geophysical data such as that of horizontal wind components, large peaks in the low frequency range of the spectrum and very low values at the high frequencies are found whenever there is a large autocorrelation value at lag one, that is, a large degree of correlation between successive values. (It will be shown that this pattern is found in all cases except under extremely turbulent conditions.) This particular

feature may be analyzed for statistical significance by assuming a red noise hypothesis; that is, assuming that the data are the same as those obtained by a first-order linear Markov process.

Gilman, Fuglister, and Mitchell (1963) have derived the following equation for determining a family of red noise curves:

$$I_h = \frac{1 - \rho^2}{1 - 2\rho h\pi/M + \rho^2} \quad (3.21)$$

where  $\rho$  is the lag 1 autocorrelation value,  $h$  is the harmonic and  $M$  is the maximum lag. Note that if  $\rho = 0$ , which is a zero correlation between successive data points, the spectrum is that of white noise. This is shown in Fig. 3.3, which has normalized variance or line ratios as the ordinate values.

For the red noise hypothesis, the 95 percent confidence limit to be shown in the spectra of lateral and longitudinal data were found by "chi-square over degrees of freedom", or  $\chi^2/\nu$ . The effective degrees of freedom for the Hanned spectra may be found by

$$\nu = \frac{2N - M/2}{M} \quad (3.22)$$

where  $N$  is the number in the data set (500) and  $M$  the maximum lag. This equation for finding effective degrees of freedom, Eq. (3.22), is explained in Blackman (1966), and Eddy, et al (1968, Chap. 15).

The values of coherence computed by Eq. (3.19) were tested by use of a table prepared by Mitchell (1966) by interpolation of values found by Amos and Koopmans (1963). The 95 percent significance level is found to be 0.283 for the Hanned spectra of 500 values used in horizontal wind component data cross-spectra. Therefore, any value of 0.283 or higher was taken to be

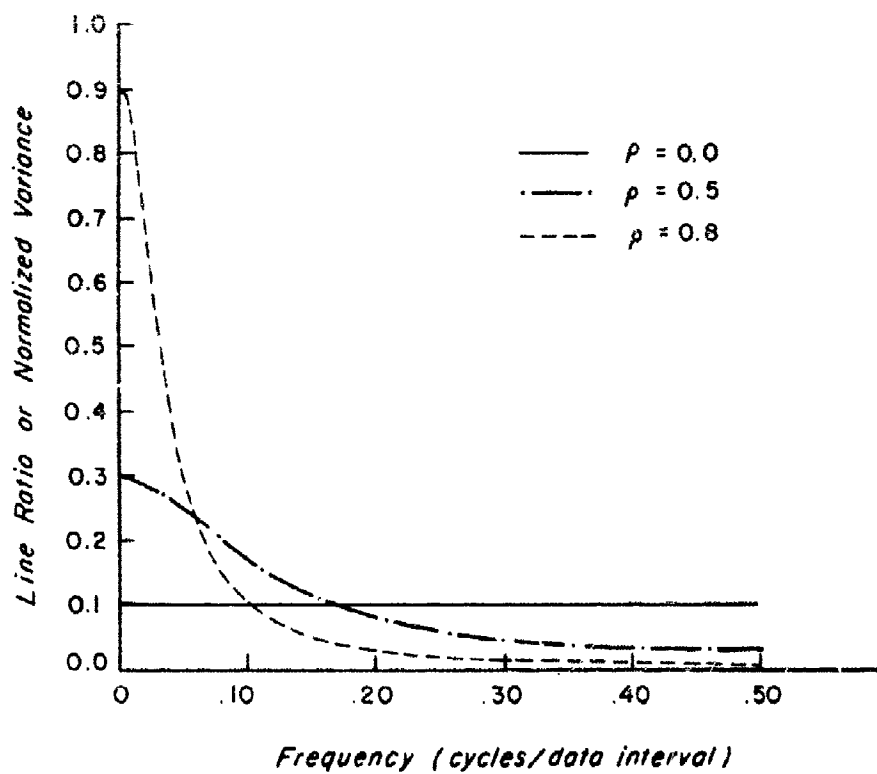


Fig. 3.3 Spectra of Red Noise for Lag 1 Autocorrelation Values of 0.0, 0.5, and 0.8

statistically significant.

In nearly all of the distributions, the skewness statistic and kurtosis statistic were small values. Testing the values for normality may be accomplished by computing the standard error (one standard deviation) for the skewness approximated by  $(6/N)^{1/2}$  (Brooks and Carruthers, 1953) where N is the number of observations. The standard error for the kurtosis may be roughly approximated by  $(24/N)^{1/2}$ . These assume that the N observations are independent, which is not the case in most of the data samples. But the autocorrelation functions presents an indication of the degrees of freedom. For example, if the autocorrelation value goes to zero at lag 50, then the ratio  $N/50$  may be used as the number of independent observations; hence, where  $N=2450$ ,  $(\frac{6}{N/50})^{1/2} = 0.35$  and  $(1.96 \times 0.35) = 0.686$  which means that 95 times out of 100 the skewness value shall be between -0.686 and 0.686 in a normal distribution. The tests are based on the theory of errors and only give a first guess as to the normality of the distributions.

#### D. Analysis of Data Samples

##### 1. Evening Data Samples Taken at the Beach Tower

Case I-BN: Beach Nighttime Sampling Period 1000 sec (2213-2217 CDT)

The autocorrelation functions for Case I-BN are shown in Fig. 3.4(a) and (b) for the lateral and longitudinal components, respectively. The integral scales for the longitudinal case may be approximated for the 1 meter (m) level. For the other two levels and all three levels for the lateral component, the functions show that perhaps a longer period is needed to approximate the "scale." The functions for both the lateral and longitudinal components at the 1 and 6.7 m (henceforth called the "7 m" level) levels show rapid up-and-down motion or oscillations superimposed on the autocorrelation curve. This may be indicative of high frequency (short wavelength) components. Also, the



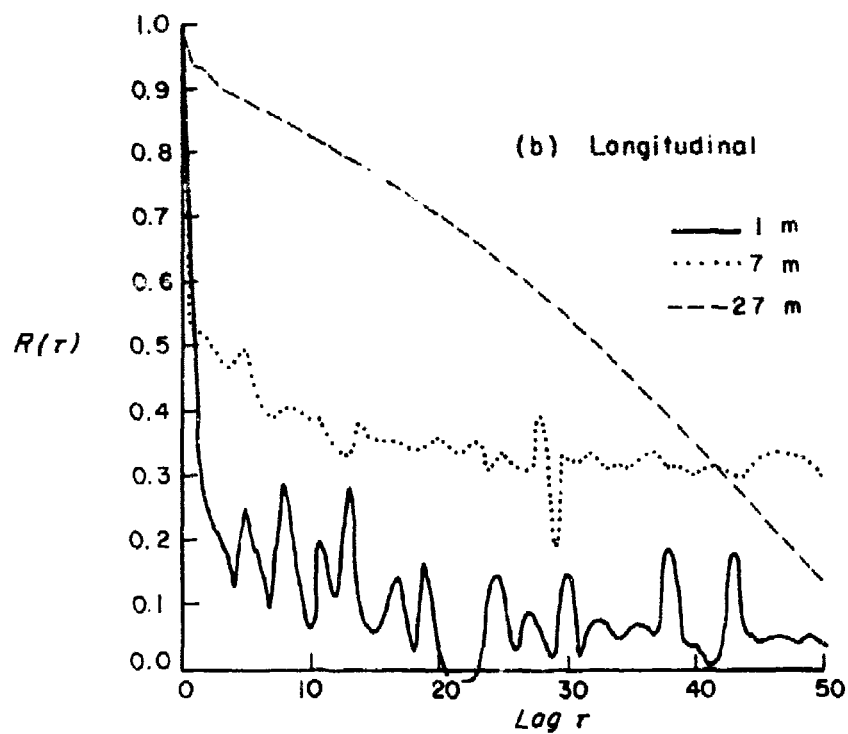
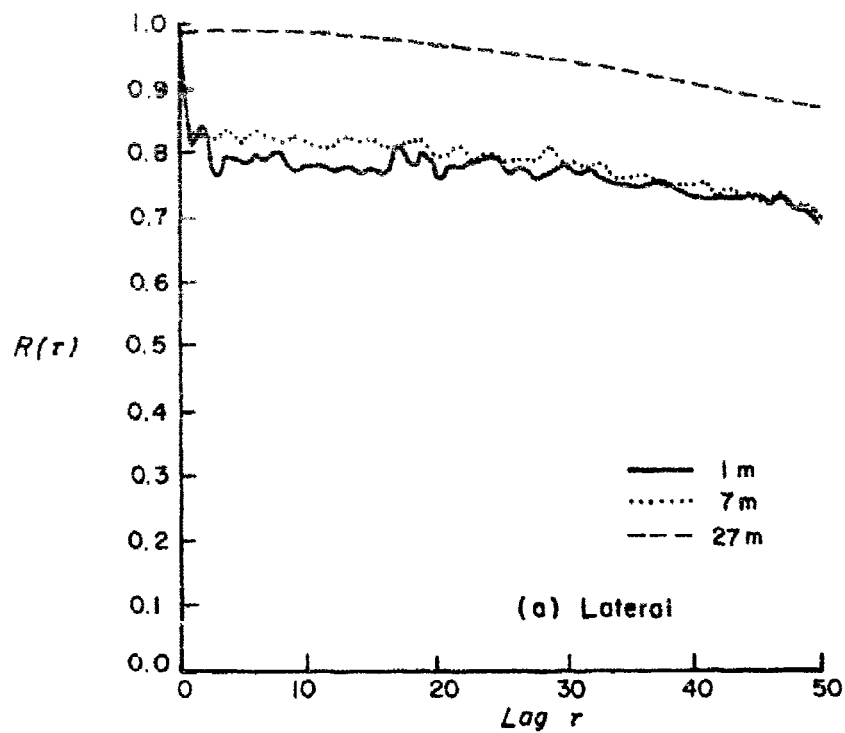


Fig. 3.4 Autocorrelation Functions of Wind Components,  
Case I-BN

function for the longitudinal component at 1 m is similar to the one in Fig. 3.2 for 500 random numbers.

The normalized Hanned spectra for the lateral components are shown in Fig. 3.5 (a), (b), (c), for the 1, 7, and 27 m levels, respectively. Even at the lowest levels most of the variance is in the low frequencies, in fact, nearly 60 percent of the total variance is contained in the zero, 1st, and 2nd harmonics.

Applying the null hypothesis that the peaks are those of white noise, the hypothesis is rejected only for 0.01 cycles/2 sec at the 95th percentile. The only conclusion one may draw here is that the data are from a process other than white noise. As the 5 percent a posteriori confidence limit (not drawn), most of the high frequencies are rejected at both the bottom and middle levels. The value for the lag 1 autocorrelation at the 1 m level is 0.81; therefore, applying the null hypothesis that the difference between the data spectrum and a red noise spectrum is not significant, from Eq. (5.2) and a significance test, the 95 percent curve is drawn as shown in Fig. 3.5.

It is seen that at frequencies 0.00, 0.01, 0.40, 0.41, 0.42, and 0.46 to 0.50 cycles/2 sec, the hypothesis is rejected. This implies that at certain frequencies the wind component data may be similar to that obtained by a first-order linear Markov process, that is, that the observation depends on the previous observation.

From Taylor's hypothesis discussed in Chapter III relating the time  $t$  to the length  $x$ , and the mean wind  $\bar{U}$ ,  $t = x/\bar{U}$ , (referred to by Munn (1966) as "frozen turbulence"), the frequencies may be converted to wavelengths.

For example,

$$P = \frac{0.50 \text{ cycles/2 sec}}{1.45 \text{ meters/sec}} = \frac{0.50 \text{ cycles}}{2.90 \text{ meters}}$$

$$(P)^{-1} = 5.8 \text{ meters/cycle} = 5.8 \text{ meters in wavelength}$$

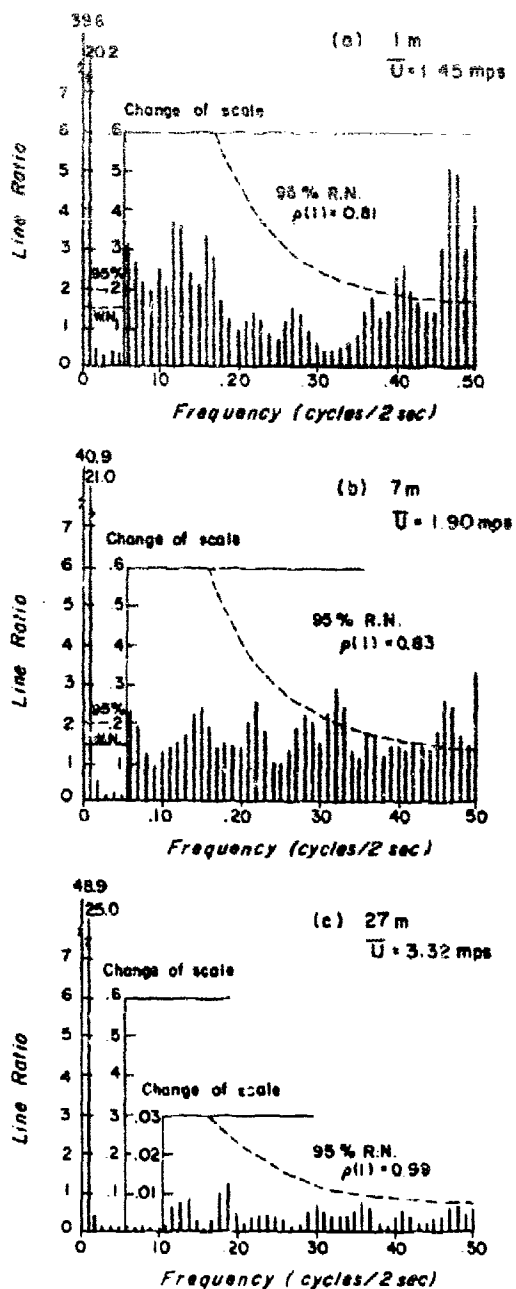


Fig. 3.5 Spectra of Lateral Components at 1, 7, and 27 m Levels, Case I-BN

Applying the white and red noise 95 percentile confidence limits, the significant frequencies at 1 m are those corresponding to 290 m, and 7.2 m and the region from 6.3 m to 5.8 m in length.

This gap in the significant frequencies; that is, the large space between the significant frequencies, is not difficult to imagine since the basic hypothesis in Chapter II is that there is a slowly varying component with a rapidly varying frequency component superimposed. Thus, the slowly varying component is approximately 290 meters or larger in wavelength, and the high frequency is approximately 7 meters and shorter, with the longer waves containing most of the energy.

At 7 m the 95 percentile of the red noise hypothesis shows that the significant frequencies are 0.00, 0.01, 0.32, 0.33, 0.36, 0.37, 0.45 through 0.50 cycles/2 sec. These, with the exception of 0.00 cycles/2 sec, correspond to wavelengths of 380 m and to the 12 m region and to the region between 8.4 and 7.6 meters.

At 27 m for the lateral component, the spectrum shows only the 0.00 and 0.01 (664 m wavelength) to be significant at the 95 percentile of the white noise and red noise hypotheses. These two frequencies account for over 99 percent of the total variance indicating little, if any, eddy energy such as that found at the two lower levels for shorter eddies or wavelengths. This may be substantiated by the 5 percent level of significance for white noise (not plotted) which indicates that the values from frequencies 0.03 to 0.50 might not be due to white noise but to some other cause.

Prewidening the data with a low-band pass filter given by the difference filter  $x(t) = u(t) - 0.6u(t - 1)$ , the new analysis is shown in Fig. 3.6. Again, the low frequency region contains nearly 97 percent of the energy. A difference filter of  $x(t) = u(t) - u(t - 1)$  applied to the data gives the auto-

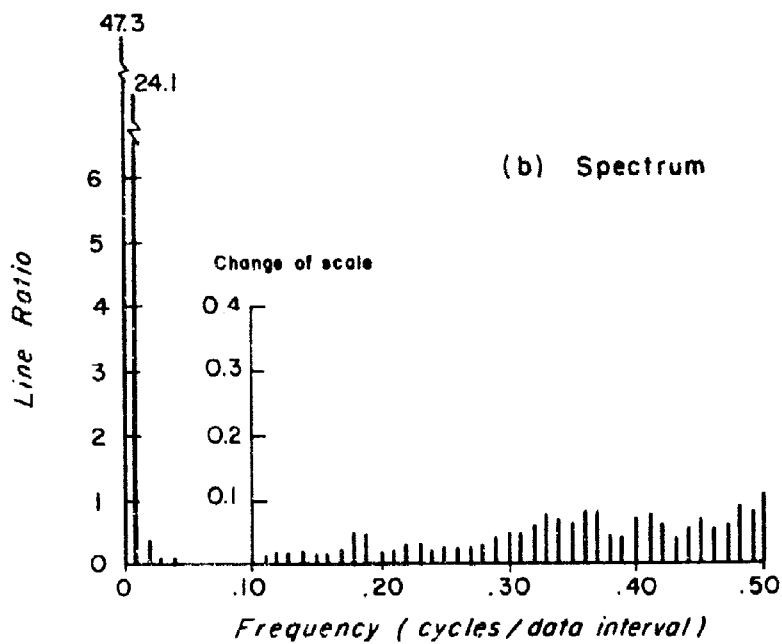
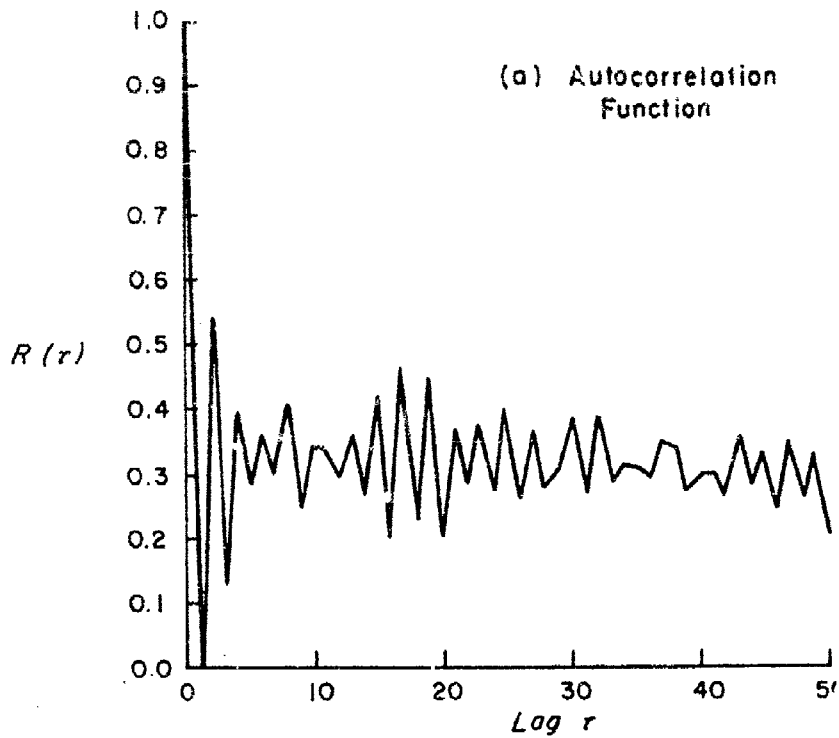


Fig. 3.6 Spectrum Analysis of Lateral Component at 27 m. Data  
Prewhitened by Difference Filter  $u(t) - 0.6u(t-1)$ ,  
Case I-BN

correlation function curve shown in Fig. 3.7 and a spectrum indicating that frequencies 0.42, 0.47, 0.48 and 0.50 cycles/2 sec may be significant at the white noise 95 percentile a posteriori confidence band. These correspond to wavelengths of 15.8, 14.1, 13.8, and 13.3 meters. The red noise hypothesis is not applied in this case because the gain function has increased the middle and high frequencies so much that the noise level may be amplified. This noise may be attributed to the instruments, recorders, digitizers, and truncation. Duchon (1968) discusses the problem of instrument-induced red noise as a function of the time lag and shows that the longer the instrument time lag, the redder the spectrum. This also depends on the sampling frequency. The conclusion to be drawn from this is that the wave length of the physical wave may be much longer than our sampling time will allow, i.e. the "window" being used for the data at that level is too small. Therefore, a sampling period longer than 1000 sec should be used.

The autocorrelation functions of the longitudinal components showed that these Eulerian time correlations reached lower values than the lateral components, but only the one for the 1 m level reached a value of zero.

The spectra of these longitudinal components are shown in Fig. 3.8 for the three levels. The spectrum for the 1 m level clearly shows the energy distributed over the entire frequency range. The 95 percent white noise a posteriori confidence limit (1.5) shows the first 3 frequencies (plus the one at 0.00) and 0.36 and 0.37 cycles/2 sec to significantly differ from white noise. The red noise 95 percent confidence limit further isolates the lower frequencies and emphasizes the importance of 0.36 cycles/2 sec and adds to the higher frequencies the 45th harmonic. These correspond to wavelengths of 290, 145, and 97 meters in the lower region and in the high region to about 8 and 6 meters. This compares with the wavelength of 290, 7 and 6 meters for the

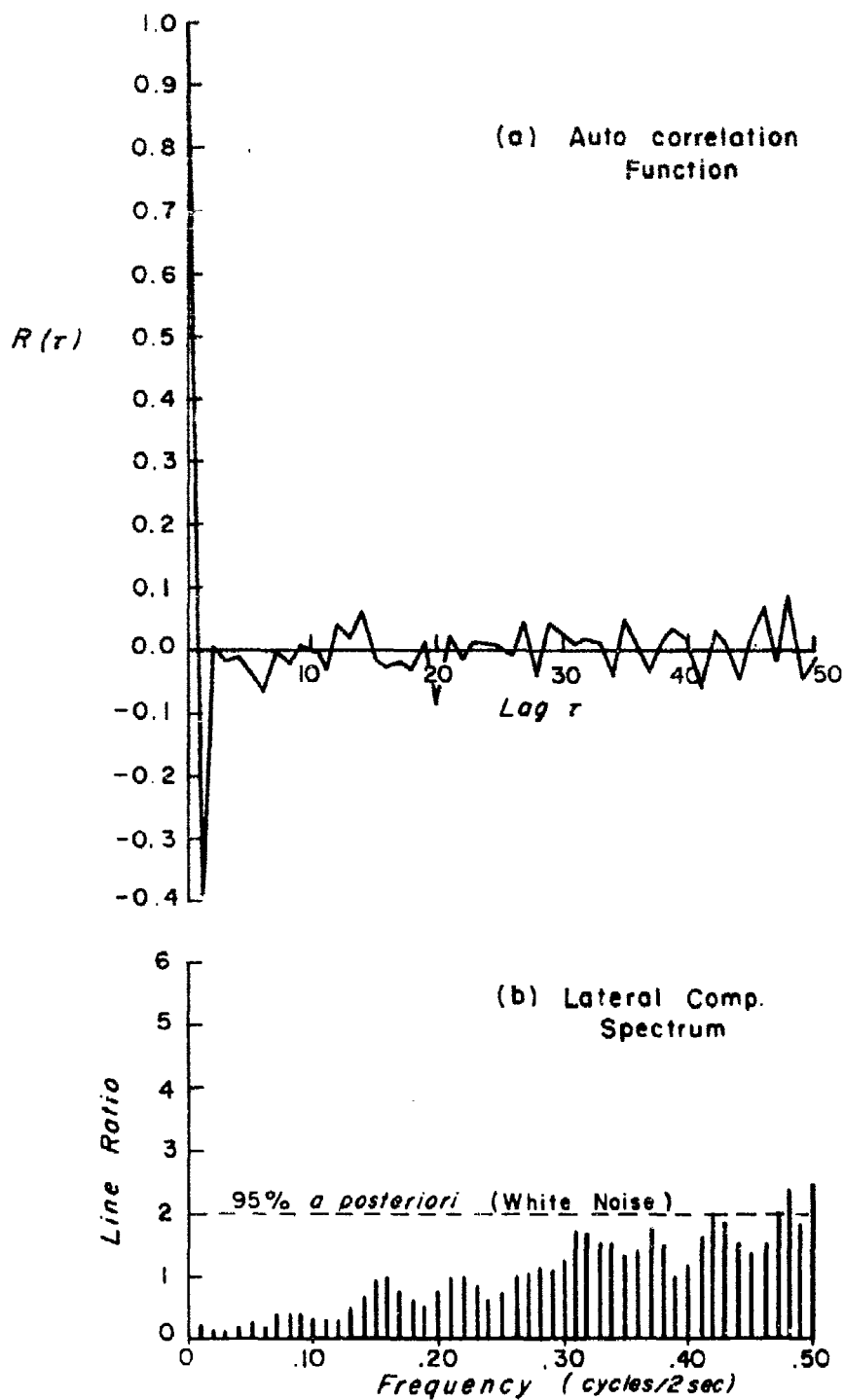


Fig. 3.7 Spectrum Analysis of Lateral Component at 27 m. Data  
 Prewhitened by Difference Filter  $u(t)-u(t-1)$ ,  
 Case I-BN

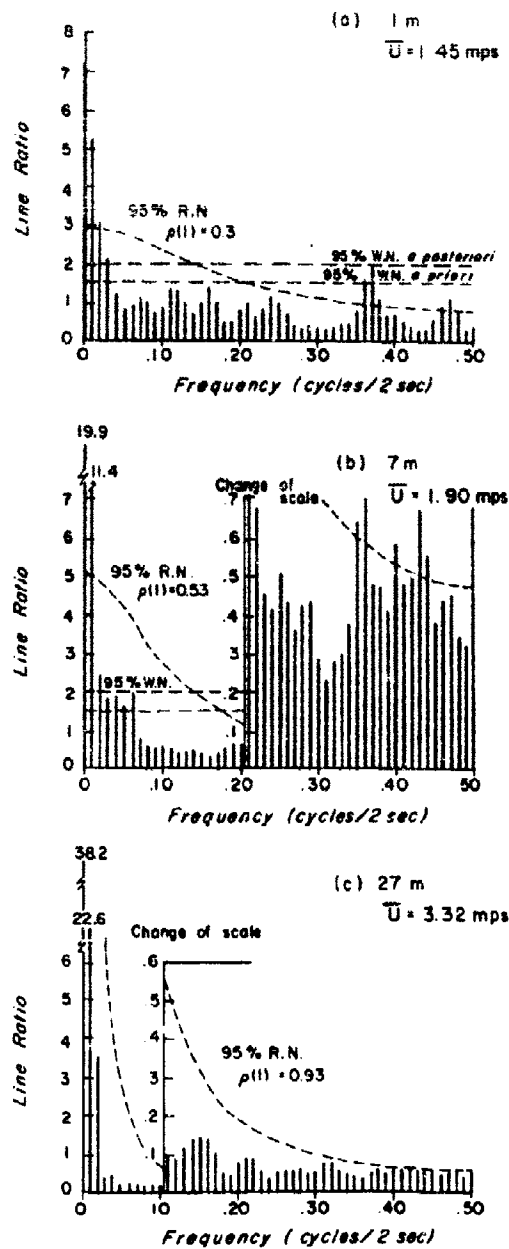


Fig. 3.8 Spectra of Longitudinal Components at 1, 7, and 27 m Levels, Case I-EN



lateral component at the same level. The short wavelength of 6 m is common to both components, the 7-8 meter wavelength is perhaps common, but there are more wavelengths present in the longitudinal component.

At the 7 m level the frequencies which might be significant for the longitudinal component correspond to wavelengths of 380 and 190 meters in the low frequency range and to about 11 to 8 meters in the higher frequencies. Comparing these to the lateral values, the high frequency end is the same (8 m). The other lateral wavelengths were 380, 12, and 9-8 meters. Again, there are more wavelengths present in the longitudinal case. If a crude simplified model of the physical phenomenon were made based on these two levels, one could picture an eddy or perturbation resulting from differential heat radiation from the earth's surface with a horizontal dimension of 200 to 400 meters. As the eddy traveled along the wind, mechanical turbulence induced by the friction of the surface boundary would produce the shorter wavelengths obtained of 6 to 12 meters; furthermore, more of these "disturbances" would prevail in the downstream component. The greater energy found at the higher frequencies in the downstream case would come from the mean motion, or longer waves.

At the 27 m level there is also more energy at the high frequencies for the downstream component. Prewhitening the data shows that the region around 0.40 cycles/2 sec (16 meter wavelength) might be significant, as shown in Fig. 3.9.

The cross-correlations of the lateral components and of the longitudinal components are shown in Fig. 3.10. It appears that the sampling interval is too short, especially for the lateral components. However, the lateral cross-correlations suggest that the correlation between levels is nearly the same for the 7 to 27 m and 1 to 27 m intervals (about 0.90) and the lowest correlation is between 1 to 27 m (0.86). A possible explanation for this might

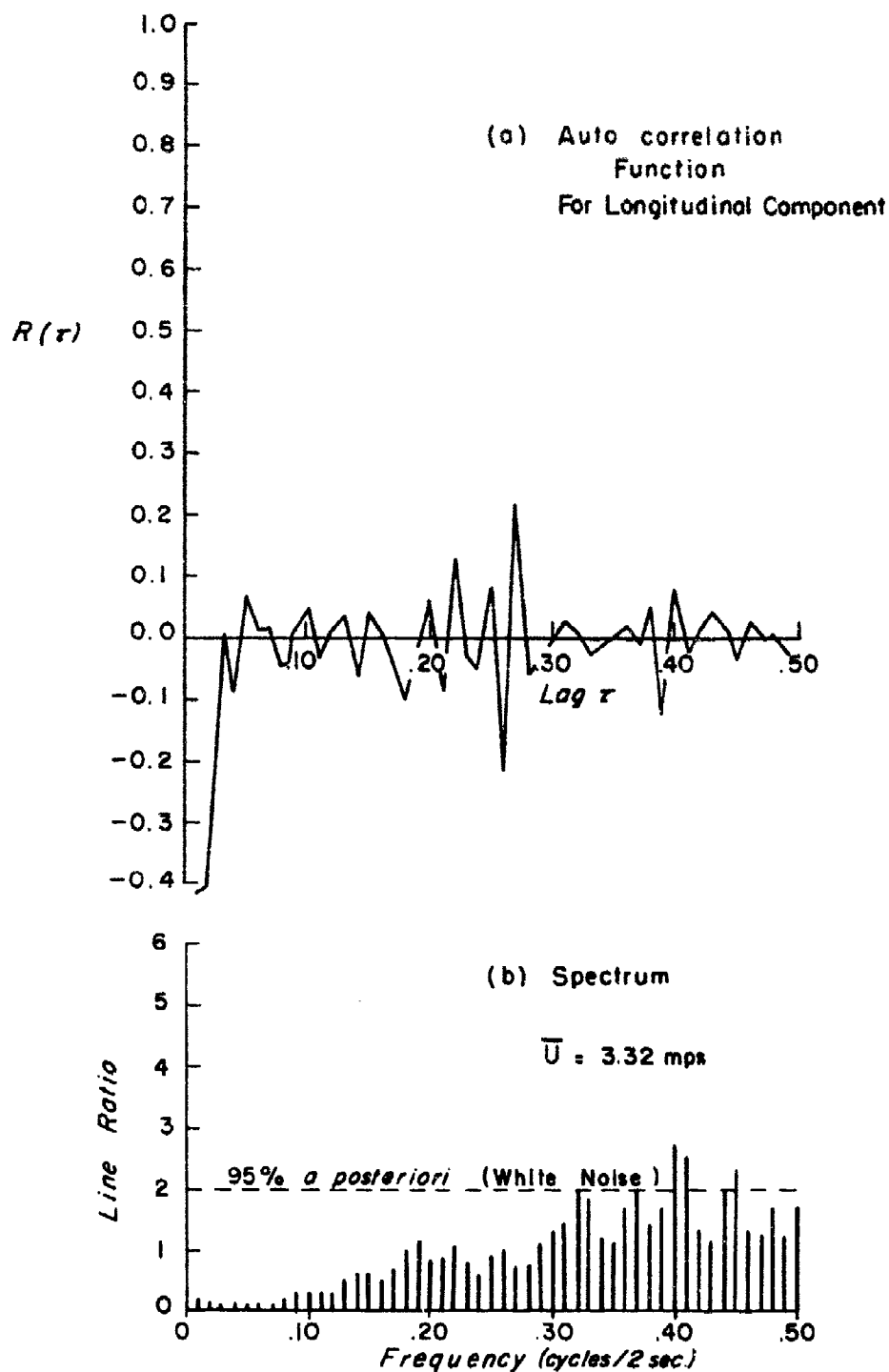


Fig. 3.9 Spectrum Analysis of Longitudinal Component at  
27 m. Data Prewhitened by Difference Filter  
 $u(t)-u(t-1)$ , Case I-BN

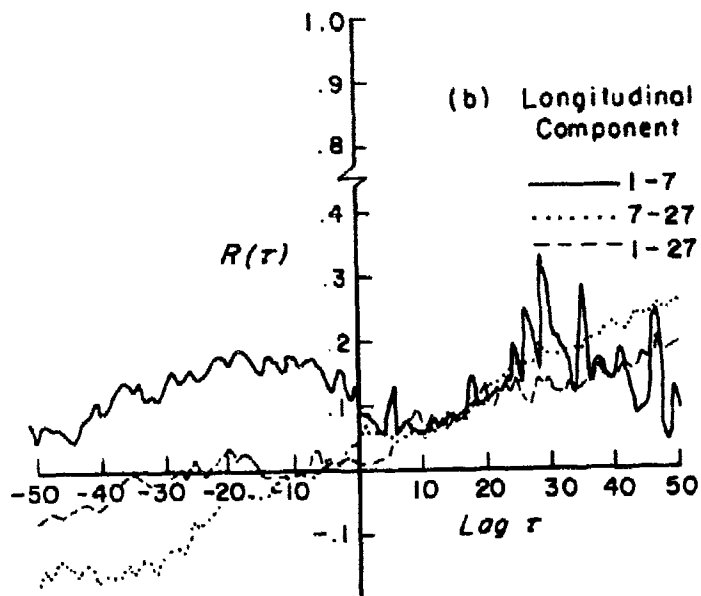
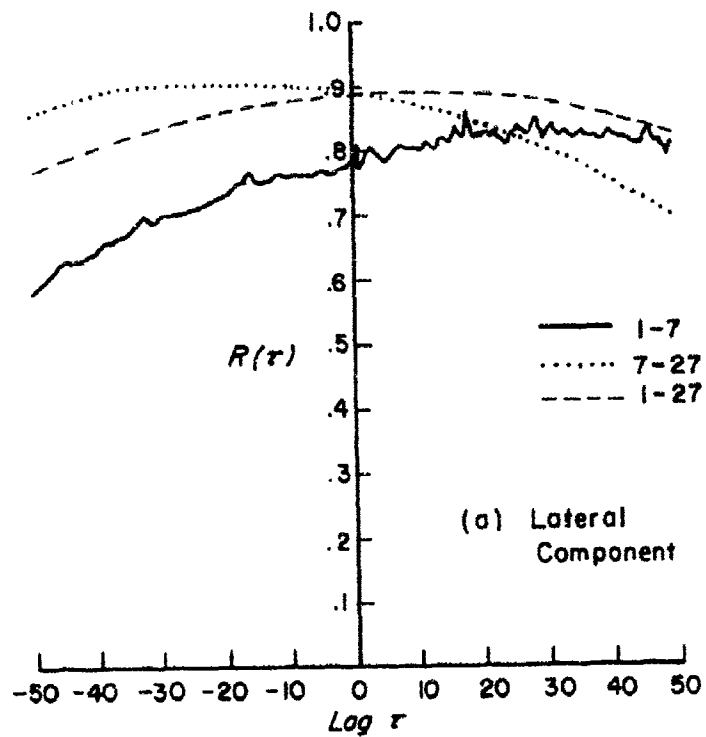


Fig. 3.10 Cross-correlation Functions of Components, Case I-BN

be made with the simplified model of the eddy just discussed. As this eddy moves downwind, the surface retards the eddy at the lower layer. Thus the correlation between the lowest level and the next higher one should be somewhat less than the correlation between 7 and 27 meters. Longitudinally, the correlation between the levels is not clear, although it appears to be small. The correlations obtained with a longer sampling period are discussed in the next section for sample Case II-BN.

The coherence function given by Eq. (3.19) was computed for the inter- and intra-level components. Fig. 3.11 shows the coherence between the u and v components at the 1 m level. The 95 percent a priori confidence limit is placed at 0.283. The highest coherence is shown to be at the higher frequencies, suggesting again a semblance of "horizontal homogeneity" at the short wavelengths which may be attributed to mechanical turbulence.

The same results are shown in Table III.3 for the values equal to or greater than 0.283. The table shows the highest coherence values at 0.37 and 0.48 cycles/2 sec at 1 m, and at 0.39 cycles/2 sec at the 7 m level.

Table III.3. Significant Values of  
Coherence, Case I-BN

Frequency (cyc/2sec)	Lateral Component			Long. Component		
	1-7m	7-27m	1-27m	1-7m	7-27m	1-27m
.00	.938	.960	.988	.328		None
.01	.925	.955	.979			$\geq .283$
.02	.502	.759	.293	.295		
.03	.849					
.06	.431					
.09			.451			
.11		.392				
.35				.300		
.40	.307					
.41	.387				.340	
.50						

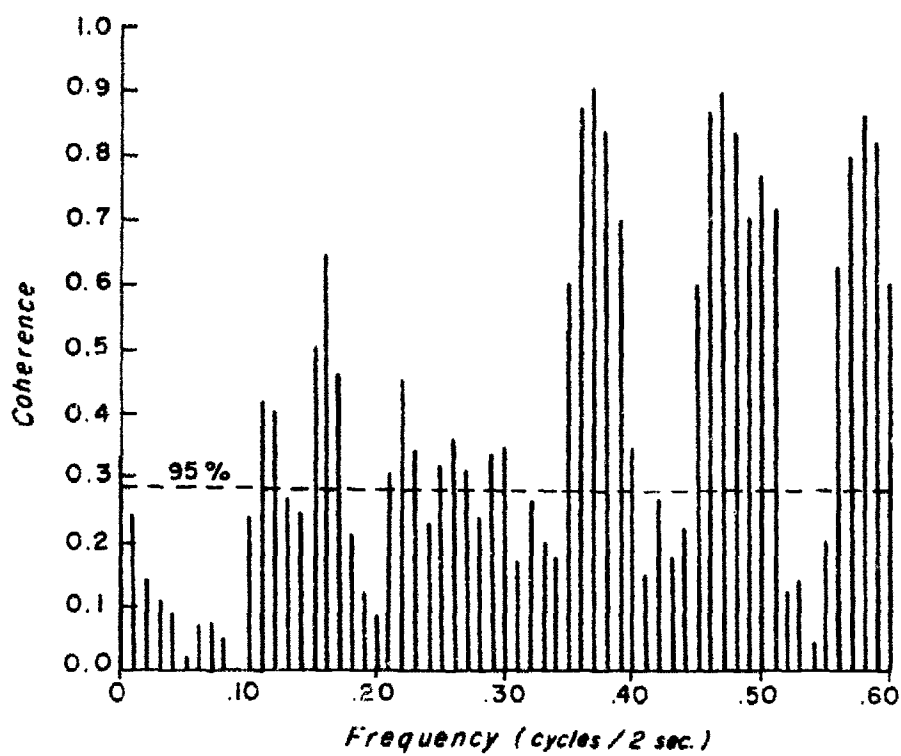


Fig. 3.11 Values of Coherence Between Components at 1 m,  
Case I-EN

The coherence between the lateral components show high values at the low frequencies for all three level intervals, i.e., 1 to 7, 7 to 27, and 1 to 27 meters. The coherence between 1 and 7 m give values which are above the level of significance at the 0.40 and 0.41 cycles/2 sec region. This corresponds to 4.6 m and 9.5 m wavelengths at 1 and 7 meter levels, respectively. This could be interpreted that as a wavelength of 5 m passes the 1 m level, a 9.5 m wave occurs at the 7 m level. This suggests a broadening of the "eddy" upward, as speculated in the earlier model. At the other intervals, only the low frequencies (long wavelengths) are correlated.

The coherence between the downstream components show significant values at 0.35 cycles/2 sec between the 1 and 7 meter levels which correspond to 5.4 and 10.9 meters in wavelengths. These are somewhat longer than for the lateral component (4.6 and 9.5 m) which might be explained as an elongation of the eddies along the wind. Between the 7 m and 27 m levels the significant wavelengths are 9.3 and 16.2 m, respectively, which suggests that the disturbance reaches at least to 27 m altitude and enlarges, but is only discernible in the longitudinal component. Between 1 and 27 meters height there is no significant frequency, which means that an occurrence at the bottom level was not accompanied by a similar one consistently at the top level.

A comparison of the integral scales of the longitudinal components by taking one-quarter of the values at the zero intercept shows that the values obtained are approximately 2, 5, and 9 (seconds) for the 1, 7, and 27 meter levels, respectively. This may be interpreted as an increase in the scales upward in the longitudinal component. Thus, the "average size of the eddies" may be said to increase upward. (It should be noted, however, that the low end of the spectrum is not precise because of the small "window" used in the sampling period. Therefore, these values are only crude approximations.)

Case II-BN: Beach Nighttime, Sampling Period 4000 seconds

This sampling period includes the 1000 seconds of Case I-BN discussed in the previous section; specifically, the first 1000 seconds are the same.

The autocorrelation functions for the lateral and longitudinal components using a sampling time of 4000 seconds are shown in Figs. 3.12 (a) and (b). (Since the sampling interval of one sample/8 seconds was obtained by arithmetically averaging four one-sample-per-2-second values, this is tantamount to using a low pass filter, i.e., filtering out some of the higher frequencies.) The patterns suggest that the sampling period is perhaps adequate, because the functions decrease as time increases and attain or approach a value of zero correlation. The functions for both the 1 m and 7 m level longitudinal curves also indicate high frequency eddies superimposed on larger eddies.

The spectra of the lateral components for the 1, 7, and 27 m levels are shown in Fig. 3.13 (a), (b), and (c), respectively, with the 95 percent confidence limits for the white noise a posteriori hypothesis and the red noise hypothesis for lag 1 autocorrelation. At the first level the frequencies which may be significant with the corresponding wavelengths using Taylor's hypothesis are as follow:

0.00 cycle/8 sec	
0.01	133.0 m
0.29	46.1
0.30	44.5
0.39	34.3
0.40	33.4
0.45	29.7
0.46	29.0
0.50	26.7

It is seen that this longer sampling period, while being a better window for

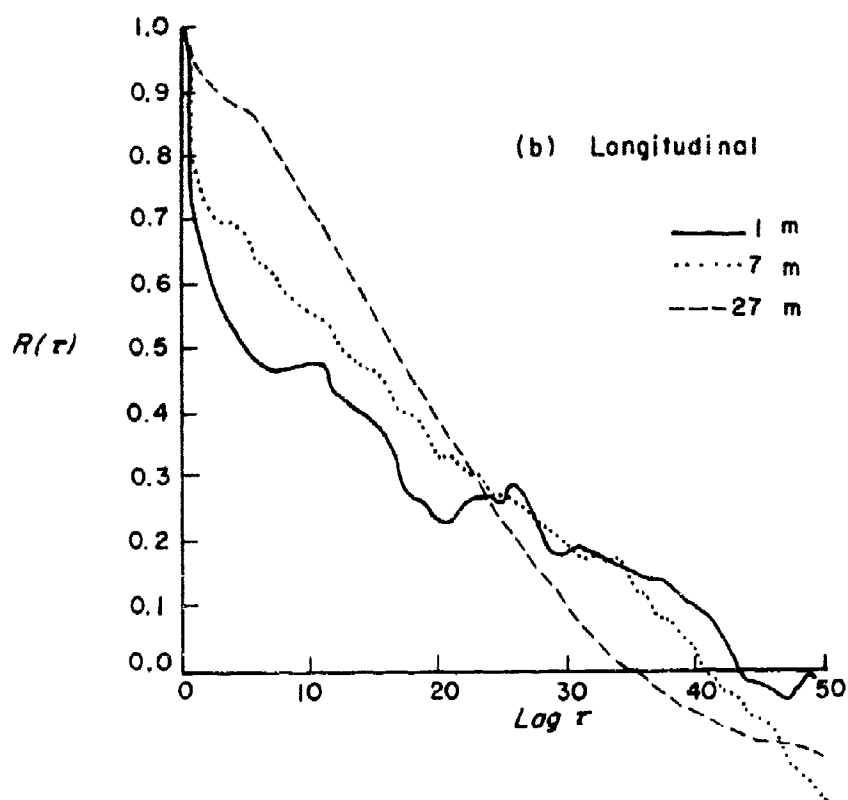
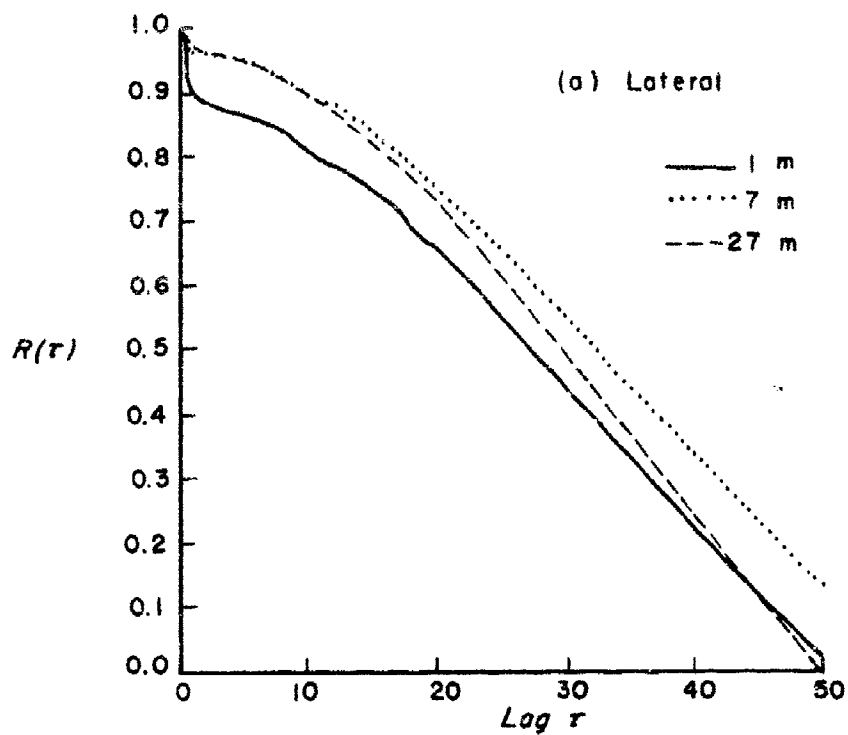


Fig. 3.12 Autocorrelation Functions of Wind Components,  
Case II-BN



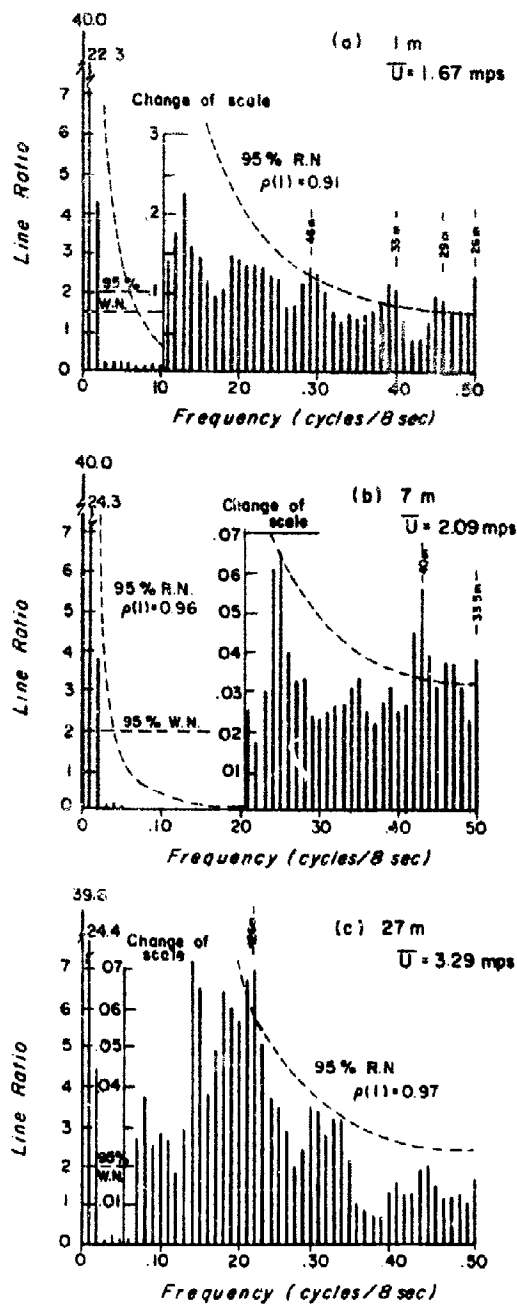


Fig. 3.13 Spectra of Lateral Components at 1, 7, and 27 m Levels, Case II-BN

computing the autocorrelations, sacrifices the smaller wavelengths. The spectra at the 7 m level shows significant peaks at 0.00, 0.01, and 0.02 and at 0.25 cycles/8 sec and also in the frequency region of 0.42 to 0.47 and 0.50 cycles/8 sec. This corresponds to wavelengths of 1672 and 836 meters, another of 67 meters, and also the region between 40 meters to 33 meters.

The lateral component at the 27 m level shows peaks at frequencies corresponding to 2632 and 1316 meter wavelengths and 126 to 120 meters.

The downwind component (Fig. 3.14 (a)) for the 1 m level shows significant wavelengths of 1336, 688, and 445 meters for the long waves, and about 35 meters for the short waves. The middle level shows significant wavelengths of 1672, 836, 557 and 62 meters and others between 42 to 38 meters. At the top level the significant wavelengths are 2632 m, 1316 m, and the 82 to 67 meter region and 53 meters.

The wavelengths computed from the significant wavelengths are shown in Table III.4 for the lateral and longitudinal components. It is seen that

Table III.4: Wavelengths Computed from  
Significant Frequencies, Case II-BN

1 m		7 m		27 m	
Lat.	Long.	Lat.	Long.	Lat.	Long.
1336	1336	1672	1672	2632	2632
668	668	836	836	1316	1316
	445	67	62		
45	35	40		126	82
34			42	120	67
29		36	38		53
27		33			

for a sampling period of 4000 seconds (about 67 minutes) the eddy appears to be elongated along the wind at the 1 and 7 m levels because the shorter wave-

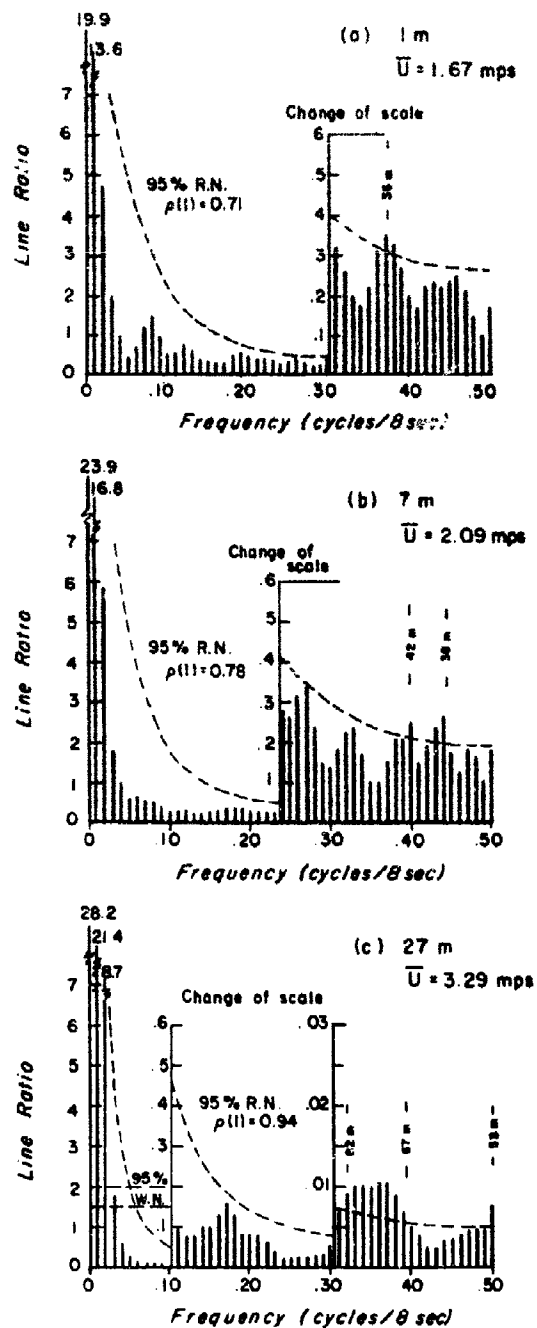


Fig. 3.14 Spectra of Longitudinal Components at 1, 7, and 27 m Levels, Case II-BN

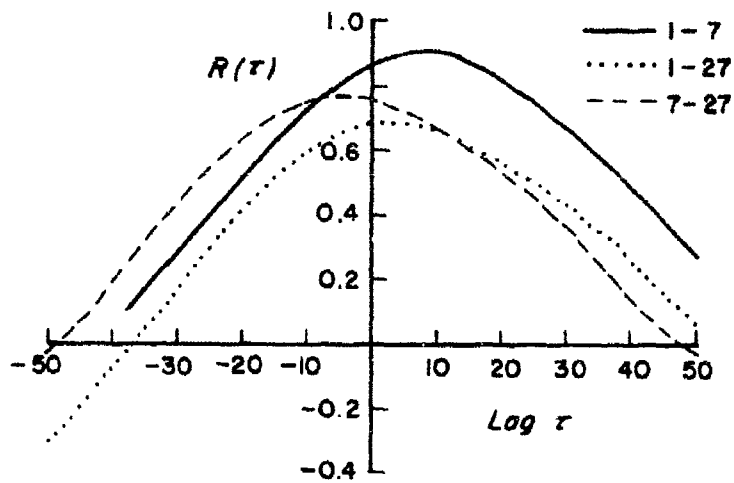
lengths are found with the lateral component. This table does not show the relative energy at these wavelengths. However, the spectra show the energy to be much less at high frequencies for the lateral component. Therefore, mechanical turbulence appears to be the main cause of these eddies, and in the period of just over one hour, an apparent elongation downstream of those eddies is noticed at the lower two levels.

At the shorter sampling period of 1000 sec (16.67 min), the smallest eddies computed were of the same diameter at both components at the lower levels. This could still be the case because in the stable regime, the smaller eddies could be circular in the shorter time period and the longer ones elongated downstream with time.

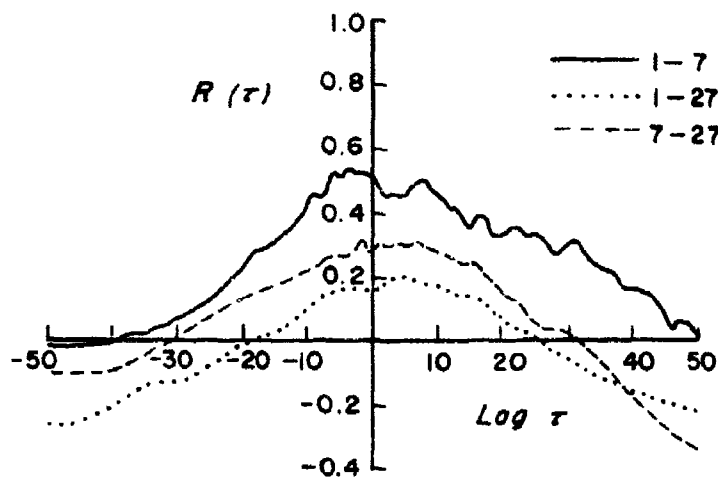
At 27 meters, the spectra (Figs. 3.13 (c) and 3.14 (c)) and Table III.4 show the longitudinal component with more shorter wavelengths with values of 82 to 67 meters and 53 meters, and the lateral with values in the 126 to 120 meters region.

The cross-correlations between levels are shown in Fig. 3.15 for the two components. The correlations for the lateral components are higher than those of the longitudinal components, indicating again longer wavelengths predominate in the lateral. But more important is that during the period of 66.67 minutes sampling time, the correlation between the 1 m and 7 m levels is the highest, with the 7 m to 27 m correlation the next highest, and the smallest correlation between the 1 m and 27 m levels. This is true for both components, indicating that perhaps the eddies extend to at least 7 meters but to a lesser extent to the 27 m level.

The correlation value of 0.90 for the lateral components between the 1 and 7 m levels, compared with a value of 0.54 for the downstream component, support the assumption of mechanical turbulence because this would cause more



(a) Lateral



(b) Longitudinal

Fig. 3.15 Cross-correlation Functions of Components Between Levels, Case II-BN

eddy "diameters" to be found downstream than between the two levels in the lateral. These somewhat "constant" lateral diameters would give higher correlations.

The magnitude spectra and coherence values for the lateral components are shown in Fig. 3.16. The magnitude spectrum is shown to illustrate that the coherence may be a better parameter to use in the cross-spectral analysis of wind components. In both Fig. 3.16 and Fig. 3.17, the magnitude values do show some peaks in line variances, but these peaks are not as prominent as the coherence values. As expected, the increases in coherence values occur with those of the magnitude spectrum since both parameters are computed using the real and complex parts of the cross-spectra as given in Eqs. (3.14) and (3.15). The magnitude value is the magnitude of the vector in a complex plane in which the co-spectrum is the real value and the quadrature spectrum is the imaginary component.

In the high frequency region, only 0.33 cycles/8 sec is significant for the coherence values between 1 m and 7 meters. This corresponds to wavelengths of about 40 and 50 meters. The highest values of coherence for all the cross-spectra in Figs. 3.16 and 3.17 on the high frequency ends of the spectra occur in the downstream components between 1 m and 7 m at 0.35 cycles/8 sec. The wavelengths here are 38 and 48 meters which compare to 40 and 50 meters in the lateral. This may perhaps be interpreted as an "equilibrium" diameter for an eddy, given the conditions in terrain, stability, and wind profile. Between 1 m and 27 m, the coherence value is also the highest in the high frequency region of downstream wind as shown in Fig. 3.17 (b). At this frequency, the wavelength at 27 meters is 75 m and at the 1 meter level, it is 38 m, again illustrating that the eddy is perhaps discernable at the high level in the downstream component.

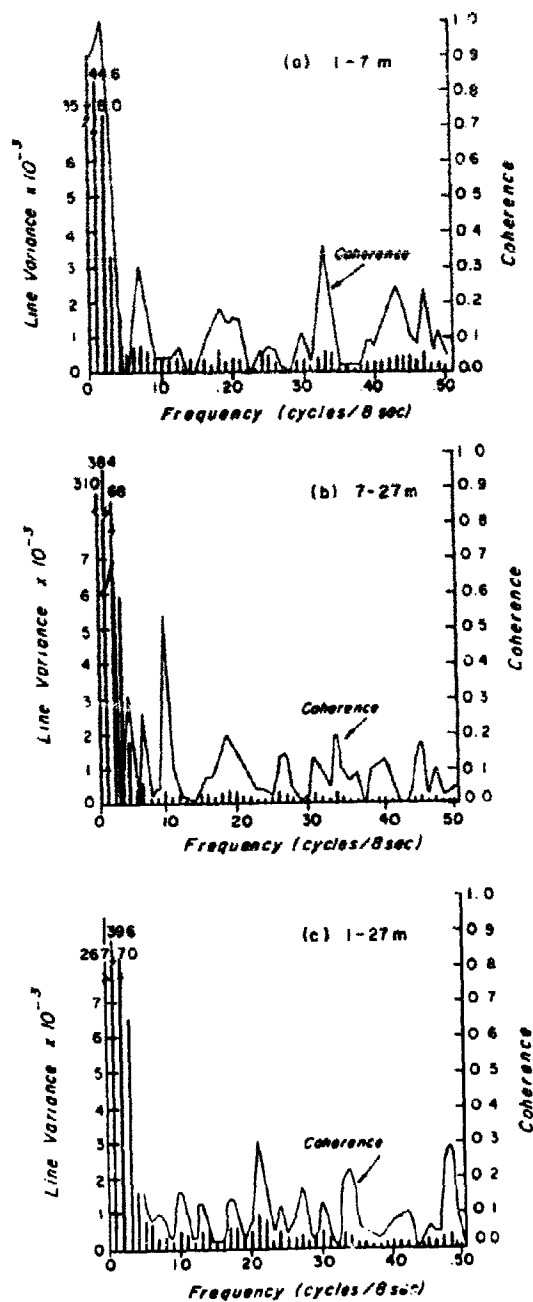


Fig. 3.16 Magnitude Spectra and Coherence Values for Lateral Components, Case II-BN

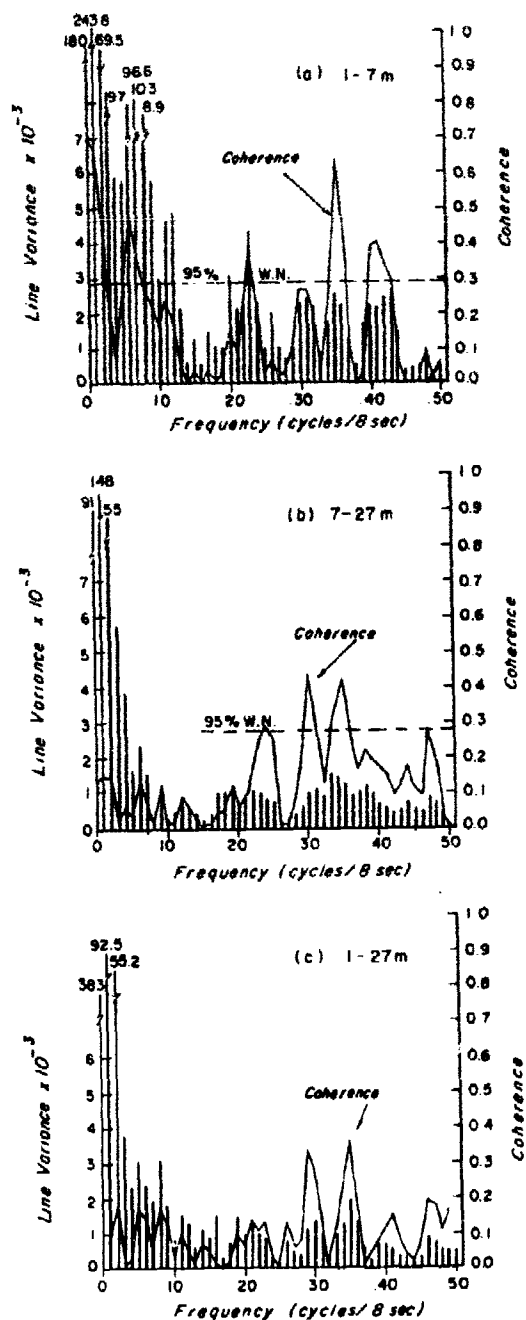


Fig. 3.17 Magnitude Spectra and Coherence Values for Longitudinal Components, Case II-EN



As noted in the beginning of this section, the autocorrelation function crossed the zero intercept in all data samples except the 7 m lateral component. Therefore, the integral scale may be assumed to exist for the realizations investigated. The values obtained using the  $F(0)$  value of Eq. (1.24) give approximately equal values of 10 sec for all 3 longitudinal components and values of about 5, 6, and 7 sec for the lateral components at 1, 7, and 27 meters.

Case III-BN: Beach Nighttime, Sampling Period 4000 seconds

This case covers the period of 66.67 minutes following the period of Case II-BN. The atmosphere has become slightly more stable.

The autocorrelation functions are shown in Fig. 3.18. A comparison of these curves to those 4000 seconds earlier shows that the autocorrelation curve for the 27 m level decreases more slowly with lag, indicating perhaps more energy in the low frequency end of the spectrum and less energy in the high frequencies. The atmosphere has therefore apparently become more stable at this level. The wind speed of this offshore flow (land breeze) has increased slightly at all three levels from the values one hour before.

The spectra for the 1 m level are shown in Fig. 3.19. As noted in the previous case, the longitudinal component has more relative variance in the higher frequencies. The highest significant frequency without prewhitening is 0.50 cycles/8 sec for the lateral and 0.40 cycles/8 sec for the longitudinal components, which correspond to 30 and 37 meter wavelengths, respectively. The eddy may be said to be elongated with the wind in this case also.

At the 7 m level the spectrum (Fig. 3.20) of the longitudinal component shows more energy at lower frequencies at the high end of the spectrum (0.36 to 0.41 cycles/8 sec) than that of the lateral component (0.44 to 0.46 cycles/8 sec), which indicates longer waves, in general, longitudinally (42 m vs 47 m).

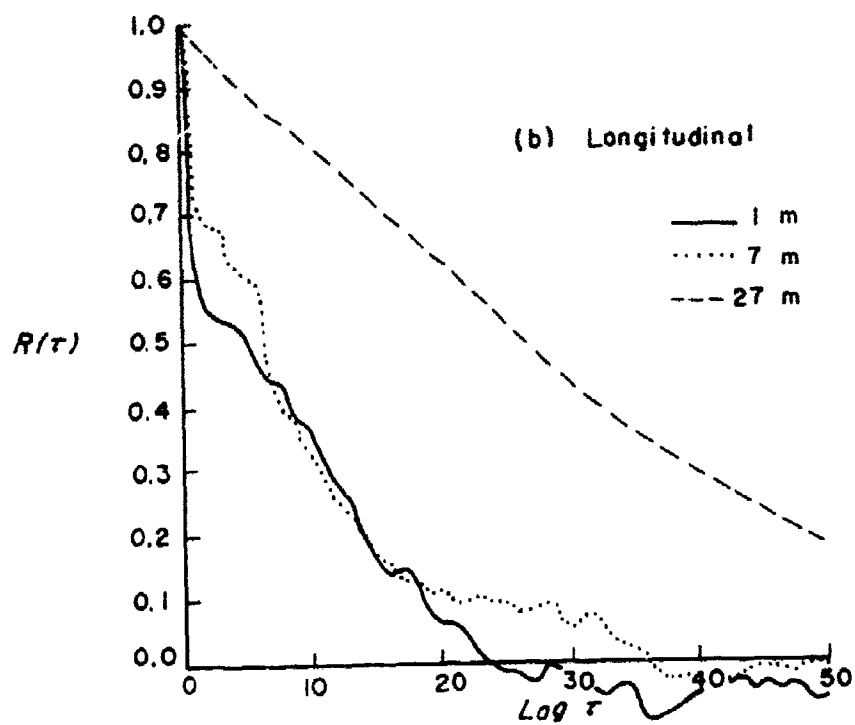
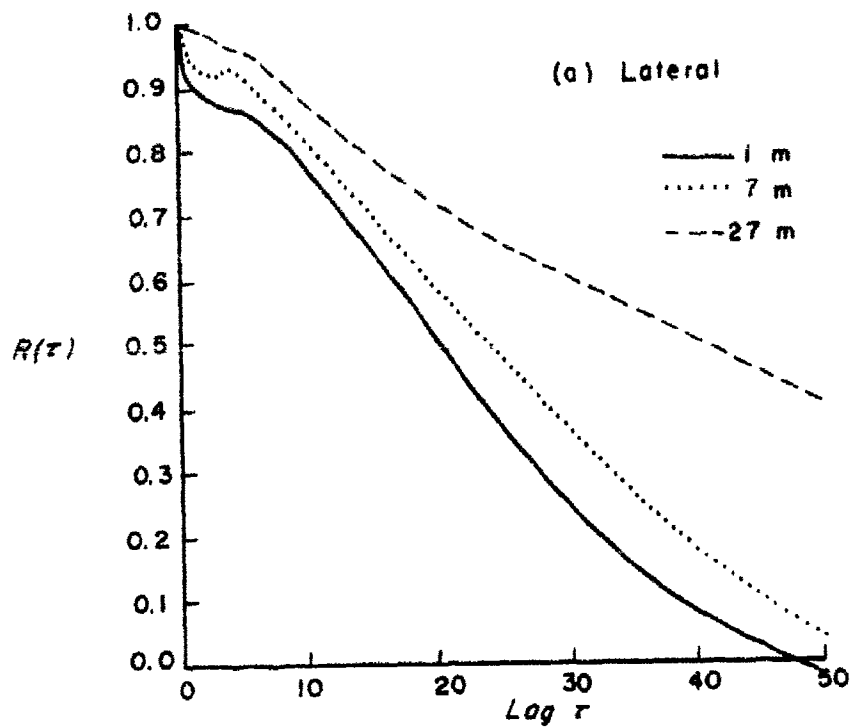


Fig. 3.18 Autocorrelation Functions of Wind Components,  
Case II-BN

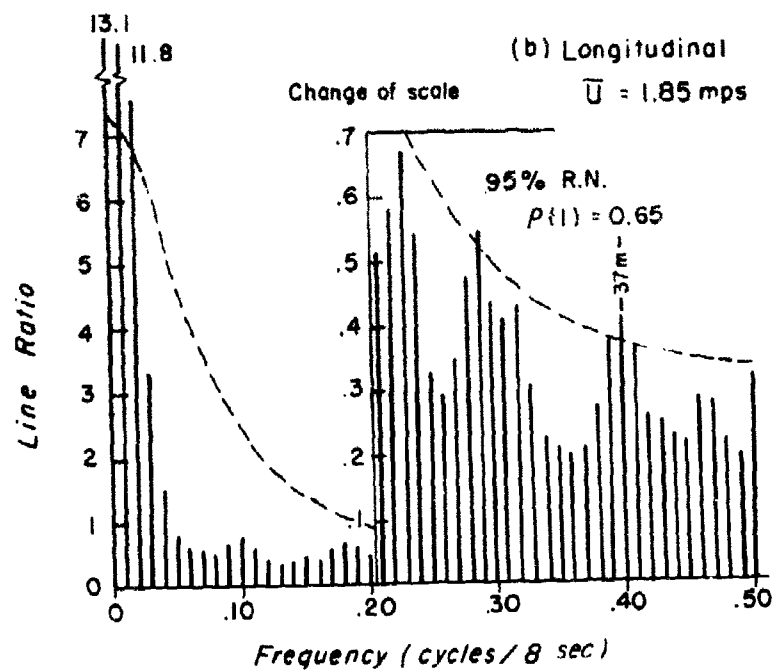
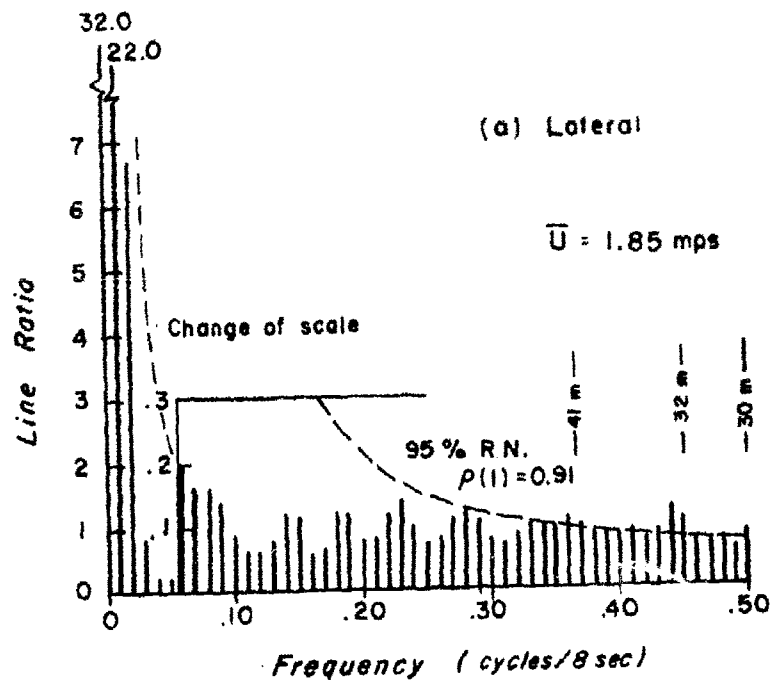


Fig. 3.19 Spectra of Components at 1 m, Case III-BN

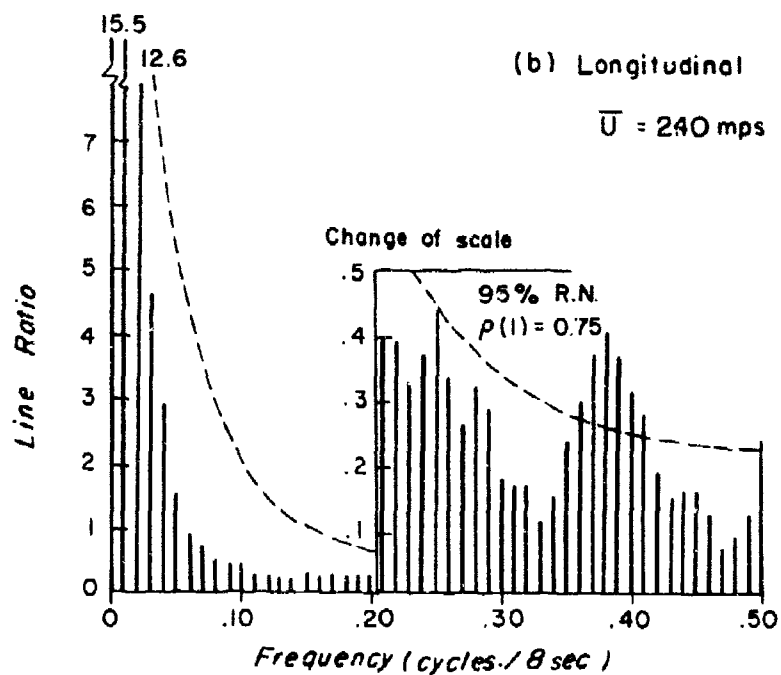
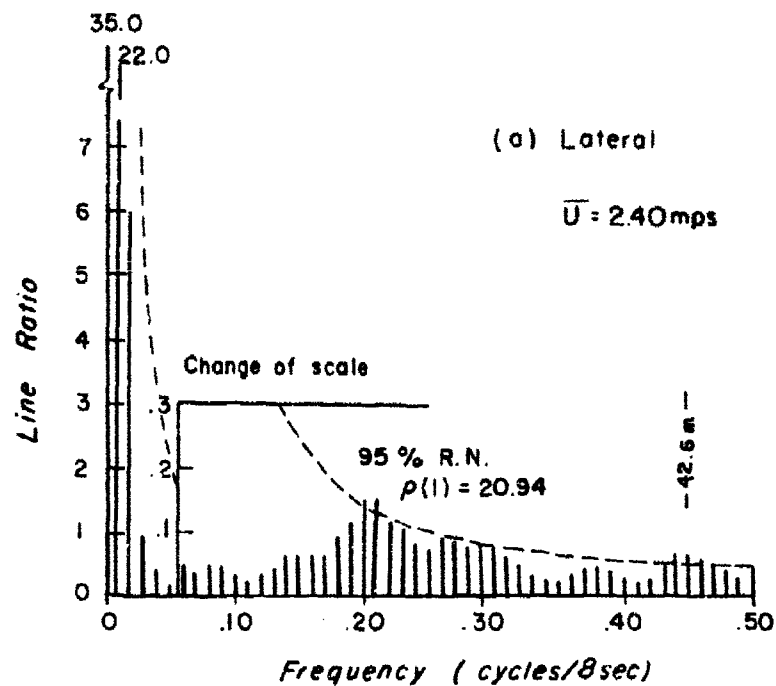


Fig. 3.20 Spectra of Wind Components at 7 m, Case III-BN

The spectra of the components at the 27 m level are shown in Fig. 3.21. Nearly all of the energy is in the long waves. Prewhitening the data by the filter  $x(t) = u(t) - u(t - 1)$ , the spectra of the same components is shown in Fig. 3.22. The longitudinal component is seen to contain significant peaks at a higher low frequency, which corresponds to smaller wavelength, than the lateral component (758 m vs 1516 m). For the rest of the spectrum, both components appear to be about the same.

The cross-correlation between levels for the longitudinal components are shown in Fig. 3.23. As in the previous hour, the correlation is greater between 1 and 7 meters and least between 1 and 27 meters. The longitudinal components correlation (not shown) also were similar to those of the previous hour. The correlations longitudinally, however, were somewhat higher than before, indicating more stable conditions.

The highest value of coherence was again between the longitudinal components at 1 and 7 m at 0.34 cycles/8 sec. This corresponds to wavelengths of 44 m and 57 m as compared to previous values of 38 and 48 meters. The increase in wind speed and stability probably accounts for these longer wavelengths.

Approximating the scales of turbulence at  $F(0)$ , the values obtained are compared to values of the previous hour:

Case III-BN			Case II-BN	
	Lat	Long	Lat	Long
1 m	8.0 sec	3.3 sec	10.0 sec	5.0 sec
7 m	8.8	3.9	10.0	5.9
27 m	10.1	9.1	9.9	7.1

Case IV-BN: Beach Nighttime, Sampling Period 8000 seconds

The sampling period of 8000 sec or approximately 2 hours and 13

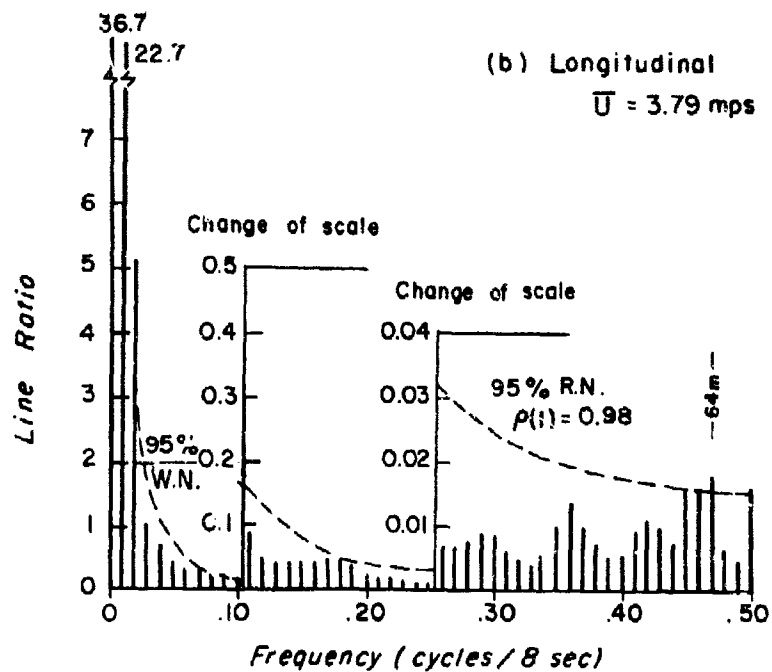
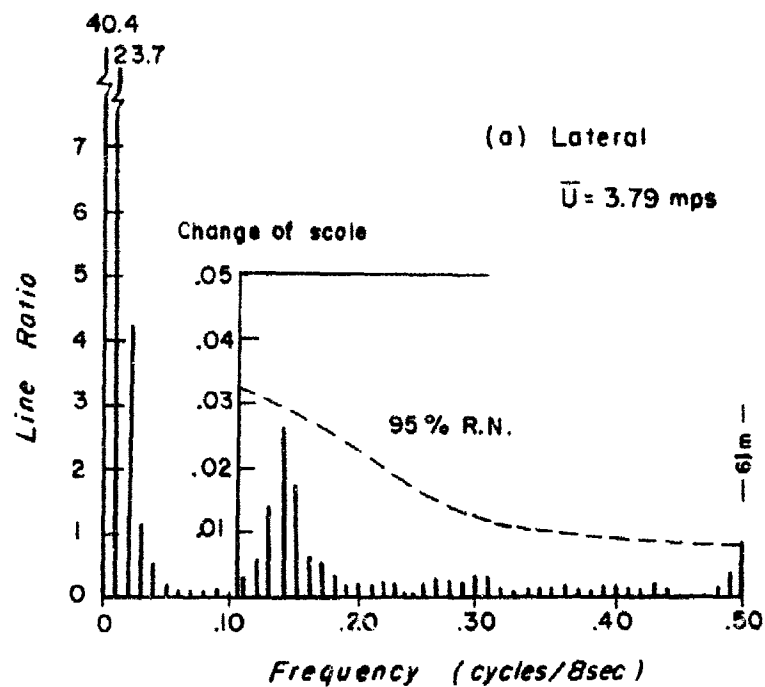


Fig. 3.21 Spectra of Wind Components at 27 m, Case III-BN

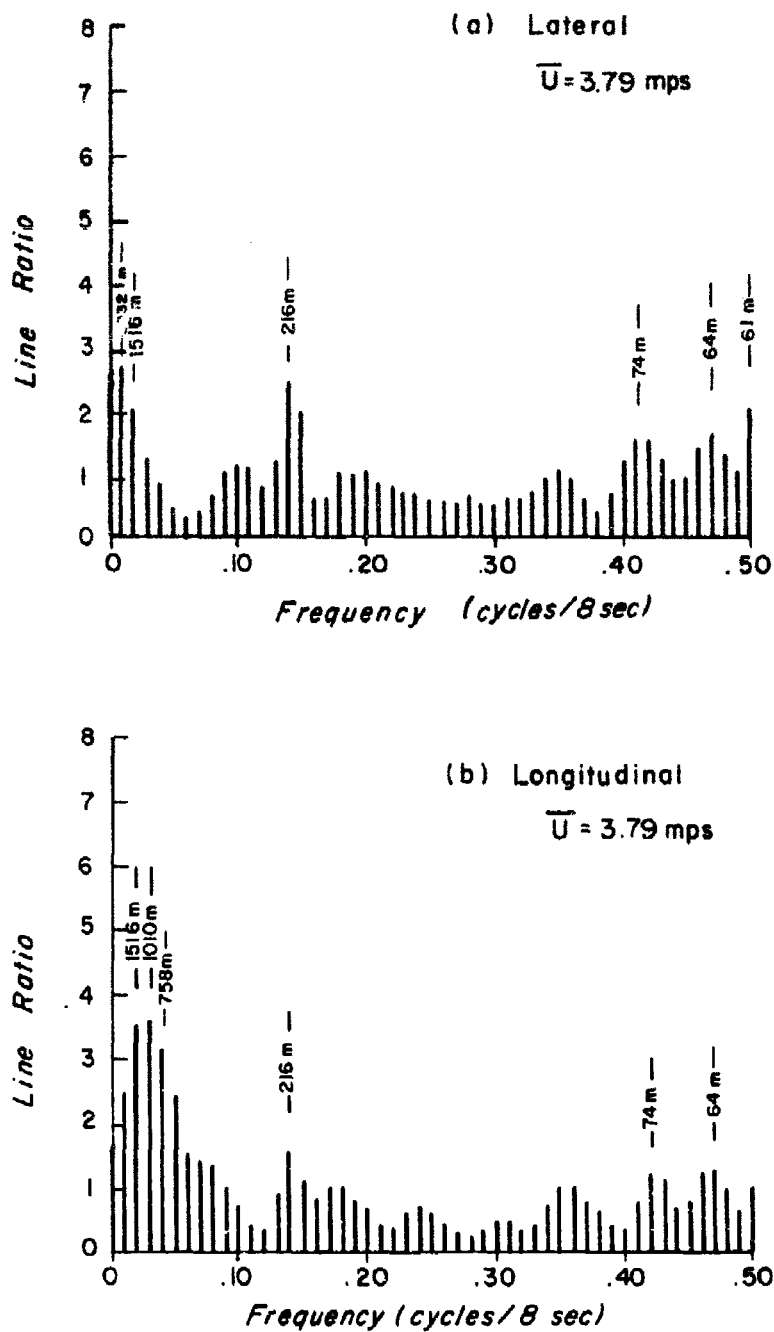


Fig. 3.22 Spectra of Components at 27 m After Prewhitening of Data

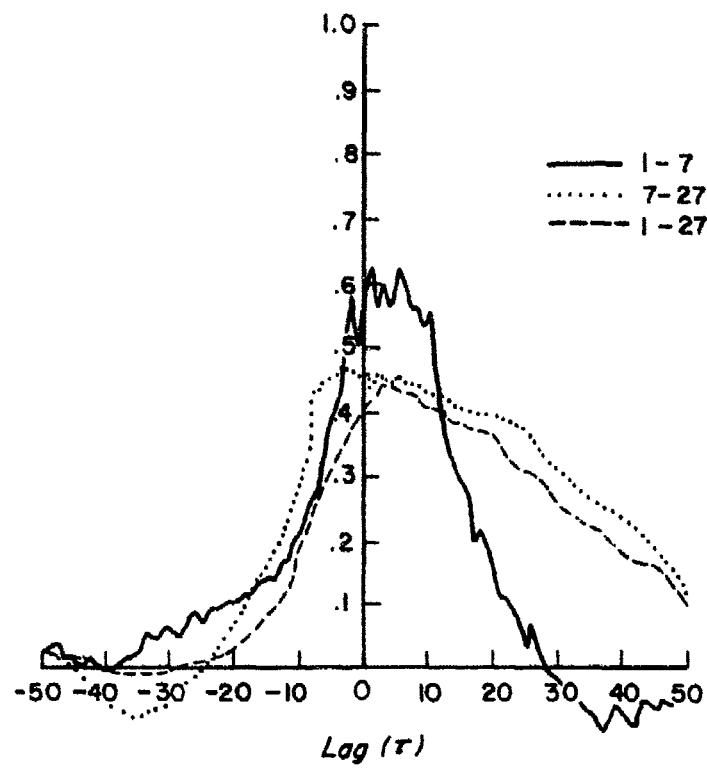


Fig. 3.23 Cross-correlation Functions of Longitudinal Components, Case III-BN



minutes includes the two 4000 sec periods described above. As before, the 500 data points were obtained by averaging consecutive data points. This time every 8 samples (1 sample per 2 seconds) were averaged, thus essentially using another low-pass filter which further attenuated the high frequencies. This practice, while rather delicate because of the decimation which may occur (Blackman, 1966 Chap. 10) is nevertheless preferable in this case since the other recourse would be to sample every 8th data point, which might lead to serious aliasing problems.

The autocorrelation functions are shown in Fig. 3.24. These show that there is a trend in the lateral component data and more trend in the longitudinal component data. (The cause will be discussed later in Sec. 2.) If these were the only samples available for analysis, it would be advisable to remove the trend; e.g., by means of a least squares routine.

The spectra of the components for the lower two levels are shown in Figs. 3.25 and 3.26. The 27 m level data was prewhitened with a high-pass filter in order to show the high frequency portion. The spectrum of these data is shown in Fig. 3.27. The wavelengths which correspond to the significant frequencies are shown in Table III.5.

Table III.5. Wavelengths Computed From Significant Frequencies Case IV-BN

Wavelengths (meters)								
Lat.	1 m	Long.	Lat.	7 m	Long.	Lat.	27 m	Long.
2784		2784	3536		3536	5536		5536
1392		1392	1768		1768	2768		2768
928		928				1845		1845
			101		104			1384
103		80	95		98			1107
99		77	86		86	198		923
62		66	74		71	191		615
58		58	71					
56								

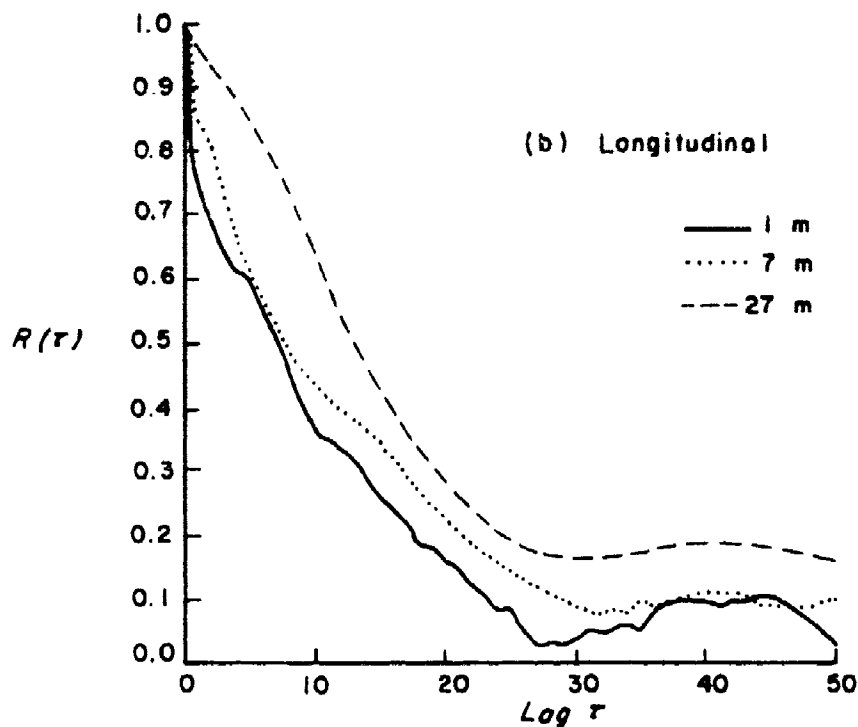
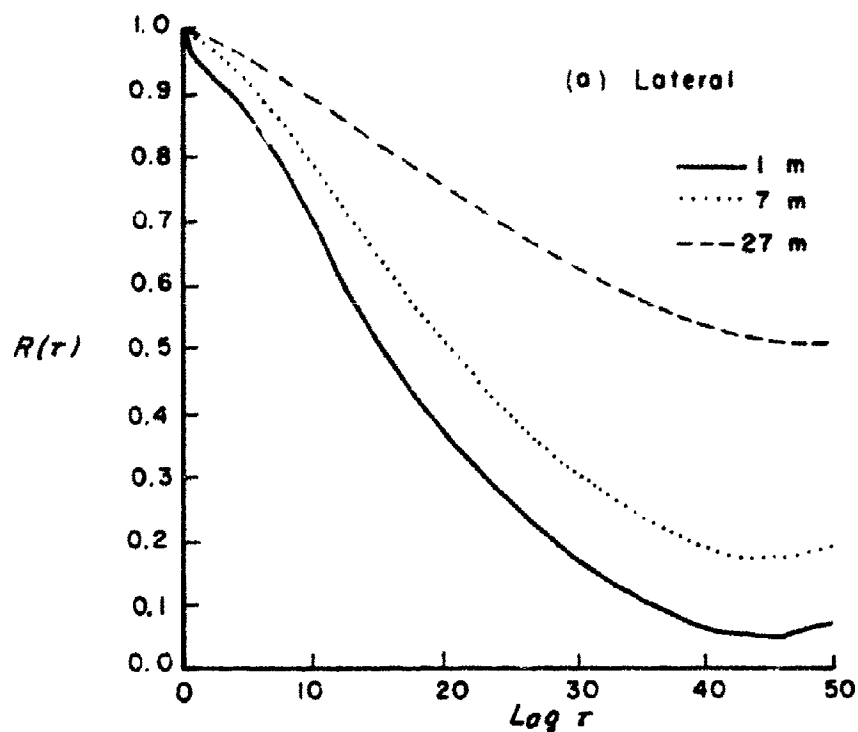


Fig. 3.24 Autocorrelation Functions of Wind Components,  
Case IV-BN

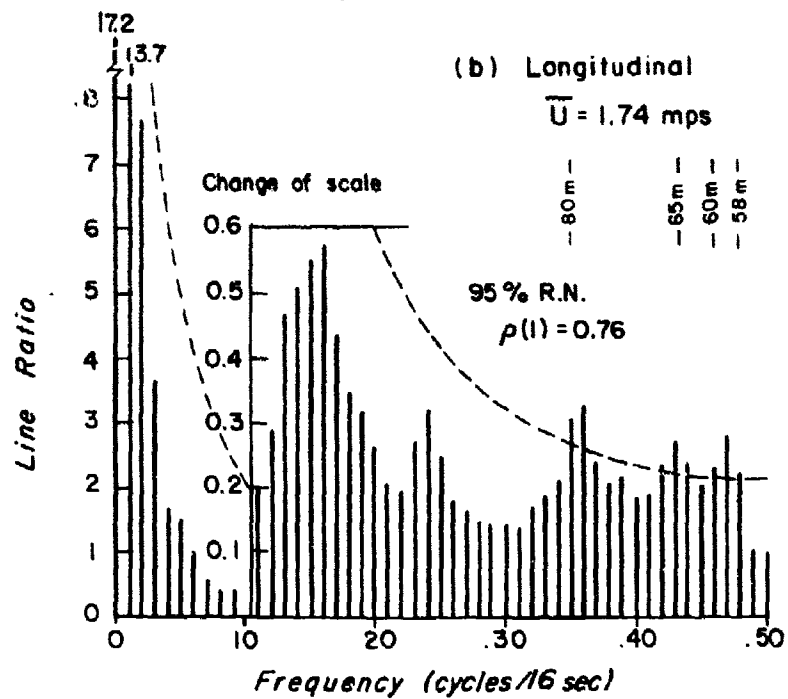
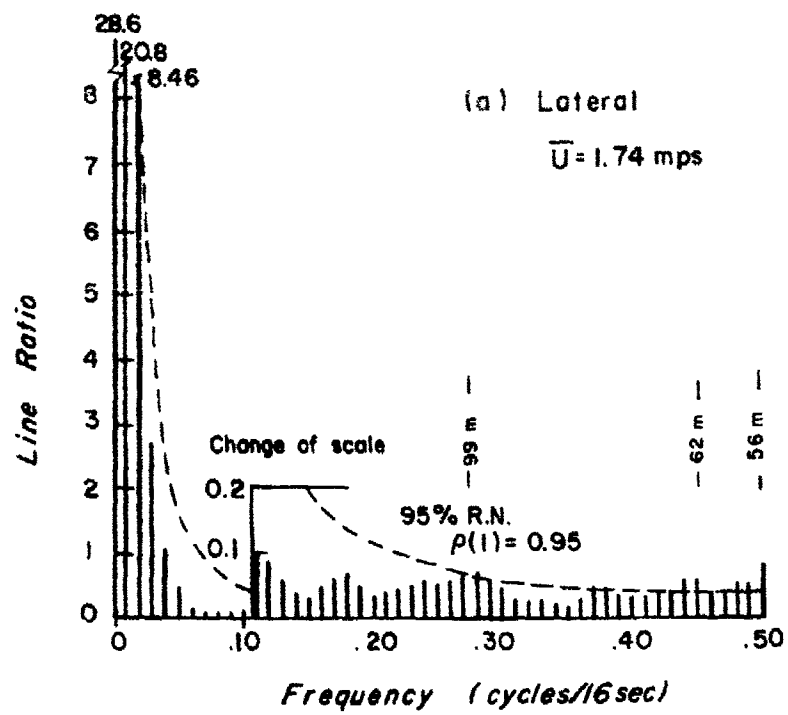


Fig. 3.25 Spectra of Wind Components at 1 m Level,  
Case IV-BN

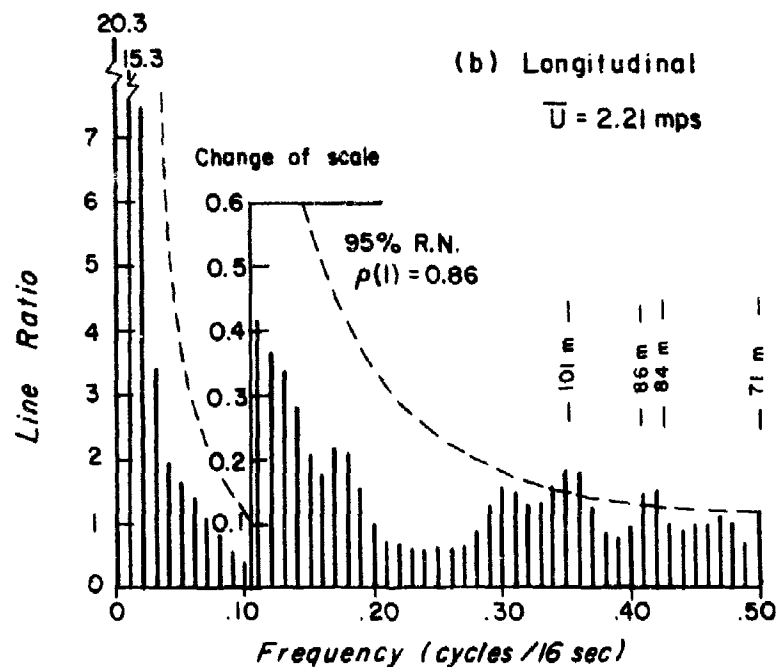
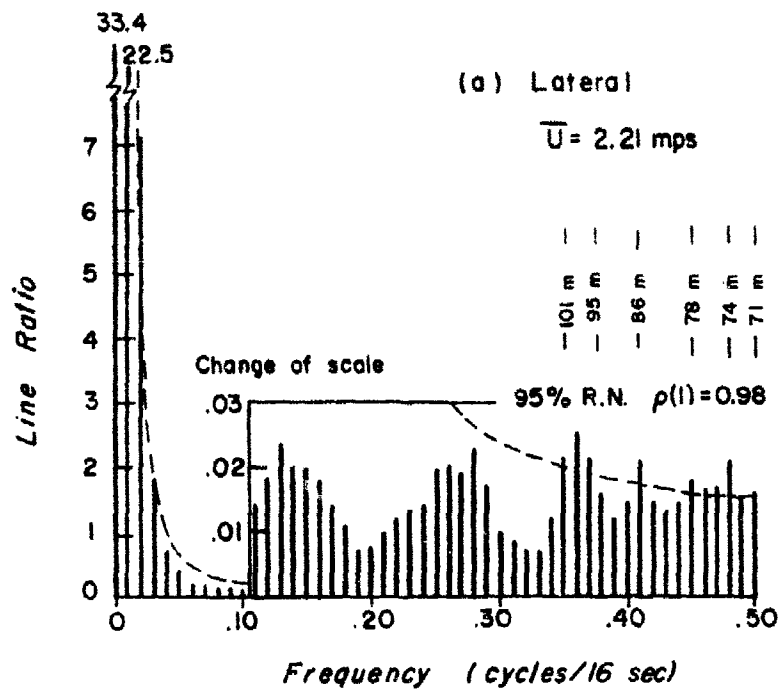


Fig. 3.26 Spectra of Wind Components at 7 m Level, Case IV-BN

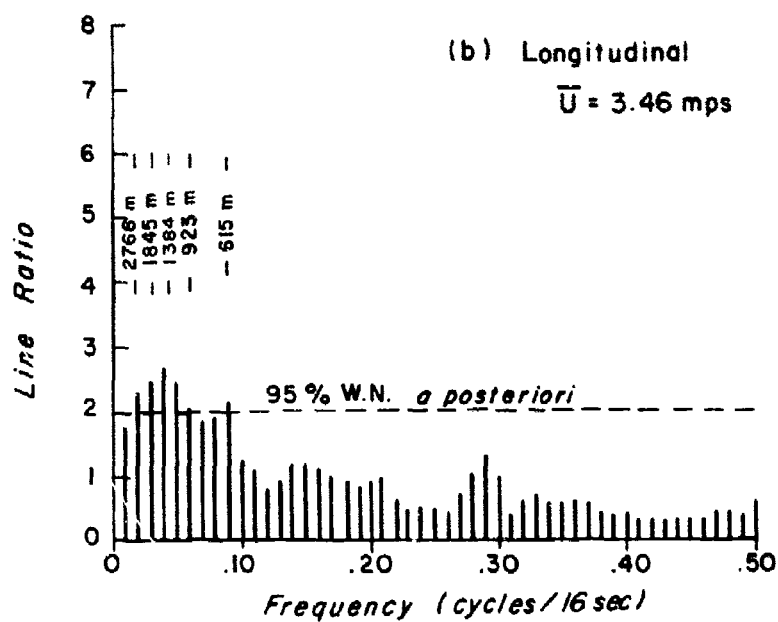
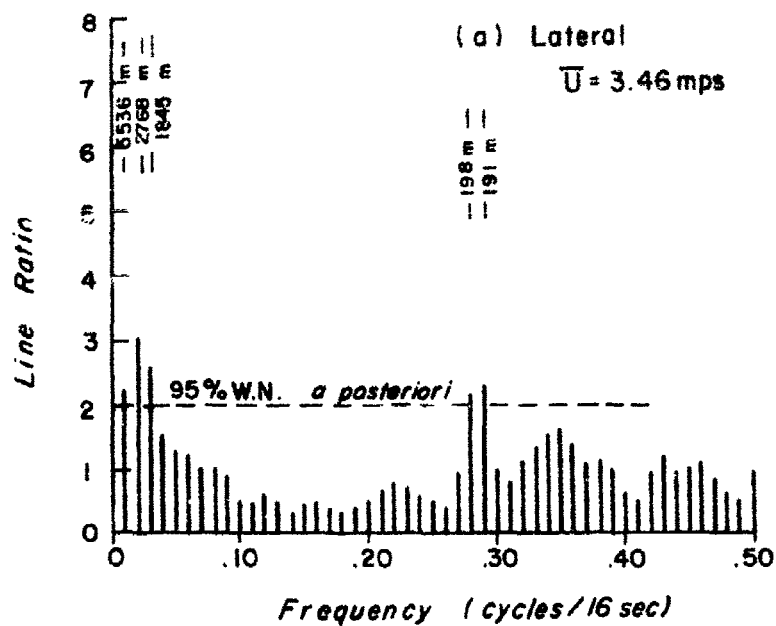


Fig. 3.27 Spectra of Components at 27 m Level After Prewhitening of Data, Case IV-BN

In general, the elongation downstream is still present at the lower levels and is more evident at 27 m. This does not contradict the earlier results for the 4000 sec sampling periods because the longer averaging time might have smoothed out the smaller wavelengths, or more likely, the longer sampling period does not detect the smaller waves. During this long period of time, these long wavelengths, which do not necessarily have to be eddy diameters per se but could be waves caused by the wind shear (or perhaps internal gravity waves), show the effects of stabilization of the atmosphere.

## 2. Evening Data Samples Taken at the Canal Tower

The time period of 2213-0027 CDT is the same as the Beach period. The land breeze is the dominant feature during the entire period. Light winds prevailed, especially at the 1 meter level, at times becoming calm.

Although the wind directions were the same at both locations (northerly flow), the canal site was under a more stable regime. The profiles of the dry bulb temperature and wet bulb temperature are shown in Appendix E for the canal and for the beach (only the period from 0000 to 0100 CDT are shown for the canal due to a malfunction of the dry bulb thermistor prior to midnight). The canal air temperature is warmer than the beach, indicating that the cooling effect has passed at the canal site and has progressed to the beach. (The temperature inversion shown at the beach is due to radiative cooling.) Subsiding air is present at the canal site causing the warmer temperature. The lowest layer at the canal is still cooler because of radiative cooling of the ground at 0000 hours. By 0100 hours, the subsiding air has warmed all levels and a more stable regime is present. The subsiding air, being drier and warmer, explains the temperature profiles (both dry and wet) at 0100 CDT for the canal site.

Case I-CN: Canal Nighttime, Sampling Period 1000 seconds

This case is at the same time period (2213-2230 CDT) as Case I-BN

for the beach site. The mean wind, however, is lighter for this location than at the beach.

The autocorrelation functions are shown in Fig. 3.28. As in Case I-BN for the beach, the curves indicate longer waves laterally than longitudinally. The longitudinal curves for the two bottom levels show a rather sinusoidal configuration; this could be attributed to the light winds with occasional periods of calm. A longer sampling interval with averaged observations would perhaps be better in this case. In general, the curves are similar to those of Case I-BN (Fig. 3.4).

The spectrum curves (not shown) for the three levels were used to obtain the wavelengths shown in Table III.6. These wavelengths are associated

Table III.6. Comparison of Wavelengths at Beach and Canal  
Stations for Period 2213-2220 CDT

Beach I-BN						Canal I-BN					
1 m		7 m		27 m		1 m		7 m		27 m	
Lat	Long	Lat	Long	Lat	Long	Lat	Long	Lat	Long	Lat	Long
290	290	380	380	664	664	162	162	332	332	470	470
	145		190	332	332			166	166		235
	97	12	11	14	17	4	6		110		
	8			13	15	3	3	10	83	13	15
7	7	8	8					7	65	9	9
6	6								55		
									47		
									27		
									15		

with frequencies whose values were statistically significant. The wavelengths obtained from Case I-BN are also shown for comparison purposes. The computed wavelengths are a function of the wind speeds; therefore, a comparison of the smallest or largest values cannot be made, because the winds are stronger at the beach. (Perhaps a point shown here is that the size of the smallest eddies

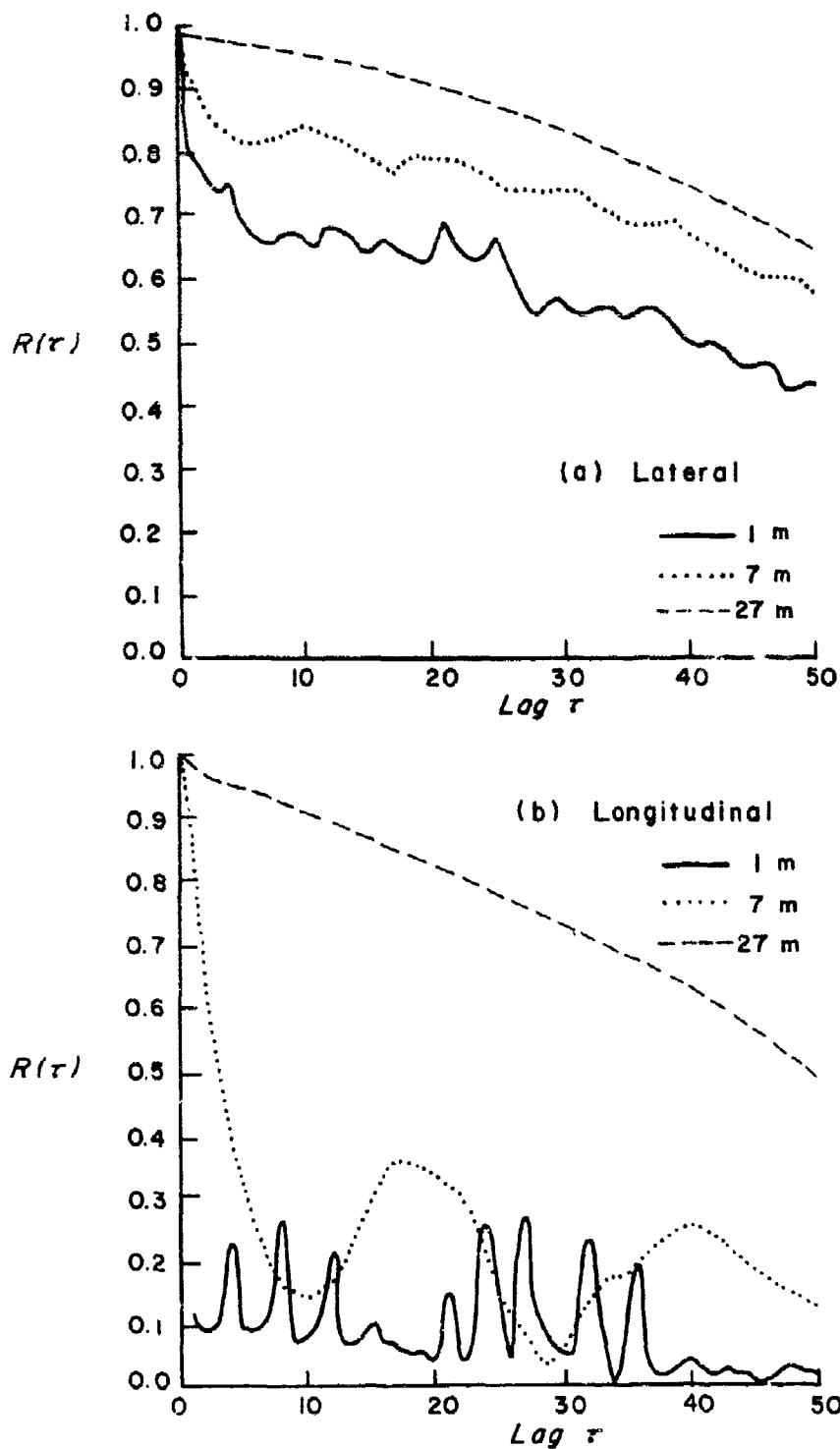


Fig. 3.28 Autocorrelation Functions of Wind Components,  
Case I-CN



or wavelengths are the smallest ones detected by this method of computation using spectral estimates. That smaller sizes were present is shown by using the slower winds at the canal site, i.e., 3 meters at the canal vs 6 meters at the beach. Furthermore, a sampling period of one sample per second could theoretically give wavelengths half as long than those obtained.) The comparisons which may be made are between the wavelengths which could be resolved at both locations and also the relative wavelengths laterally and longitudinally.

From the values shown, at the lowest level the horizontal "shape" is circular at both locations. This circular configuration implied by the values extends upward at the beach to 27 meters, but is not quite as evident at the 7 m level at the canal.

As in Case I-BN, a longer sampling period is needed to obtain more general characteristics to make a comparison of the two locations.

Cases II-CN and III-CN: Canal Nighttime, Sampling Periods 4000 seconds

The autocorrelation functions for Case II-CN is shown in Fig. 3.29. Compared to those from the beach location at the same period of 2213-2320 CDT (Case II-BN) shown in Fig. 3.12, these curves show more fluctuations in both components and presumably more energy at higher frequencies longitudinally. In fact, Case III-CN shown in Fig. 3.30 for a period between 2320-0027 CDT is more similar to the one at the beach in Case II-BN (Fig. 3.12). This illustrates that the land breeze regime which was at the canal location between the period 2213-2320 CDT is similar to the one present at the beach one hour later, or from 2320-0027 CDT, as presupposed by the temperature profiles. At the canal, however, the lateral components indicated more energy in the lower frequencies, perhaps caused in part by lighter winds, implying a more stable regime.

The wavelengths computed from the significant frequencies of the spectra (not shown) are given in Table III.7 for Case II-CN and Case III-CN.

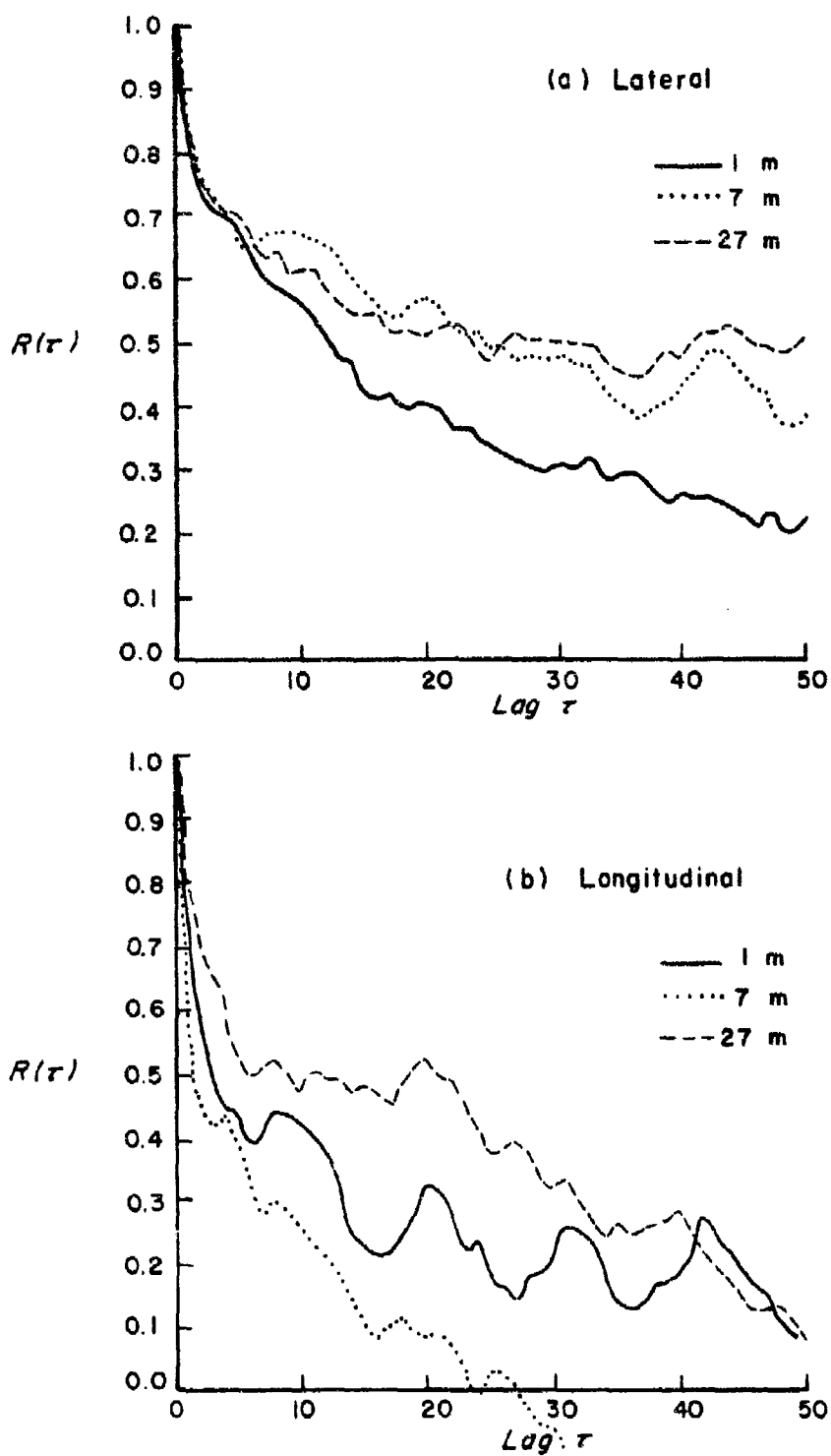


Fig. 3.29 Autocorrelation Functions of Wind Components,  
Case II-CN

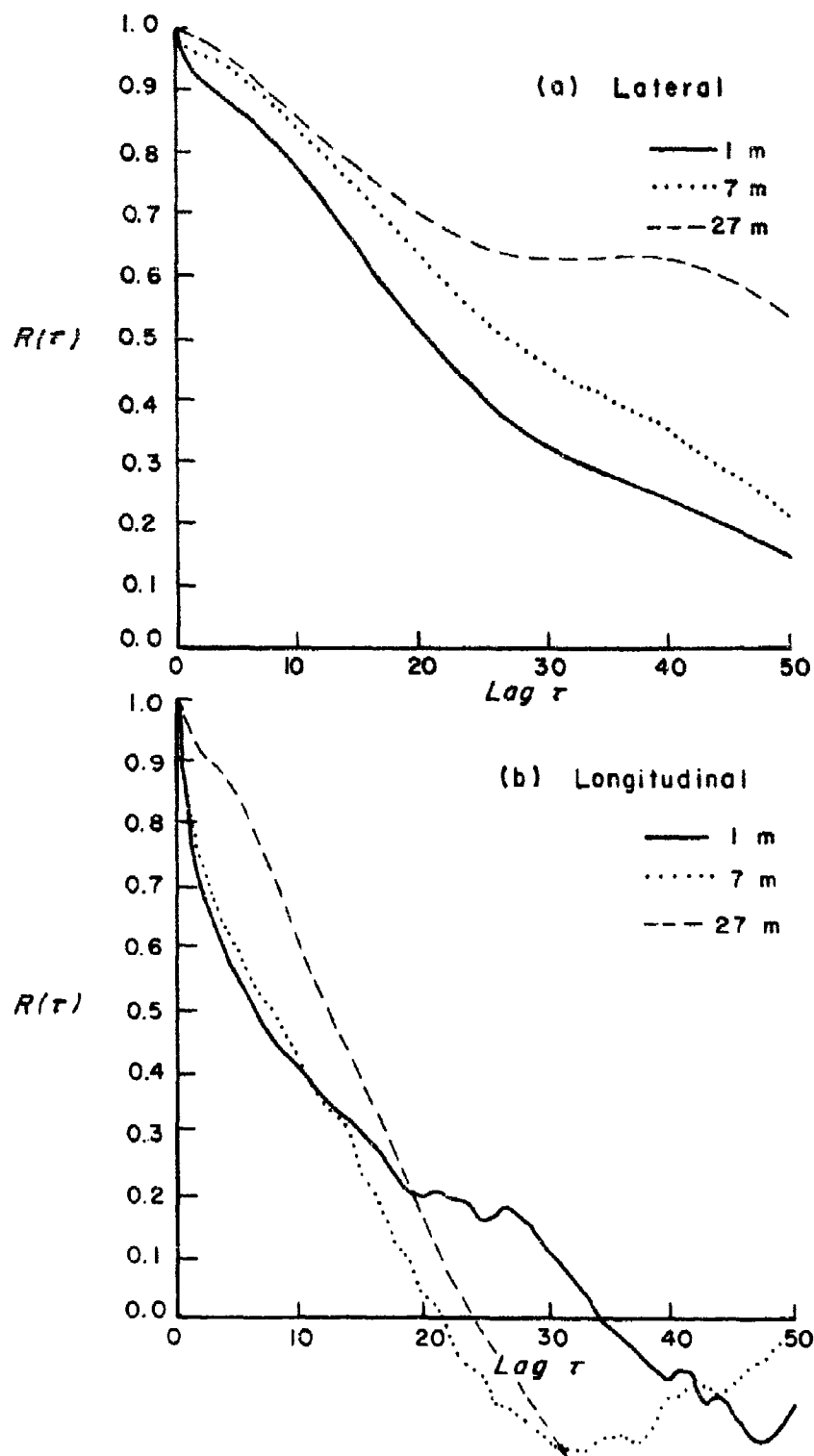


Fig. 3.30 Autocorrelation Functions of Wind Components,  
Case III-CN

Table III.7. Wavelengths Computed From Significant  
Frequencies, Cases II-CN, III-CN, and IV-CN

Case II-CN (2213-2320) 4000 sec Wavelengths (m)								
	1 m	Long	Lat	7 m	Long	Lat	27 m	Long
		720	1324		1324	1872		1872
360		360	672		672	936		936
240		240	448		448	624		624
33		180	53		331	103		468
20		19	51		265	53		375
			32		58			75
10		14			55	48		
					30	37		69
								42
$\bar{U} = 0.90$ mps				$\bar{U} = 1.68$ mps			$\bar{U} = 2.34$ mps	37

Case III-CN (2320-0027) 4000 sec Wavelengths (m)								
Lat	1 m	Long	Lat	7 m	Long	Lat	27 m	Long
928		928	1672		1672	2544		2544
464		464	836		836	1272		1272
309		309	48		557	848		848
22		232	42		60	170		127
		24						
19			34		47	57		116
					36	55		102
$\bar{U} = 1.16$ mps			$\bar{U} = 2.09$ mps			$\bar{U} = 3.18$ mps		
						88		

Case IV-CN (2213-0027) 8000 sec Wavelengths (m)								
Lat	1 m	Long	Lat	7 m	Long	Lat	27 m	Long
1616		1616	2944		2944	4272		4272
808		808	1472		1472	2136		2136
539		539	981		981	152		1091
37		85	164		740	119		237
32		43	155		103	100		225
		32	73		63	95		214
			66					159
			60					95
$\bar{U} = 1.01$ mps			$\bar{U} = 1.84$ mps			$\bar{U} = 2.67$ mps		93

There are two other differences between these two periods at the canal. The first is that the mean wind was somewhat lighter during the earlier period (Case II-CN). The second difference is that the short waves of the lateral and longitudinal component are nearly equal for the 7 m and 27 m samples of Case II-CN, whereas Case III-CN one hour later indicates an elongation with the wind as has already been observed at the beach site at the same sampling time.

The similarity of the canal period of Case III-CN with the later period of the beach has already been noted for the temperature profiles and the autocorrelation functions. The spectra also indicate similar elongation of the wavelengths with the wind for these two samples between the two locations.

As for the earlier case for the Canal it might be deduced that, using this method of analysis, light winds under stable conditions do not indicate an elongation of the eddies (or wavelengths). Instead, a circular pattern is denoted much the same as indicated using a shorter sampling period of 1000 seconds.

#### Case IV-CN: Canal Nighttime, Sampling Period 8000 seconds

The wavelengths derived from the 8000 second sampling period, Case IV-CN, shown in Table III.7 also indicate a similar circular pattern; but the mean winds are light, while the sampling period is long. Therefore, at least for these samples, there appears to be a connection between the magnitude of the wind and the indication of elongation with the wind of the eddies, depending on the sampling period. It should be noted, however, that these cases of light winds involve some periods of calm, and are not steady winds of small magnitude. These periods of calm might be the cause of these differences.

The autocorrelation functions of the components for 8000 seconds sampling period are shown in Fig. 3.31. All of the curves indicate a trend in the data samples. The trend indicated is longer and more evident than

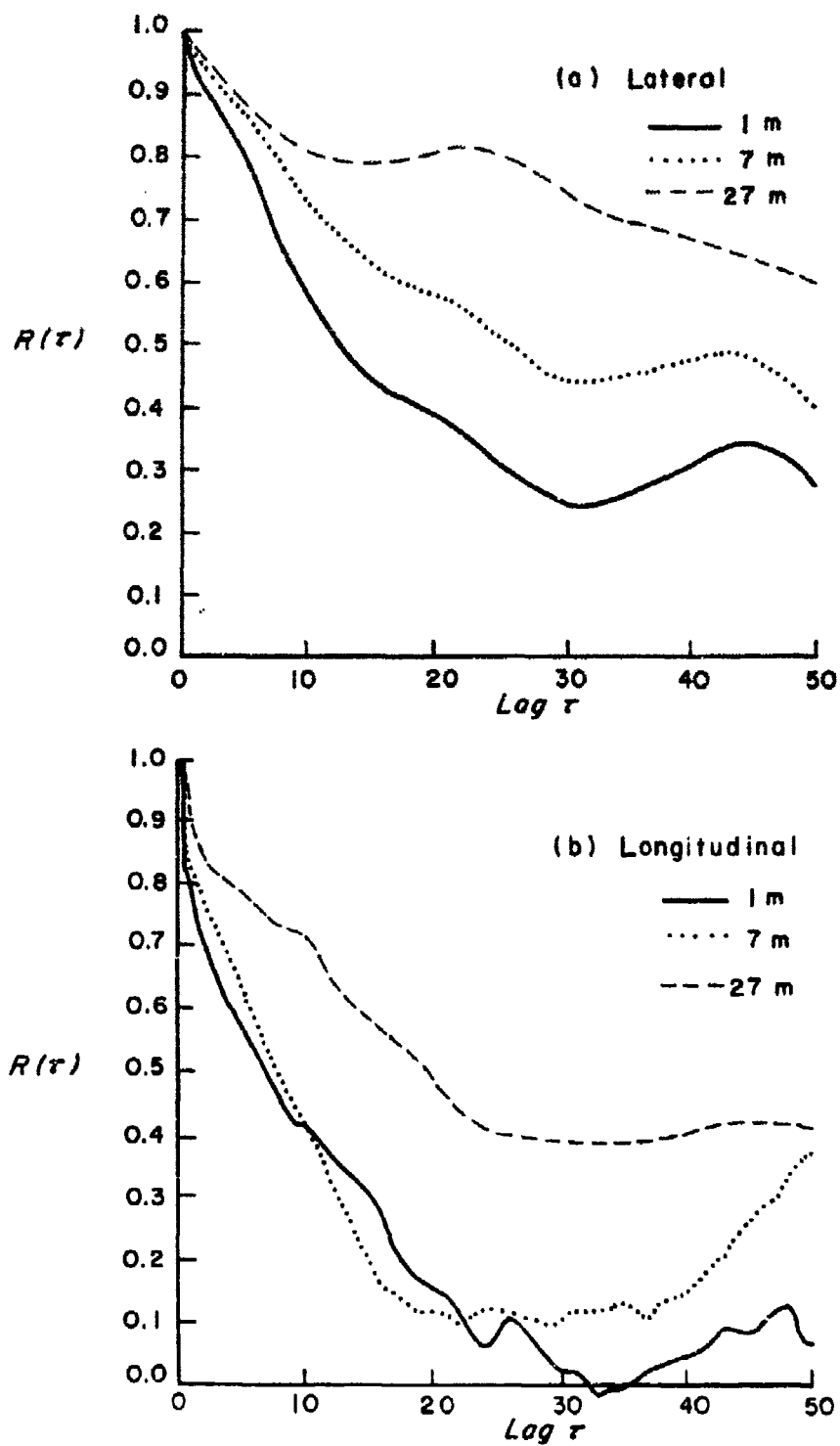


Fig. 3.31 Autocorrelation Functions of Wind Components,  
Case IV-CN

that at the beach at the same period (see Fig. 3.24). The increasing wind speeds, more pronounced at the canal, might account for most of the trend; however, some of the trend might be due to the gradual change in direction of the wind.

### 3. Daytime Data Samples Taken at the Beach Tower

Case I-BD: Beach Daytime, Sampling Period 1000 seconds

This sampling period covered the period of 1000 CDT to 1017 CDT when the wind direction was from the east. The regime could not be said to be a sea breeze but "becoming" a sea breeze, although the past history of an air parcel would be maritime air modified as it went across about two hundred meters of land.

Autocorrelation curves of the components shown in Fig. 3.32 show very similar patterns between the lateral and longitudinal components, suggesting perhaps an approach to horizontal isotropy (the curves would have to be exactly alike at a given level for isotropic turbulence). The curves show an indication of near equal distribution of energy laterally and longitudinally at a given level; in the stable case the lateral component had most of the energy in the long waves and the longitudinal component had more energy distributed over the spectrum.

The spectra of the data for the 1 m level is shown in Fig. 3.33. These are similar in the low frequency region which is associated with wavelengths from 360 meters to 90 meters and the high frequency region of wavelengths of 8 meters. There are still longer scales in the lateral component; however, an approximation of the integral scale of turbulence by the energy at the zero frequency gives a value of 4.6 sec for the lateral and a value of 3.3 sec for the downstream component. (The same conclusion of relative scales could perhaps have been reached by comparing the two autocorrelation curves

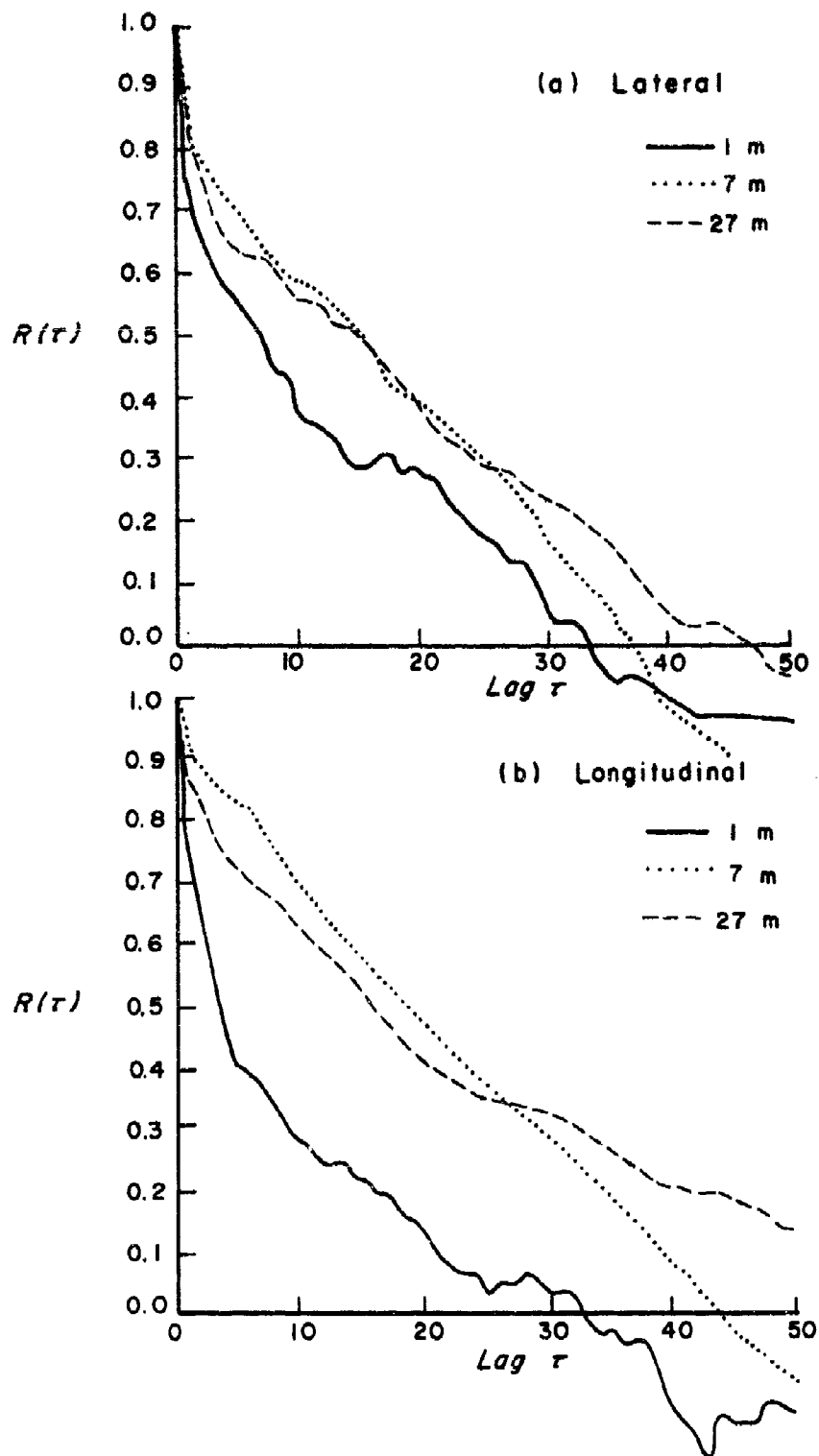


Fig. 3.32 Autocorrelation Functions of Wind Components, Case I-BD



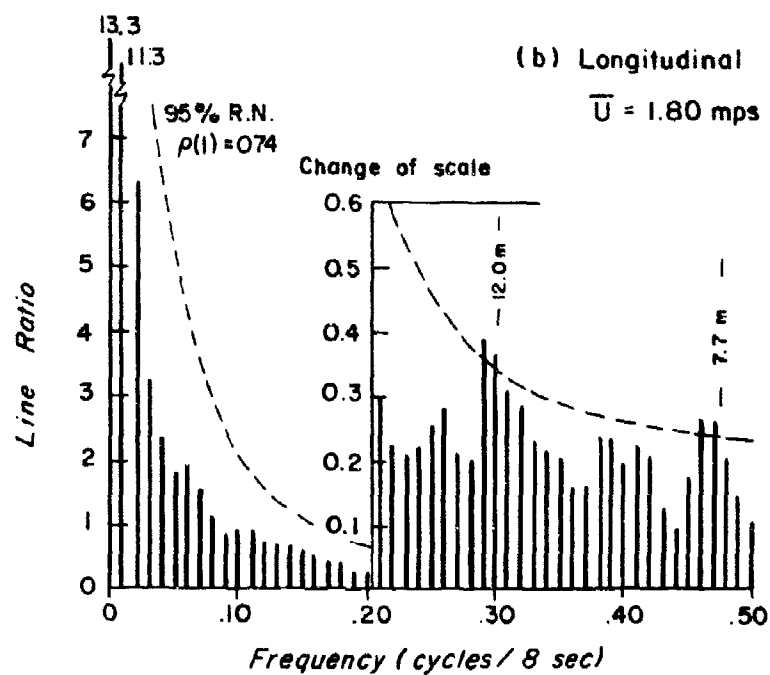
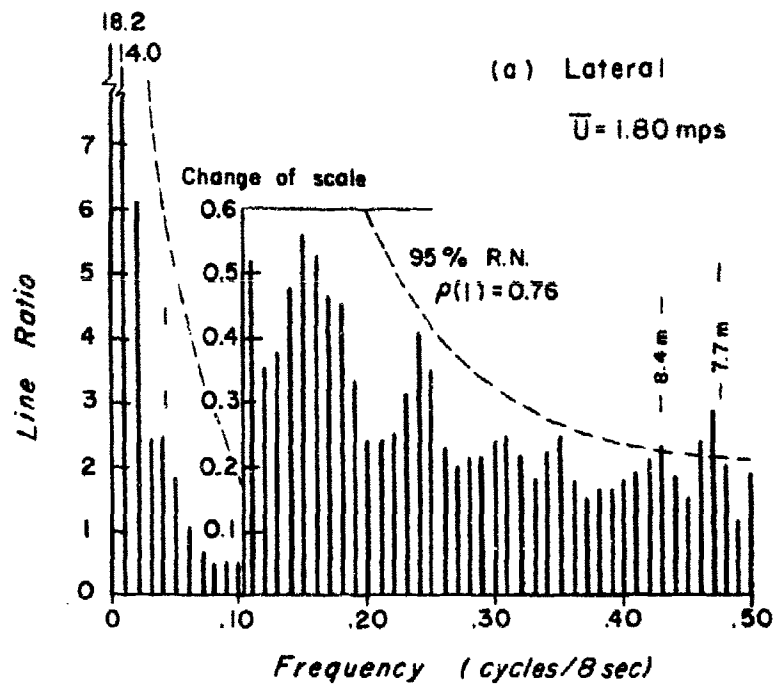


Fig. 3.33 Spectra of Wind Components at 1 m Level, Case I-BD

for the 1 m level.) The local isotropic turbulence is implied because the energy at the high frequency end is nearly the same for both components.

At 7 m (Fig. 3.34) above the ground, where the mean wind is essentially the same (1.80 mps at 1 m and 1.82 mps at 7 m), the low frequency portion of the spectrum shows wavelengths of 364 and 182 meters for both components, and about 14 meters on the lateral and about 18, 11, and 7 meters for the longitudinal (downstream) components.

The long meandering wind in the lateral sense for the stable case is no longer present, for the longer wavelengths are essentially the same. As a result of the sun's heating of the earth's surface, buoyancy or convective forces are now contributing to the turbulence, as well as mechanical effects. This is shown in the "circular" pattern of the wavelengths at the 1 m level. At the other two levels, there are more high frequency contributions longitudinally, as shown in Figs. 3.34 and 3.35. To summarize, the approximate significant wavelengths are shown in Table III.8. It appears that even though the

Table III.8. Wavelengths Computed From Significant Frequencies Case I-BD

1 m			7 m			27 m		
Lat		Long	Lat		Long	Lat		Long
360		360	364		364	444		444
180		180	182		182	222		222
120		120	14		18	17		11
90		90			12			10
		12			11			9
8		8			7			

wind is from the east, and has a maritime history, the surface heating is enough to create thermal turbulence. Also, at this sampling period the upper levels show some elongation laterally. The increase in wavelengths upward is to a much lesser degree than with the stable case.

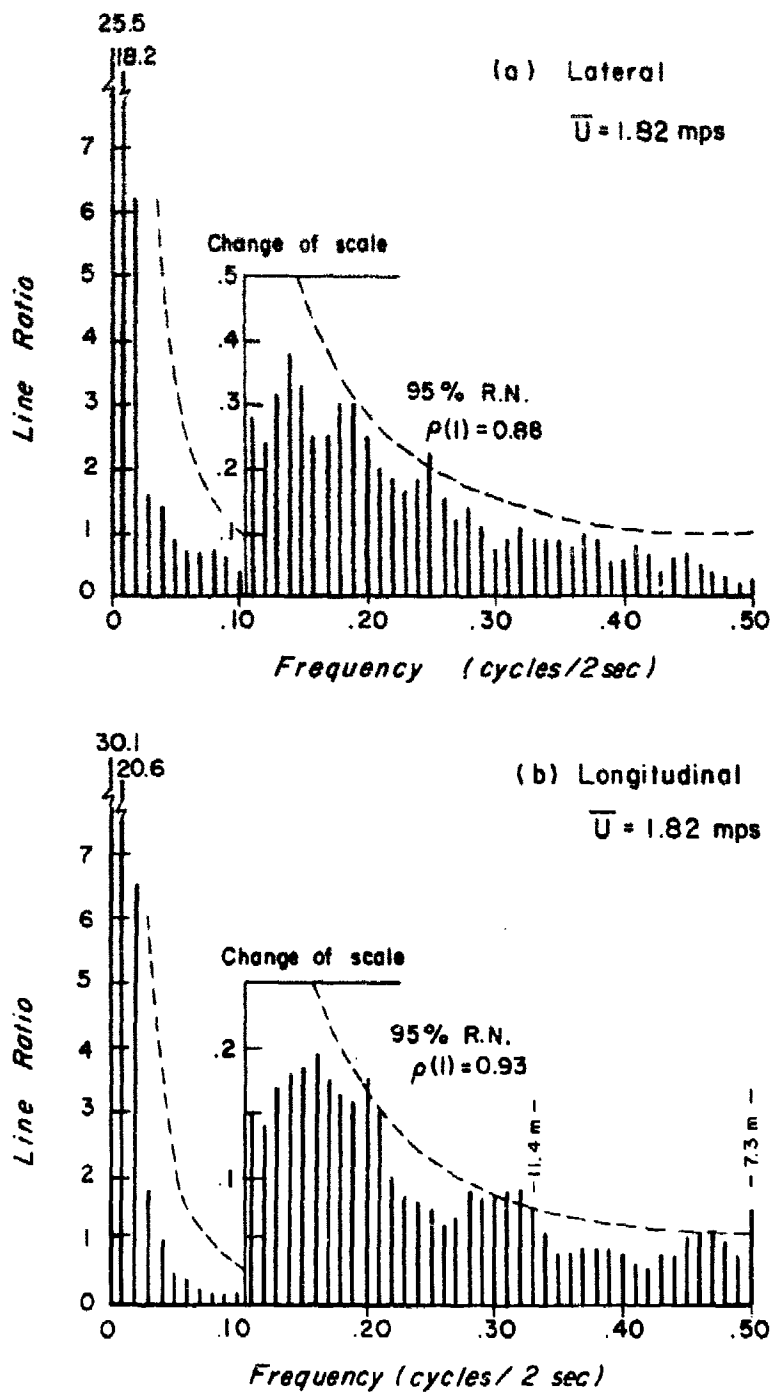


Fig. 3.34 Spectra of Wind Components at 7 m Level, Case I-BD

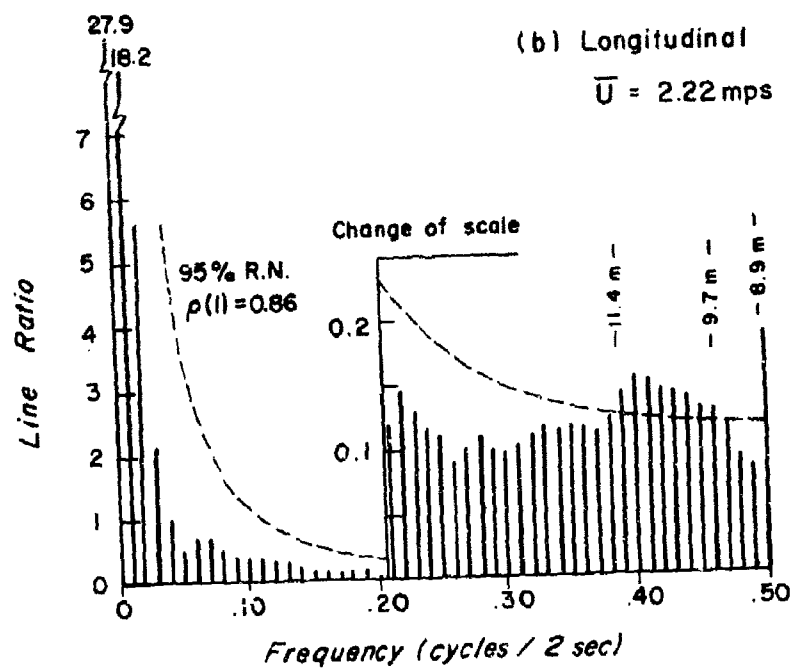
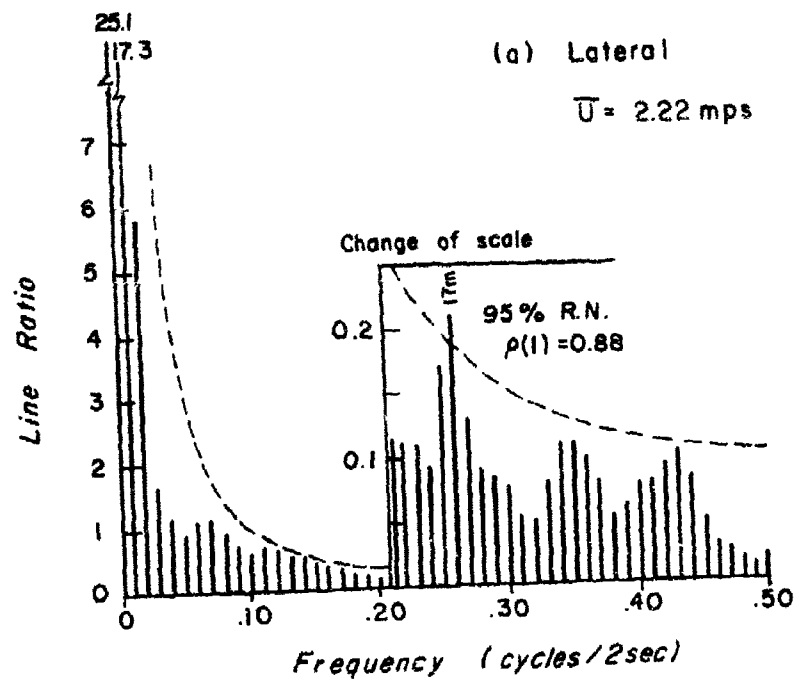


Fig. 3.35 Spectra of Wind Components at 27 m Level, Case I-BD

The cross-correlation curves are shown in Fig. 3.36. There is high correlation of the same components between levels, with the lowest value obtained by correlating the 1 m and 27 m levels. The correlations between levels 1 m and 7 m and between 7 m and 27 m are nearly the same. Furthermore, the correlations of the lateral components are nearly equal to those of the longitudinal components for the same levels; in the stable atmosphere, the longitudinal correlations between levels were lower than lateral correlations. This indicates that the convective type turbulence equally influences the horizontal components, at least up to the size of wavelengths implied by this type of analysis.

An important feature shown in these correlations is that the winds, although veering with time, do not veer simultaneously. It is rather difficult to determine from the correlation curves which level is "ahead" of the other. An examination of the plots of the components for this time period does not give a clear picture of the veering either. It was evident from studying the "strip charts", such as the one shown in Appendix A, that a decrease in wind speed took place during the transition period from the land-breeze to the sea-breeze regime. This occurred first at the top level, then the middle level, and the bottom level was the last to turn. The bivariate statistics computed for the actual components (Appendix F) show that Case I-BD from 1000-1017 CDT and Case III-BD from 1005-1022 CDT have the lowest mean winds. These two cases occurred during this transition period.

Case III-BD: Beach Daytime-Sampling Period 1000 seconds

These are for the period 1005-1022 CDT for winds from an ESE direction, thus traversing slightly less land area than Case I-BD.

The correlation functions are shown in Fig. 3.37; to a small degree, longer waves laterally are indicated for the 7 m level and 27 m level. The spectra for the three levels are given in Figs. 3.38, 3.39, and 3.40. The

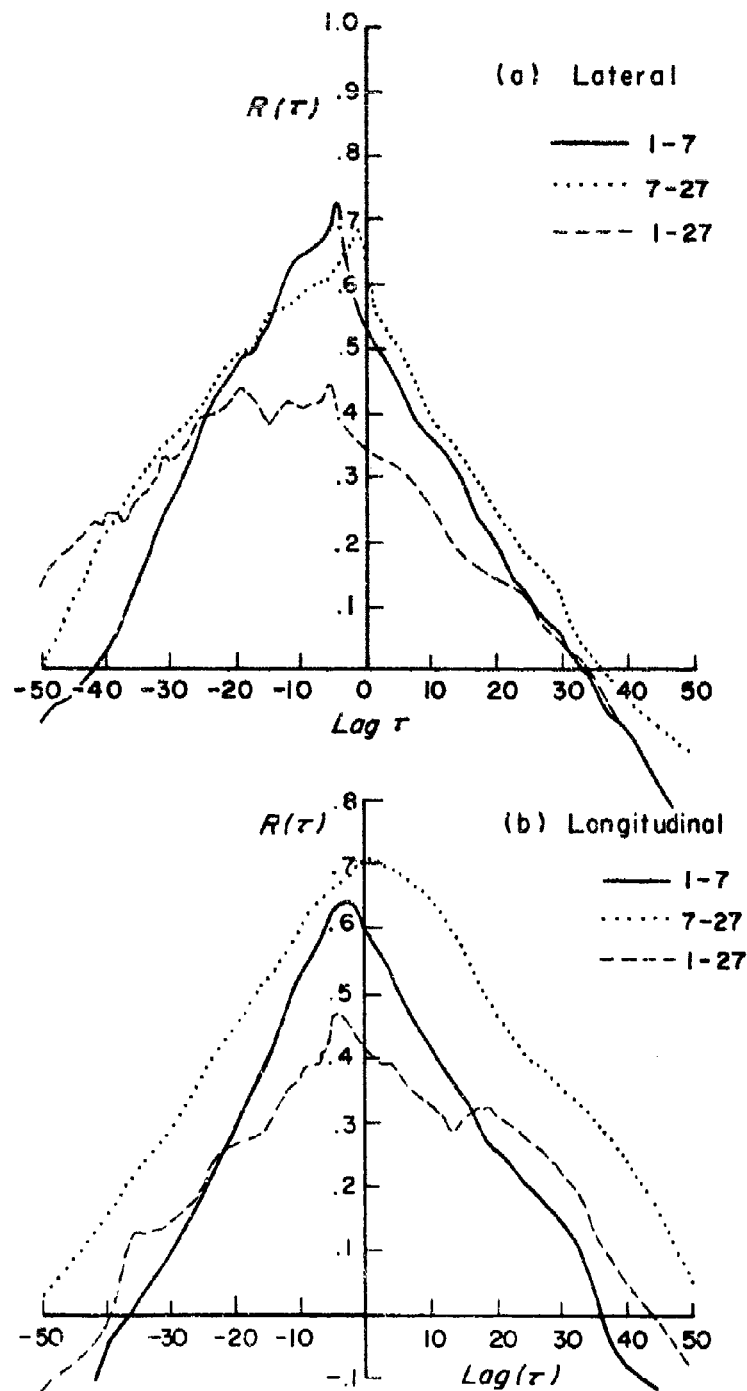


Fig. 3.36 Cross-correlation Functions of Components, Case I-BD

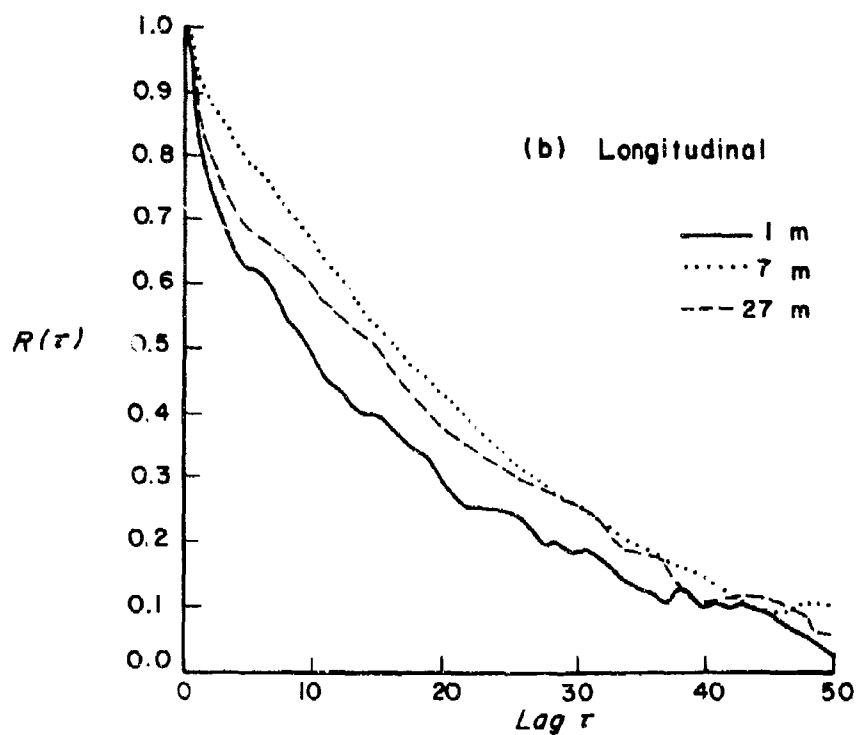
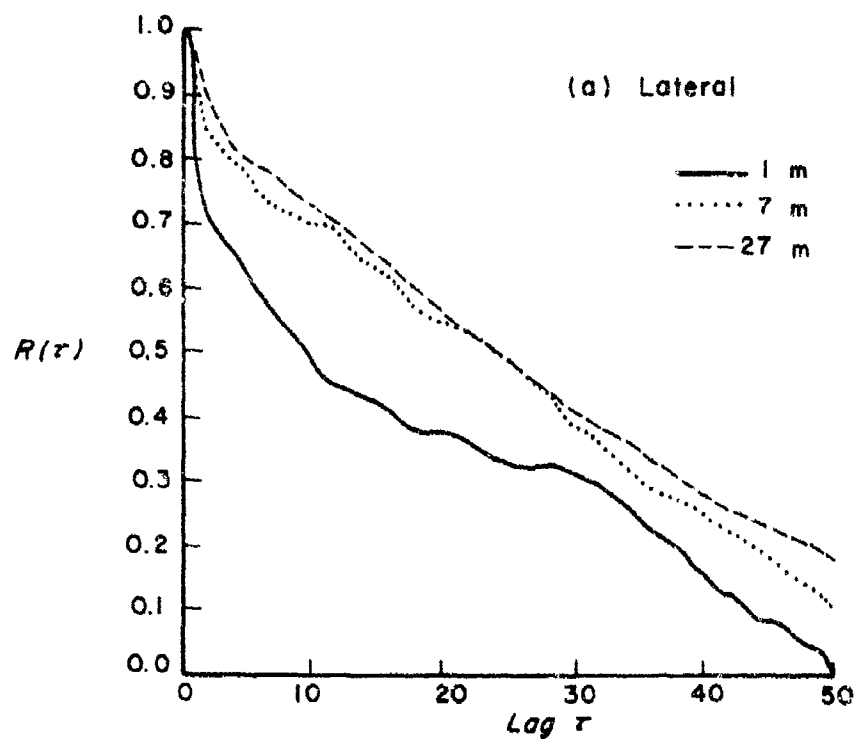


Fig. 3.37 Autocorrelation Functions of Wind Components,  
Case III-BD

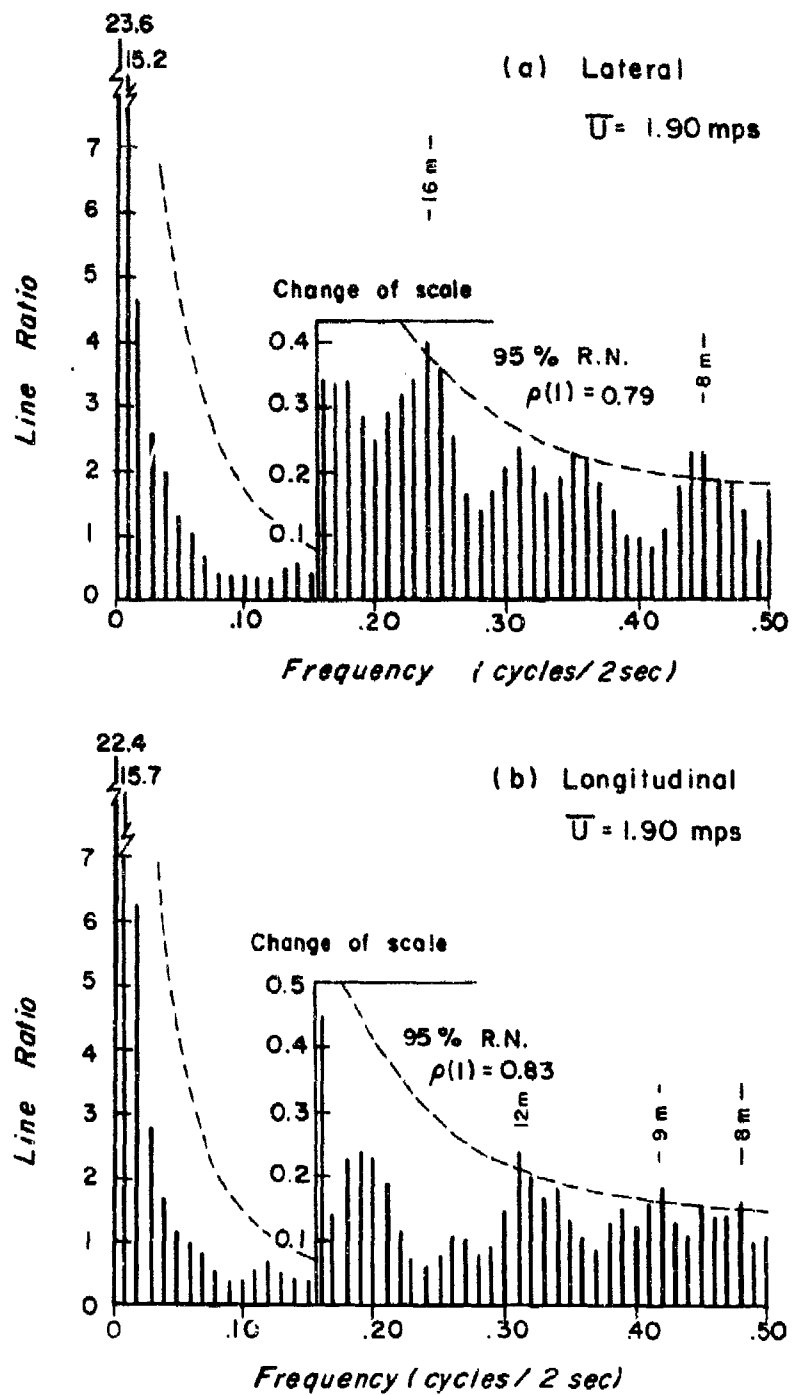


Fig. 3.38 Spectra of Wind Components at 1 m Level, Case III-BD



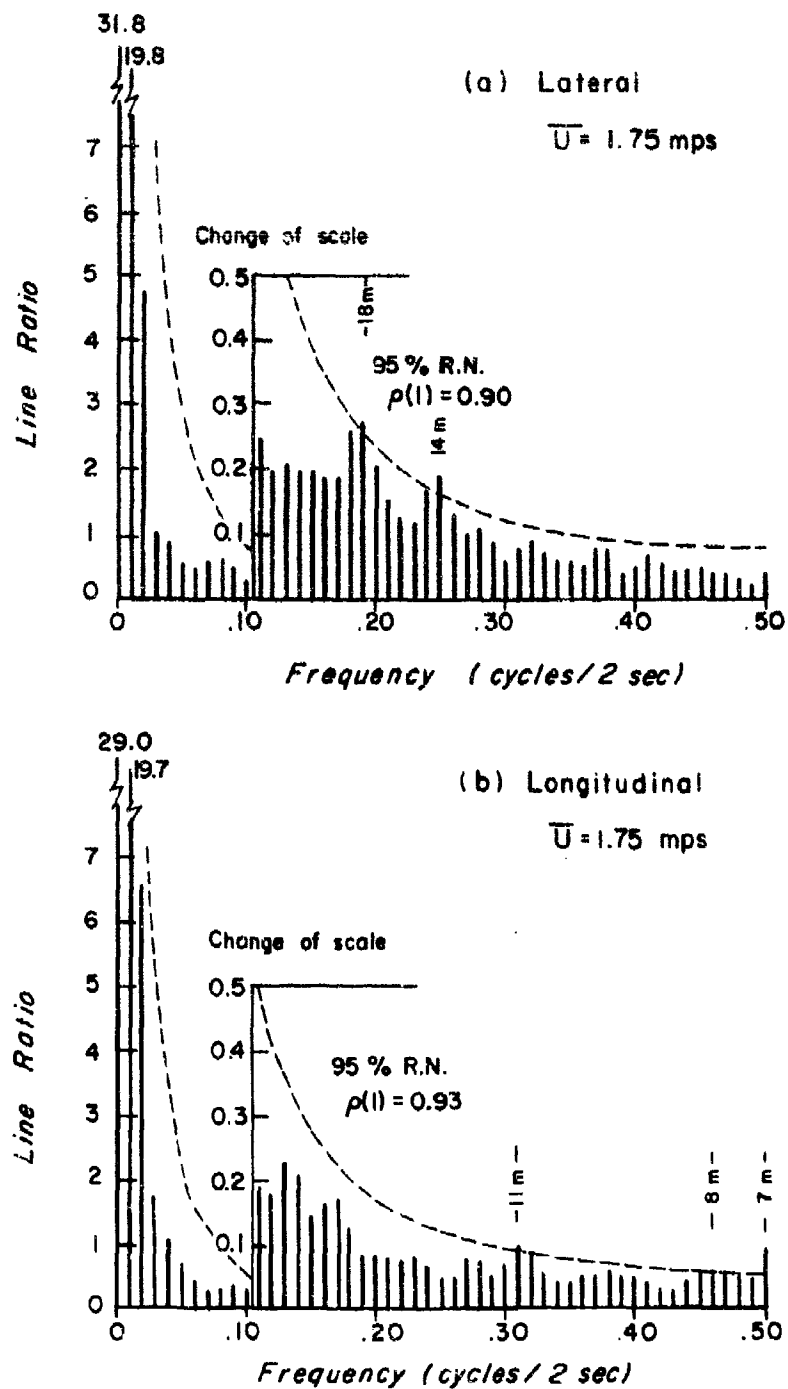


Fig. 3.39 Spectra of Wind Components at 7 m Level, Case III-BD

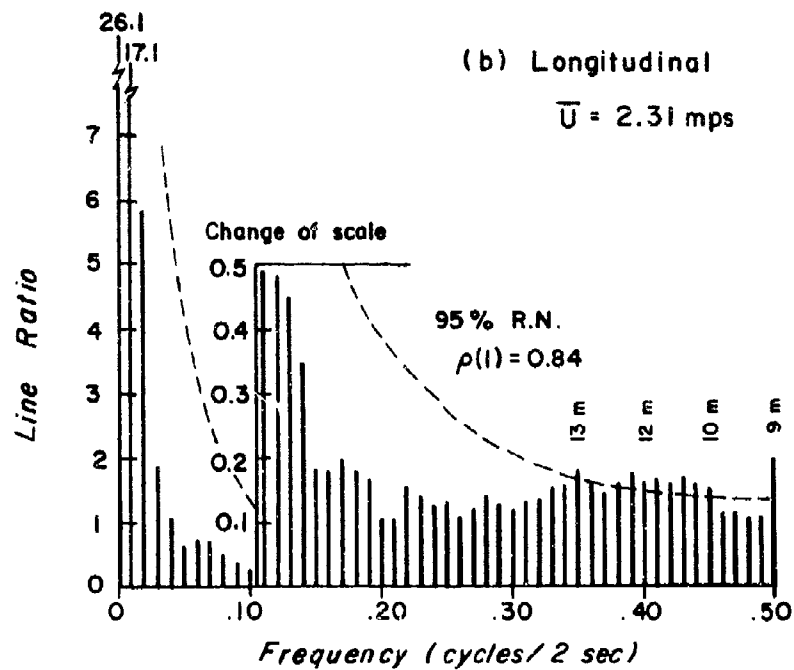
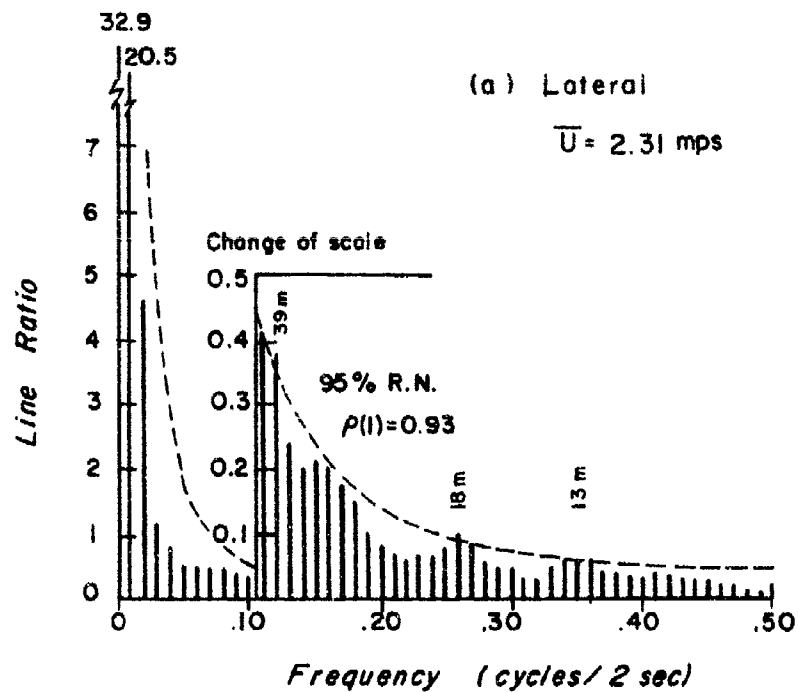


Fig. 3.40 Spectra of Wind Components at 27 m Level, Case III-BD

figures in Table III.9 are obtained from these spectra.

Table III.9. Wavelengths Computed From Significant Frequencies, Case III-BD

Lat	1 m	Long	Lat	7 m	Long	Lat	27 m	Long
380		380	350		350	426		426
190		190	175		175	231		231
127		127	117		11	39		13
95		15	18		8	18		10
16		8	14		7	13		9
8								

The bottom level shows a somewhat circular configuration (local horizontal isotropy) and the other two levels show a lateral elongation and smaller wavelengths as in Case I-BD. The correlations also showed a similar pattern of high correlations and indicate the winds turned at different periods for the three levels.

Case II-BD: Beach Day, Sampling Interval 1000 seconds

In Case II-BD, which occurred during the period immediately following Case I-BD, the wind started to increase in speed. The circular pattern in the eddies extends to at least the 7 m level. The auto-correlations and spectra are shown in Figs. 3.41 to 3.44. Note that even though the auto-correlation functions indicate longer waves laterally, the spectra still show enough energy at the middle and high frequencies to give equal wavelengths across-the-wind and downwind. This is probably due to increased surface heating causing convective turbulence to penetrate at least up to 27 m.

Case IV-BD: Beach Daytime, Sampling Interval 1000 seconds

Approximately thirty minutes later at 1047-1104 CDT, the winds have veered to the SE and are now definitely of maritime origin. Because of the increase in surface heating, the integral scales are smaller than those during

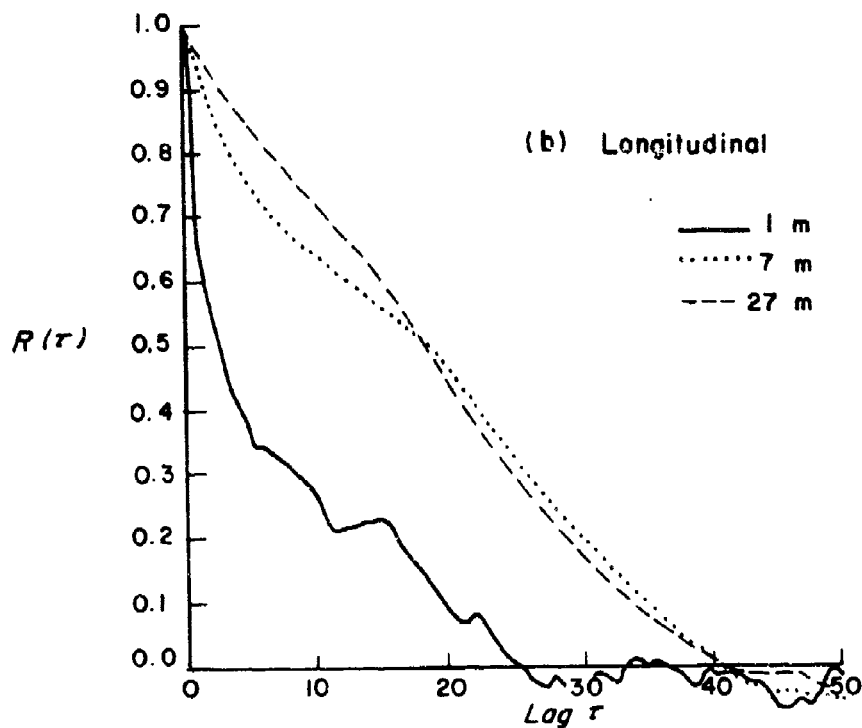
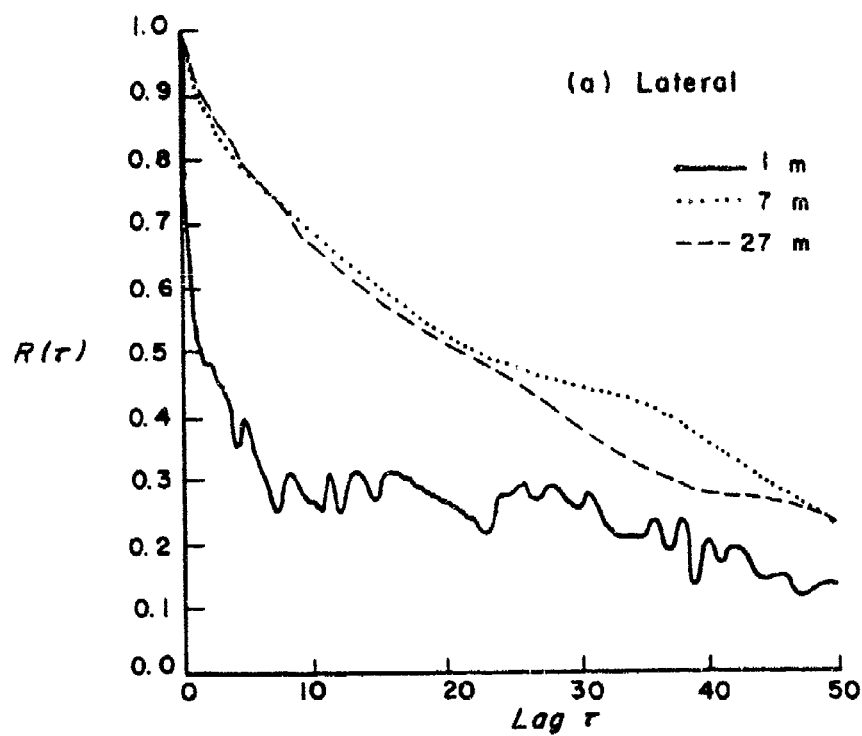


Fig. 3.1 Autocorrelation Functions of Wind Components, Case II-BD

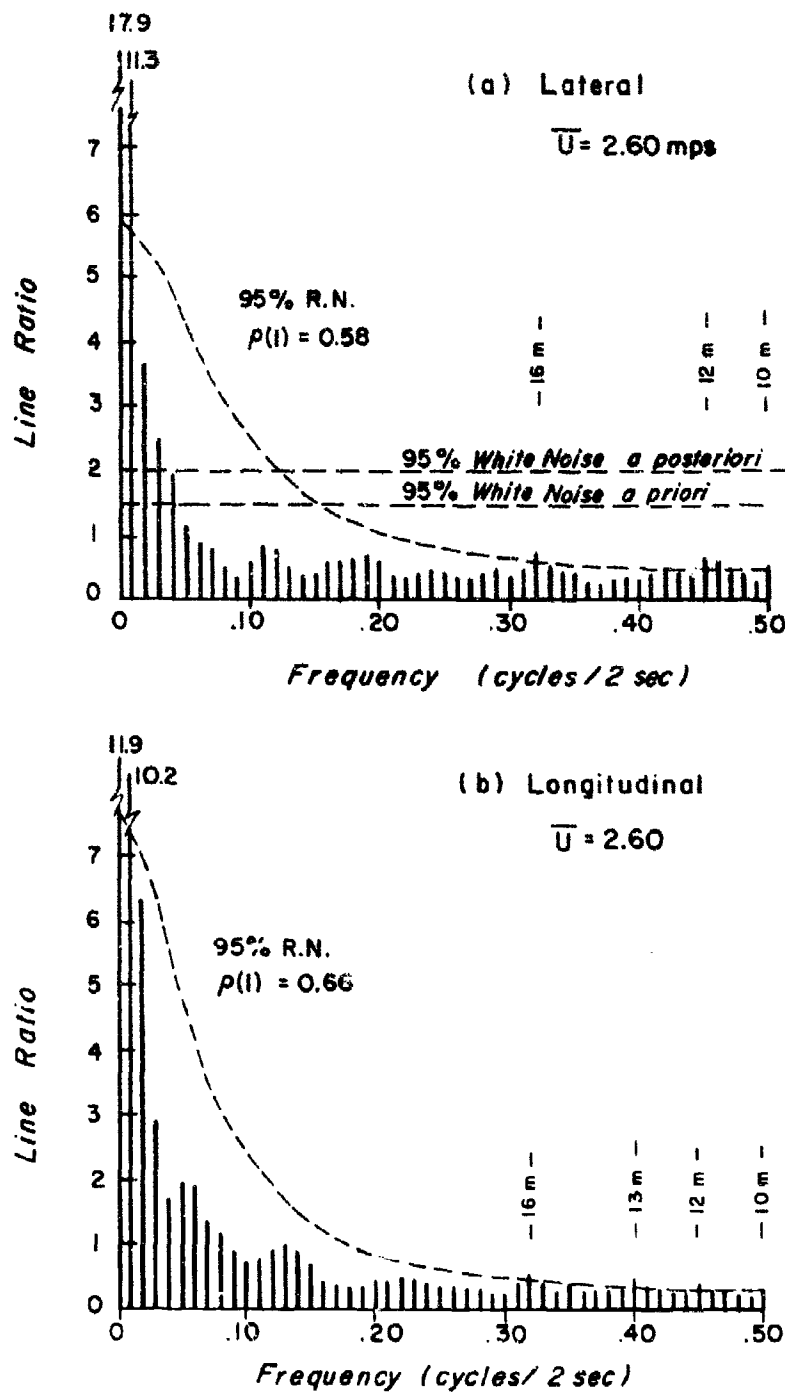


Fig. 3.42 Spectra of Wind Components at 1 m Level, Case II-BD

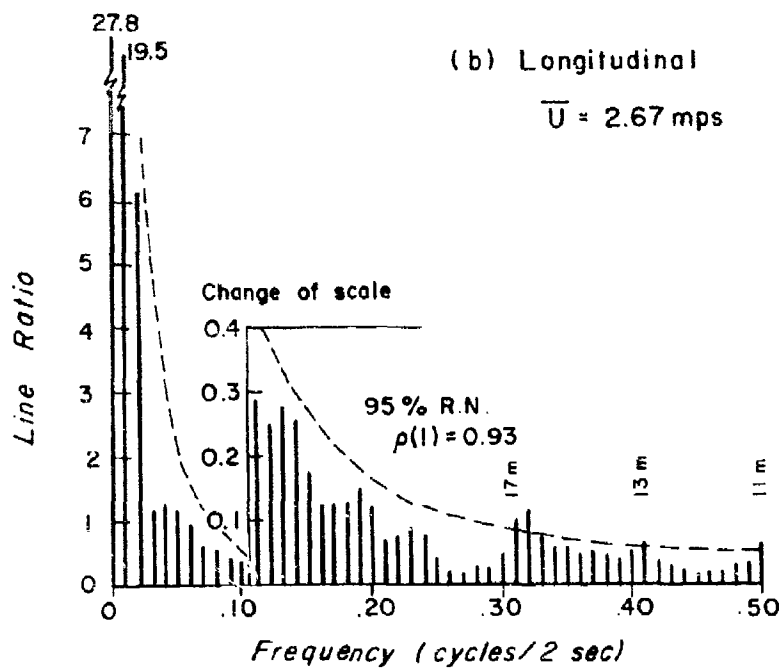
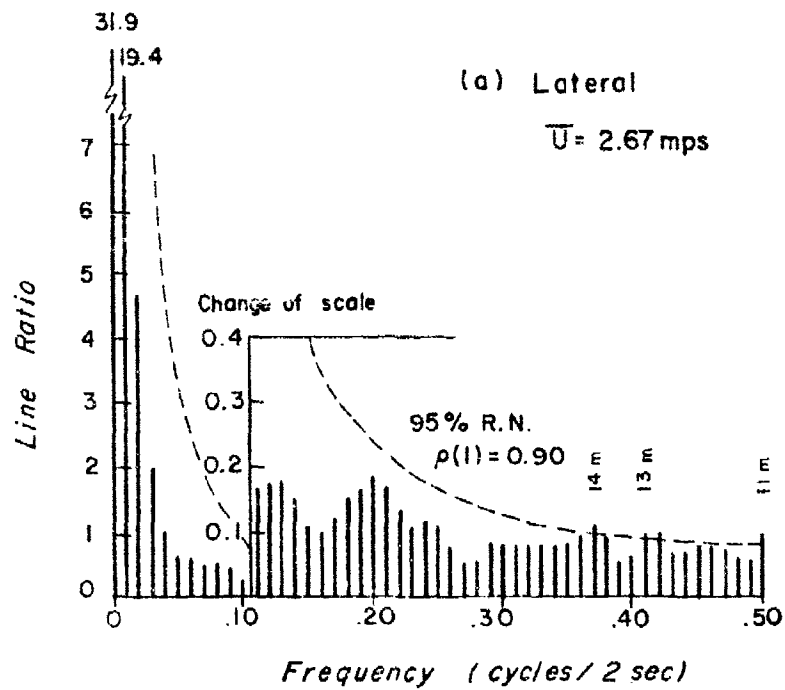


Fig. 3.43 Spectra of Wind Components at 7 m Level, Case II-BD

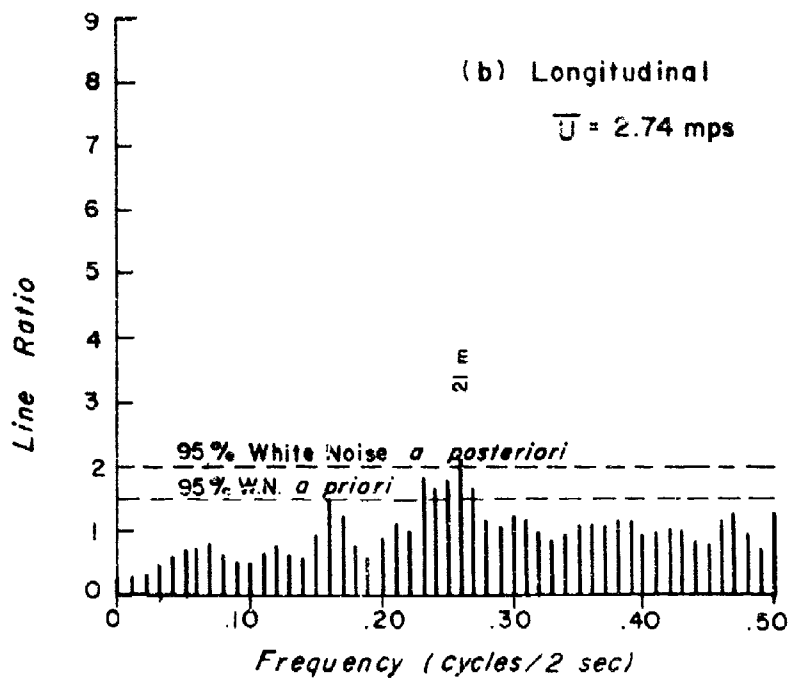
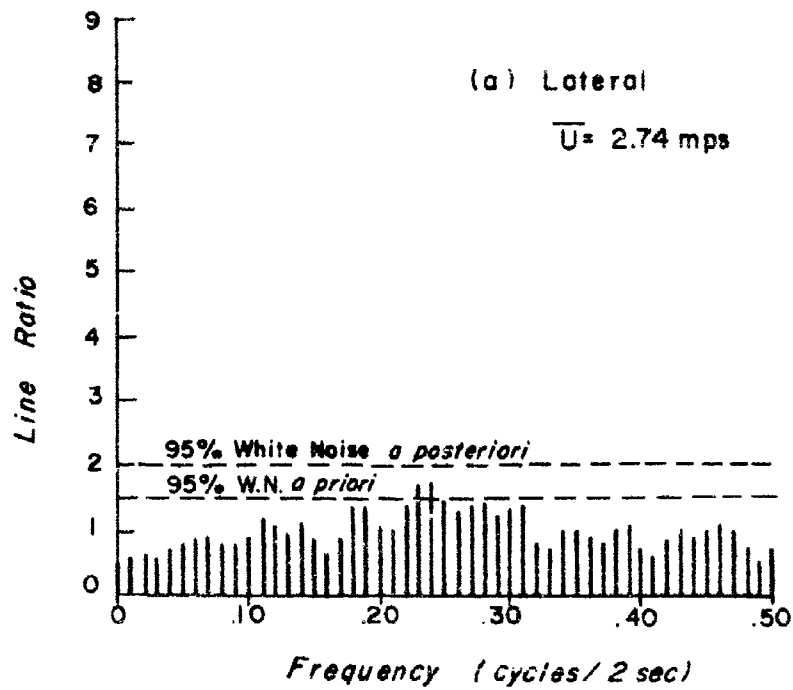


Fig. 3.44 Spectra of Wind Components at 27 m Level, Case II-BD

the transition period from a land-breeze regime to a definite sea-breeze regime. Fig. 3.45 shows the auto-correlation curves for this period. The trend is rather pronounced during this period and is due to the rapid veering of the wind and not to the wind speeds as the winds did not increase appreciably during these 17 minutes. At the 1 m level, the spectrum shows more distribution of the energy among the entire frequency range, although long waves still predominate (Fig. 3.46). An approach to horizontal local isotropy is implied by the similar values at the high frequencies of the components. At 7 m, the spectrum (not shown) depicted equal wavelengths, and at 27 m, the lateral spectrum showed higher frequencies were significant; i.e., a longitudinally elongation this time, instead of lateral as in the previous three cases when the wind was in the transition period.

Case V-BD: Beach Daytime, Sampling Period 1000 seconds

Still later (1103-1120 CDT), the veering with time of the wind has decreased as indicated by the trend in the correlation curves of Fig. 3.47. The energy is even more uniformly distributed among the spectra as shown in Fig. 3.48 for the 1 m level and a circular shape of the eddy is indicated for this level. At the 7 m and 27 m levels, an elongation with the wind is indicated by the spectra in Figs. 3.49 and 3.50.

Cases VI-BD and VII-BD: Beach Daytime, Sampling Periods 4000 seconds

These two cases which covered the periods 1000-1107 CDT and 1103-1210 CDT are different because the first period covers the transition from land breeze to sea breeze; the latter period covers the sea breeze regime only. In this latter the significant high frequencies were the same for both components; i.e., equal wavelengths, for the first two levels. Thus, the buoyancy effect is noticeable at large wavelengths; e.g., about 43 meters at the bottom level and 54 meters at the 7 meter height. The autocorrelation for Case VII-BD



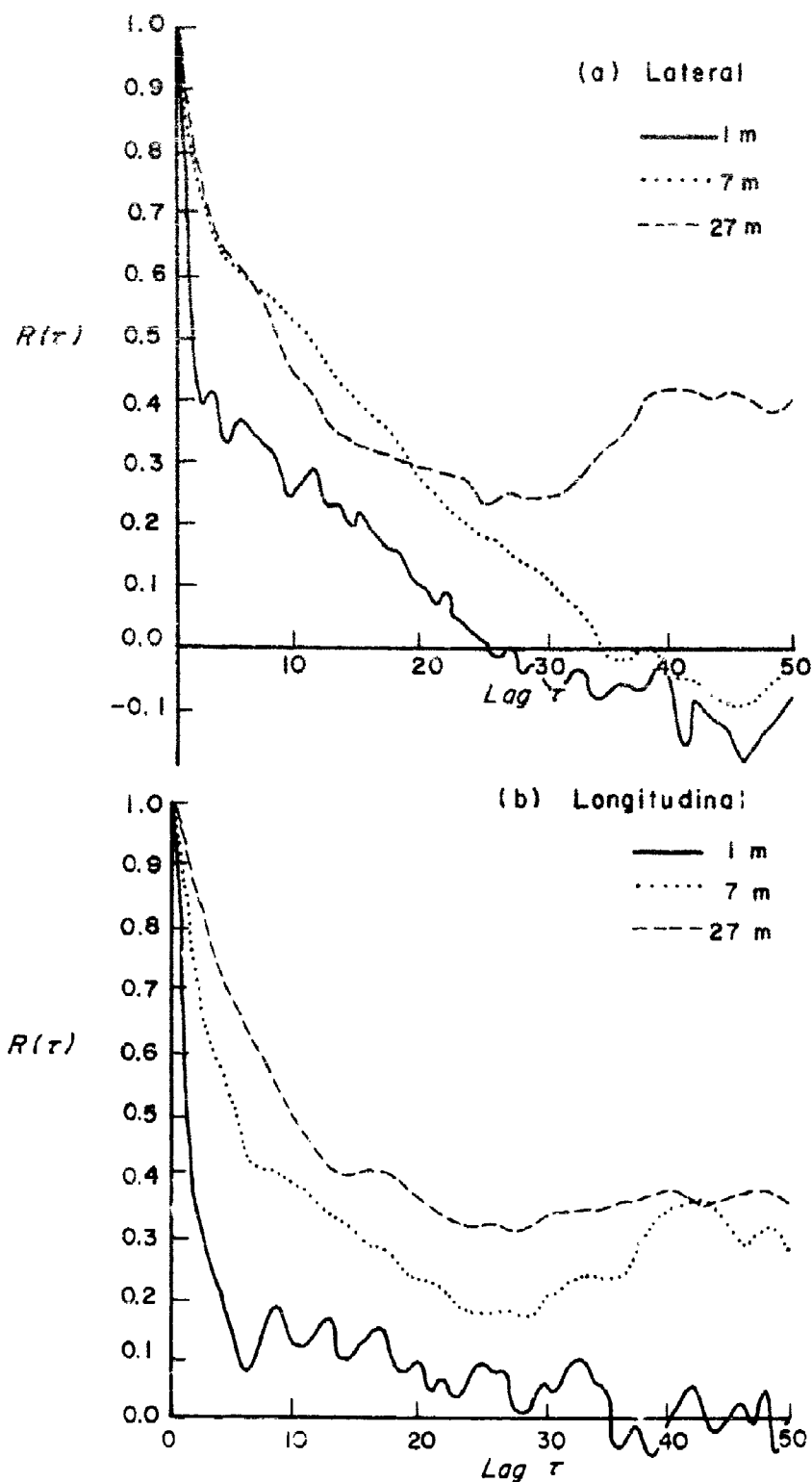


Fig. 3.45 Autocorrelation Functions, Case II-BD

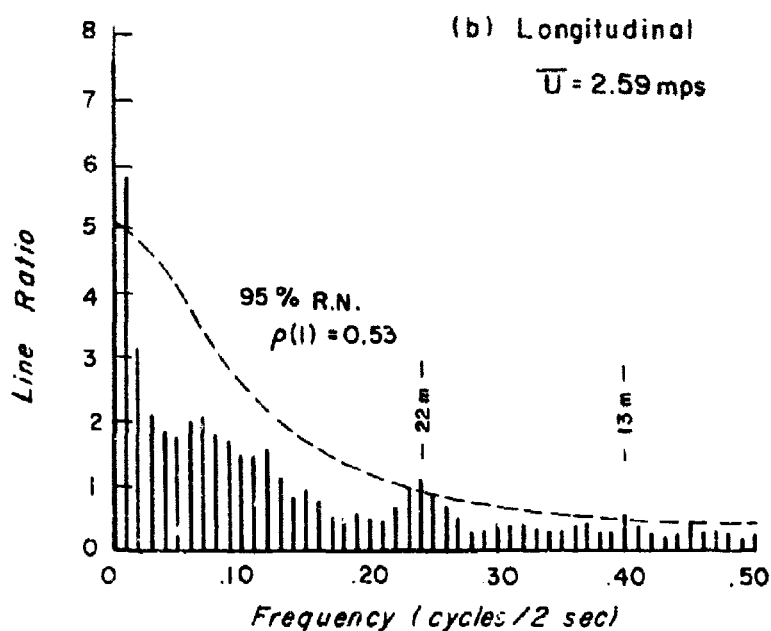
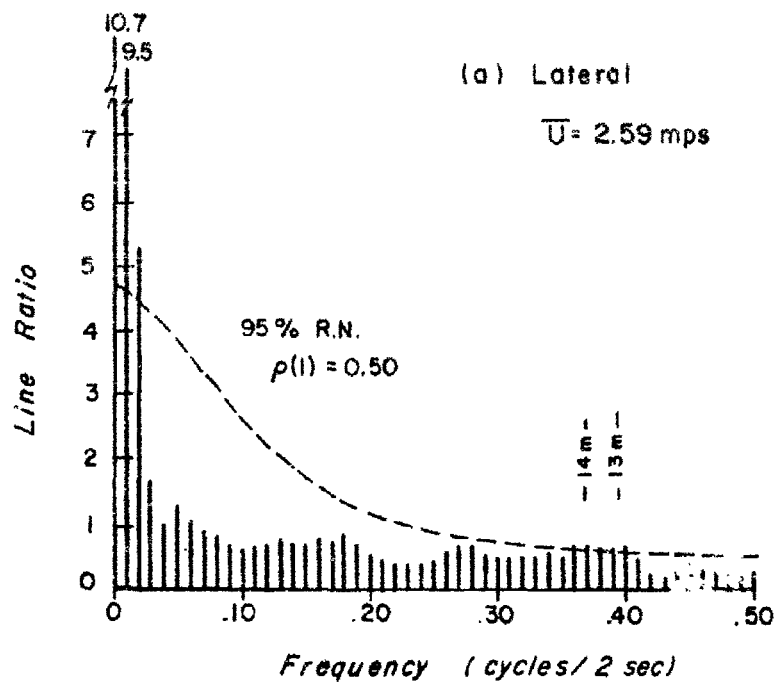


Fig. 3.46 Spectra of Wind Components at 1 m Level,  
Case IV-BD

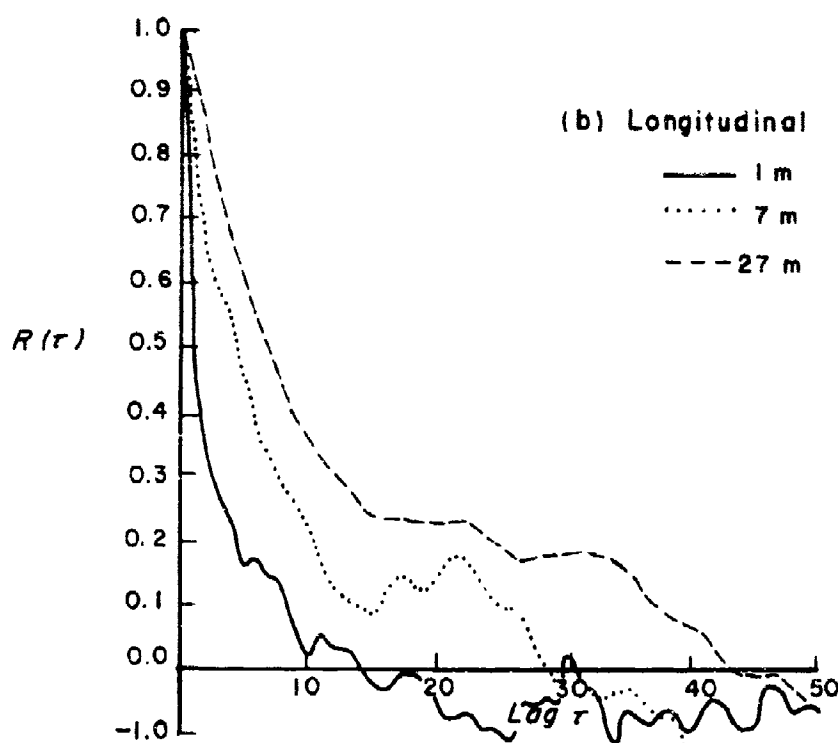
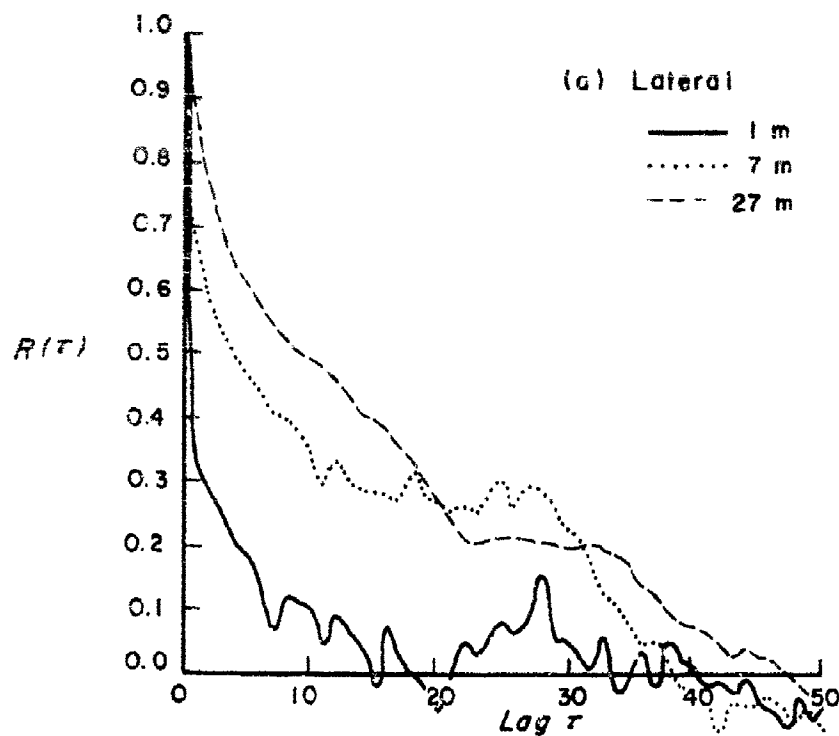


Fig. 3.47 Autocorrelation Functions of Wind Components,  
Case V-BD

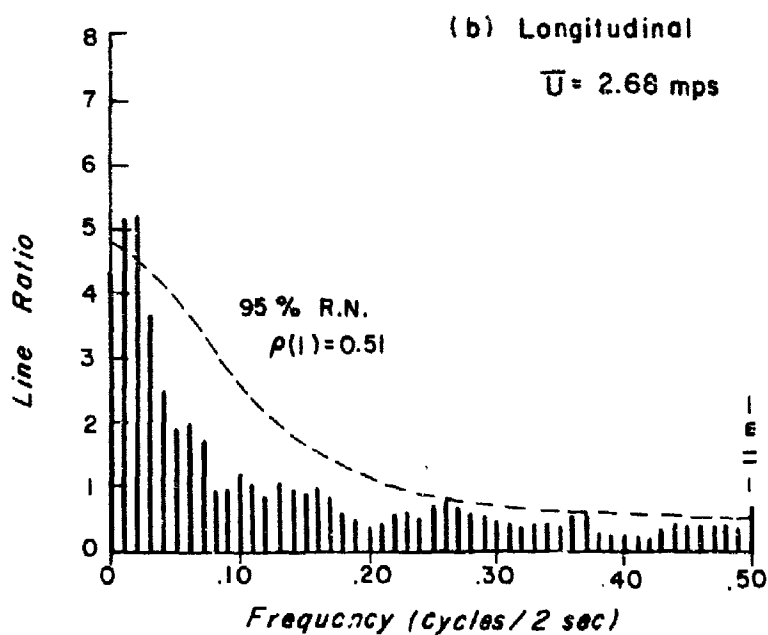
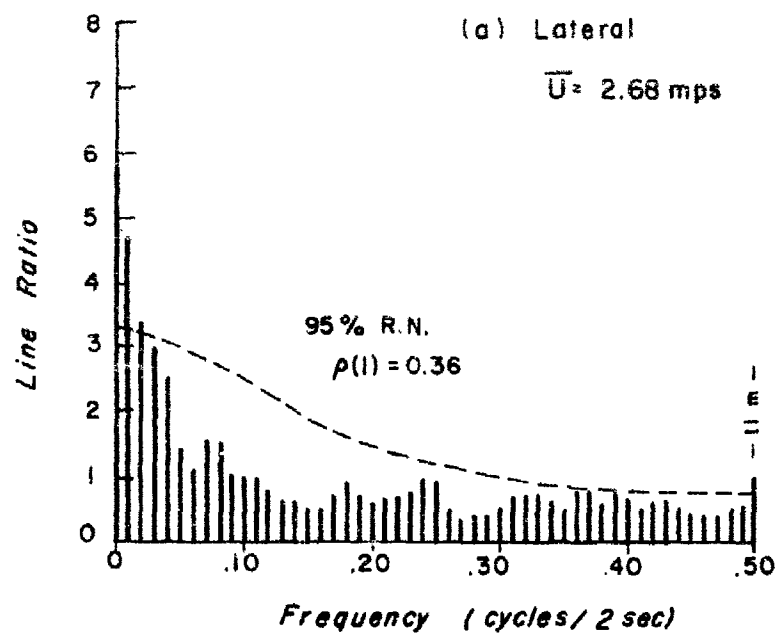


Fig. 3.48 Spectra of Wind Components at 1 m Level, Case V-BD

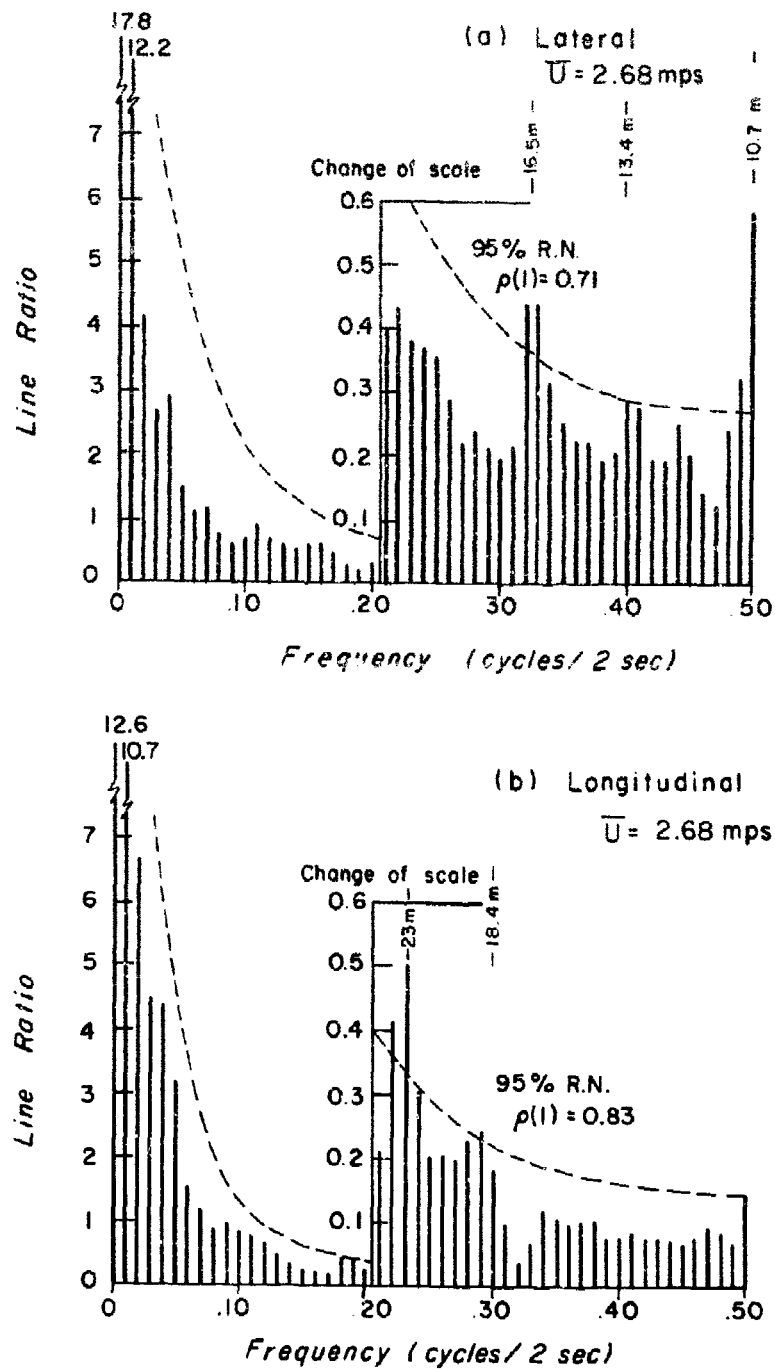


Fig. 3.49 Spectra of Wind Components at 7 m Level, Case V-BD

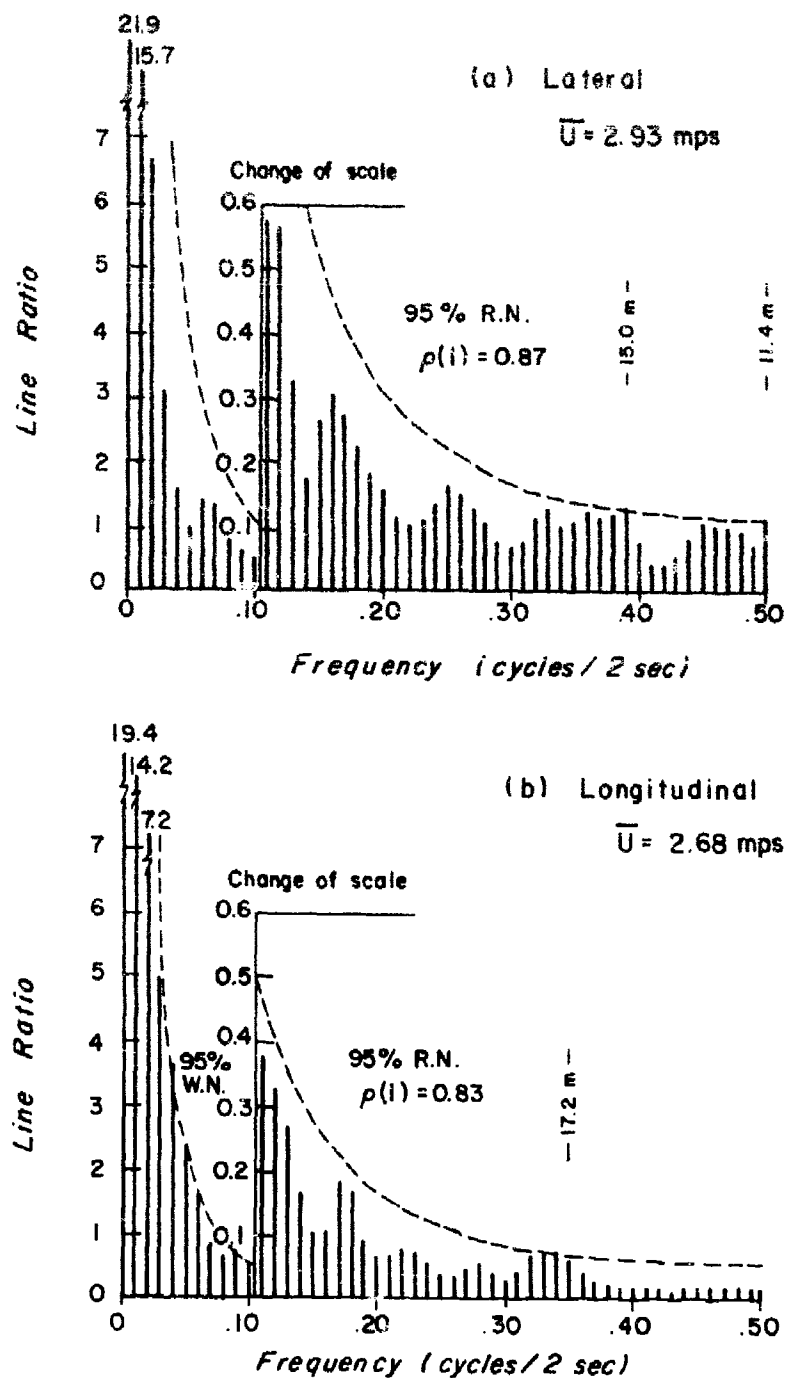


Fig. 3.50 Spectra of Wind Components at 27 m Level, Case V-BD

and the spectra for the two lower levels are shown in Figs. 3.51 to 3.53.

The cross-correlations between levels were very high using this longer sampling period, as shown in Fig. 3.54 for Case VI-BD. This implies that the eddies or convective disturbance extends to at least 27 m both downwind and across the wind.

#### 4. Daytime Data Samples taken at the Canal Tower

In the investigation of the samples from the beach site, it was found that the sea breeze phenomena was observed to cause a gradual veering of the winds with time. In this manner, the sea-breeze may be said to travel inland much the same way as the land-breeze traveled toward the sea.

Because of this gradual movement inland, the canal site observations did not register the same change in atmospheric regimes until a later time. From the data obtained, the winds at the beach veered to a sea-breeze regime between approximately 1005 to 1015 CDT, whereas the canal wind changed between 1155 to 1210 CDT, a difference of nearly two hours between the two locations 4.8 kilometers (3 miles) apart. Therefore, not all of the data samples selected for comparison overlap in time.

Case I-CD: Canal Daytime, Sampling Period 1000 seconds

This case covered the period between 1103 and 1120 CDT; a period dominated by the land breeze regime with winds from the ENE.

The autocorrelation curves for the two components are shown in Fig. 3.55. These indicate that 1000 seconds is an adequate sampling period. Another of the features is the similarity between the correlations of both components. This is in spite of the land breeze dominance. The affect of solar radiation causing convective turbulence is thus the dominant factor here at all three levels. Also, the similarity between the respective curves may be indicative of some horizontal homogeneity caused by this surface heating.

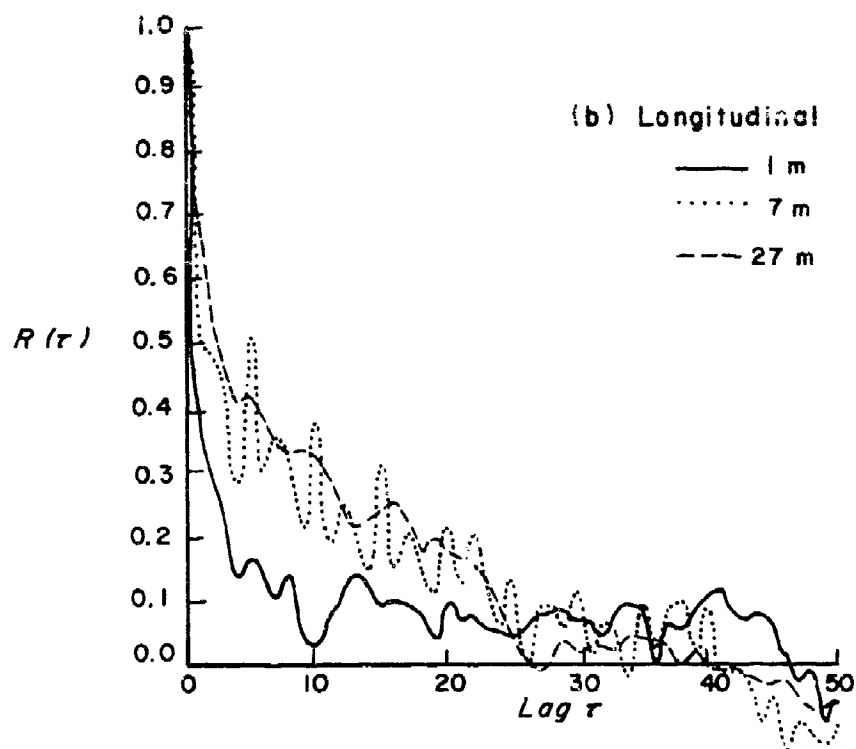
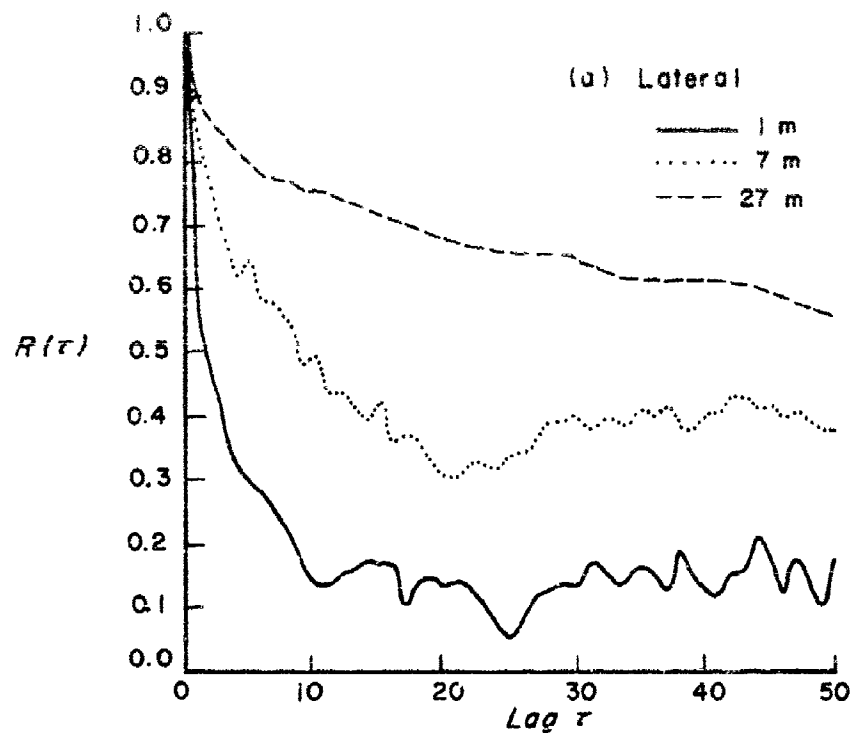


Fig. 3.51 Autocorrelation Functions of Wind Components,  
Case VII-BD



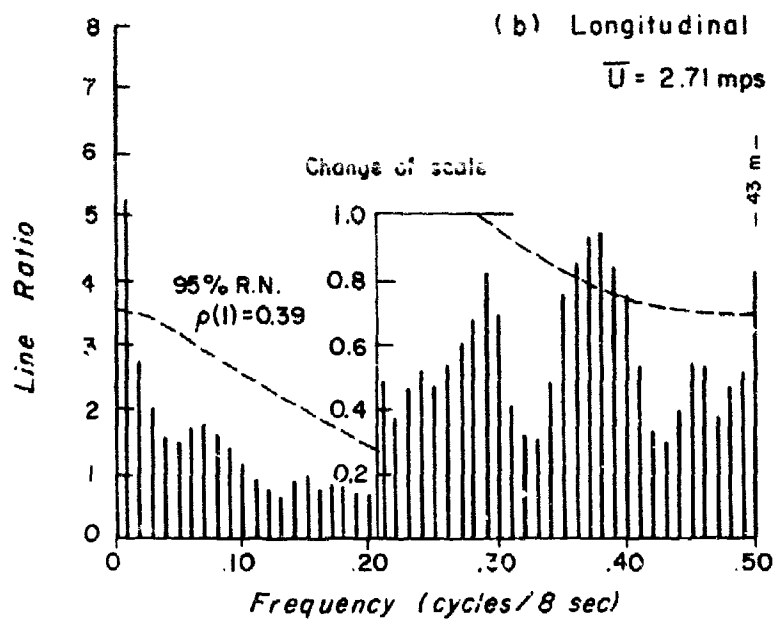
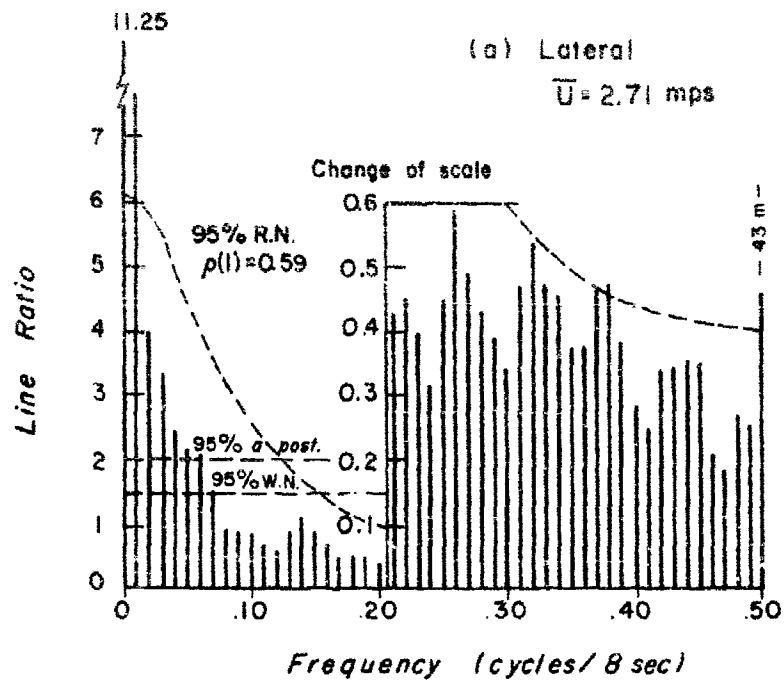


Fig. 3.52 Spectra of Wind Components at 1 m Level, Case VII-BD

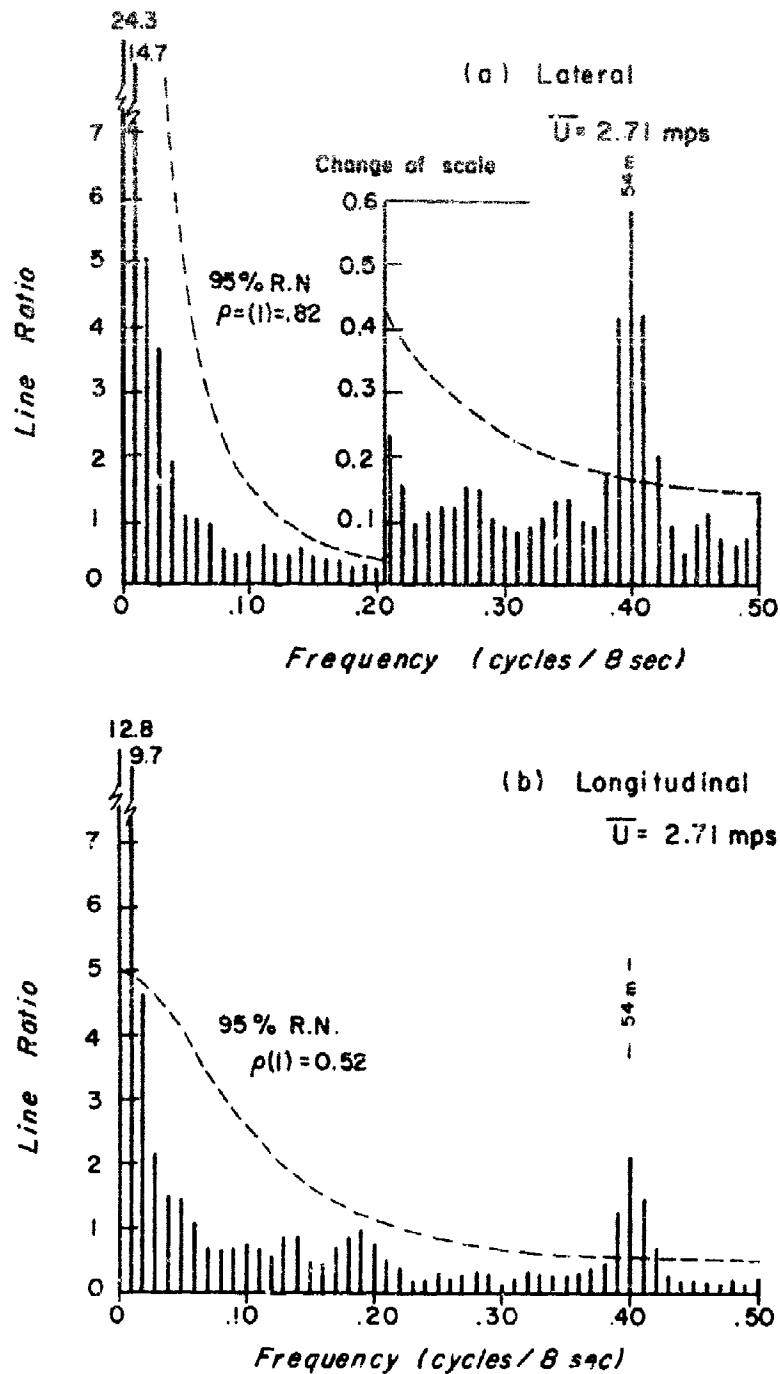


Fig. 3.53 Spectra of Wind Components at 7 m Level, Case VII-BD

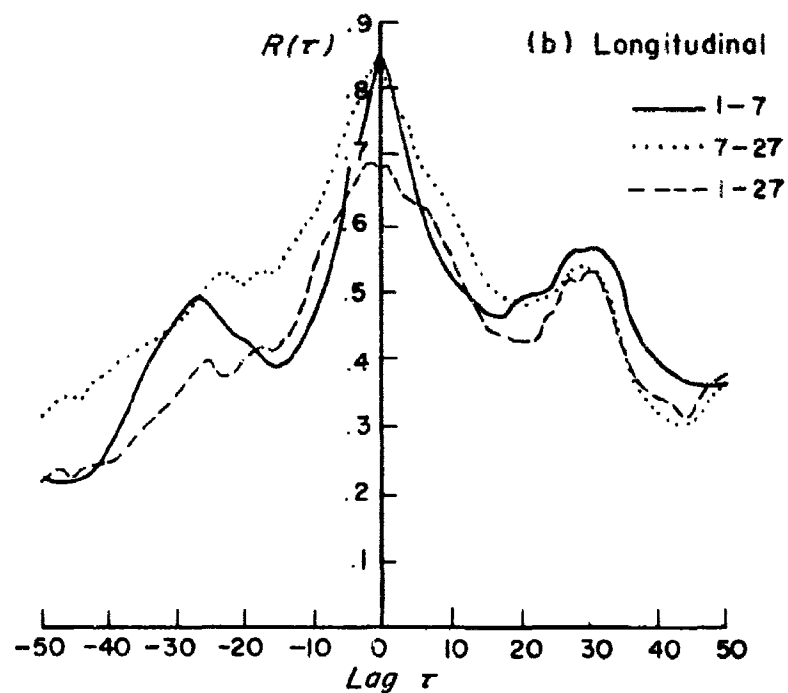
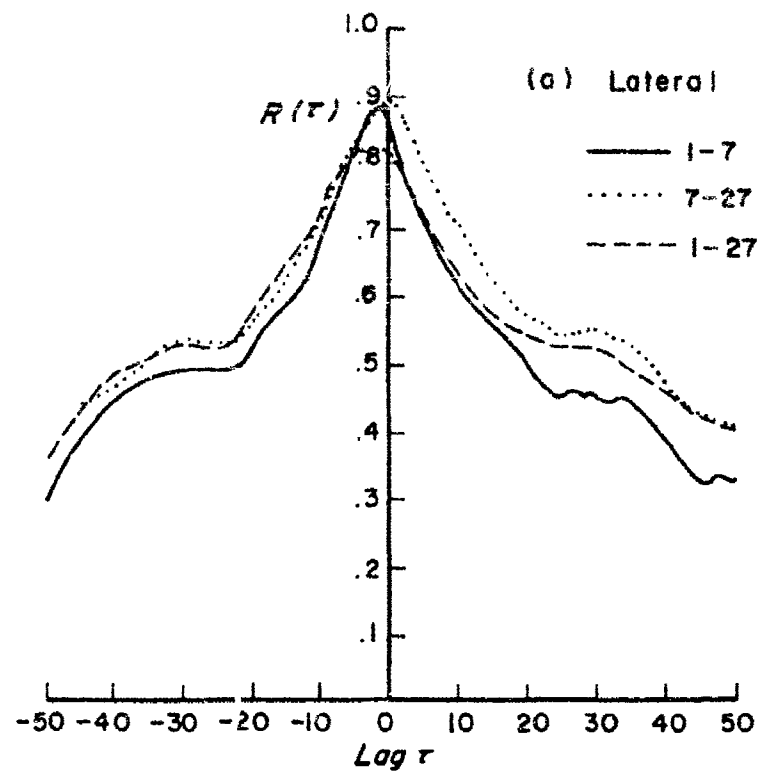


Fig. 3.54 Cross-correlation Functions of Components Between Level, Case VI-BD

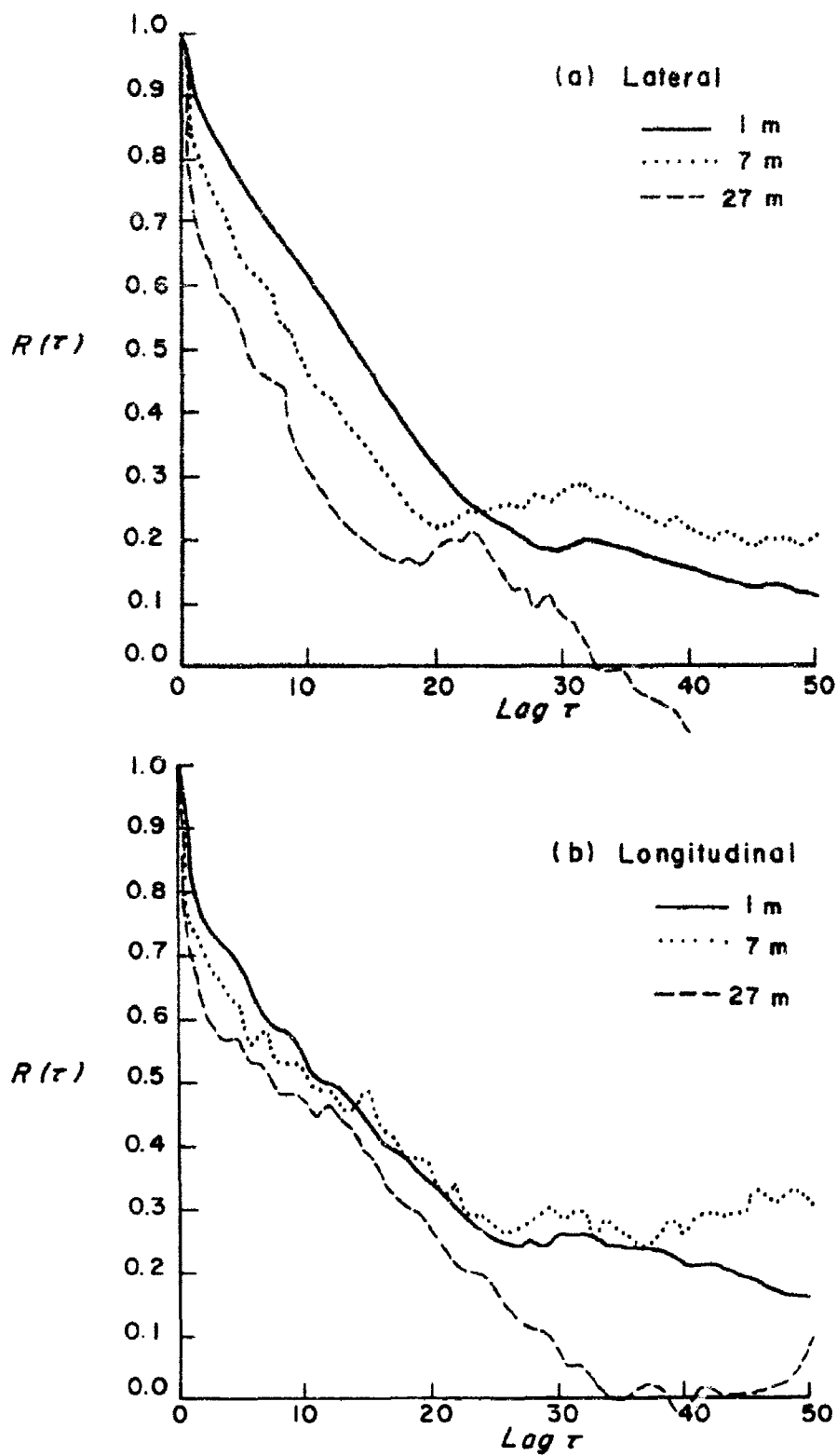


Fig. 3.55 Autocorrelation Functions of Wind Components, Case I-CD

The spectra for the three levels are given in Figs. 3.56, 3.57, and 3.58. The similarity between the spectra of the components at the same level indicate a close approach to horizontal local isotropy; i.e., that the distribution of the energy among the spectrum is invariant with respect to the coordinate axis. The shape of the eddies for this case is nearly circular with the top level indicating slightly more energy at the high frequencies in the lateral component, (elongation with the wind).

A comparison of this case with the beach data shows that the closest comparison is with Case II-BD for the period 1017-1034 CDT when the winds were already in the sea breeze regime. In this case, for the beach site, the shapes of the eddies implied by the spectra were circular for the three levels. Before that time, the shapes indicated in Case I-BD and Case III-BD were circular at the bottom and elongated laterally at the top levels. This suggests that the effect of surface roughness and thermal convection on the high frequency end of the spectrum are similar. For example, Case I-BD has lighter offshore winds and stronger thermal convection whereas Case II-BD has stronger onshore winds and less intense thermal convection.

The cross-correlation curves between the same components at different levels is shown in Fig. 3.59. The correlations are nearly equal for both components as expected, and the highest correlation is between the 1 m level and the 7 m level. The correlations between the 1 m and 27 m levels and the 7 m and 27 m levels are nearly equal. Thus the eddy caused by convection may be said to be more evident between 1 m and 7 m, than between 7 m and 27 meters.

The curves also show that the veering of the winds implied by the autocorrelation curves occurs with one level ahead of the others, as was the case at the beach. But these cross-correlations also show that the veering of the winds at the three levels was not as organized as at the beach, i.e., there

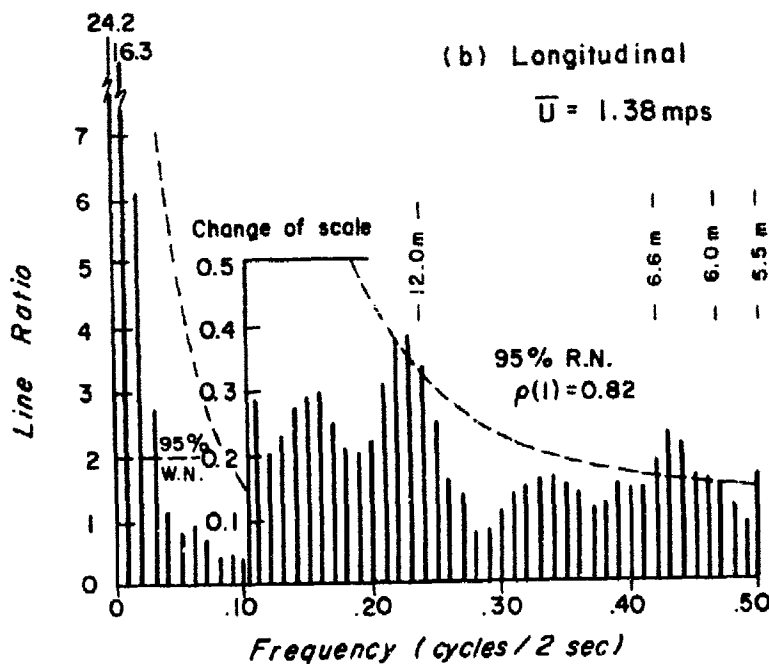
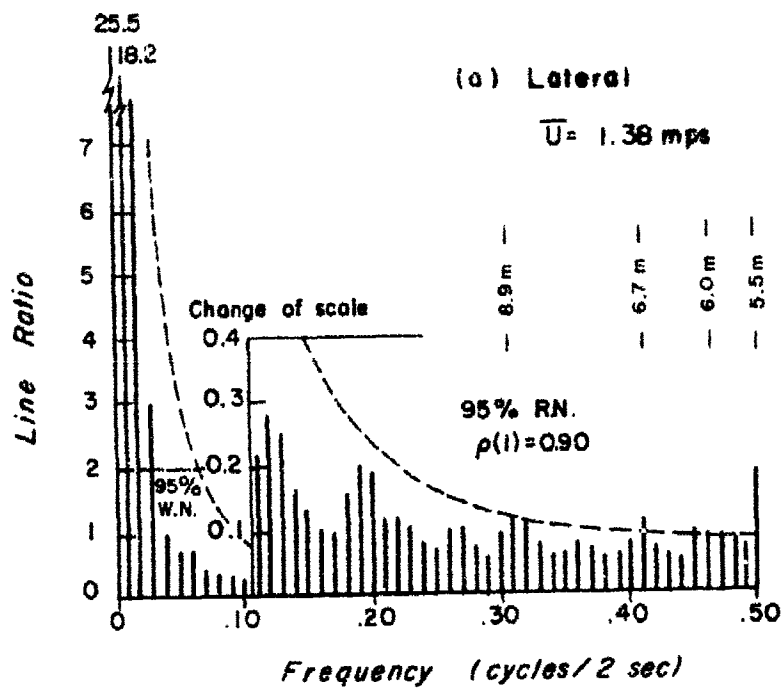


Fig. 3.56 Spectra of Wind Components at 1 m Level, Case I-CD

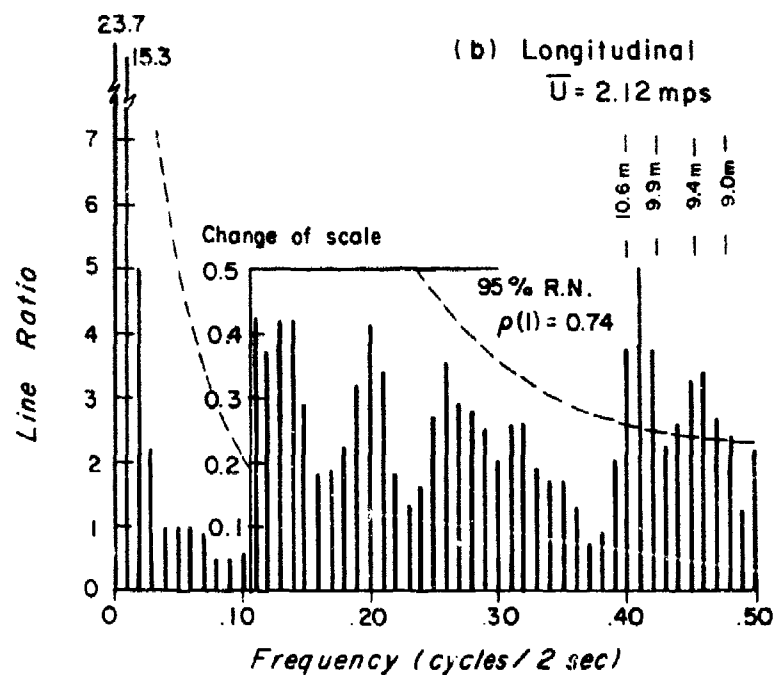
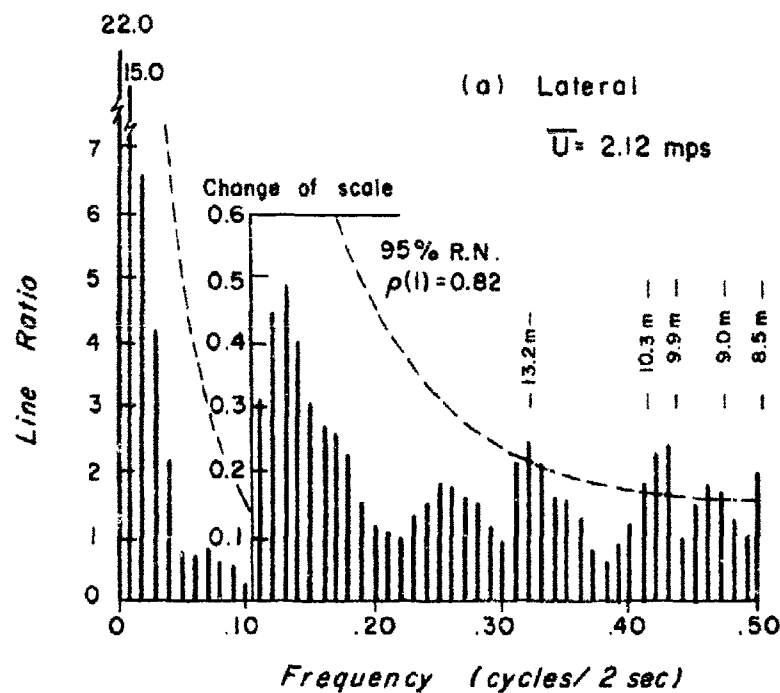


Fig. 3.57 Spectra of Wind Components at 7 m Level, Case I-CD

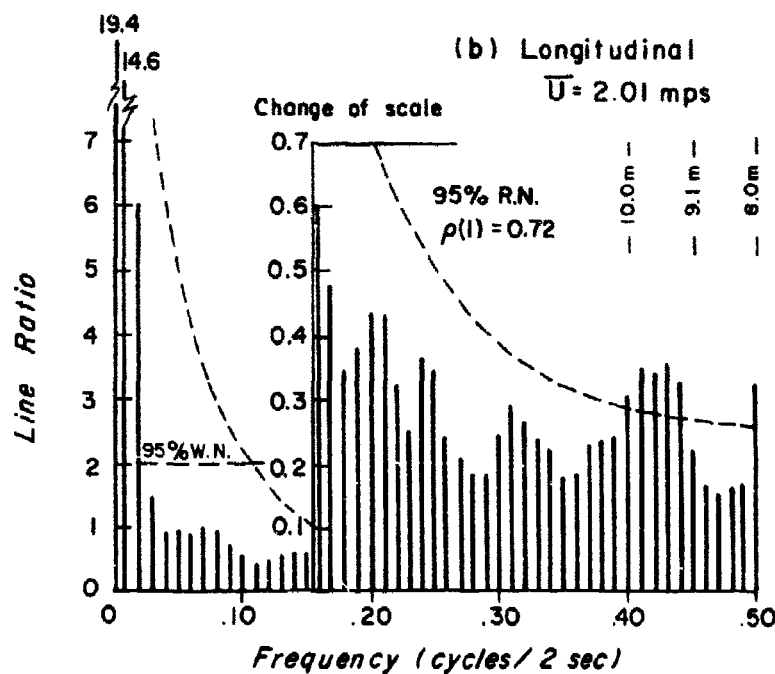
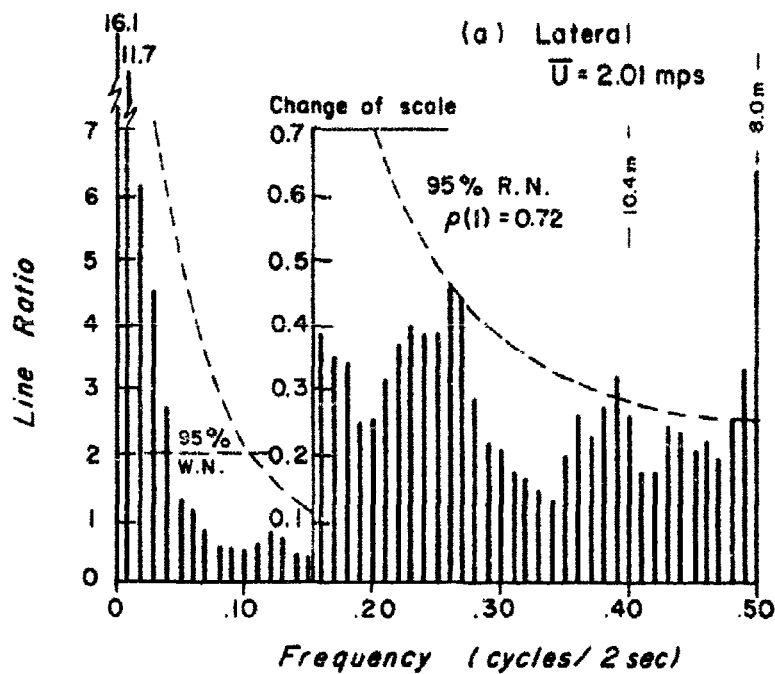


Fig. 3.58 Spectra of Wind Components at 27 m Level, Case I-CD



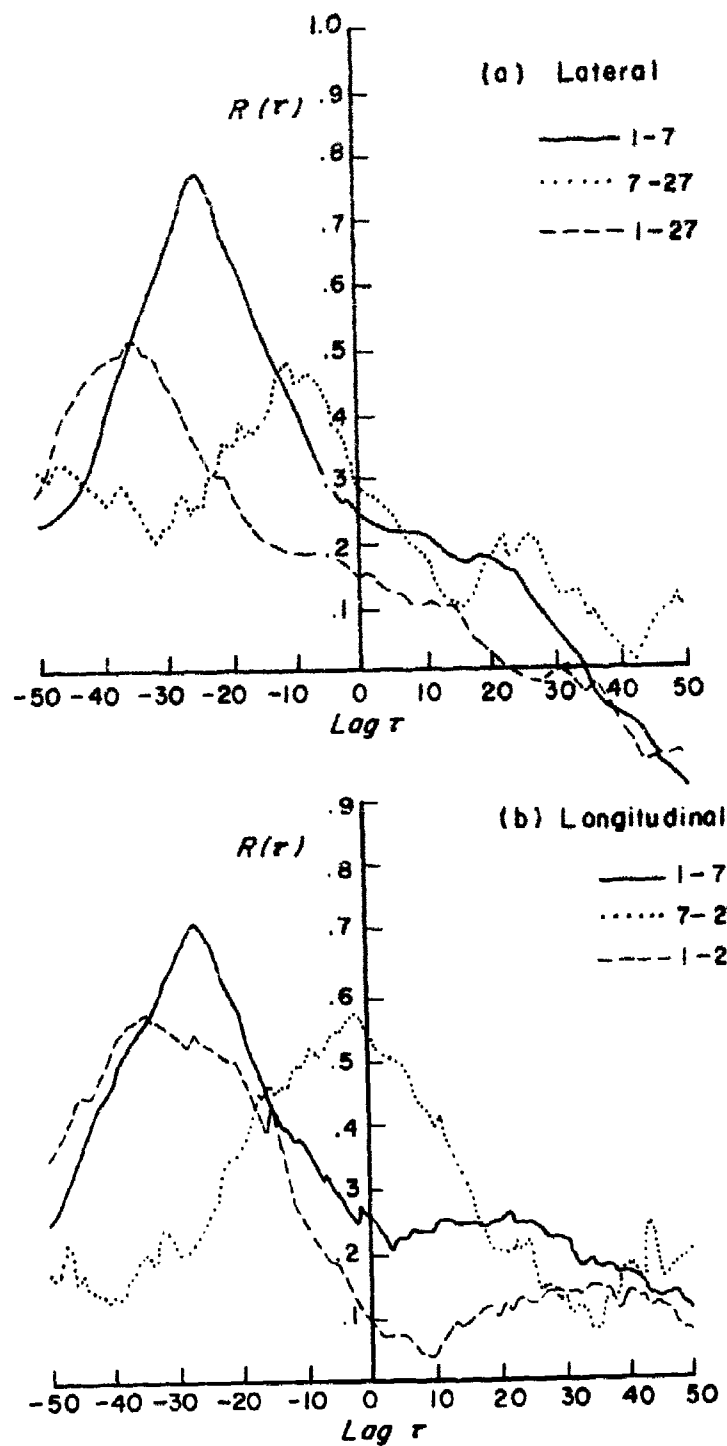


Fig. 3.59 Cross-correlation Functions of Components Between Levels, Case I-CD

were more fluctuations at the canal during the period sampled. Again, this could be attributed to the heat convection.

Case II-CD: Canal Daytime, Sampling Period 1000 seconds

This case occurred during 1155-1212 CDT, or at noon. During this time the transition from a land breeze to a sea breeze occurred. As in the case studied at the beach site, the transition was characterized by a decrease in wind speeds at all three levels.

The autocorrelation curves and spectra for the components at the three levels are shown in Figs. 3.60 to 3.63. More energy in the longitudinal long waves is indicated by the correlations; the spectra lend support to this.

The cross-correlation curves of the components (Fig. 3.64) show higher correlations between the downstream components than between the lateral components, further supporting the indication of longer waves downstream at this sampling interval and at these low wind speed values.

Case III-CD: Canal Daytime, Sampling Period 1000 seconds

About thirty minutes after the change to a sea breeze flow, the stronger wind was from a line normal to the coast line; thus, a flow of maritime origin which had traversed 4.8 km of land during mid-day. The autocorrelation curves and spectra are shown in Figs. 3.65 to 3.68. At the 1 m level the spectrum (Fig. 3.66) shows a "circular" pattern at the higher frequencies, corresponding to about 7 meters in wavelength and indicated local isotropy. The two higher levels show a slight elongation downstream, e.g., the smaller wavelengths at these levels were about 10 m laterally and 11 m longitudinally.

A comparison of these with the beach site (Cases IV-BD and V-BD) shows that a similar slight downstream elongation also occurred after the sea breeze was in effect. Prior to that a lateral pattern was found in both locations, for the 7 m and 27 m levels at the beach (Cases I-BD and III-BD) and at

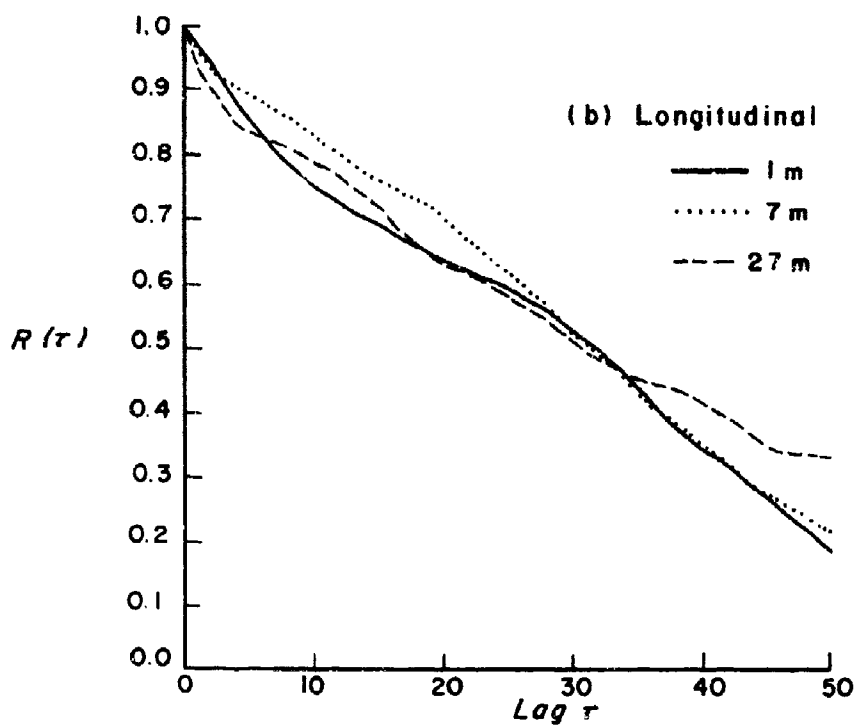
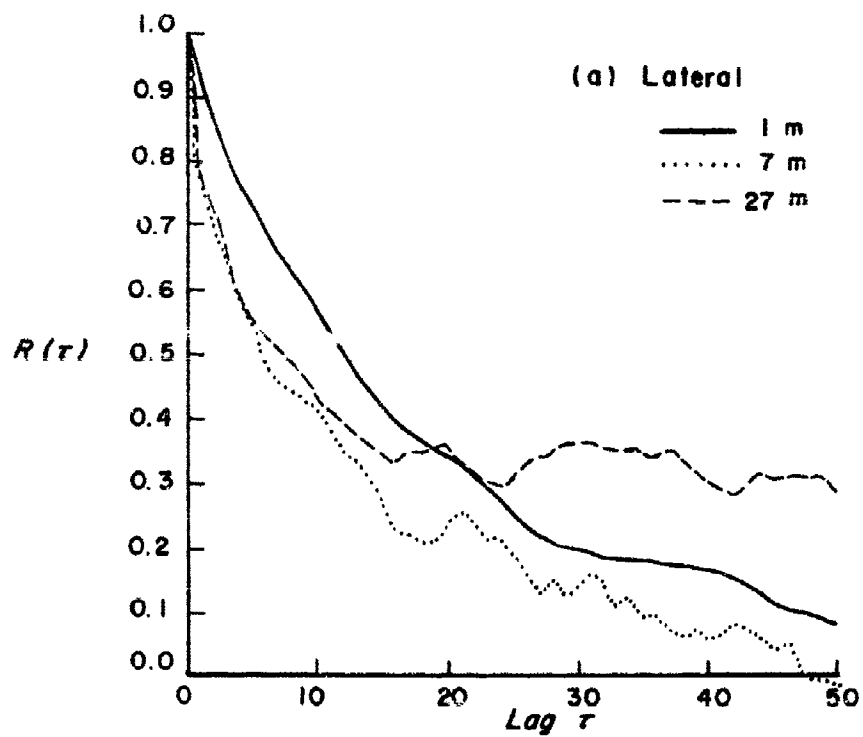


Fig. 3.60 Autocorrelation Functions of Wind Components,  
Case II-CD  
132

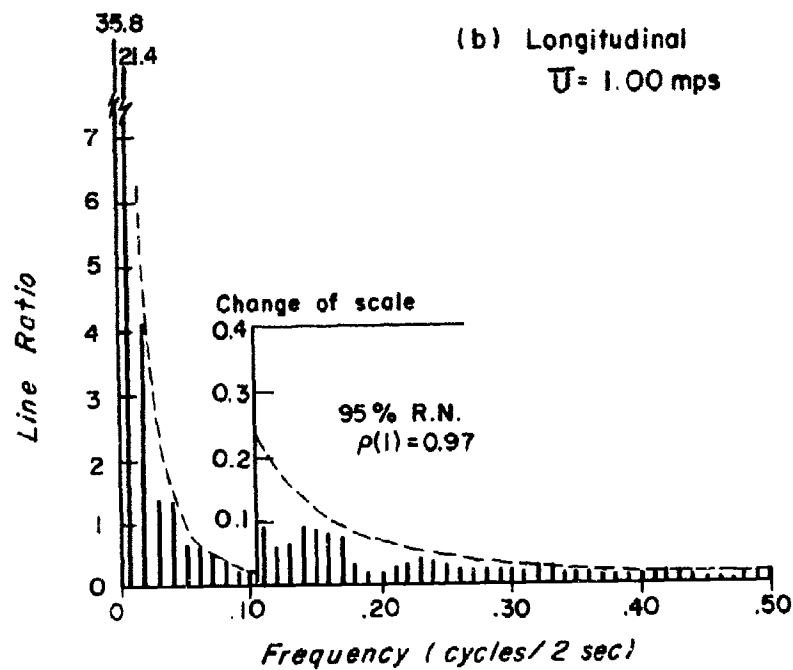
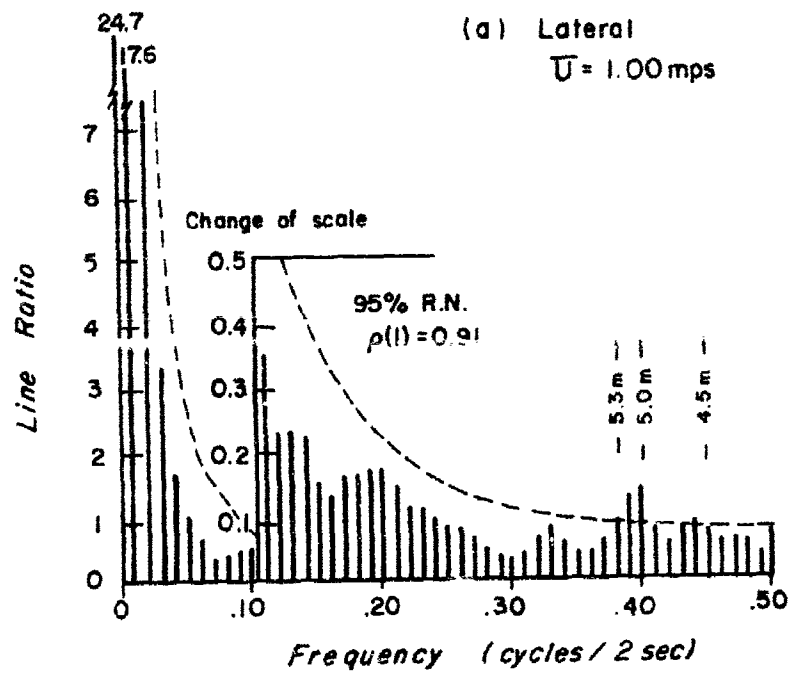


Fig. 3.61 Spectra of Wind Components at 1 m Level, Case II-CD

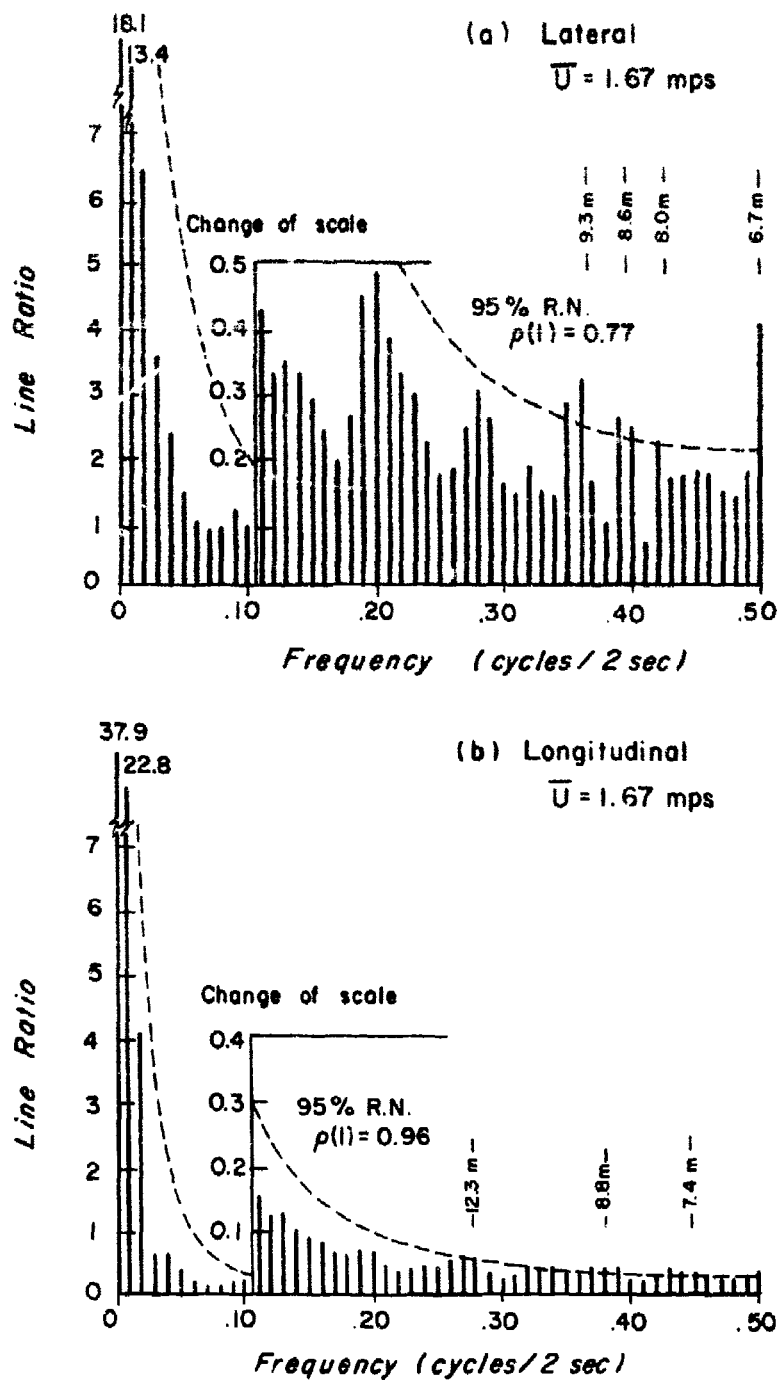


Fig. 3.62 Spectra of Wind Components at 7 m Level, Case II-CD

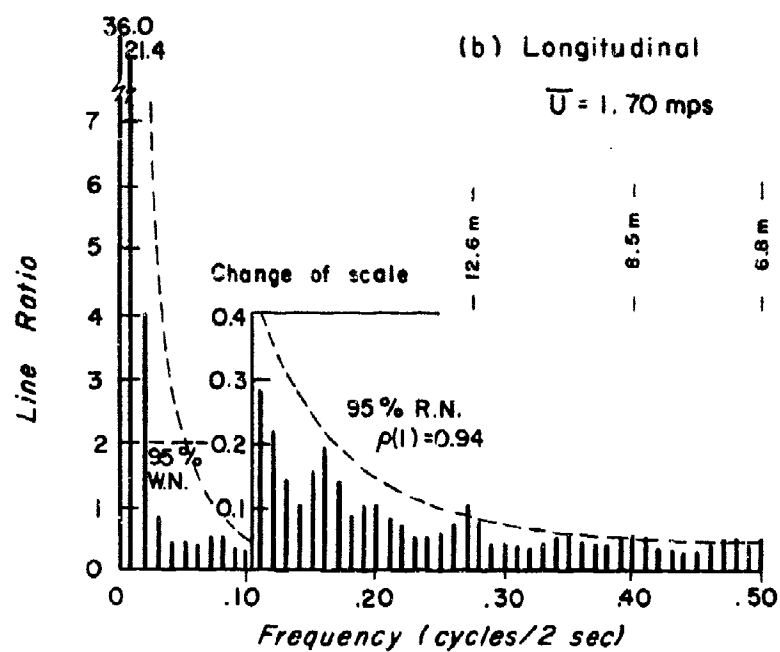
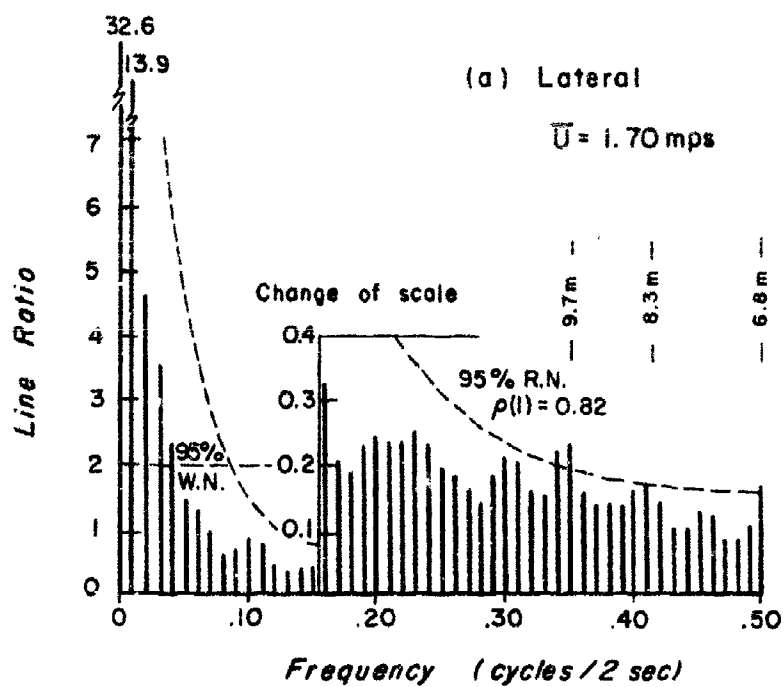


Fig. 3.63 Spectra of Wind Components at 27 m Level, Case II-CD

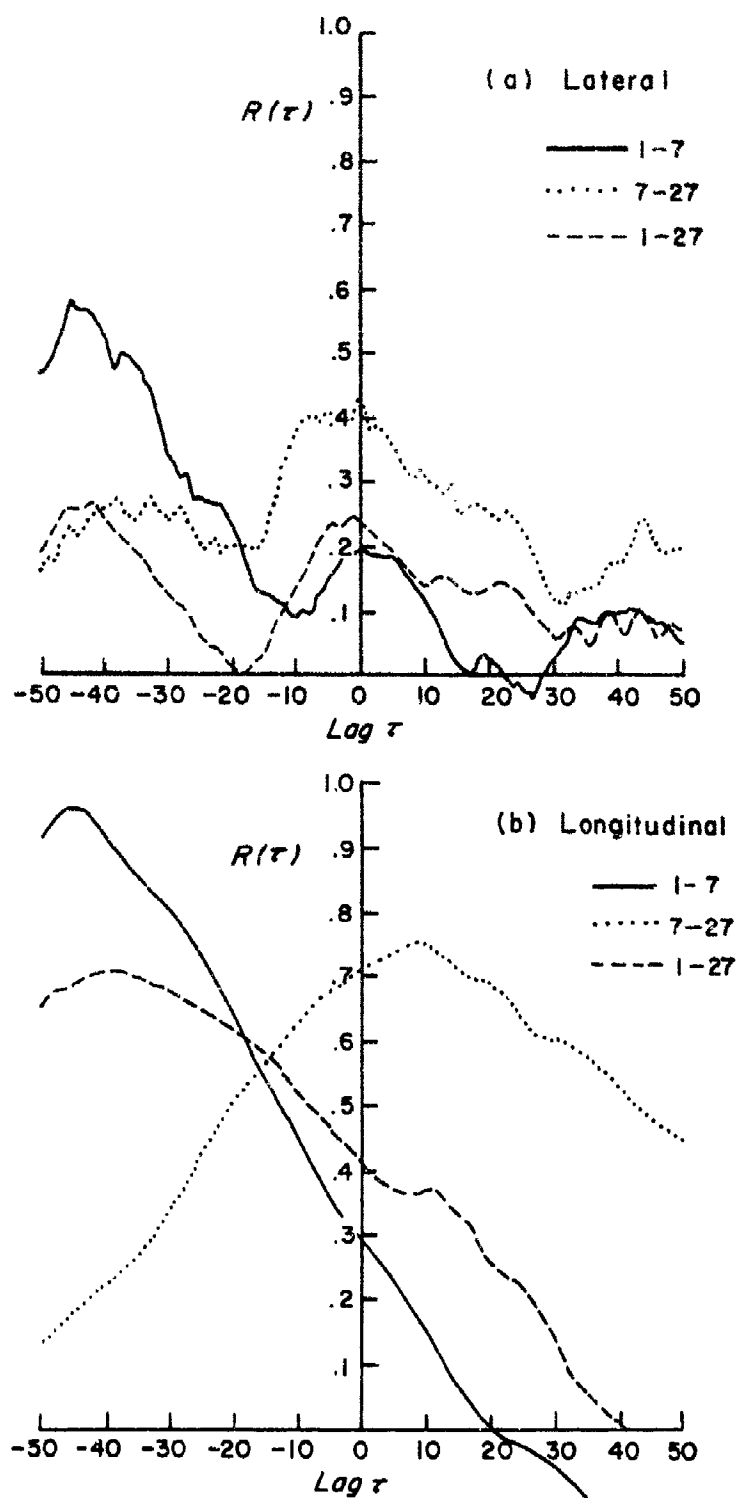


Fig. 3.64 Cross-correlation Functions of Components Between Levels, Case II-CD

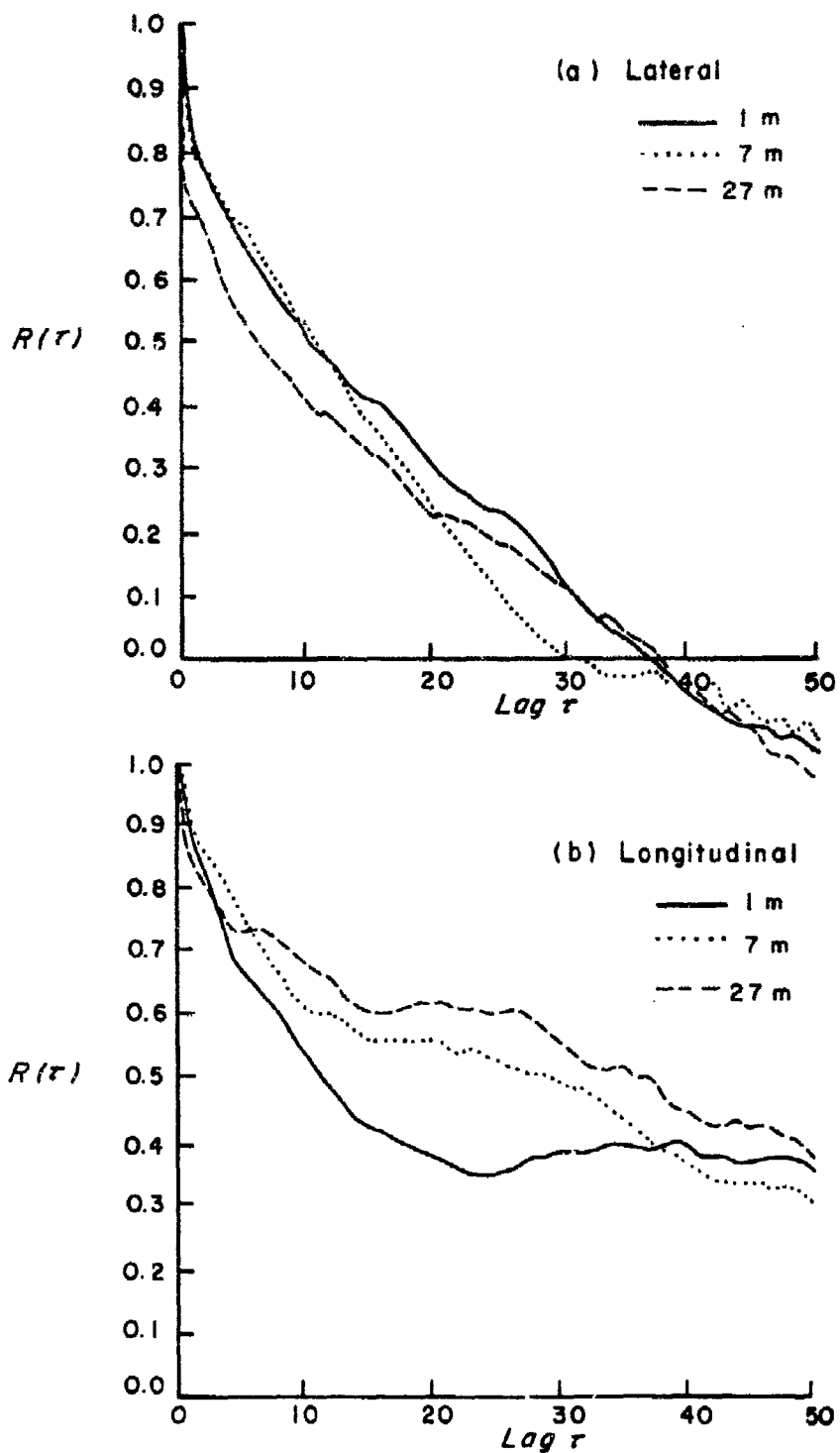


Fig. 3.65 Autocorrelation Functions of Wind Components,  
Case III-CD



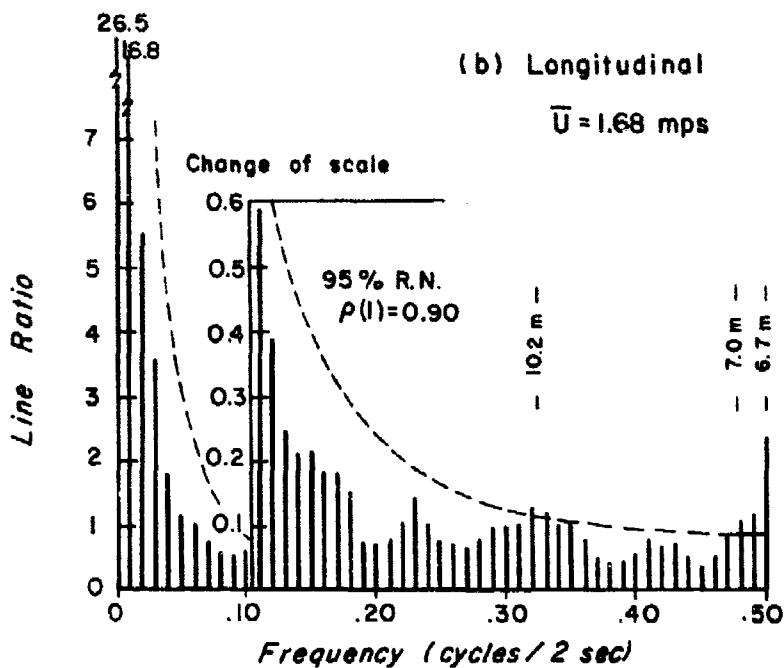
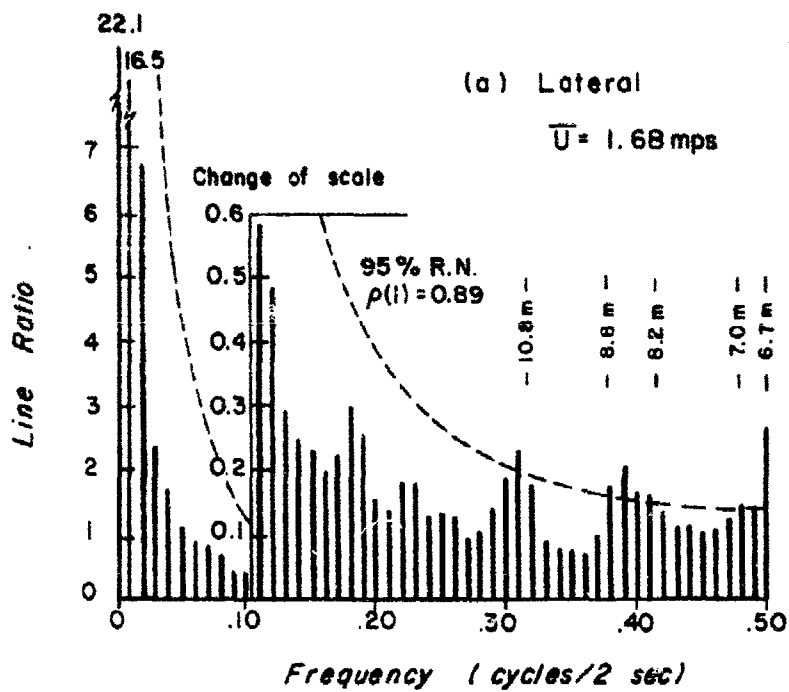


Fig. 3.66 Spectra of Wind Components at 1 m Level, Case III-CD

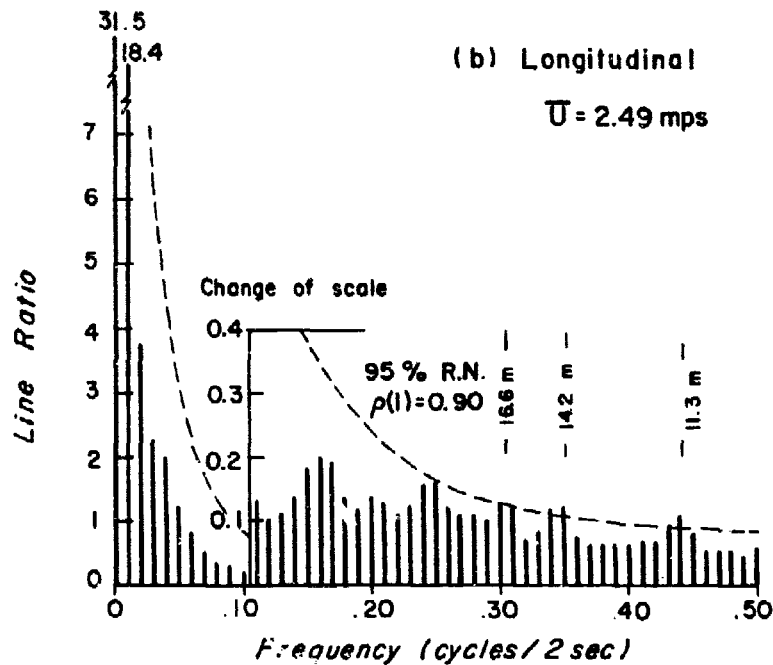
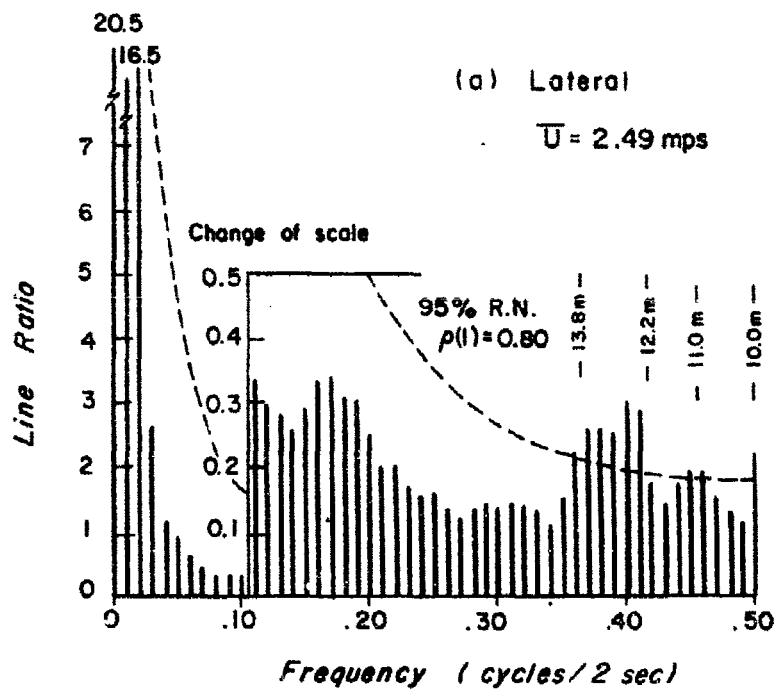


Fig. 3.67 Spectra of Wind Components at 7 m Level, Case III-CD

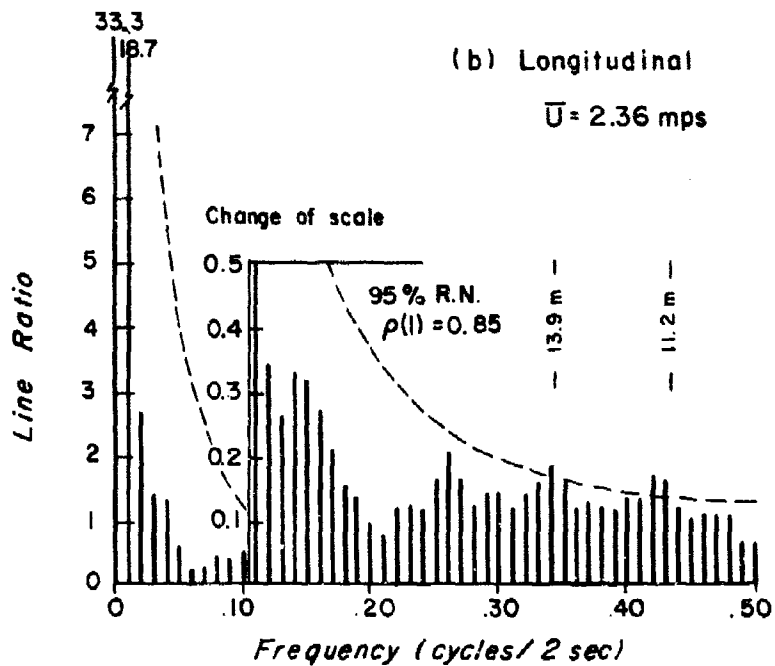
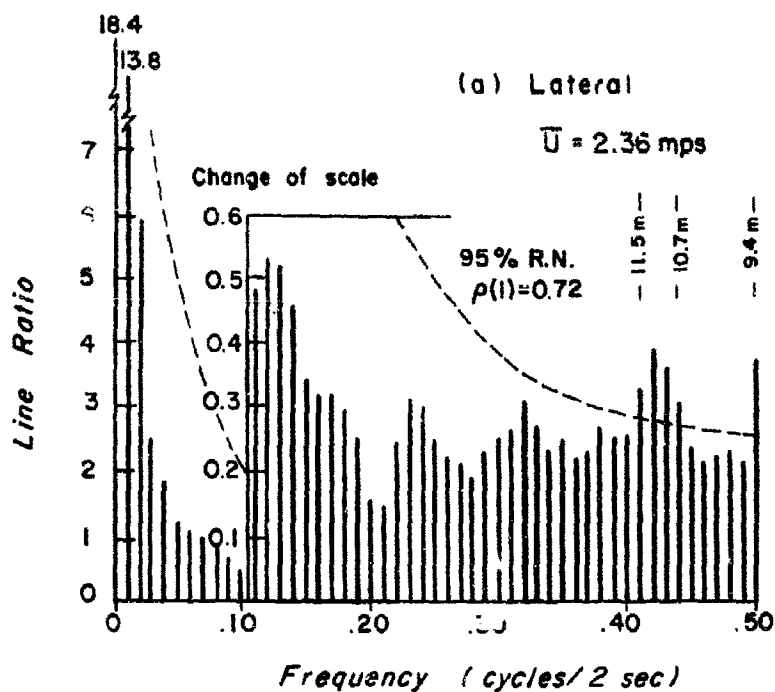


Fig. 3.68 Spectra of Wind Components at 27 m Level, Case III-CD

the 27 m level at the canal (Case III-CD).

Cases IV-CD, V-CD, and VI-CD: Canal Daytime, Sampling Periods 4000 seconds

These cases for 1103-1210 CDT, 1155-1302 CDT, and 1210-1317 CDT all included some of the transition period. As in the case of the components of the beach study, the correlation curves show the trend for this longer period (Figs. 3.69 and 3.70). Because of the longer trends indicated in the data, only general characteristics may be obtained from the spectra (Figs. 3.70, 3.71, and 3.72). The general features of the 1 m level spectra included a similar distribution of energy among the frequencies for both components at the 1 m level, which is an indication of horizontal isotropic turbulence.

A comparison of these sampling periods with those of the stable evening cases indicates that these longer sampling periods do not show a distinct preferred elongation with or across the wind at the two upper levels, such as the downstream elongation of the longer evening cases. During these longer sampling periods, however, the cross-correlations between levels (Figs. 3.73 and 3.74) were again high both laterally and longitudinally compared to the evening cases which had high correlations only for the lateral components.

Case VII-CD: Canal Daytime, Sampling Interval 8000 seconds

This case for the period 1103-1317 CDT showed that the sampling period was longer than needed to do this type of study. The affects of the veering and the increase in wind speeds combined to give a pronounced trend in the data (Fig. 3.75). This would require a trend removal procedure before further analysis could be made. But since it has been shown that a 1000 sec sampling period was adequate for analysis of the daytime cases, the trend removal was not done in this particular analysis.

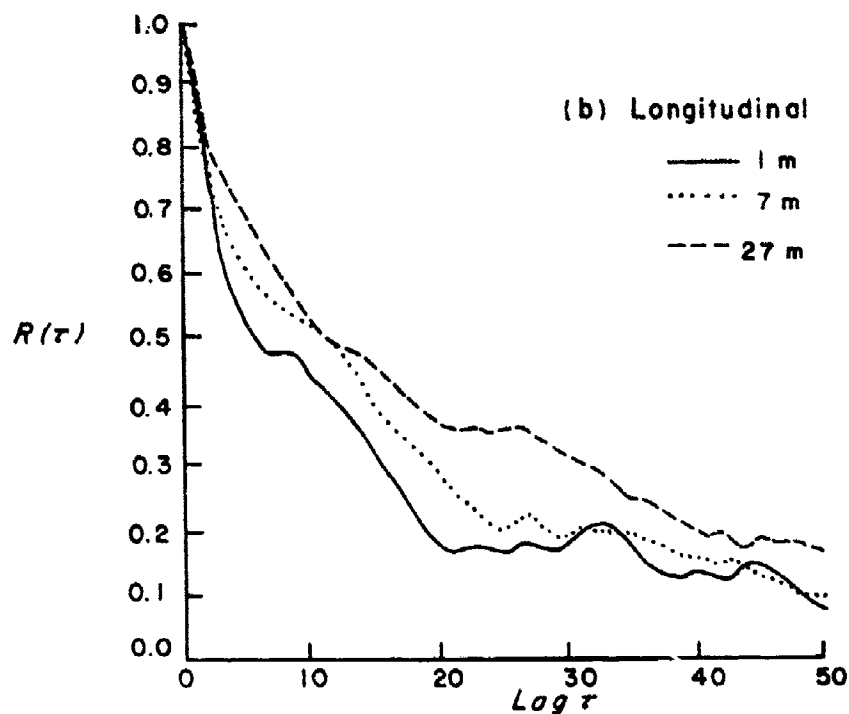
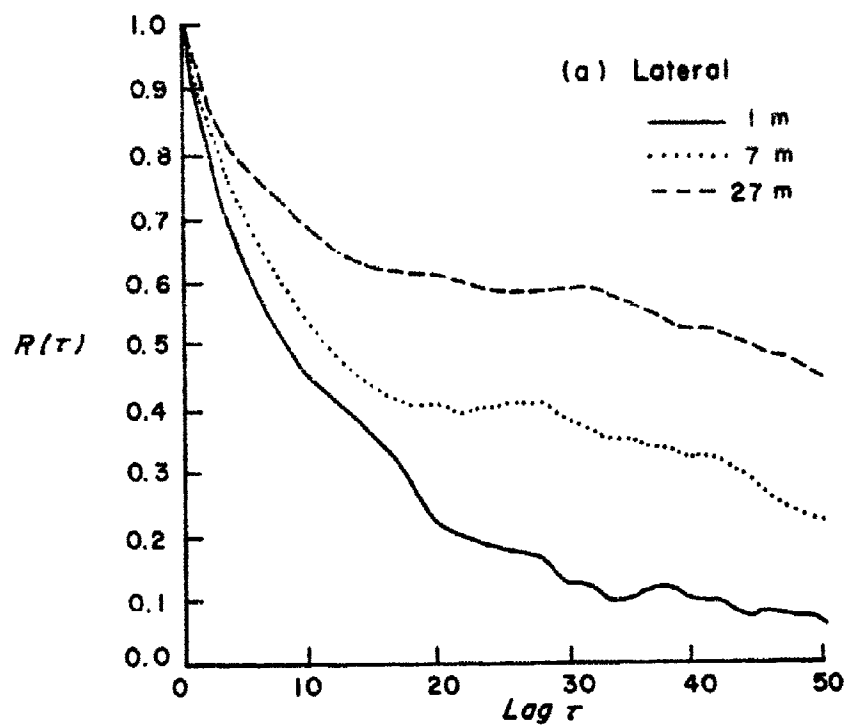


Fig. 3.69 Autocorrelation Functions of Wind Components,  
Case IV-CD

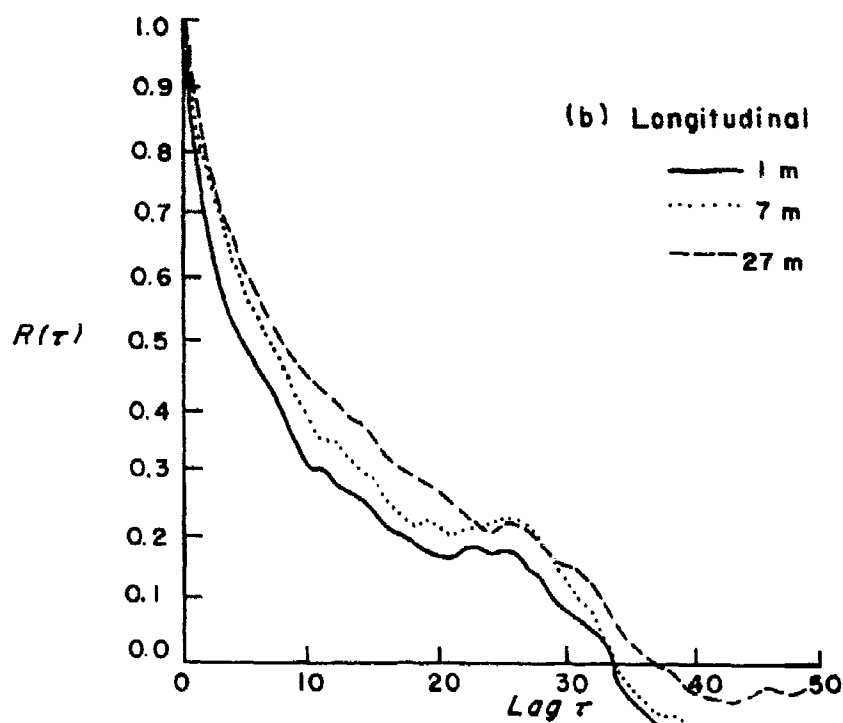
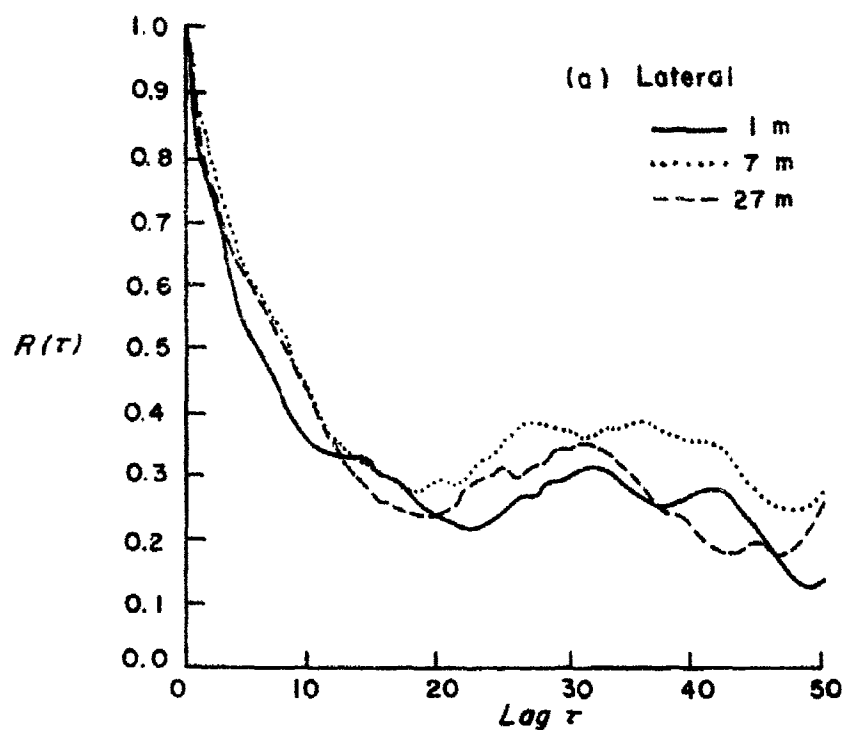


Fig. 3.70 Autocorrelation Functions of Wind Components,  
Case VI-CD

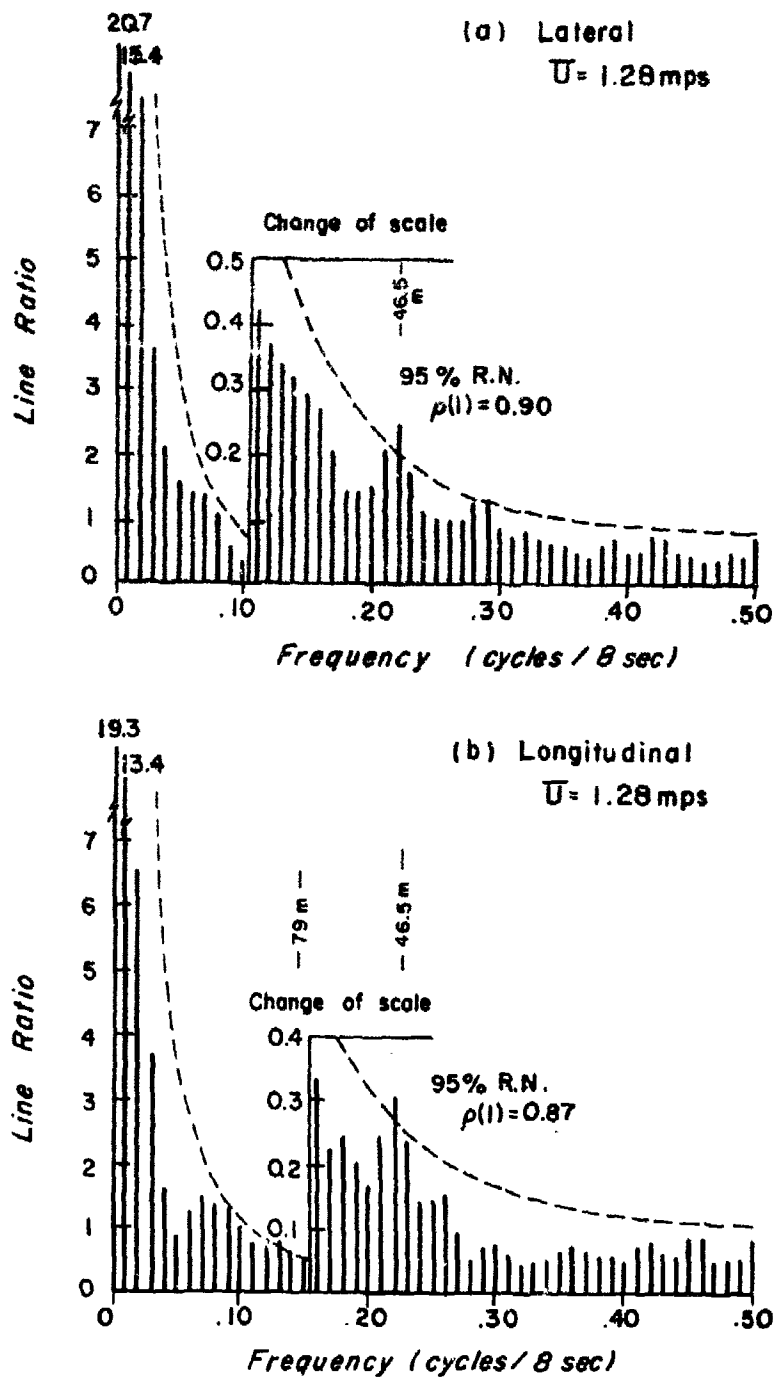


Fig. 3.71 Spectra of Wind Components at 1 m Level, Case IV-CD

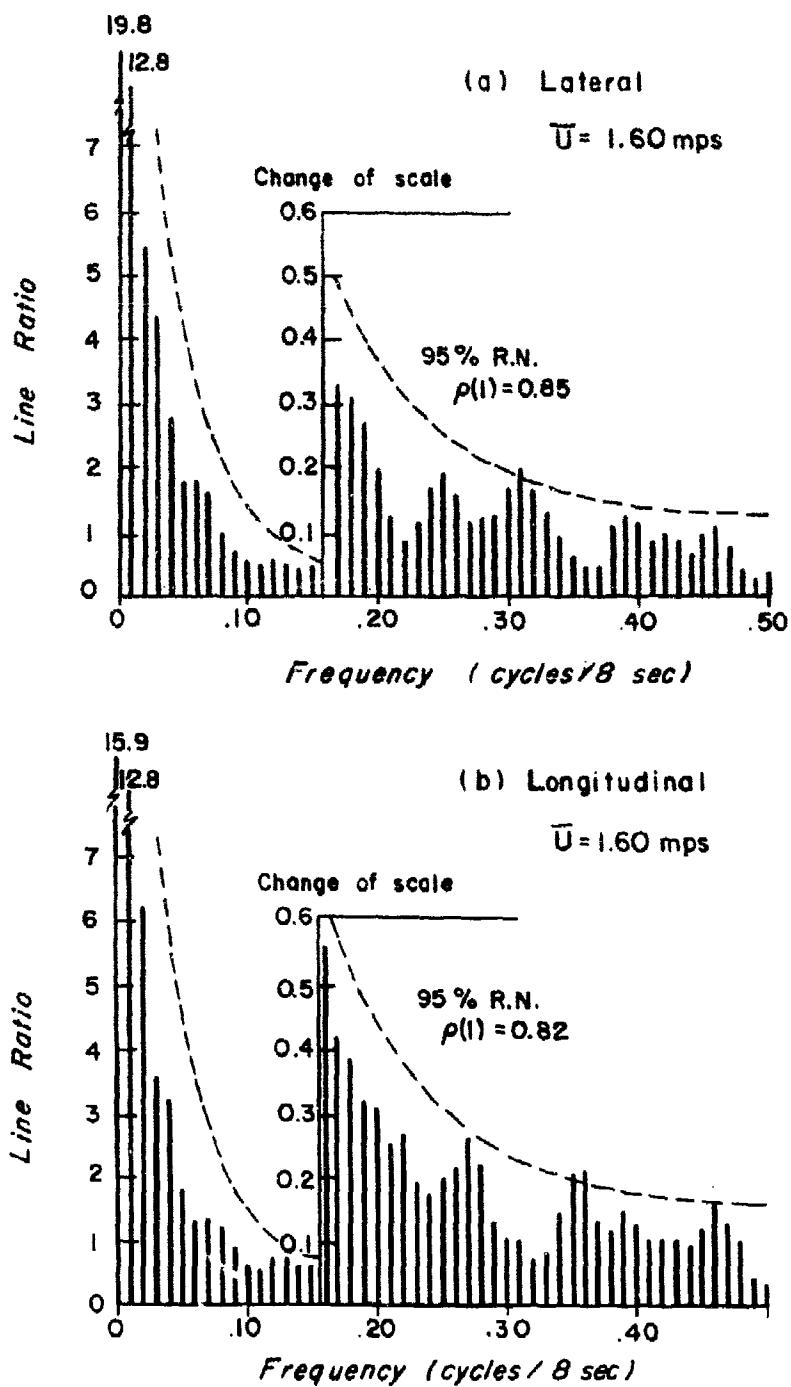


Fig. 3.72 Spectra of Wind Components at 1 m Level, Case VI-CD



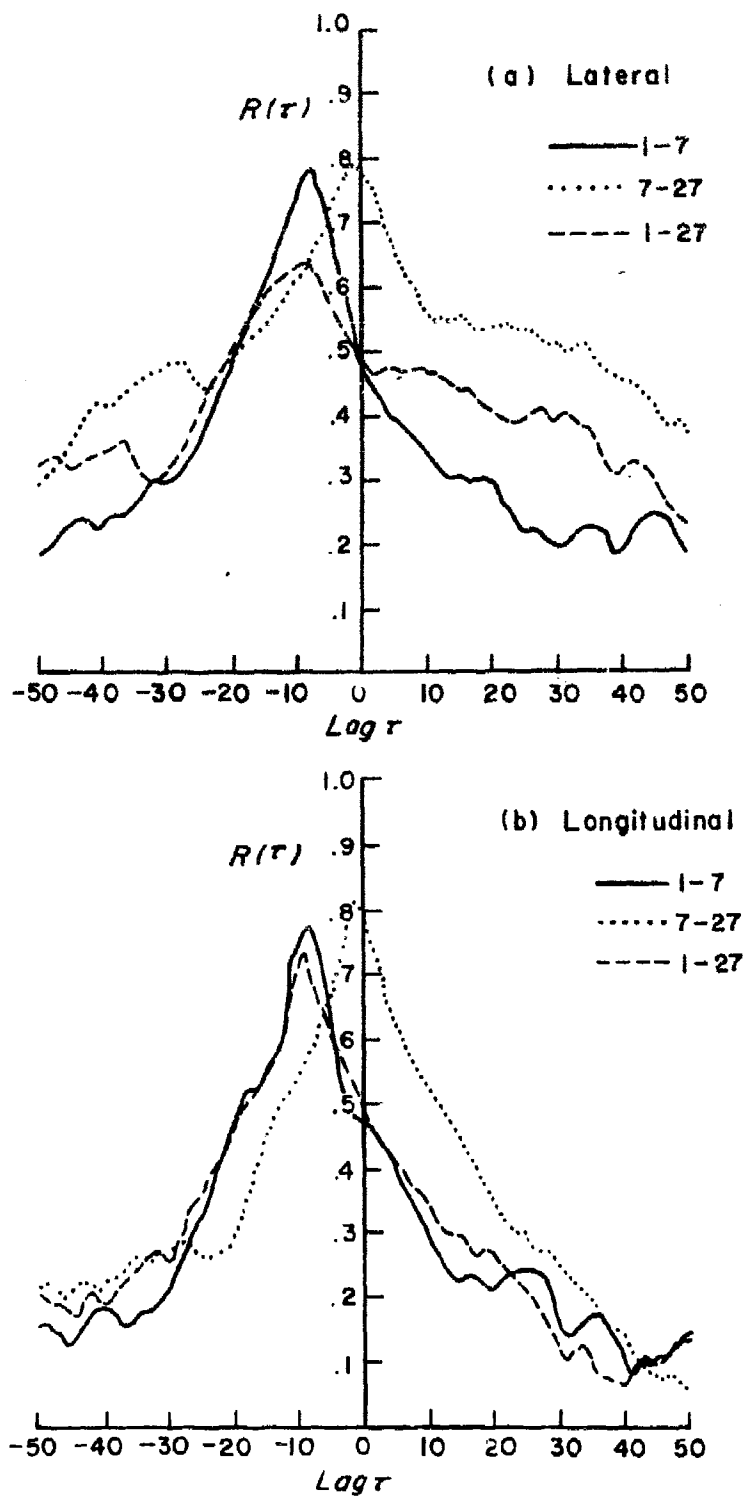


Fig. 3.73 Cross-correlation Functions of Components Between Levels, Case IV-CD

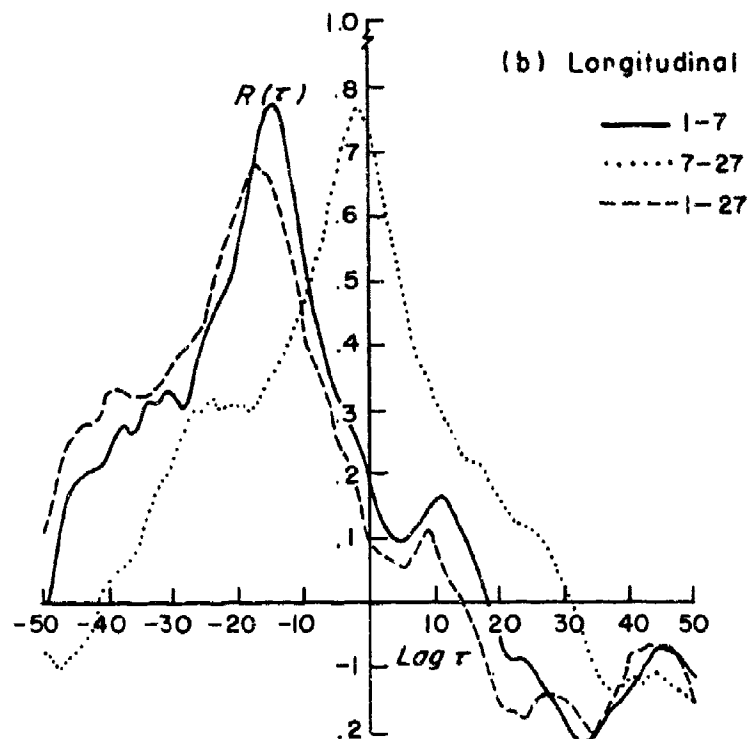
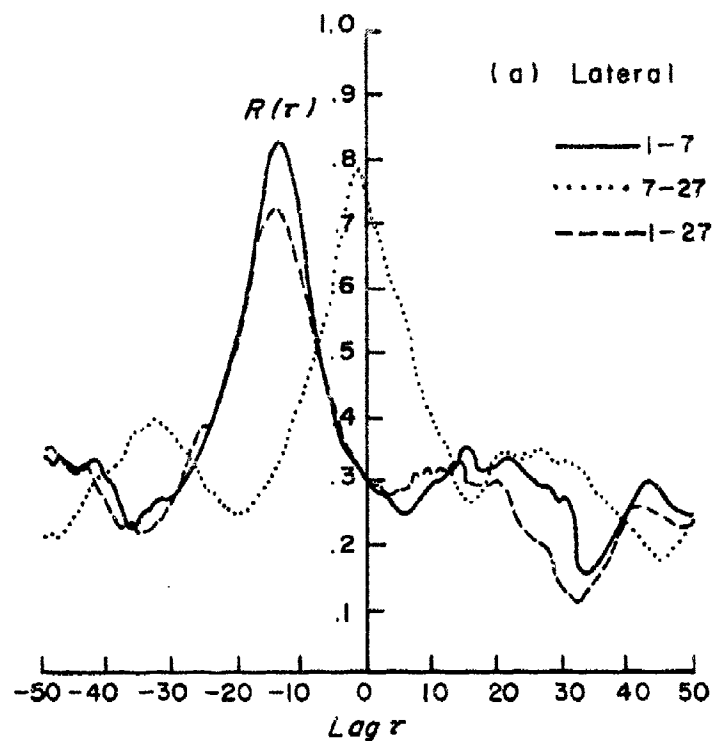


Fig. 3.74 Cross-correlation Functions of Components Between Levels, Case VI-CD

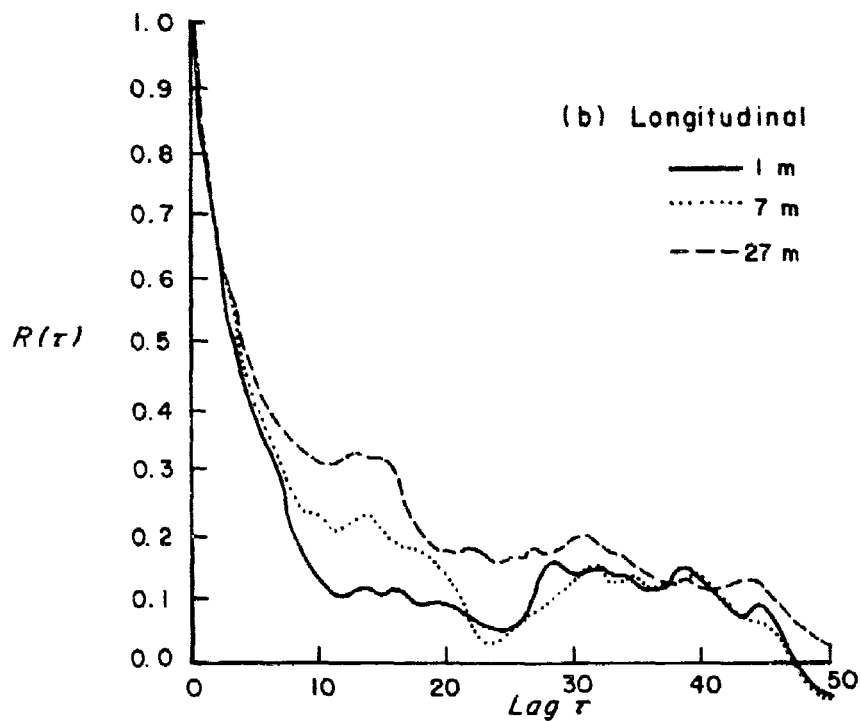
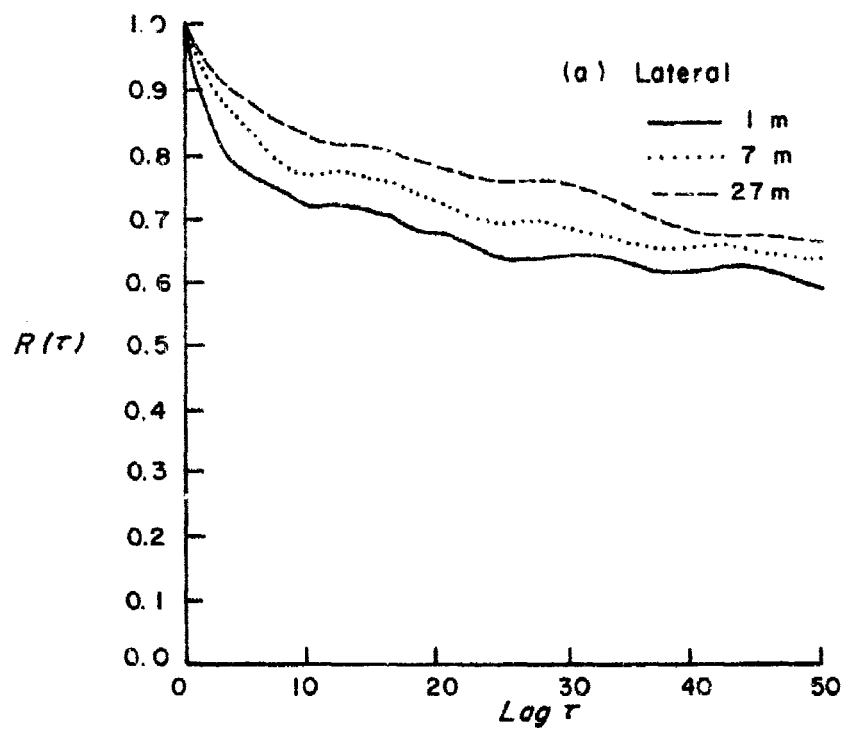


Fig. 3.75 Autocorrelation Functions of Wind Components,  
Case VII-CD

#### IV. SUMMARY AND CONCLUSIONS

The hypothesis that there are changes in the turbulent structure of the wind caused by the earth's surface characteristics and thermal variations, and that these changes can be detected by spectral analysis has been verified by the wind observations taken at two towers erected approximately 4.8 km apart near the Texas Gulf coast. The particular data samples included the land-sea-breeze phenomenon, which allowed samples to be taken in onshore and offshore wind flow during the course of a fourteen hour experiment. The wind measurements were taken at three elevations at both towers. Previous studies of the wind structure have been done using at most two elevations; moreover, these earlier studies have not been made in a land-sea-breeze regime.

It was shown that by recording and digitizing the data electronically, the spectra of the wind velocity components may be used to postulate the wind structure by testing the variance spectral estimates for statistical significance with two hypothesis; namely, white noise and red noise. The spectra depicted in the figures are not composite; but rather, each spectrum represents a data sample. The confidence limits are shown in each figure. Furthermore, partly because of the recording and digitizing techniques employed, the data did not need prewhitening prior to the spectral analysis. Only in very stable (thermal) cases was there a need to filter the data.

Throughout the data analysis, the assumption has been made that Taylor's hypothesis relating the mean wind, time, and space is true for all data samples studied for 1000 sec periods and 4000 sec periods. No attempt was made to verify the validity of this hypothesis- the experiment would have required many wind sensors placed close together to obtain space correlations and time correlations. Panofsky et al (1958) investigated the validity of Taylor's hypothesis using data obtained by other experimenters and found a

satisfactory agreement for low levels (or intensities) of turbulence. The general requirement is that the intensity be less than unity, as shown theoretically by Gifford (1956). According to Lumley and Fanofsky (1964), the limited information available indicates that Taylor's hypothesis is generally applicable except for low wave number components, i.e., low frequency components, of vertical velocity fluctuations. These were not considered in this study.

The bivariate statistics for the components are shown in Appendix F for the daytime samples, using the actual winds. The same statistics for the downstream and lateral components are shown after the rotation of the coordinate axes. The information obtained from the first is the wind direction (approximate) measured with respect to a North-South coordinate system, and the statistical parameters of the wind vector and wind components. Rotating the axes, of course, does not change the values of some of the parameters such as the vector standard deviation of wind velocity, the vector coefficient of variation, or the wind standard deviations along the minor and major axes of the ellipse, since these are all invariant with coordinate rotations. After rotation of the axes, the intensity of turbulence,  $S_u/\bar{U}$ , may be computed, where  $S_u$  is the sample standard deviation of the downstream component and  $\bar{U}$  is the sample mean wind. The intensities were all less than unity as shown in the Tables F.3 and F.4. The values of the Beach samples were consistently lower than those of the Canal. This is due both to smaller values of wind speeds and greater standard deviations of the downstream wind. The smaller wind speed values were a result of the land-breeze effect still observed in the canal area whereas a sea-breeze had begun at the beach. The larger standard deviations of the downstream components were probably due to the convective forces on the relatively lighter winds at the lower measurement level, and in some cases, by the somewhat erratic pattern of the turning of the winds

towards onshore flow at all levels caused indirectly by the thermal convection in the land area. As illustrated by Case III-CD at the canal, even after the winds were normal to the coast and with the subsequent increase in wind speeds, the standard deviations at all three levels were still high- giving intensity-of-turbulence values of 0.37, 0.39, and 0.32 for the 1 meter, 7 meter, and 27 meter levels, respectively. Panofsky et al (op. cit.) found that Taylor's hypothesis was valid up to intensity values of at least 0.26. An experiment such as the one proposed to test Taylor's hypothesis using a network of anemometers over an extensive area would be needed to determine the upper limit of the intensity of turbulence for Taylor's hypothesis to be valid. For some of the beach samples, however, the values at all three levels were well below the 0.26 value, e.g., Cases II-BD, IV-BD, and V-BD.

After the computation of the various statistical parameters and the spectral analyses on the horizontal velocity components, some of the findings are summarized as follow:

In the stable evening cases, where offshore flow or "land-breeze" occurred, one of the prominent features found is the long lateral meandering waves. It is difficult to say whether mechanical turbulence is the foremost cause of these long waves that appear on the low frequency end of the spectrum even though it is probably the cause of the turbulence which appears at the high frequency end at the lower two levels. This is due to the fact that waves appear to be quite separated from the rest of the spectra, i.e., generally only the first one or two harmonics are significant. The adjoining harmonics have negligible energy, as shown, for example, in Fig. 3.5, for a 1000 sec sampling period and Figs. 3.13 and 3.19 for 4000 sec sampling periods for the beach evening cases. Similar spectra were obtained from the canal data. Perhaps differential radiational cooling over the flat terrain induced these waves.

The longitudinal component in the stable cases also showed more energy at the low frequencies of the spectra. In the spectra of the lateral component the energy was restricted to the first harmonic; while in the longitudinal spectra, the energy was distributed among more of the lower harmonics.

A comparison of the two components to obtain some geometric interpretation at the high end of the frequency spectra shows that the smallest wavelengths detected by this method were on the order of 6 meters for the stable case at the beach, and 3 meters for the canal at the 1 m level for both components for the 1000 second sampling period. The suggested configuration occasionally extended upward to the 27 meter level with increasing diameters up to about 10 to 15 meters.

An increase of the sampling period to 4000 seconds indicated that the smallest eddies detected were in the order of 25 to 30 meters. This longer sampling period shows that these eddies were elongated downstream. However, in cases in which calm winds occurred during the sampling periods such as those at the canal site, the elongation was not detected. Because of these periods of calm at the canal, the results for the stable cases should not be as reliable as the beach data in which no calm intervals occurred.

The cross-correlations of the same components between levels showed a higher correlation laterally than downstream implying more significant wavelengths along the wind. The correlations between the 1 m and 7 m levels were higher than between 7 m and 27 m or 1 m and 27 m for the 4000 second periods. Thus the 25 meter to 40 meter diameter eddies were more discernable at the lower levels.

The 1000 sec sampling periods were found to be inadequate for the stable case to fully detect the longer lateral wavelengths. A 4000 sec period was found to be better, in spite of the averaging process which caused high

frequencies to be filtered. However, for the unstable (daytime) case, the 1000 sec period was found to be satisfactory. A sampling rate faster than 1 sample per 2 seconds was found to be desirable in some of the day cases where some possible aliasing was indicated.

The effect of instability on the lateral component spectra was found to be an increase of energy at the low frequencies and little change in the high frequencies. Thus, it appears that more waves were superimposed on the long waves of the stable case. An increase in wind, however, might have an effect on the high frequencies, according to Lumley and Panofsky (1964), by increasing the energy of the high frequencies. The evidence is rather limited (e.g., Cases II-BD and III-BD) to reach any conclusions from this particular study. For the longitudinal direction, thermal stability had some effect on the low frequencies but not as much as in the lateral direction. Wind speed should have affected the high frequency end as indicated by Ely (1958), but as in the lateral component, the only information of a stronger wind occurred with an increase in solar radiational heating. Therefore, it is difficult to determine if the increase in wind was the factor in these increases in energy at the high frequencies.

The daytime samples for the 1000 sec periods showed that the smallest eddies detected (9 to 14 meters) were elongated downstream at the three levels, but as the solar radiation increased, the eddies at the lowest level became circular as horizontal local isotropy was approached (e.g., Cases III-CD, III-BD, IV-BD, V-BD). The eddies did not increase in size appreciably upward as in the stable case.

The cross-correlation between components at different levels for the unstable cases showed high values for the longitudinal and lateral components, implying distinct nearly circular eddies caused by convection. The correlations



of the same component between 1 m and 27 m was consistently slightly lower than those between 1 m - 7 m, and 7 m - 27 m, again implying a more distinct eddy at the lower levels.

The cross-correlations also showed that the winds did not veer simultaneously into a sea-breeze flow. The graphical plots indicated that the top level turned first, and the bottom level last. The time interval, however, was on the order of a few minutes.

A comparison of the two locations during the daytime with onshore flow indicated that the spectra at the beach for the 1 m level showed proportionally less energy at the low frequencies (Fig. 3.48) than the spectra at 1 m for the canal (Fig. 3.66). This could be due to wind of maritime origin abruptly crossing a rougher and warmer surface and thus having the energy distributed among higher frequencies at the expense of the longer waves. For the canal cases, which were at a later time, the increase in solar radiational heating could account for the increase in energy found in the spectra. At the 7 meter height, the increase was more pronounced at the canal site (Figs. 3.49 and 3.67). At the highest level of 27 m, the comparison showed longer waves at the beach than at the canal (Figs. 3.50 and 3.58). This could be interpreted as a loss in energy of the long waves due to convection over land.

The explanations thus given of the possible reasons for the information obtained from the spectra imply that if the same three levels were measured over the water, most of the energy would be in the long waves, with the longest waves at the highest level. This hypothesis would have to be examined by conducting such an experiment.

Cross-spectral analysis between the two towers for 2 1/2 hour-record periods at night, showed the highest correlation between the lateral components at 27 m; the next highest between the lateral components at 7 m and the lowest

correlations between the lateral components at the 1 m level, and among all of the longitudinal components. This should be expected since the 27 m lateral components showed long waves to be the predominant feature. Because of the mechanical turbulence longitudinally, the correlations between the towers were small. The coherence values were low for all the frequencies except for the lowest frequency for all the cross-spectra between the two towers, indicating that the two time series were similar in long waves only.

The general features which appeared to be significant using 1000 sec periods and onshore flow at the beach and offshore flow at the canal (daytime) were the low correlation values between the two towers but high coherence values at the higher frequencies. Because of the different regimes occurring simultaneously near midday, this could be interpreted as a detection of two types of turbulence; mostly mechanical at the beach and the other caused by surface heating under light wind conditions at the canal. This high coherence was not detected at the higher levels.

The other cross-spectra between the two towers for the 1000 sec period showed negligible correlation values and no significant coherence values. This implies that two entirely different time series were being compared; that is, that the physical phenomena at the beach location were different from that of the canal. The only exceptions were as mentioned above and also for the samples taken 30 minutes after the sea breeze had begun. In these, there were high coherence values at the 7 and 27 m levels for low frequency and high frequency ranges for the downstream component. These two samples were not simultaneous, but nearly two hours apart; a comparison is therefore impossible to make.

The coherence was found to be a very sensitive measure of agreement between two series. (Bogart et al (1962) also found this to be the case, using other types of data.) Since the data were digitized electronically, the problem

of noise in the high frequency region introduced by hand digitizing was not present in the coherence computations.

Because of the numerous types of data interpretation which can be made of spectral estimates of wind components, (such as "power laws"), a deliberate attempt has been made to present the spectra in graphical form. Other investigators might find these of further use.

In order to make better interpretations of the wind phenomena, the vertical component is needed. Although the measurement of this vertical component at three levels would necessitate different instrumentation, it is recommended that any future experiments include the three wind components. The same experimental procedures, data reduction, and spectral analysis described in the text could be employed in the investigation of the three-component wind structure.

## APPENDIX A

### A.1 Sample Record of Analog Data

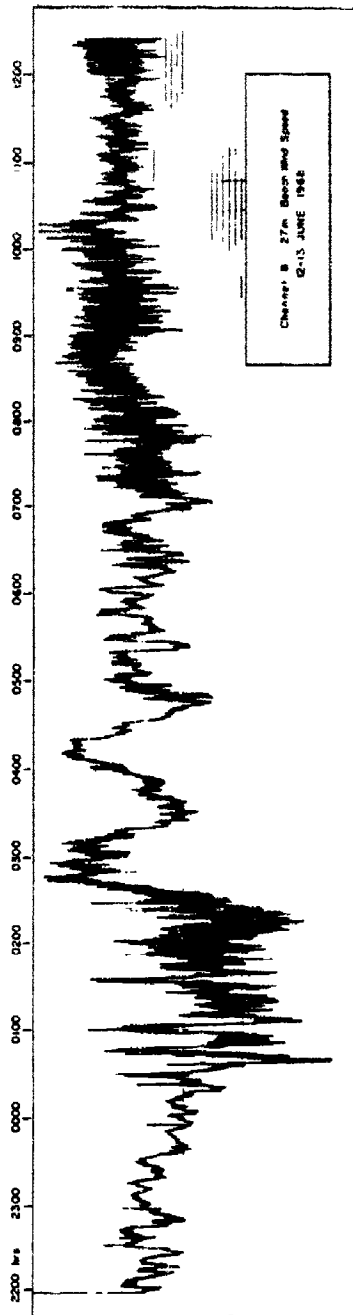
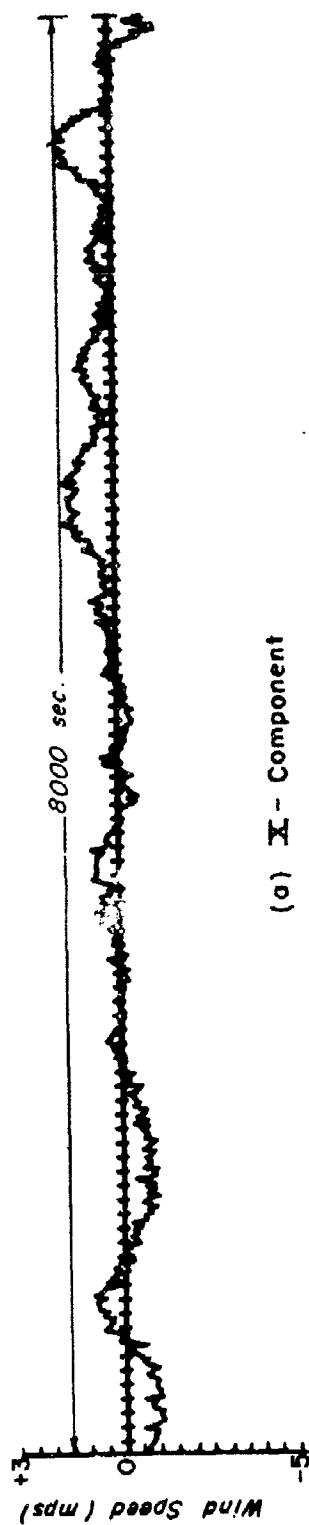


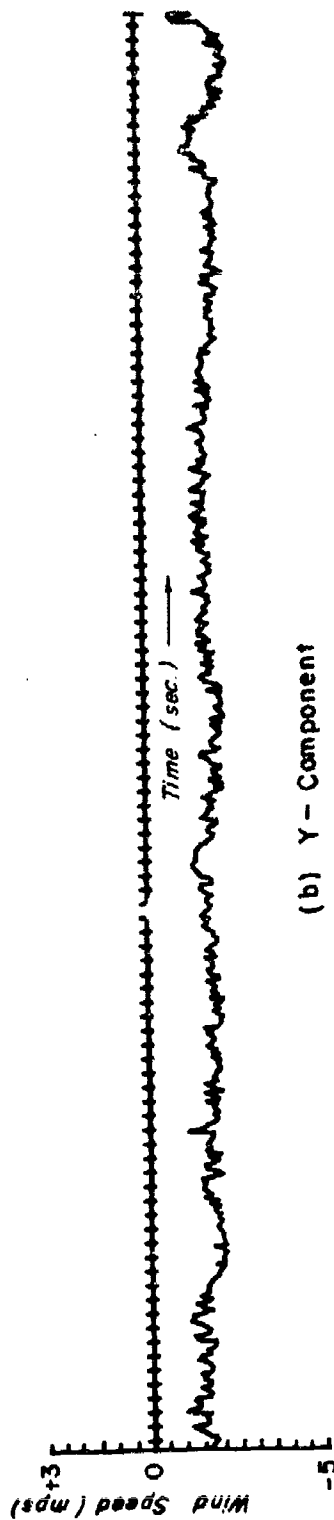
Fig. 4.1.1 Sample Record of Analog Data

## APPENDIX B

Samples of plots of the x - and y - components of Velocity	Page
B.1 Case IV-BN Beach Tower 1 m Level 12/2213-13/0027 CDT	160
B.2 Case IV-BN Beach Tower 7 m Level 12/2213-13/0027 CDT	161
B.3 Case IV-BN Beach Tower 27 m Level 12/2213-13/0027 CDT	162
B.4 Case IV-CN Canal Tower 1 m Level 12/2213-13/0027 CDT	163
B.5 Case IV-CN Canal Tower 7 m Level 12/2213-13/0027 CDT	164
B.6 Case IV-CN Canal Tower 27 m Level 12/2213-13/0027 CDT	165
B.7 Case IV-BD Beach Tower 7 m Level 13/1047-1104 CDT	166
B.8 Case IV-BD Beach Tower 27 m Level 13/1047-1104 CDT	167
B.9 Case IV-CD Canal Tower 1 m Level 13/1103-1210 CDT	168
B.10 Case IV-CD Canal Tower 7 m Level 13/1103-1210 CDT	169
B.11 Case IV-CD Canal Tower 27 m Level 13/1103-1210 CDT	170

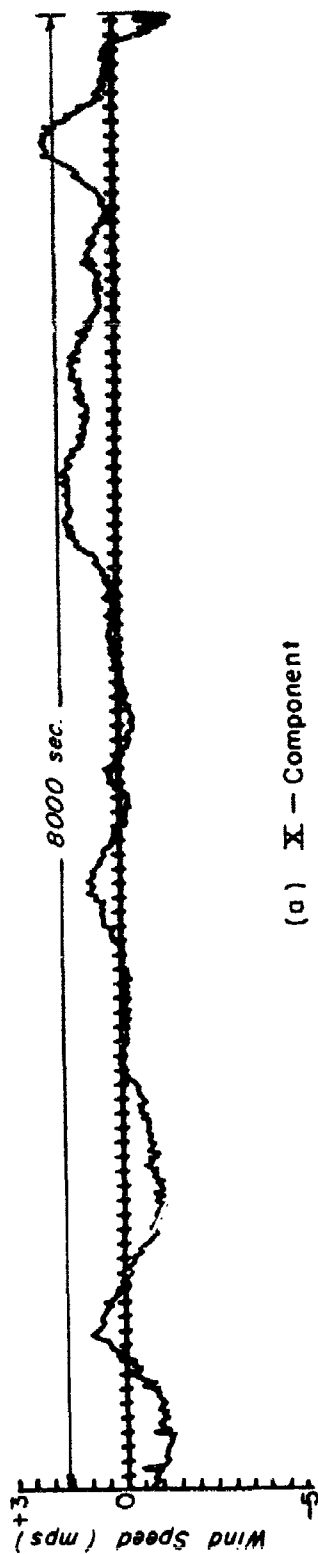


(a) X - Component

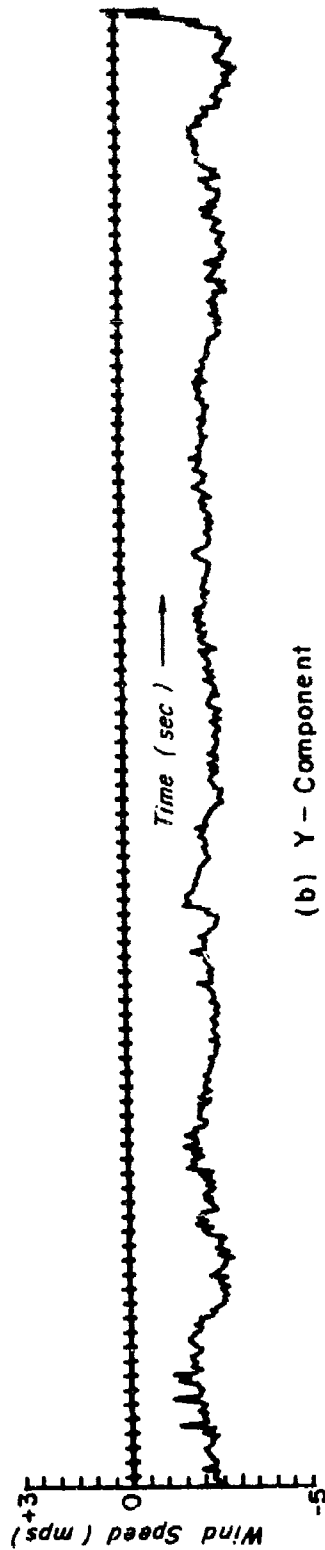


(b) Y - Component

Fig. B.1 Sample of plots of the x- and y-components of velocity  
Case IV-BN Beach Tower 1 m Level 12/2213-13/0027 CDF



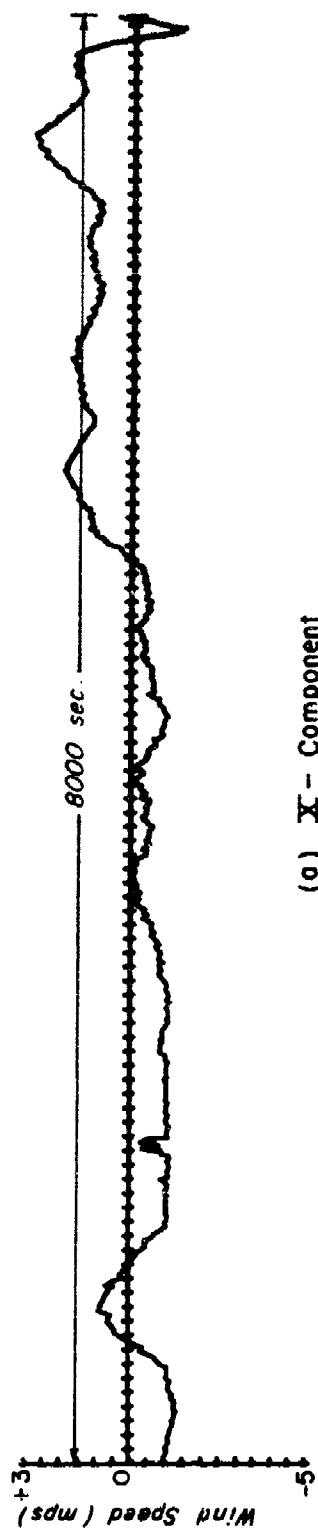
(a) X - Component



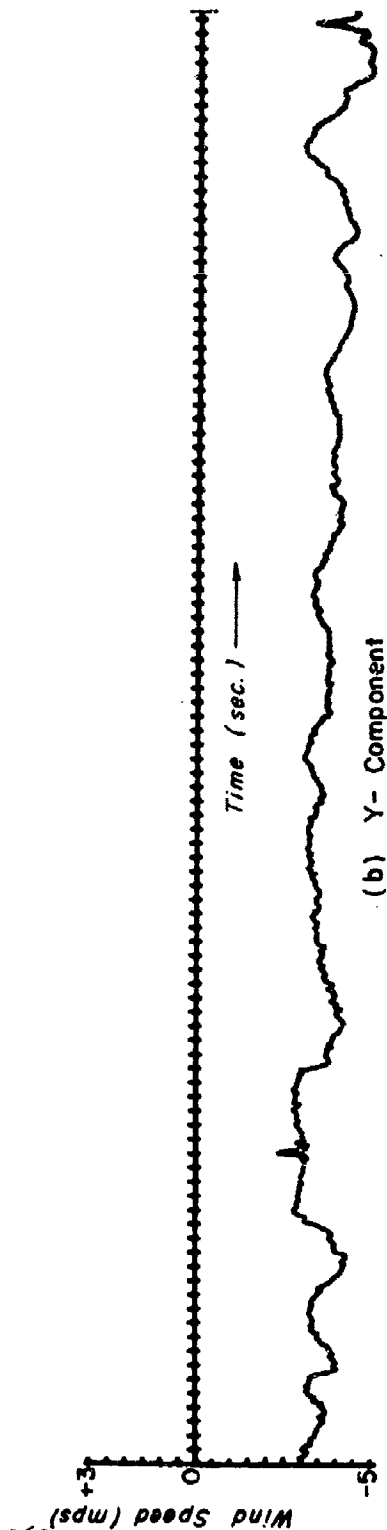
(b) Y - Component

Fig. B.2 Sample of plots of the x- and y-components of velocity  
Case IV-BN Beach Tower 7 m Level 12/2213-13/0027 CDF



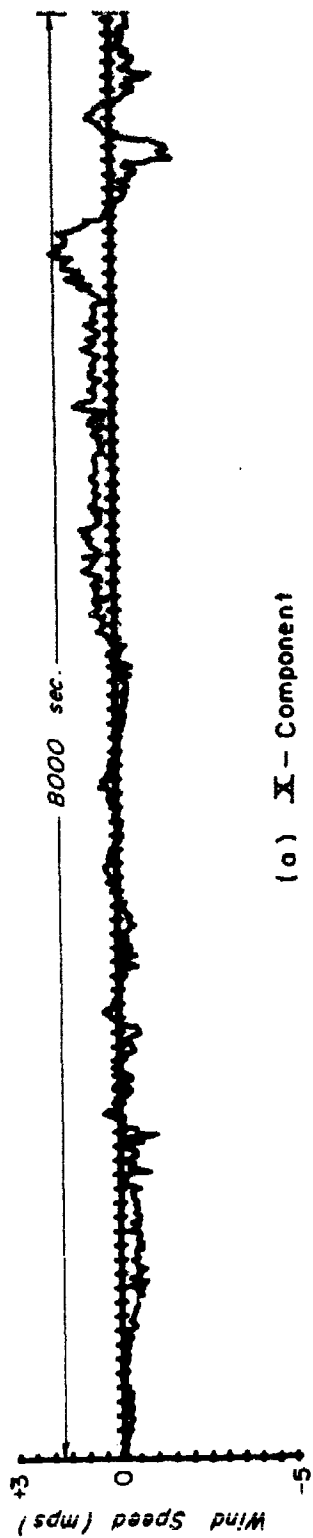


(a) X-Component

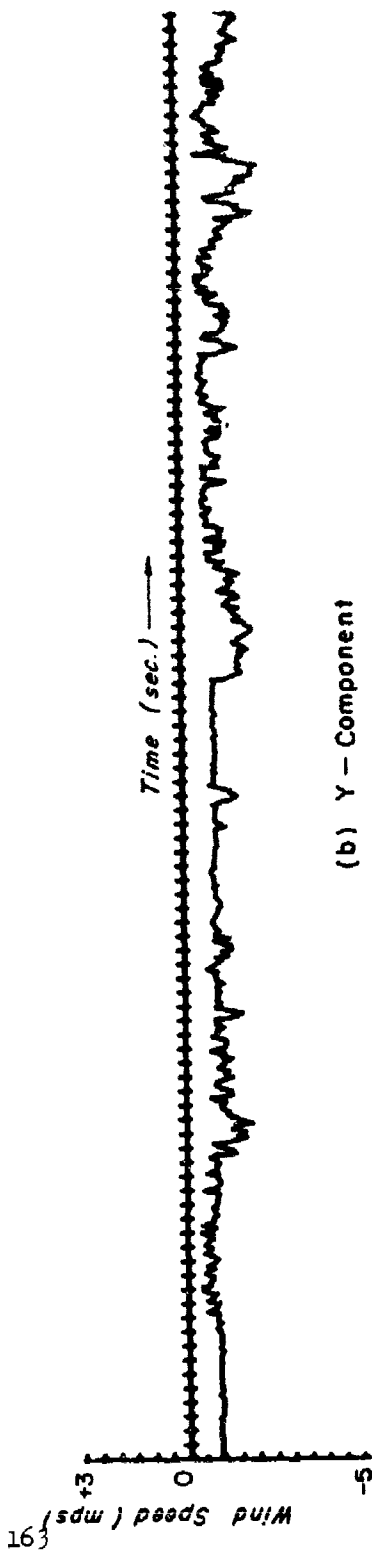


(b) Y-Component

Fig. B.3 Sample of plots of the x- and y-components of velocity  
Case IV-BN Beach Tower 27 m Level 12/2213-13/0027 CDT

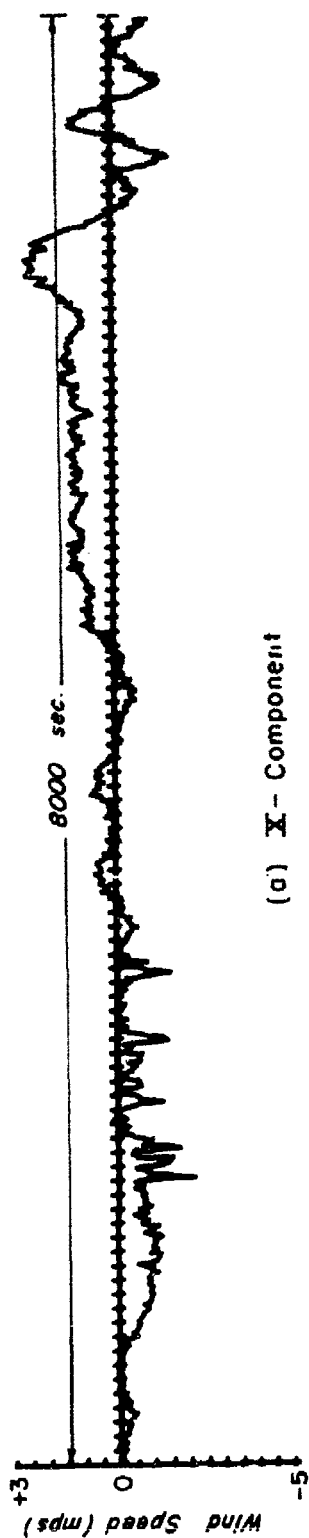


(a) X - Component

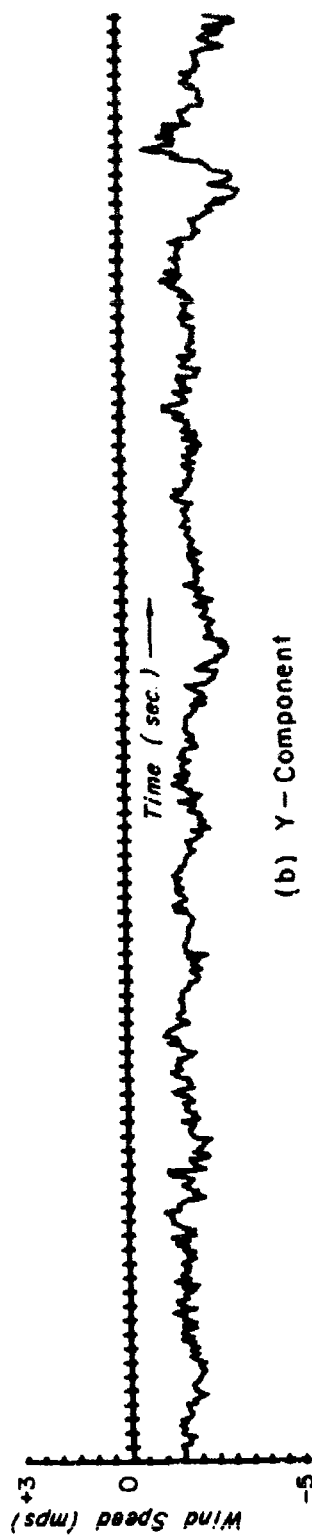


(b) Y - Component

Fig. B.4 Sample of plots of the x- and y-components of velocity  
Case IV-CN Canal Tower 1 m Level 12/2213-13/0027 CDF

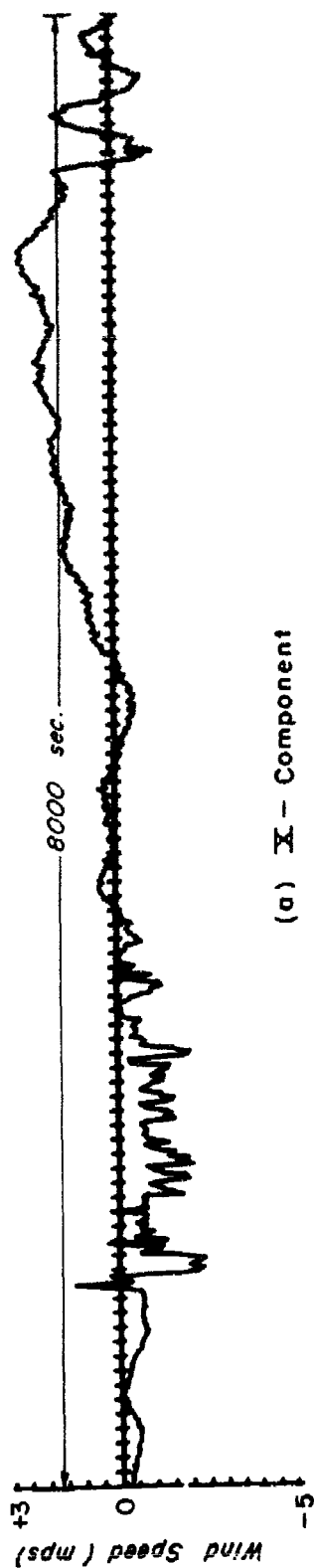


(a) X - Component

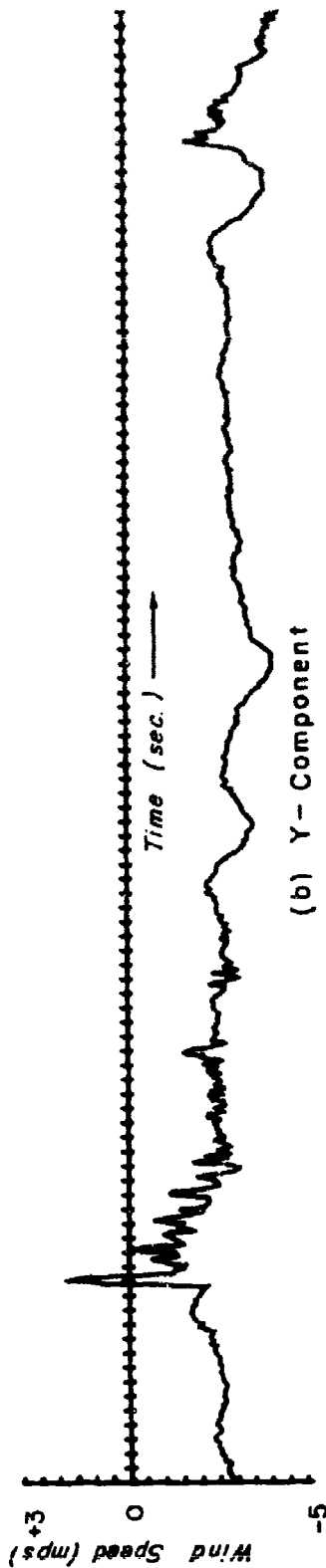


(b) Y - Component

Fig. B.5 Sample of plots of the x- and y-components of velocity  
Case IV-CN Canal Tower 7 m Level 12/2213-13/0027 CDT



(a) X - Component



(b) Y - Component

Fig. B.6 Sample of plots of the x- and y-components of velocity  
Case IV-CN Canal Tower 27 m Level 12/2213-13/0027 CDT

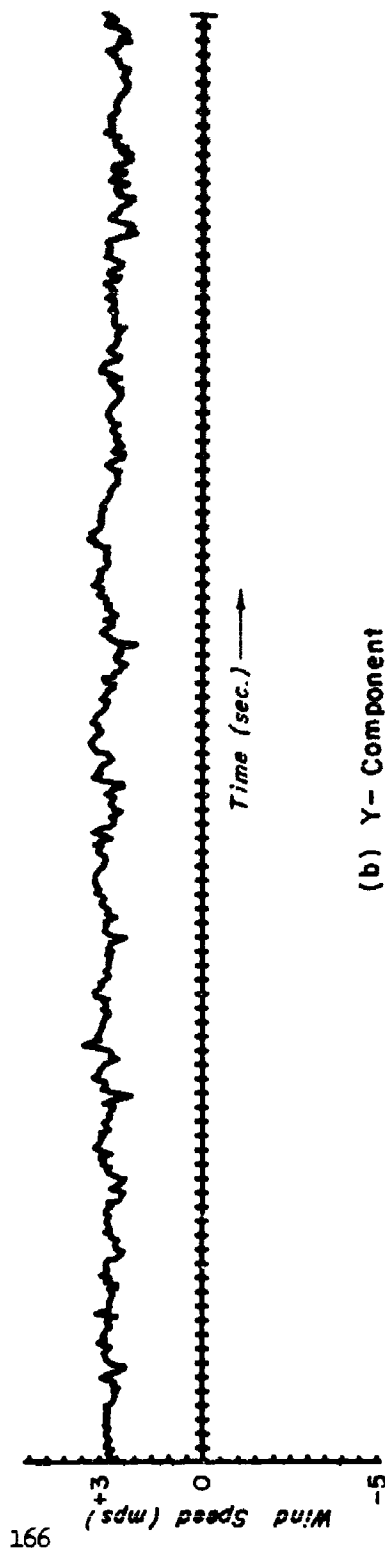
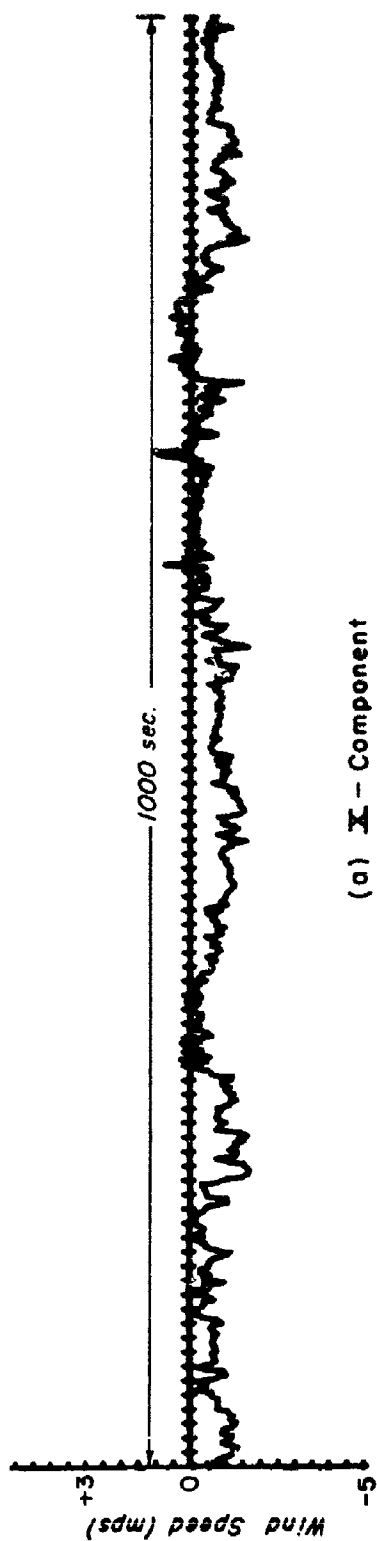


Fig. B.7 Sample of plots of the x- and y-components of velocity  
Case IV-BD Beach Tower 7 m Level 13/1047-1104 CDF

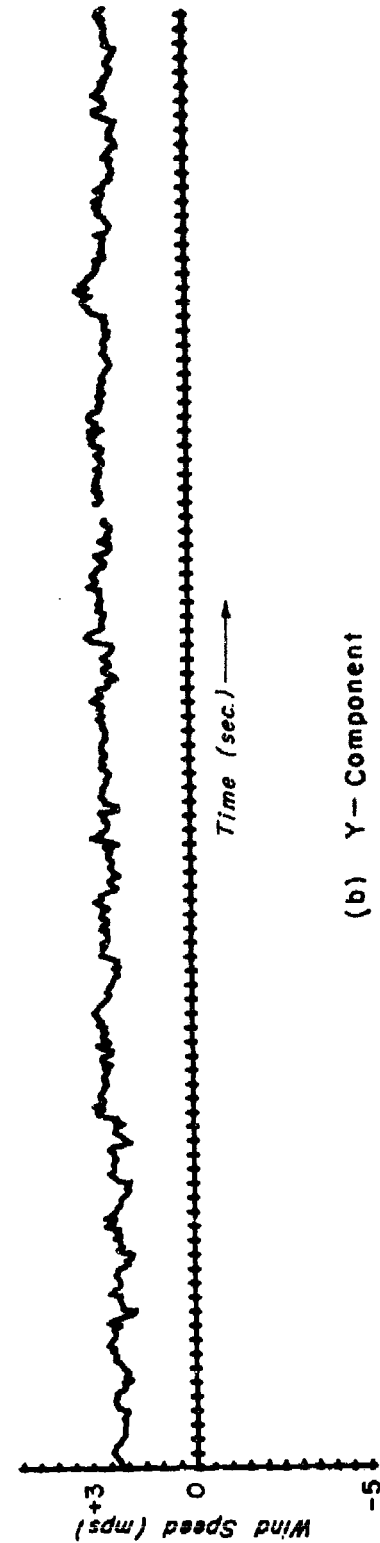
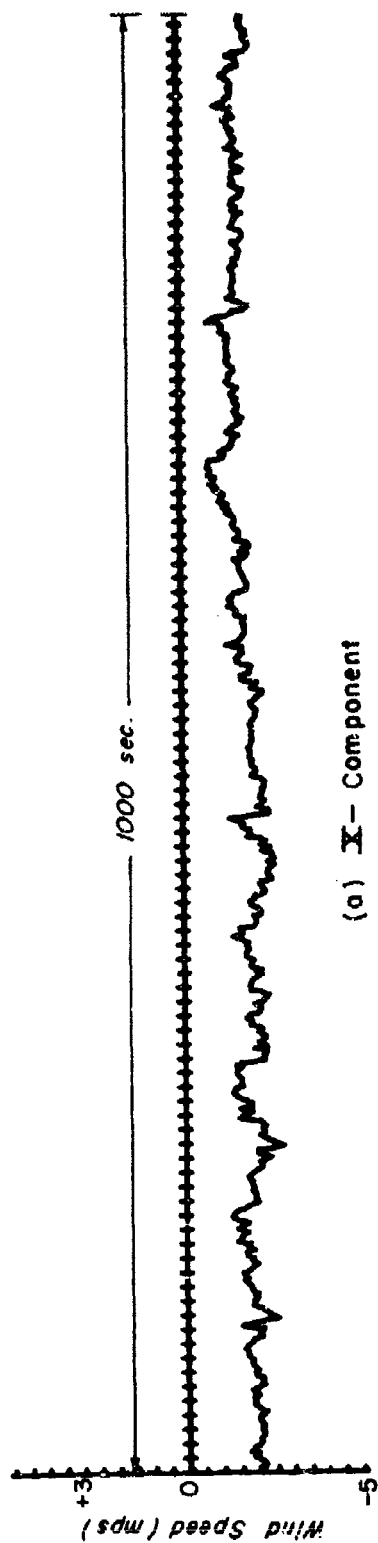
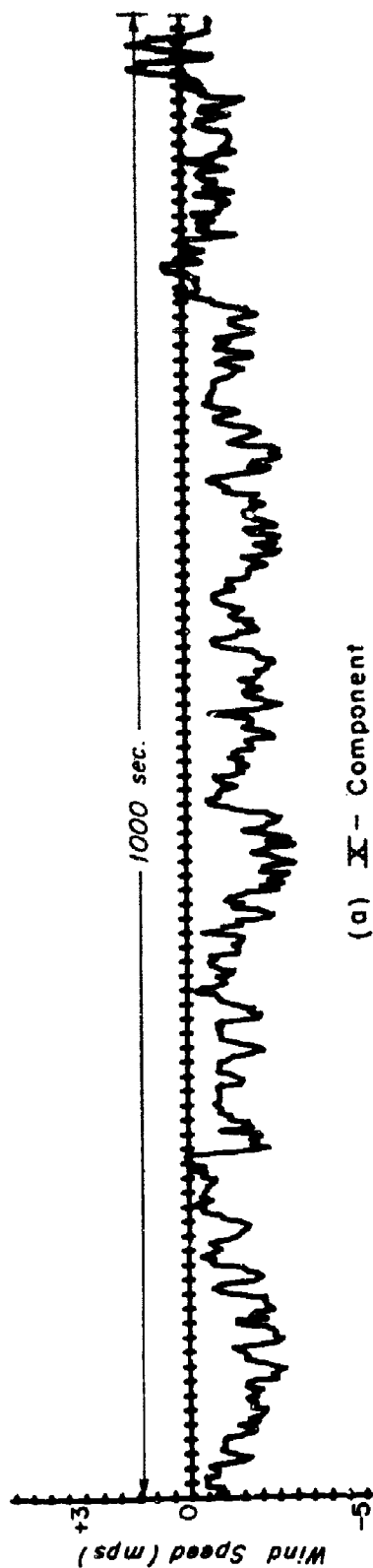
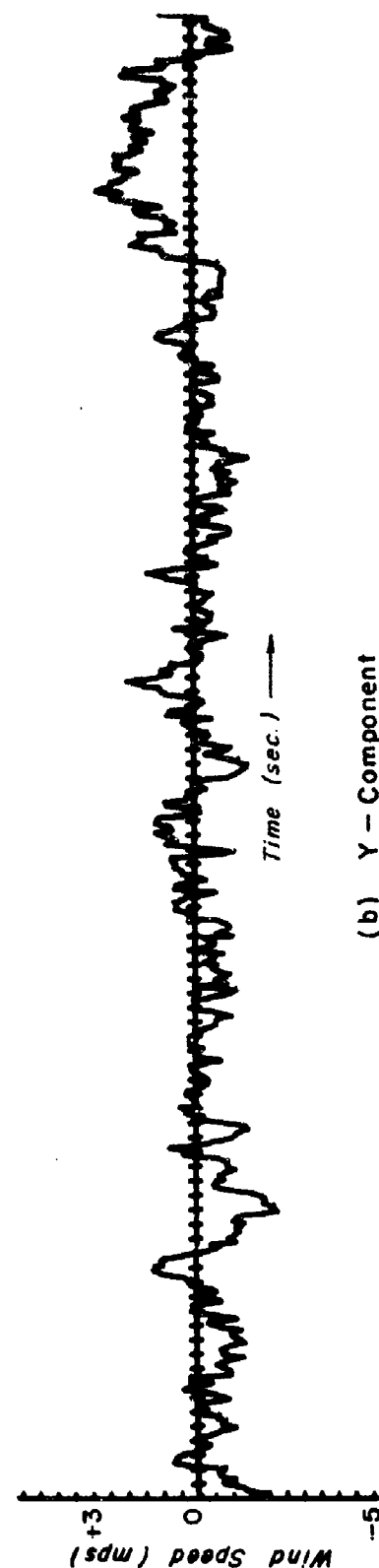


Fig. B.8 Sample of plots of the x- and y-components of velocity  
Case IV-BD Beach Tower 27 m Level 13/1047-1104 CDF



(a) X - Component



(b) Y - Component

Fig. B.9 Sample of plots of the x- and y-components of velocity  
Case IV-CD Canal Tower 1 m Level 13/1103-1210 CDT

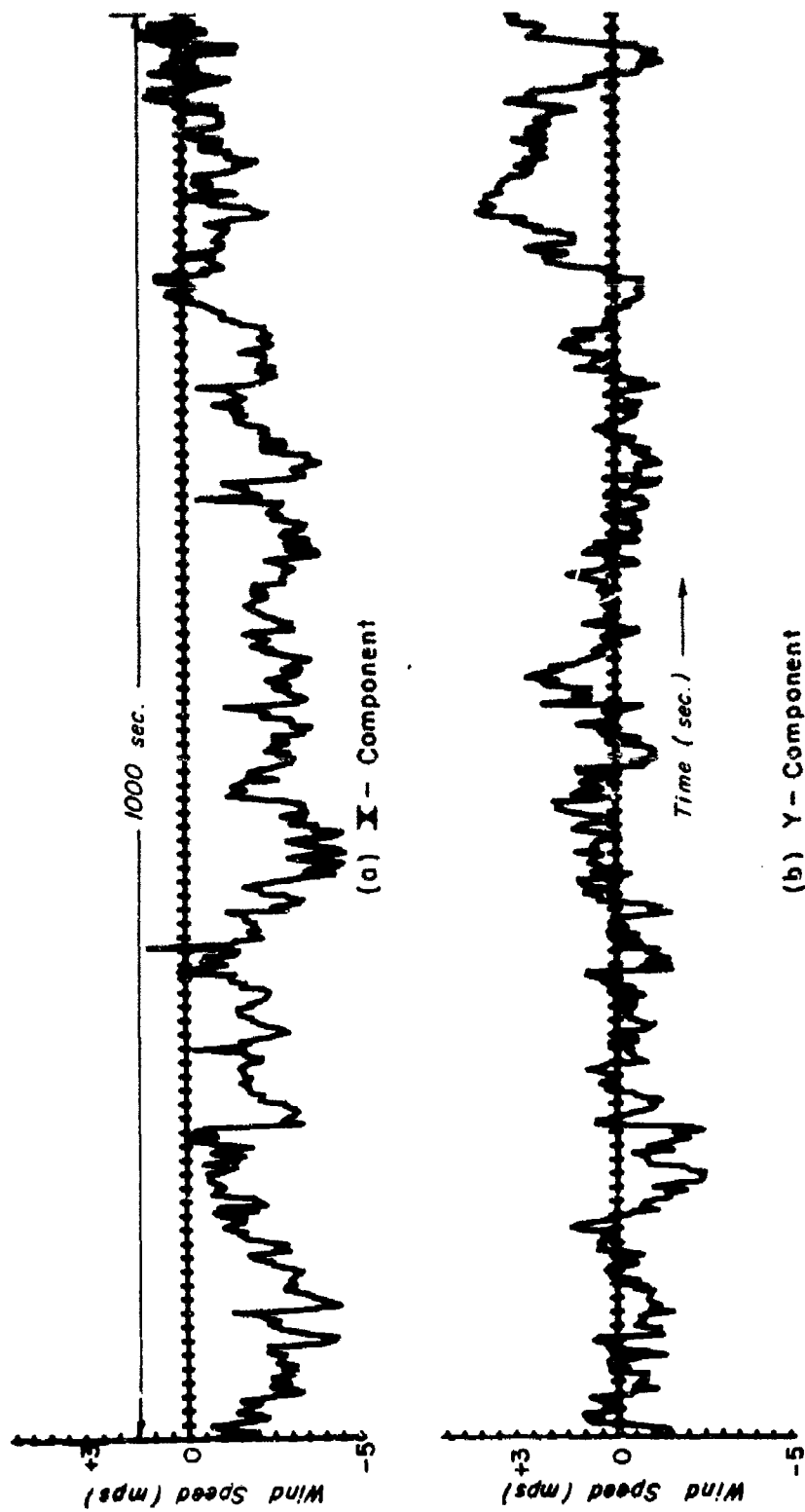
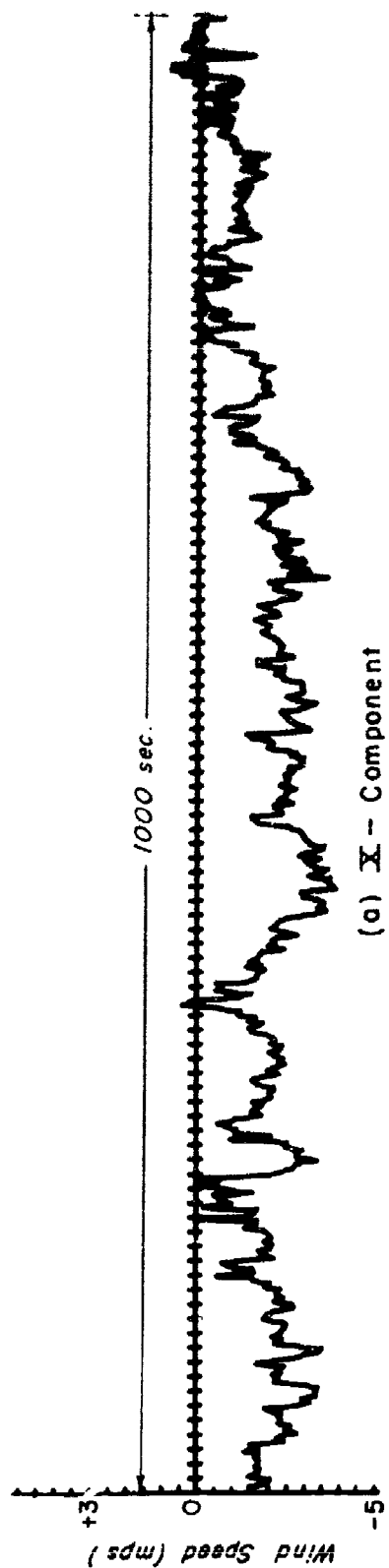
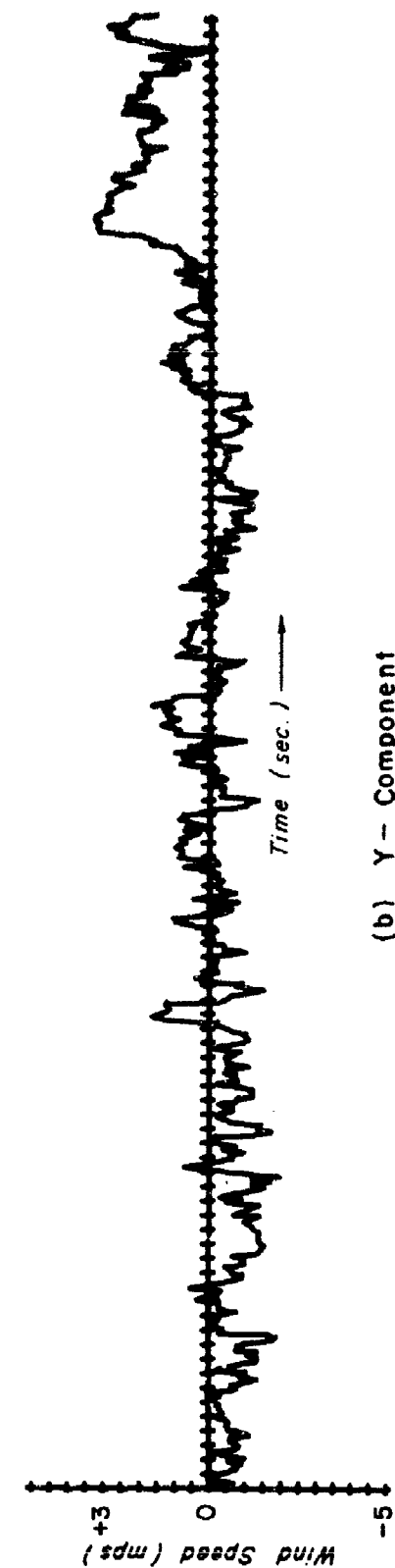


Fig. B.10 Sample of plots of the x- and y-components of velocity  
Case IV-CD Canal Tower 7 m Level 13/1103-1210 CDF





(a) X - Component



(b) Y - Component

Fig. B.11 Sample of plots of the x- and y-components of velocity  
Case IV-CD Canal Tower 27 m Level 13/1103-1210 CDT

#### APPENDIX C

##### Statistics of Daytime Samples

- (a) mean
- (b)  $s^2$  (variance)
- (c)  $s$  standard deviation
- (d) Skewness
- (e) Kurtosis
- (f)  $\chi^2$  from chi-square Goodness-of-Fit

Frequency Distributions for Beach Daytime Cases  
Based on X- and Y-components

CASE I

	1 m		7 m		27 m	
	X	Y	X	Y	X	Y
Time	13/1000 - 1017					
mean	-1.800	.092	-1.670	.723	-2.217	-.121
S <sup>2</sup>	.241	.803	.554	.555	.389	.755
S	.491	.896	.745	.745	.624	.869
Skewness	-.147	.106	-.503	.168	.881	.270
Kurtosis	.484	-.797	.743	-.317	6.485	-.724
Chi-square	60.5	76.4	235.4	62.2	75.3	98.4

CASE II

	1 m		7 m		27 m	
	X	Y	X	Y	X	Y
Time						
mean	-2.062	1.587	-1.341	2.256	-2.454	1.230
S <sup>2</sup>	.378	.501	.344	.247	.265	.356
S	.615	.708	.587	.497	.515	.597
Skewness	.171	-.632	-.275	-1.565	-.163	-.852
Kurtosis	-.228	.940	-.242	2.601	-.455	.565
Chi-square	20.5	62.9	32.6	273.4	62.2	124.0

CASE III

	1 m		7 m		27 m	
	X	Y	X	Y	X	Y
Time						
mean	-1.828	.524	-1.368	1.089	-2.095	.358
S <sup>2</sup>	.256	1.074	.274	.910	.246	1.061
S	.506	1.036	.523	.954	.496	1.030
Skewness	-.043	-.109	-.113	.040	2.244	-.215
Kurtosis	.308	-.716	3.159	-.970	15.191	-1.063
Chi-square	40.2	59.9	163.1	94.1	45.7	140.5

Frequency Distributions for Beach Daytime Cases  
Based on X- and Y-components

CASE IV

	1 m		7 m		27 m	
	X	Y	X	Y	X	Y
Time						
mean	-1.431	2.163	-.610	2.586	-1.701	2.290
S <sup>2</sup>	.388	.230	.195	.054	.106	.041
S	.623	.479	.442	.232	.326	.203
Skewness	.335	-.399	.351	-.268	.124	-.113
Kurtosis	.269	.089	.162	.040	.061	.026
Chi-square	60.1	79.2	21.1	47.0	35.1	26.2

CASE V

	1 m		7 m		27 m	
	X	Y	X	Y	X	Y
Time			1103 - 1120 (1000 sec)			
mean	-1.194	2.397	-.237	2.670	-1.530	2.499
S <sup>2</sup>	.424	.220	.133	.074	.098	.039
S	.651	.469	.364	-.271	.313	.196
Skewness	-.232	-.518	.295	-.265	.274	.369
Kurtosis	-.599	.229	.027	-.213	-.251	.070
Chi-square	108.6	----	24.1	27.4	28.4	27.9

CASE VI

	1 m		7 m		27 m	
	X	Y	X	Y	X	Y
Time			1000 - 1107 (1000 sec)			
mean	-1.788	1.432	-1.193	2.031	-2.135	1.354
S <sup>2</sup>	.278	.979	.446	.802	.276	1.163
S	.527	.989	.668	.896	.525	1.078
Skewness	.113	-.981	-.635	-1.289	-.256	-.948
Kurtosis	-.022	.171	.843	.534	.304	-.160
Chi-square	21.2	196.6	2351.4	462.5	63.7	243.3

Frequency Distributions for Beach Daytime Cases  
Based on X- and Y-components

CASE VII

	1 m		7 m		27 m	
	X	Y	X	Y	X	Y
Time	1103 - 1214 (4000 sec)					
mean	-.942	2.540	.265	2.693	-.920	2.773
s <sup>2</sup>	.297	.177	.273	.110	.272	.101
S	.545	.420	.523	.332	.521	.318
Skewness	-.057	-.154	.208	-.331	.033	-.037
Kurtosis	-.147	-.271	-.347	.525	-.390	-.465
Chi-square	29.7	23.5	35.1	37.5	35.6	23.7

Frequency Distributions for Canal Day Cases  
Based on X- and Y-components

CASE I

Level	1 m		7 m		27 m	
Comp	X	Y	X	Y	X	Y
Time	1103 - 1120 CDT					
mean	-1.278	-.524	-2.060	-.501	-1.889	-.699
$s^2$	.523	.566	1.062	.890	.676	.372
S	.72	.75	1.03	.94	.82	.61
Skewness	0.421	.221	.562	-.145	.979	.123
Kurtosis	.488	-.224	1.395	-.725	2.430	.250
Chi-square	55.1	34.6	34.4	62.7	39.9	38.5

CASE II

Level	1 m		7 m		27 m	
Comp	X	Y	X	Y	X	Y
Time	1155 - 1212 CDT					
mean	-.600	.802	-.572	1.565	-.572	1.603
$s^2$	.561	1.038	.777	1.897	.429	.793
S	.75	1.02	.88	1.38	.65	.890
Skewness	.693	-.277	-.013	-.522	.096	-.159
Kurtosis	.431	-1.110	-.106	-.774	-.513	-1.029
Chi-square	125.8	227.5	40.0	282.1	66.2	208.0

CASE III

Level	1 m		7 m		27 m	
Comp	X	Y	X	Y	X	Y
Time	1236 - 1253 CDT					
mean	-.510	1.602	-.855	2.335	-.939	2.161
$s^2$	.667	.436	1.161	1.037	.781	.625
S	.82	.66	1.08	1.02	.88	.79
Skewness	.092	-.137	-.048	.080	-.097	-.098
Kurtosis	-.435	-.428	-.800	-.573	-.465	-.307
Chi-square	19.8	34.5	47.3	56.8	52.2	44.7

Frequency Distributions for Canal Day Cases  
Based on X- and Y-components

CASE IV

Level	1 m		7 m		27 m	
Comp	X	Y	X	Y	X	Y
Time	1103 - 1210 CDT					
mean	-1.279	-.053	-1.895	.254	-1.725	.121
S <sup>2</sup>	.529	.708	1.196	1.415	.800	1.110
S	.727	.841	1.094	1.190	.894	1.050
Skewness	.396	.582	.322	.639	.360	.822
Kurtosis	.506	.162	-.178	.149	-.297	.101
Chi-square	96.6	73.0	27.3	110.8	48.9	124.8

CASE V

Level	1 m		7 m		27 m	
Comp	X	Y	X	Y	X	Y
Time	1155 - 1302 CDT					
mean	-.355	1.470	-.335	2.343	-.634	2.129
S <sup>2</sup>	.714	.667	1.393	1.226	.667	.591
S	.845	.817	1.180	1.107	.817	.769
Skewness	.298	-.964	.287	-.919	.303	-.633
Kurtosis	-.399	.772	-.451	.936	.000	.001
Chi-square	34.7	180.0	26.0	148.7	50.1	111.7

CASE VI

Level	1 m		7 m		27 m	
Comp	X	Y	X	Y	X	Y
Time	1210 - 1317 CDT					
mean	-.321	1.572	-.283	2.379	-.629	2.123
S <sup>2</sup>	.703	.458	1.369	.883	.660	.567
S	.838	.677	1.170	.940	.812	.753
Skewness	.143	-.712	.181	-.342	.220	-.534
Kurtosis	-.345	.878	-.432	-.227	-.110	-.125
Chi-square	45.2	1101.7	38.0	34.1	60.4	94.5

Frequency Distributions for Canal Day Cases  
Based on X- and Y-components

CASE VII

	1 m		7 m		27 m	
	X	Y	X	Y	X	Y
Time	1103 - 1317 CDT					
mean	-.800	.759	-1.089	1.317	-1.177	1.122
$s^2$	.801	1.208	1.857	2.213	.988	1.807
S	.895	1.099	1.363	1.488	.994	1.344
Skewness	.302	-.191	.198	-.125	.046	-.177
Kurtosis	-.274	-1.096	-.434	-1.074	-.400	-1.268
Chi-square	41.1	125.4	33.8	93.0	47.9	169.1



## APPENDIX D

Bivariate Statistics for x and y components

Table D.1 Beach Evening

Table D.2 Canal Evening

Gain Function

Fig. D.1 Gain Function for First Difference Filter  $y(t) = x(t) - x(t - 1)$

Computations:

1. Gain Function
2. Spectral Estimate Multiplier

Table D.1. Bivariate Statistics for x- and y-components  
Beach Evening

Sampling Period	CASE I: 2213 - 2230 CDT				CASE II: 2213 - 2320			
	1000 sec		4000 sec		1000 sec		4000 sec	
	1 m	7 m	27 m	1 m	1 m	7 m	27 m	1 m
Resultant Wind (deg/mps)	009/1.45	011/1.90	007/3.32	005/1.67	005/2.09	010/3.29		
Degrees off Downstream	+ 9	+ 11	+ 7	+ 5	+ 5	+ 10		
Vector Standard dev. of Wind	.75	.82	.82	.61	.67	.66		
Vector Coeff. of Variation	.52	.43	.25	.37	.32	.20		
Mean E-W component ( $\bar{X}$ )	-.23	-.38	-.42	-.13	-.19	-.58		
Mean N-S component ( $\bar{Y}$ )	-1.43	-1.86	-3.29	-1.67	-2.08	-3.24		
Correlation Coeff.	.20	.26	.03	.10	.00	-.10		
Variance of x-component	.454	.536	.616	.27	.33	.29		
Variance of y-component	.123	.140	.061	.10	.11	.15		
Standard dev. of x-comp ( $S_x$ )	.67	.73	.78	.52	.58	.54		
Standard dev. of y-comp ( $S_y$ )	.35	.37	.25	.31	.34	.38		
$S_y/\bar{X}$ (Relative Turbulence)	-1.50	-.99	-.58	-2.38	-1.78	-.66		
$S_x/\bar{Y}$ (Relative Turbulence)	-.47	-.39	-.24	-.31	-.28	-.17		
Wind Standard dev. along Maj. Axis	.68	.74	.78	.53	.58	.54		
Wind Standard dev. along Min. Axis	.34	.36	.25	.31	.34	.38		
Angle of Rotation of Maj. Axis	7.95	9.88	.50	5.12	0	182		

Table D.1. Bivariate Statistics for x- and y-components  
Beach Evening

Sampling Period	CASE III: 2320 - 0027			CASE IV: 2213 - 0027		
	1 m	7 m	27 m	1 m	7 m	27 m
	4000 sec			8000 sec		
Resultant Wind (deg/mps)	346/1.85	345/2.4	346/3.79	355/1.74	354/2.21	357/3.46
Degrees off Downstream	-14	-15	-14	-5	-6	-3
Vector Standard dev. of Wind	.67	.80	1.04	.70	.85	1.17
Vector Coeff. of Variation	.36	.33	.27	.40	.38	.34
Mean E-W component ( $\bar{X}$ )	.43	.61	.92	.15	.21	.17
Mean N-S component ( $\bar{Y}$ )	-1.80	-2.32	-3.68	-1.73	-2.21	-3.46
Correlation Coeff.	.32	.10	-.18	.09	-.11	-.43
Variance of x-component	.34	.44	.93	.39	.55	1.18
Variance of y-component	.11	.20	.15	.11	.17	.20
Standard dev. of x-comp ( $S_X$ )	.58	.66	.97	.62	.74	1.08
Standard dev. of y-comp ( $S_Y$ )	.34	.44	.39	.33	.41	.44
$S_Y/\bar{X}$ (Relative Turbulence)	.78	.72	.42	2.22	1.93	2.60
$S_X/\bar{Y}$ (Relative Turbulence)	-.32	-.29	-.26	-.36	-.34	-.31
Wind Standard dev. along Maj. Axis	.60	.66	.97	.62	.74	1.10
Wind Standard dev. along Min. Axis	.31	.44	.38	.33	.41	.39
Angle of Rotation of Maj. Axis	14.31	6.85	1.75	4.02	1.75	1.69

Table D.2. Bivariate Statistics of x- and y-components  
Canal Evening

CANAL: EVENING	CASE I: 2213 - 2230			CASE II: 2213 - 2320		
	1 m	1000 sec	4000 sec	1 m	1 m	21 m
Sampling Period						
Resultant Wind (deg/mps)	012/.81	009/1.66	009/2.35	007/.90	009/1.68	011/2.34
Degrees off Downstream	+ 12	+ 9	+ 9	+ 7	+ 9	+ 11
Vector Standard dev. of Wind	.27	.42	.34	.41	.65	1.10
Vector Coeff. of Variation	.34	.25	.15	.46	.39	.47
Mean E-W comp ( $\bar{X}$ )	-.16	-.26	-.37	-.12	-.27	-.46
Mean N-S comp ( $\bar{Y}$ )	-.79	-1.64	-2.32	-.89	-1.66	-2.29
Correlation Coeff.	-.08	-.23	-.79	-.19	-.10	-.18
Variance of x-comp	.04	.11	.03	.09	.31	.56
Variance of y-comp	.03	.06	.08	.08	.11	.65
Standard dev. of x-comp ( $S_X$ )	.21	.34	.18	.31	.56	.75
Standard dev. of y-comp ( $S_Y$ )	.17	.24	.29	.28	.33	.80
$S_Y/\bar{X}$ (Relative Turbulence)	-1.06	-.94	-.77	-2.34	-1.22	-1.74
$S_X/\bar{Y}$ (Relative Turbulence)	-.26	-.21	-.08	-.34	-.34	-.33
Wind Standard dev. along Maj. Axis	.21	.35	.33	.32	.56	.85
Wind Standard dev. along Min. Axis	.26	.23	.10	.26	.33	.70
Angle of Rotation of Maj. Axis	170	163	120	160	175	124

Table D.2. Bivariate Statistics of x- and y-components  
Canal Evening

	CASE III: 2320 - 0027			CASE IV: 2213 - 0027		
	1 m	7 m	27 m	1 m	7 m	27 m
CANAL: EVENING						
Sampling Period		4000 sec			8000 sec	
Resultant Wind (deg/mps)	347/1.16	345/2.09	342/3.18	356/1.01	356/1.84	355/2.67
Degrees off Downstream	-13	-15	-18	-4	-4	-5
Vector Standard dev. of Wind	.75	1.01	1.01	.65	.96	1.34
Vector Coeff. of Variation	.65	.48	.32	.64	.52	.50
Mean E-W comp ( $\bar{X}$ )	.26	.54	1.00	.07	.14	.27
Mean N-S comp ( $\bar{Y}$ )	-1.13	-2.02	-3.02	-1.01	-1.84	-2.66
Correlation Coeff.	.28	.33	.44	.03	-.03	-.27
Variance of x-comp	.38	.79	.82	.28	.70	1.23
Variance of y-comp	.18	.23	.21	.14	.20	.56
Standard dev. of x-comp ( $S_x$ )	.62	.89	.90	.52	.85	1.11
Standard dev. of y-comp ( $S_y$ )	.42	.47	.46	.38	.45	.75
$S_y/\bar{X}$ (Relative Turbulence)	1.60	.87	.46	5.13	3.24	2.80
$S_x/\bar{Y}$ (Relative Turbulence)	-.55	-.44	-.30	-.52	-.46	-.42
Wind Standard dev. along Maj. Axis	.64	.91	.93	.52	.85	1.14
Wind Standard dev. along Min. Axis	.39	.44	.40	.38	.45	.70
Angle of Rotation of Maj. Axis	17.52	13.20	15.54	2.21	-1.37	-17.08

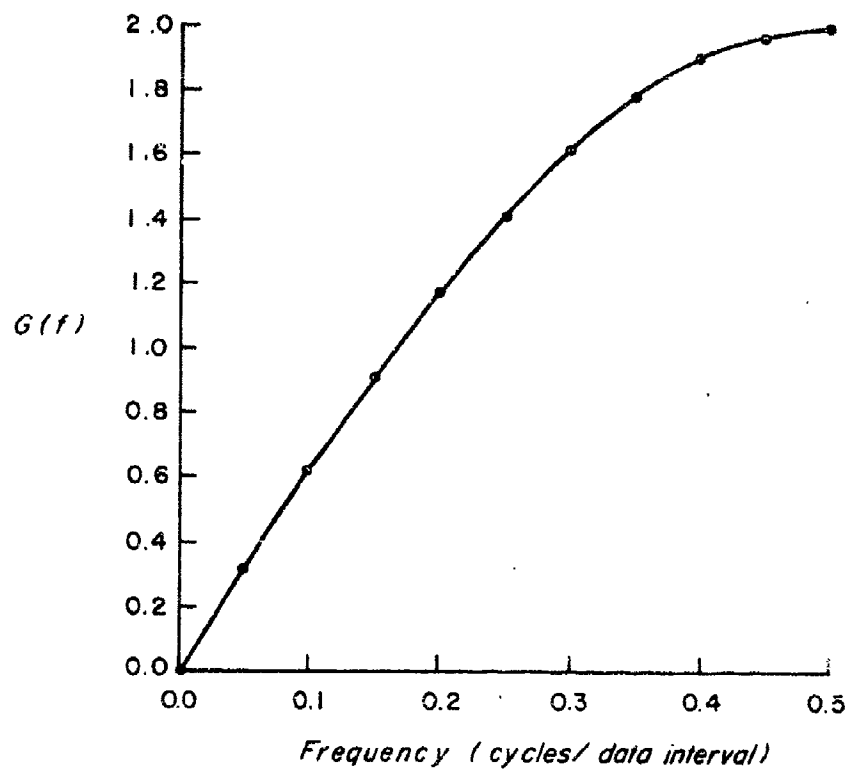


Fig. D.1 Gain Function for First Difference  
Filter  $y(t) = x(t) - x(t - 1)$

1. Computation of Gain Function for  $y(t) = x(t) - x(t - 1)$ :

The response function for  $x(t) - x(t - 1)$  is

$$H(f) = 1 - e^{-j2\pi f}$$

From complex variables:

$$\sin \pi f = \frac{e^{j2\pi f} - e^{-j2\pi f}}{2j}$$

multiplying by  $e^{-j2\pi f}$ ,

$$e^{-j2\pi f} \sin \pi f = \frac{1 - e^{-j2\pi f}}{2j}$$

or

$$2je^{-j\pi f} \sin \pi f = 1 - e^{-j2\pi f}$$

$$\text{therefore } H(f) = 2je^{-j\pi f} \sin \pi f$$

and the gain function,

$$\text{Gain}(f) = 2|\sin \pi f|$$

2. Spectral Estimate Multiplier:

The spectral estimate is multiplied by

$$1 - e^{-j2\pi f} \quad \text{using filter } y(t) = x(t) - x(t - 1)$$

therefore

$$(1 - e^{-j2\pi f})(1 - e^{-j2\pi f}) = 2 - 2e^{-j2\pi f}$$

$$= 2 - 2 \cos 2\pi f.$$

#### APPENDIX E

Profiles for the "Beach" Tower and "Canal" Towers (Evening Hours) of Dry  
and Wet Bulb Temperatures

Fig. E.1 Temperature Profiles 12/2200 - 13/0100 CDT, Beach Tower

Fig. E.2 Temperature Profiles 13/0000 - 0100 CDT, Canal Tower



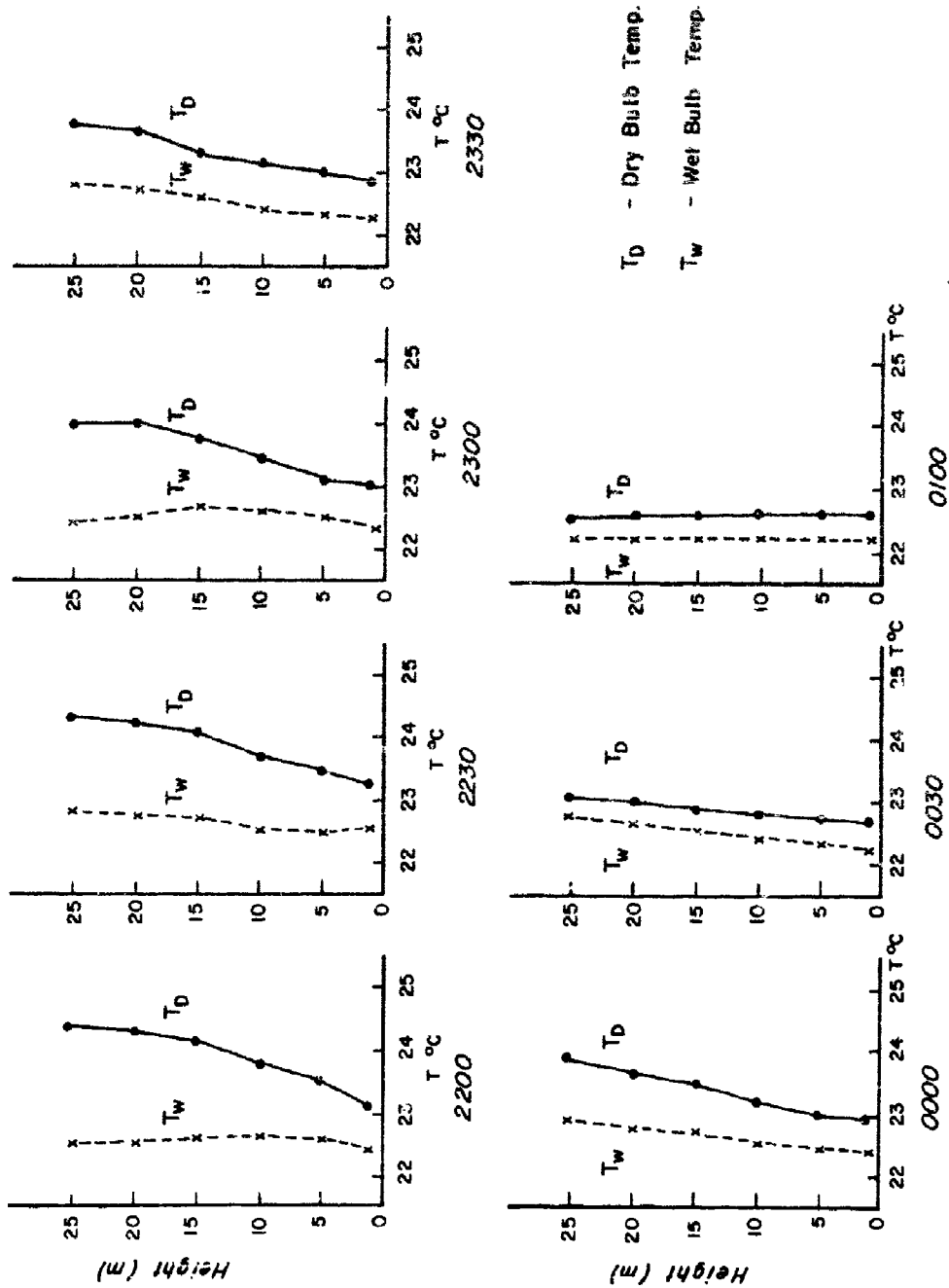


Fig. E.1 Temperature Profiles 12/2200 - 13/0100 CDT, Beach Tower

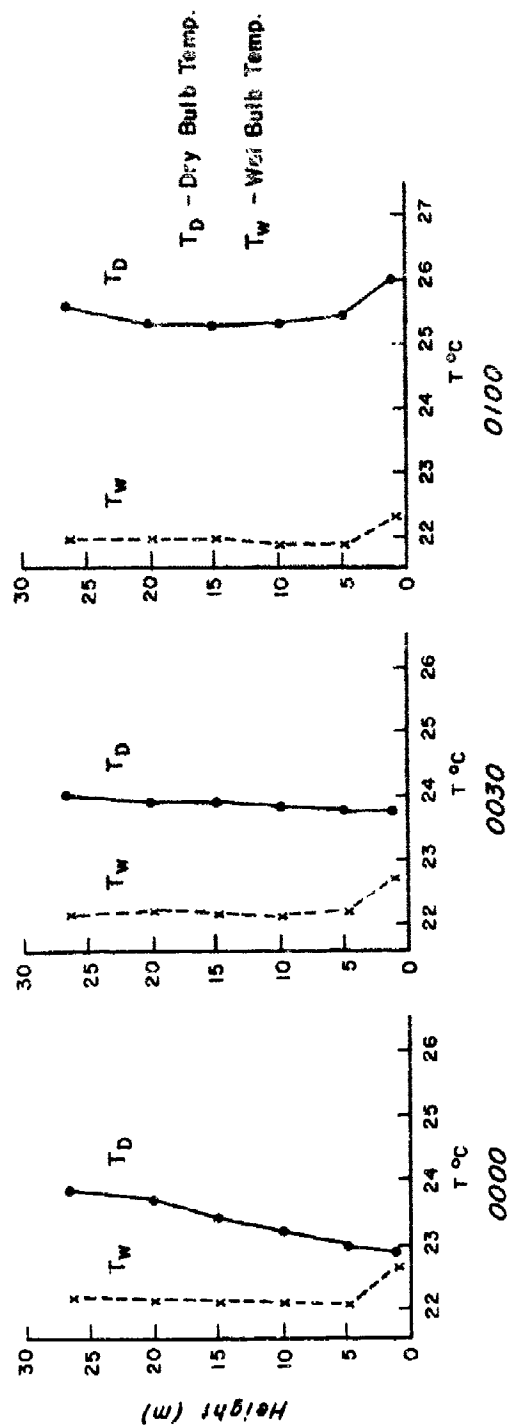


Fig. E.2 Temperature Profiles 13/000 - 0100 CDT,  
 Canal Tower

#### APPENDIX F

Table F.1 Bivariate Statistics of x- and y-components for Beach Daytime  
Samples

Table F.2 Bivariate Statistics of x- and y-components for Canal Daytime  
Samples

Table F.3 Bivariate Statistics of Wind Components After Axes Rotation for  
Beach Daytime Samples

Table F.4 Bivariate Statistics of Wind Components After Axes Rotation for  
Canal Daytime Samples

Table F.1. Bivariate Statistics of x- and y-components  
for Beach Daytime Samples

	CASE I - BD			CASE II - BD		
	1 m	7 m	27 m	1 m	7 m	27 m
Sampling Period (sec)		1000 sec (1000 - 1017 CDT)	097/2.22	128/2.60	1000 sec (1017 - 1034 CDT)	117/2.74
Resultant Wind Vector	093/1.80	113/1.82			149/2.67	
Vector Standard dev. of Wind Velocity	1.02	1.05	1.07	.94	.77	.79
Vector Coeff. of Variation	.57	.58	.48	.36	.29	.29
Mean E-W component ( $\bar{X}$ ) mps	-1.80	-1.67	-2.22	-2.06	-1.34	-2.45
Mean N-S component ( $\bar{Y}$ ) mps	-1.09	.72	-.12	1.59	2.26	1.23
Correlation Coefficient ( $R_{xy}$ )	-.19	.04	.01	.42	.19	.30
Variance of X-component $S_x^2$	.241	.55	.39	.38	.34	.25
Variance of Y-component $S_y^2$	.803	.56	.75	.50	.25	.36
Standard deviation $S_x$	.49	.74	.62	.62	.59	.51
$S_y$	.90	.75	.87	.71	.50	.60
$S_{\bar{X}}$	-.50	-.45	-.39	-.34	-.37	-.24
$S_{\bar{Y}}$	5.36	1.03	-5.15	.39	.26	.42
Wind Stand. dev. along Maj. Axis	.90	.76	.87	.80	.61	.64
Wind Stand. dev. along Min. Axis	.48	.73	.62	.50	.47	.46
Angle of Rotation of the Maj. Axis $\psi$	82	45	89	54	25	58

Table F.1. Bivariate Statistics of x- and y-components  
for Beach Daytime Samples

	CASE III - BD			CASE IV - BD		
	1 m	7 m	27 m	1 m	7 m	27 m
Sampling Period (sec)		1000 sec (1005 - 1022 CDT)			1000 sec (1047 - 1104 CDT)	
Resultant Wind Vector	106/1.90	129/1.75	100/2.31	147/2.59	167/2.66	143/2.85
Vector Standard dev. of Wind Velocity	1.15	1.09	1.14	.79	.50	.38
Vector Coeff. of Variation	.61	.62	.54	.30	.19	.13
Mean E-W component ( $\bar{X}$ ) mps	-1.63	-1.37	-2.10	-1.43	-.61	-1.70
Mean N-S component ( $\bar{Y}$ ) mps	.53	1.09	.36	2.16	2.59	2.29
Correlation Coefficient ( $R_{xy}$ )	-.50	.15	-.42	.49	.07	.22
Variance of X-component $S_x^2$	.26	.27	.25	.39	.20	.11
Variance of Y-component $S_y^2$	1.07	.91	1.06	.23	.05	.04
Standard deviation $S_x$	.51	.52	.50	.62	.44	.33
$S_y$	1.04	.95	1.03	.48	.23	.20
$S_y/\bar{X}$	-.57	-.70	-.49	-.34	-.38	-.12
$S_x/\bar{Y}$	.95	.48	1.39	.29	.17	.14
Wind Stand dev. along Maj. Axis	1.05	.96	1.06	.69	.44	.35
Wind Stand dev. along Min. Axis	.48	.52	.44	.38	.23	.20
Angle of Rotation of the Maj. Axis $\theta$	100	83	104	31	3	12

Table F.1. Bivariate Statistics of x- and y-components  
for Beach Daytime Samples

Sampling Period	CASE V - BD			CASE VI - BD		
	1 m	7 m	27 m	1 m	7 m	27 m
Resultant Wind Vector	154/2.68	4000 sec (1103 - 1120 CDT)	175/2.68	129/2.29	4000 sec (1000 - 1107 CDT)	122/2.53
Vector Standard dev. of Wind Velocity	.80	.45	.37	1.12	1.12	1.20
Vector Coeff. of Variation	.30	.17	.13	.49	.47	.47
Mean u component ( $\bar{X}$ ) mps	-1.19	-.24	-1.53	-1.79	-1.19	-2.13
Mean v component ( $\bar{Y}$ ) mps	2.40	2.67	2.50	1.43	2.03	1.35
Correlation Coefficient ( $R_{xy}$ )	.49	-.22	.08	.22	.43	.32
Variance of X-component $S_x^2$	.42	.13	.10	.28	.45	.28
Variance of Y-component $S_y^2$	.22	.07	.04	.98	.80	1.16
Standard deviation $S_x$	.65	.36	.31	.53	.67	.53
$S_y$	.47	.27	.20	.99	.90	1.08
$S_y/\bar{X}$	-.39	-1.14	-.13	-.55	-.75	-.51
$S_x/\bar{Y}$	.27	.14	.13	.37	.33	.39
Wind Stand dev. along Maj. Axis	.71	.37	.31	1.00	.97	1.09
Wind Stand dev. along Min. Axis	.38	.26	.20	.51	.56	.49
Angle of Rotation of the Maj. Axis $\psi$ 28		162	4	81	62	80

Table F.1. Bivariate Statistics of x- and y-components  
for Beach Daytime Samples

	CASE VII - BD		
	1 m	7 m	27 m
Sampling Period	4000 sec (1103 - 1214 GMT)		
Resultant Wind Vector	160/2.71	185/2.71	162/2.92
Vector Stand dev. of Wind Velocity	.69	.62	.61
Vector Coeff. of Variation	.25	.23	.21
Mean X component ( $\bar{X}$ ) mps	-.94	.27	-.92
Mean Y component ( $\bar{Y}$ ) mps	2.54	2.69	2.77
Correlation Coefficient ( $R_{xy}$ )	.52	.02	.59
Variance of -component $S_{\bar{x}}^2$	.30	.27	.27
Variance of -component $S_{\bar{y}}^2$	.18	.11	.10
Standard deviation $S_x$	.55	.52	.52
$S_y$	.42	.33	.32
$S_y/\bar{X}$	-.45	1.25	-.35
$S_x/\bar{Y}$	.21	.19	.19
Wind Stand dev. along Maj. Axis	.61	.52	.56
Wind Stand dev. along Min. Axis	.32	.33	.33
Angle of Rotation of the Maj. Axis $\psi$	32	1	24

Table F.2. Bivariate Statistics of x- and y-components  
for Canal Daytime Samples

	CASE I - CD				CASE II - CD			
	1 m	7 m	27 m	1 m	7 m	1000 sec	160/1.67	160/1.70
Sampling Period (sec)		1000 sec (1103 - 1120 CDT)	070/2.01	143/1.00	1000 sec (1155 - 1212 CDT)			
Resultant Wind Vector	068/1.38							
Vector Stand dev. of Wind Velocity	1.04	1.40	1.02	1.26	1.64			1.11
Vector Coeff. of Variation	.76	.66	.51	1.26	.98			.65
Mean E-W component ( $\bar{X}$ ) mps	-1.28	-2.06	-1.89	-.60	-.57			-.57
Mean N-S component ( $\bar{Y}$ ) mps	-.52	-.50	.70	.80	1.56			1.60
Correlation Coefficient ( $R_{xy}$ )	-.15	-.27	-.27	-.12	-.14			-.17
Variance of X-component ( $S_x^2$ )	.52	1.06	.68	.56	.78			.43
Variance of Y-component ( $S_y^2$ )	.57	.89	.37	1.04	1.90			.79
Standard deviation X-comp ( $S_x$ )	.72	1.03	.82	.75	.88			.66
Y-comp ( $S_y$ )	.75	.94	.61	1.02	1.38			.89
$S_y/\bar{X}$	-.59	-.46	-.32	-1.70	-2.41			-1.56
$S_x/\bar{Y}$	-1.38	-2.06	-1.18	-.93	.56			.41
Wind Stand dev. along Maj. Axis	.79	1.12	.85	1.03	1.39			.90
Wind Stand dev. along Min. Axis	.68	.84	.57	.74	.87			.64
Angle of Rotation of the Maj. Axis # 128		162	159	100	98			104



Table F.2. Bivariate Statistics of x- and y-components  
for Canal Daytime Samples

	CASE III - CD			CASE IV		
	1 m	7 m	27 m	1 m	7 m	27 m
Sampling Period (sec)		1000 sec (1236 - 1253 CDT)	157/2.36	4000 sec (1103 - 1210 CDT)		
Resultant Wind Vector	162/1.68	160/2.49		088/1.28	098/1.91	094/1.73
Vector Stand dev. of Wind Velocity	1.05	1.48	1.19	1.11	1.62	1.38
Vector Coeff. of Variation	.62	.60	.50	.87	.85	.80
Mean E-W component ( $\bar{X}$ ) mps	-.51	-.85	-.94	-1.28	-1.90	-1.72
Mean N-S component ( $\bar{Y}$ ) mps	1.60	2.34	2.16	-.05	.25	.12
Correlation Coefficient ( $R_{xy}$ )	.25	.13	.17	.05	.15	.34
Variance of X-component ( $S_x^2$ )	.67	1.16	.78	.53	1.20	.80
Variance of Y-component ( $S_y^2$ )	.44	1.04	.63	.71	1.42	1.11
Standard deviation X-comp ( $S_x$ )	.82	1.08	.58	.73	1.09	.89
Y-comp ( $S_y$ )	.66	1.02	.79	.84	1.19	1.05
$S_y/\bar{X}$	-1.30	-1.19	-.84	-.66	-.63	-.61
$S_x/\bar{Y}$	.51	.46	.41	-13.64	4.31	7.37
Wind Stand dev. along Maj. Axis	.85	1.12	.92	.84	1.24	1.14
Wind Stand dev. along Min. Axis	.61	.97	.75	.72	1.04	.78
Angle of Rotation of the Maj. Axis $\psi$	25	34	29	80	60	58

Table F.2. Bivariate Statistics of x- and y-components  
for Canal Daytime Samples

	CASE V - CD			CASE VI - CD		
	1 m	7 m	27 m	1 m	7 m	27 m
Sampling Period (sec)		4000 sec (1155 - 1302 CDT)	163/2.22	168/1.60	4000 sec (1210 - 1310 CDT)	166/2.21
Resultant Wind Vector	166/1.51	172/2.37	1.12	1.08	173/2.40	1.11
Vector Stand dev. of Wind Velocity	1.18	1.62	.50	.67	.63	.50
Vector Coeff. of Variation	.78	.68	-.63	-.32	-.28	-.63
Mean E-W component ( $\bar{X}$ ) mps	-.36	-.34	2.13	1.57	2.38	2.12
Mean N-S component ( $\bar{Y}$ ) mps	1.47	2.34	.06	.16	.09	.11
Correlation Coefficient ( $R_{xy}$ )	.15	.06	.67	.70	1.37	.66
Variance of x-component ( $S_x^2$ )	.71	1.39	.59	.46	.88	.57
Variance of y-component ( $S_y^2$ )	.67	1.23	.82	.84	1.17	.81
Standard deviation X-comp ( $S_x$ )	.84	1.18	.77	.68	.94	.75
Y-comp ( $S_y$ )	.82	1.11	-1.21	-2.10	-3.32	-1.20
$S_y/\bar{X}$	-2.30	-3.30	.38	.53	.49	.38
$S_x/\bar{Y}$	.57	.50	.83	.86	1.18	.83
Wind Stand dev. along Maj. Axis	.89	1.19	.76	.65	.93	.73
Wind Stand dev. along Min. Axis	.76	1.09	.23	.18	.11	.28
Angle of Rotation of the Maj. Axis	39	22				

Table F.2. Bivariate Statistics of x- and y-components  
for Canal Daytime Samples

	CASE VII - CD		
	1 m	7 m	27 m
Sampling Period (sec)	8000 sec (1103 - 1317 CDT)		
Resultant Wind Vector	134/1.10	140/1.71	134/1.63
Vector Stand dev. of Wind Velocity	1.42	2.02	1.67
Vector Coeff. of Variation	1.28	1.18	1.03
Mean E-W component ( $\bar{X}$ ) mps	-.80	-1.09	-1.18
Mean N-S component ( $\bar{Y}$ ) mps	.76	1.32	1.12
Correlation Coefficient	.46	.50	.55
Variance of X-component ( $S_x^2$ )	.80	1.86	.99
Variance of Y-component ( $S_y^2$ )	1.21	2.21	1.81
Standard deviation X-comp ( $S_x$ )	.89	1.36	.99
Y-comp ( $S_y$ )	1.10	1.49	1.34
$S_y/\bar{X}$	-1.37	-1.37	-1.14
$S_x/\bar{Y}$	1.18	1.04	.89
Wind Stand dev. along Maj. Axis	1.23	1.75	1.50
Wind Stand dev. along Min. Axis	.71	1.01	.74
Angle of Rotation of the Maj. Axis	57	50	59

Table F.3. Bivariate Statistics of Wind Components After Axis  
Rotation for Beach Daytime Samples

	CASE I - BD				CASE II - BD			
	1 m		7 m		1 m		7 m	
	1000 sec (1000 - 1017 CDT)	200/1.82	1.05	270/2.22	270/2.60	1000 sec (1017 - 1034 CDT)	270/2.62	270/2.74
Sampling Period (sec)	270/1.80	1.02						
Downstream Vector								
Vector Stand dev. of Wind Velocity								
Vector Coeff. of Variation								
Mean Longitudinal Comp. ( $\bar{u}$ ) mps								
Mean Lateral Comp. ( $\bar{v}$ ) mps								
Correlation Coefficient ( $R_{uv}$ )								
Variance of u-component $S_u^2$								
Variance of v-component $S_v^2$								
Standard deviation (Long.) $S_u$								
(Lat.) $S_v$								
Intensity of Turbulence $ S_u/\bar{u} $								
Relative Gustiness $ S_v/\bar{v} $								
Wind Stand dev. along Maj. Axis								
Wind Stand dev. along Min. Axis								
Angle of Rotation of the Maj. Axis $\theta$								
Skewness:								
Long. u-comp								
Lat. v-comp								
Kurtosis:								
Long. u-comp								
Lat. v-comp								

Table F.3. Bivariate Statistics of Wind Components After Axis  
Rotation for Beach Daytime Samples

	CASE III - BD				CASE IV - BD			
	1 m	7 m	27 m	1000 sec (1005 - 1022 CDT)	1 m	7 m	27 m	1000 sec (1047 - 1104 CDT)
Sampling Period (sec)	270/1.90	270/1.75	270/2.13	270/2.59	270/2.66	270/2.85		
Downstream Vector	1.15	1.09	1.14	.79	.50	.38		
Vector Stand dev. of Wind Velocity	.61	.62	.54	.30	.19	.13		
Vector Coeff. of Variation	-1.90	-1.75	-2.13	-2.59	-2.66	-2.85		
Mean Longitudinal Comp. ( $\bar{u}$ ) mps	.00	.00	.00	.00	.00	.00		
Mean Lateral Comp. ( $\bar{v}$ ) mps	.57	.51	.59	-.06	-.24	-.38		
Correlation Coefficient ( $R_{uv}$ )	.404	.448	.340	.143	.058	.050		
Variance of u-component $S_u^2$	.926	.736	.967	.47	.191	.097		
Variance of v-component $S_v^2$	.64	.67	.58	.38	.24	.22		
Standard deviation (Long.) $S_u$	.96	.86	.98	.69	.44	.31		
(Lat.) $S_v$	.33	.38	.27	.15	.09	.08		
Intensity of Turbulence $ S_u/\bar{u} $	.51	.49	.46	.27	.16	.11		
Relative Gustiness $ S_v/\bar{v} $	1.05	.96	1.06	.69	.44	.33		
Wind Stand dev. along Maj. Axis	.48	.52	.44	.38	.23	.20		
Wind Stand dev. along Min. Axis								
Angle of Rotation of the Maj. Axis $\psi$ 116	122	114	93	80	66			
Skewness:								
Long. u-comp	.623	.298	1.824	.103	.048	-.080		
Lat. v-comp	-.023	-.002	.190	-.222	-.204	-.011		
Kurtosis:								
Long. u-comp	-.127	-.131	9.790	-.648	-.514	-.648		
Lat. v-comp	.060	-.425	-1.080	.326	.564	.239		

Table F.3. Bivariate Statistics of Wind Components After Axis  
Rotation for Beach Daytime Samples

	CASE V - BD				CASE VI - BD			
	1 m	7 m	27 m	1 m	7 m	27 m	1 m	27 m
Sampling Period (sec)	1000 sec (1103 - 1120 CDT)				4000 sec (1000 - 1107 CDT)			
Downstream Vector	270/2.68	270/2.68	270/2.93	270/2.29	270/2.36	270/2.53	270/2.36	270/2.53
Vector Stand dev. of Wind Velocity	.80	.45	.37	.12	1.12	1.20	.47	.47
Vector Coeff. of Variation	.30	.17	.13	.49	.47	.47	.47	.47
Mean Longitudinal Comp. ( $\bar{u}$ ) mps	-2.68	-2.68	-2.93	-2.29	-2.36	-2.53	-2.36	-2.53
Mean Lateral Comp. ( $\bar{v}$ ) mps	.00	.00	.00	.00	.00	.00	.00	.00
Correlation Coefficient ( $R_{uv}$ )	.03	-.27	-.37	.53	.46	.52	.46	.52
Variance of u-component $S_u^2$	.141	.08	.051	.439	.488	.368	.488	.368
Variance of v-component $S_v^2$	.502	.128	.086	.818	.760	1.071	.760	1.071
Standard deviation (Long.) $S_u$	.38	.28	.22	.66	.70	.61	.70	.61
(Lat.) $S_v$	.71	.36	.29	.90	.87	1.04	.87	1.04
Intensity of Turbulence $ S_u/\bar{u} $	.14	.10	.07	.29	.30	.24	.30	.24
Relative Gustiness $ S_v/\bar{v} $	.26	.13	.10	.39	.37	.41	.37	.41
Wind Stand dev. along Maj. Axis	.71	.37	.31	1.00	.97	1.09	.97	1.09
Wind Stand dev. along Min. Axis	.36	.26	.20	.51	.56	.49	.56	.49
Angle of Rotation of the Maj. Axis	91	67	63	120	122	111	122	111
Skewness:								
Long. u-comp	.403	.268	-.085	1.192	1.346	1.537	1.346	1.537
Lat. v-comp	.306	-.215	-.209	.279	.756	.672	.756	.672
Kurtosis								
Long. u-comp	-.043	-.250	.224	1.332	1.377	3.137	1.377	3.137
Lat. v-comp	-.612	.029	-.285	-.631	.271	-.481	.271	-.481

Table F.3. Bivariate Statistics of Wind Components After Axis  
Rotation for Beach Daytime Samples

	CASE VII - ED		
	1 m	7 m	27 m
Sampling Period (sec)	4000 sec (1103 - 1214 CDT)		
Downstream Vector	270/2.71	270/2.71	270/2.92
Vector Stand dev. of Wind Velocity	.69	.62	.61
Vector Coeff. of Variation	.25	.23	.21
Mean Longitudinal Comp. ( $\bar{u}$ ) mps	-2.71	-2.71	-2.92
Mean Lateral Comp. ( $\bar{v}$ ) mps	.00	.00	.00
Correlation Coefficient ( $R_{uv}$ )	.25	.11	.20
Variance of u-component $S_u^2$	.113	.112	.060
Variance of v-component $S_v^2$	.361	.271	.313
Standard deviation (Long.) $S_u$	.34	.33	.24
(Lat.) $S_v$	.60	.52	.56
Intensity of Turbulence $ S_u/\bar{u} $	.13	.12	.09
Relative Gustiness $ S_v/\bar{v} $	.22	.19	.19
Wind Stand dev. along Maj. Axis	.61	.52	.56
Wind Stand dev. along Min. Axis	.32	.33	.24
Angle of Rotation of the Maj. Axis	101	97	96
Skewness:			
Long. u-comp	.150	.325	.201
Lat. v-comp	.175	-.253	-.006
Kurtosis			
Long. u-comp	-.168	.536	1.307
Lat. v-comp	-.436	-.260	-.536

Table F.4. Bivariate Statistics of Wind Components After Axis  
Rotation for Canal Daytime Samples

	CASE I - CD				CASE II - CD			
	1 m	7 m	27 m	1000 sec (1103 - 1120 CDT)	1 m	7 m	27 m	1000 sec (1155 - 1212 CDT)
Sampling Period (sec)	270/1.38	270/2.12	270/2.01	270/1.67	270/1.00	270/1.67	270/1.70	
Downstream Vector	1.04	1.40	1.02	1.26	1.64	1.11	1.65	
Vector Stand dev. of Wind Velocity	.76	.66	.51	1.26	.98	1.67	1.70	
Vector Coeff. of Variation	-1.38	-2.12	-2.01	.00	.00	.26	.07	
Mean Longitudinal Component ( $\bar{u}$ ) mps	.00	.28	.38	.553	.641	.802	.813	
Mean Lateral Component ( $\bar{v}$ ) mps	.08	.931	.495	.98	1.37	.90	.64	
Correlation Coefficient ( $R_{uv}$ )	.471	1.021	.74	.80	.90	.82	.53	
Variance of u-component $S_u^2$	.618	.97	.70	.37	.35	.80	.38	
Variance of v-component $S_v^2$	.69	1.01	.37	.85	1.03	1.39	.90	
Standard deviation (Long.) $S_u$	.79	.46	.57	.84	.74	.87	.64	
(Lat.) $S_v$	.50	.57	.79	.68	.154	168	174	
Intensity of Turbulence $ S_u/\bar{u} $	.79	1.12	.85	.57	.588	.484	.098	
Relative Gustiness $ S_v/\bar{v} $	.79	.84	.57	.57	.034	-.008	-.190	
Wind Stand dev. along Maj. Axis	.68	1.30	1.39	3.640	-.484	-.586	-.859	
Wind Stand dev. along Min. Axis	.358	.154	.764	-.274	-.326	-.427	-.030	
Angle of Rotation of the Maj. Axis	105	130	139					
Skewness:								
Long. u-comp	.358	.513	1.073					
Lat. v-comp	.154	.438	.255					
Kurtosis:								
Long. u-comp	.764	2.006	3.640					
Lat. v-comp	-.274	-.473	-.233					



Table F.4. Bivariate Statistics of Wind Components After Axes  
Rotation for Canal Daytime Samples

	CASE III - CD				CASE IV - CD			
	1 m		7 m		1 m		7 m	
	270/1.68	1000 sec (1237 - 1253 CDT)	270/2.49	4000 sec (1163 - 1210 CDT)	270/1.28	270/1.91	270/1.73	270/1.73
Sampling Period (sec)								
Downstream Vector								
Vector Stand dev. of Wind Velocity	1.05		1.48		1.11	1.62	1.38	
Vector Coeff. of Variation	.62		.60		.87	.85	.80	
Mean Longitudinal Component ( $\bar{u}$ ) mps	-1.68		-2.49		-1.28	-1.91	-1.73	
Mean Lateral Component ( $\bar{v}$ ) mps	.00		.00		.00	.00	.00	
Correlation Coefficient ( $R_{uv}$ )	.08		.07		-.06	-.12	-.31	
Variance of u-component $S_u^2$	.380		.957		.561	1.149	.757	
Variance of v-component $S_v^2$	.724		1.242		.846	1.462	1.152	
Standard deviation (Long.) $S_u$	.62		.98		.75	1.07	.87	
(Lat.) $S_v$	.85		1.11		.840	1.21	1.07	
Intensity of Turbulence $ S_u/\bar{U} $	.37		.39		.57	.54	.50	
Relative Gustiness $ S_v/\bar{V} $	.85		.45		.66	.63	.62	
Wind Stand dev. along Maj. Axis	.85		1.12		.84	1.24	1.14	
Wind Stand dev. along Min. Axis	.61		.97		.72	1.04	.78	
Angle of Rotation of the Maj. Axis	7	14			168	158	152	
Skewness:								
Long. u-comp	-.162		-.287		.390	.303	.323	
Lat. v-comp	-.053		.038		-.550	-.788	-.867	
Kurtosis:								
Long. u-comp	-.415		-.650		.497	-.147	-.251	
Lat. v-comp	-.284		-.661		.150	.248	.117	

Table F.4. Bivariate Statistics of Wind Components After Axes  
Rotation for Canal Daytime Samples

	CASE V - CD			CASE VI - CD		
	1 m	7 m	27 m	1 m	7 m	27 m
Sampling Period (sec)	4000 sec (1155 - 1302 CDT)			4000 sec (1210 - 1317 CDT)		
Downstream Vector	270/1.51	270/2.37	270/2.22	270/1.60	270/2.40	270/2.21
Vector Stand dev. of Wind Velocity	1.18	1.62	1.12	1.08	1.50	1.11
Vector Coeff. of Variation	.78	.68	.50	.67	.63	.50
Mean Longitudinal Component ( $\bar{u}$ ) mps	-1.51	-2.37	-2.22	-1.60	-2.40	-2.21
Mean Lateral Component ( $\bar{v}$ ) mps	.00	.00	.00	.00	.00	.00
Correlation Coefficient ( $R_{uv}$ )	.12	.04	.02	.06	.04	.05
Variance of u-component $S_u^2$	.623	1.206	.576	.431	.867	.536
Variance of v-component $S_v^2$	.758	1.413	.683	.729	1.385	.690
Standard deviation (Long.) $S_u$	.79	1.10	.76	.66	.93	.73
(Lat.) $S_v$	.87	1.19	.83	.85	1.18	.83
Intensity of Turbulence $ S_u'/\bar{u} $	.52	.47	.34	.41	.38	.33
Relative Gustiness $ S_v'/\bar{v} $	.58	.50	.37	.53	.49	.38
Wind Stand dev. along Maj. Axis	.89	1.19	.83	.86	1.18	.83
Wind Stand dev. along Min. Axis	.76	1.09	.76	.65	.93	.73
Angle of Rotation of the Maj. Axis	115	104	97	97	94	102
Skewness:						
Long. u-comp	.972	.867	.554	.691	.282	.491
Lat. v-comp	-.195	-.270	-.182	-.105	-.163	-.120
Kurtosis:						
Long. u-comp	1.141	.987	.083	1.221	-.153	.101
Lat. v-comp	-.399	-.490	-.078	-.349	-.447	-.222

Table F.4. Bivariate Statistics of Wind Components After Axes  
Rotation for Canal Daytime Samples

	CASE VII - CD			
	1 m	7 m	27 m	
Sampling Period (sec)	8000 sec (1103 - 1317 CDT)			
Downstream Vector	270/1.10	270/1.71	270/1.63	
Vector Stand dev. of Wind Velocity	1.42	2.02	1.67	
Vector Coeff. of Variation	1.28	1.18	1.03	
Mean Longitudinal Component ( $\bar{u}$ ) mps	-1.10	-1.71	-1.63	
Mean Lateral Component ( $\bar{v}$ ) mps	.00	.00	.00	
Correlation Coefficient ( $R_{uv}$ )	.20	.20	.32	
Variance of u-component $S_u^2$	.541	1.078	.638	
Variance of v-component $S_v^2$	1.467	2.992	2.156	
Standard deviation (Long.) $S_u$	.74	1.04	.80	
(Lat.) $S_v$	1.21	1.73	1.47	
Intensity of Turbulence $ S_u/\bar{U} $	.67	.61	.49	
Relative Gustiness $ S_v/\bar{U} $	1.10	1.01	.90	
Wind Stand dev. along Maj. Axis	1.23	1.75	1.50	
Wind Stand dev. along Min. Axis	.71	1.01	.74	
Angle of Rotation of the Maj. Axis	101	100	103	
Skewness: Long. u-comp	.366	.239	.233	
Lat. v-comp	-.069	-.054	.137	
Skewness: Long. u-comp	.146	.259	-.279	
Lat. v-comp	-1.045	-1.064	-1.262	

## BIBLIOGRAPHY

- Almazan, J. A., "A Cross-Spectrum Analysis Technique for Evaluating Wind Sensors." Report No. 10, Atmospheric Science Group, The University of Texas at Austin. 72 pp.
- Amos, D. E. and L. H. Koopmans, 1963: "Tables of the Distribution of the Coefficient of Coherence for Stationary Bivariate Gaussian Processes." Monograph SCR-483, Sandia Corp., Albuquerque, N. M.
- Bogart, B. P., M. J. R. Healy, and J. W. Tukey, 1962: "The Frequency Analysis of Time Series for Echoes: Cepstrum, Pseudo-Autocovariances, Cross-Cepstrum and Saphe Cracking." Chapter 15, Proceedings of the Symposium on Time Series Analysis, Ed. by M. Rosenblatt, John Wiley, New York. 497 pp.
- Bendat, S., A. G. Piersol 1966: Measurement and Analysis of Random Data. John Wiley, New York. 390 pp.
- Blackman, R. B., 1965: Linear Data-Smoothing and Prediction in Theory and Practice. Addison-Wesley Pub. Co., Mass. 182 pp.
- Blackman, R. B., and J. W. Turkey, 1958: The Measurement of Power Spectra (from the Point of View of Communications Engineering). Dover Publications, New York. 190 pp.
- Brooks, C. E. P. and N. Carruthers, 1953: Handbook of Statistical Methods in Meteorology. Her Majesty's Stationary Office, London. 412 pp.
- Carslaw, H. S., 1950: Introduction to the Theory of Fourier's Series and Integrals. 3rd Edition, Dover Pub., New York. 168 pp.
- Charney, J. G., Chairman, 1969: "Plan for U. S. Comm. for the Glob. Atmos. Res. Prog., National Academy of Science, Wash., D. C., 79 pp.

- Corrsin, S. 1963: "Estimates of the Relations between Eulerian and Lagrangian Scales in Large Reynolds Number Turbulence." J. Atmos. Sci., Vol. 20, pp. 115-119.
- Crutcher, H. L., 1957: "On the Standard Vector Deviation Wind Rose." J. Meteor., Vol. 14, pp. 28-33.
- Duchon, C. E., 1968: "Techniques for Evaluating Meteorological Aircraft Data," Report No. 9, Atmospheric Science Group, The University of Texas at Austin, 93 pp.
- Eddy, A., C. E. Duchon, and J. A. Almazan, 1968: "Variance Spectrum Analysis." Report No. 8, Atmospheric Science Group, The University of Texas at Austin, 356 pp.
- Ely, R. P. Jr., 1958: "Spectral Analysis of the u-Component of Wind Velocity at three Meters." J. Meteor., Vol. 15, pp. 196-201.
- Feit, D. M., 1969: "Analysis of the Texas Coast Land Breeze." Report No. 18, Atmospheric Science Group, The University of Texas at Austin, 52 pp.
- Gentleman, W. M. and G. Sande, 1966: "Fast Fourier Transforms - For Fun and Profit." Proc. Fall Joint Compu. Conf., pp. 563-578.
- Gilman, D. L., F. L. Fuglister and J. M. Mitchell, Jr., 1963: "On the Power Spectrum of 'Red Noise'." J. Atmos. Sci., Vol. 20, pp. 182-184.
- Haurwitz, B., 1968: Lecture Notes on Advanced Dynamic Meteorology, Course No. C. E. 396M.6, The University of Texas at Austin. (Unpublished)
- Hsu, S. A., 1967: "Mesoscale Surface Temperature Characteristics of the Texas Coast Sea Breeze." Report No. 6, Atmospheric Science Group, The University of Texas at Austin. 74 pp.
- \_\_\_\_\_, 1969: "Mesoscale Structure of the Texas Coast Sea Breeze." Report No. 16, Atmospheric Science Group, The University of Texas at Austin, 237 pp.

- Kuettner, J. P. and J. Holland, 1969: "The BOMEX Project," *Bul. Amer. Meteorol. Soc.*, Vol. 50, pp. 394-402.
- Lapp, U. O. and B. Davidson, 1963: "On the Range of Validity of Taylor's Hypothesis and the Kolmogoroff Spectral Law." *J. Atmos. Sci.*, Vol. 20, pp. 569-576.
- Lumley, J. L., 1962: "Statistical Description of Turbulence," *Encyclopedia Dictionary of Physics*. Ed. by J. Thewlis, Pergamon Press, London, pp. 501-505.
- \_\_\_\_\_ and H. A. Panofsky, 1964: *The Structure of Atmospheric Turbulence*. Interscience Pub., John Wiley, New York, 239 pp.
- McPherson, R. D., 1968: "A Three-Dimensional Numerical Study of the Texas Coast Sea Breeze." Report No. 15, Atmospheric Science Group, The University of Texas at Austin, 252 pp.
- Mitchell, J. M., Jr., 1966: "Tables of Selected Coherence ( $R$ ) and Squared Coherence ( $R^2$ ) (for Special Case of Zero Coherence in Population)." Lab. for Environ. Data Res., ESSA, Wash., D. C., Unpublished Manuscript.
- Munn, R. E., 1966: "Descriptive Micrometeorology." Academic Press, New York, 245 pp.
- Panofsky, H. A., H. E. Cramer, and V. R. R. Rao, 1958: "The Relation of Eulerian Time and Space Spectra." *Quart. J. R. Meteor. Soc.*, Vol. 84, pp. 270-273.
- Pasquill, F., 1963: "Relations Between the Lagrangian and Eulerian Properties of Turbulence." *J. Atmos. Sci.*, Vol. 20, pp. 621-622.
- Taylor, G. I., 1921: "Diffusion by Continuous Movements." *Proc. London Math. Soc.*, 2nd Series, Vol. 20, pp. 196-212.

- \_\_\_\_\_, 1935: "Statistical Theory of Turbulence." Proc. R. Soc. (London), No. 873, Vol. A151, pp. 421-478.
- \_\_\_\_\_, 1938: "The Spectrum of Turbulence." Proc. R. Soc. (London), No. 919, Vol. A164, pp. 476-490.
- \_\_\_\_\_ and A. E. Greene, 1937: "Mechanism of the Production of Small Eddies from Large Ones." Proc. R. Soc. (London), No. 895, Vol. A163, pp. 499-521.
- Tukey, J. W., 1967: "An Introduction to the Calculations of Numerical Spectrum Analysis." Spectral Analysis of Time Series, pp. 25-46. Ed. by B. Harris. John Wiley, New York. 319 pp.